Itziar Ríos Ruiz

Exploring Vascular Damage: Mechanisms in Aortic Dissection, Atherosclerosis and Stent Implantation

Director/es

Martínez Barca, Miguel Ángel
Peña Baquedano, Estefanía

Universidad Zaragoza
1542

Tesis Doctoral

EXPLORING VASCULAR DAMAGE: MECHANISMS IN AORTIC DISSECTION, ATHEROSCLEROSIS AND STENT IMPLANTATION

Autor

Itziar Ríos Ruiz

Director/es

Martínez Barca, Miguel Ángel
Peña Baquedano, Estefanía

UNIVERSIDAD DE ZARAGOZA
Escuela de Doctorado

Programa de Doctorado en Ingeniería Biomédica

2023

Universidad Zaragoza
1542

Tesis Doctoral

Exploring Vascular Damage: Mechanisms in Aortic Dissection, Atherosclerosis and Stent Implantation

Autor

Itziar Ríos Ruiz

Directores

## Miguel Ángel Martínez Barca
Estefanía Peña Baquedano

Escuela de Ingeniería y Arquitectura
2023

Exploring Vascular Damage: Mechanisms in Aortic Dissection, Atherosclerosis and Stent Implantation

Author: Itziar Ríos Ruiz

Supervisor: Prof. Miguel Ángel Martínez
Co-supervisor: Prof. Estefanía Peña

Department of Mechanical Engineering
University of Zaragoza

Summary

Cardiovascular diseases remain the leading cause of death globally, and their prevalence continues to rise. These diseases are complex, involving multiple biological, chemical and mechanical factors in their development. Despite significant advances in medical research and technology, there are still gaps in our understanding of the mechanisms underlying the generation and progression of these diseases. In recent years, there has been increasing recognition of the importance of mechanical factors in the development of vascular diseases. This has led to significant progress in our understanding of these diseases and in the design of more effective treatment strategies.

Specifically, research into the impact of mechanical damage in cardiovascular diseases has emerged as a rapidly growing area of investigation. Mechanical damage plays a critical role in the initiation and progression of many cardiovascular diseases, including arterial dissection, atherosclerosis and in-stent restenosis. However, studying mechanical damage in the context of cardiovascular diseases can be challenging due to the complex and dynamic nature of the mechanical forces involved. Additionally, the cellular and molecular mechanisms underlying the response to mechanical damage are complex and interconnected, involving multiple signaling pathways and feedback loops. Therefore, studying the role of mechanical damage in cardiovascular diseases requires an interdisciplinary approach that integrates engineering, biology and medicine, as well as advanced experimental and computational methods.

This thesis explores the role of mechanical damage in the initiation and development of three vascular diseases: aortic dissection, atherosclerosis and in-stent restenosis. Our approach to studying these diseases has been broad, using various methodologies that we deemed most appropriate for each specific field of knowledge. For aortic dissection, we focused on studying the propagation of a tear by characterising the dissection properties of the vessel at the tissue level using in vitro and in silico methods. Atherosclerosis was studied at the cellular level, as we investigated the impact of mechanical tangential stress on the permeability of vascular endothelial cells in the initiation and progression of the disease. Finally, we addressed in-stent restenosis by testing a novel tool to detect and quantify the damage caused by stent struts to collagen in vessels, which is potentially linked to the development of this disease. Through these studies, we aim to contribute to a deeper understanding of the complex mechanisms of mechanical damage in vascular diseases, which could eventually lead to the development of more effective treatment strategies.

Resumen

Las enfermedades cardiovasculares son la principal causa de muerte a nivel mundial y su prevalencia sigue aumentando. Estas enfermedades son complejas e involucran múltiples factores biológicos, químicos y mecánicos. A pesar de los avances significativos en la investigación médica y tecnológica, todavía existen lagunas en nuestra comprensión de los mecanismos que subyacen a la aparición y progresión de estas enfermedades. En los últimos años, se ha experimentado un progreso significativo en el conocimiento de estas enfermedades a través del estudio de los factores mecánicos subyacentes, lo que ha permitido diseñar estrategias de tratamiento más efectivas.

En concreto, el daño mecánico juega un papel crítico en la iniciación y progresión de muchas enfermedades cardiovasculares, como la disección arterial, la aterosclerosis y la reestenosis intrastent. Sin embargo, el estudio del daño mecánico en el contexto de las enfermedades cardiovasculares es aún un reto debido a la naturaleza compleja y dinámica de las fuerzas mecánicas involucradas. Además, los mecanismos celulares y moleculares que subyacen en la respuesta al daño mecánico son complejos, están interconectados e involucran múltiples vías de señalización y retroalimentación. Por lo tanto, el estudio del papel del daño mecánico en las enfermedades cardiovasculares requiere de un enfoque interdisciplinar que integre la ingeniería, la biología y la medicina, así como de métodos experimentales y computacionales avanzados.

Esta tesis explora el papel del daño mecánico en la iniciación y el desarrollo de tres enfermedades vasculares: la disección aórtica, la aterosclerosis y la reestenosis intrastent. Nuestro enfoque para estudiar estas enfermedades ha sido amplio, y hemos empleado varias metodologías que consideramos más apropiadas para cada campo específico. Para la disección aórtica, nos enfocamos en estudiar la propagación de una delaminación mediante la caracterización de las propiedades de disección del vaso a nivel tisular, utilizando métodos in vitro e in silico. La aterosclerosis se estudió a nivel celular, ya que investigamos el impacto la tensión tangencial mecánica sobre la permeabilidad de las células endoteliales, tanto en la iniciación como en la progresión de la enfermedad. Finalmente, abordamos la reestenosis intrastent analizando una nueva herramienta para detectar y cuantificar el daño que causan las varillas del stent en el colágeno de los vasos, daño que podría estar relacionado con el desarrollo de esta lesión. A través de estos estudios, nuestro objetivo ha sido contribuir a una comprensión más profunda de los mecanismos complejos del daño mecánico en las enfermedades vasculares, lo que podría eventualmente conducir al desarrollo de estrategias de tratamiento más efectivas.

Agradecimientos

Resulta imposible, después de tantos años tan intensos, poder compactar en unas pocas palabras lo que agradezco a la gente que me ha acompañado en este camino. Ojalá os haya transmitido mi agradecimiento en el día a día, ojalá estas palabras signifiquen algo para vosotros y ojalá sigamos compartiendo experiencias que poder agradecer.

En primer lugar, os quiero dar las gracias, Fany y Miguel Ángel, por haberme guiado y acompañado todos estos años. Descubrir la bioingeniería ha sido descubrir una vocación. Como buena tesis que se precie, no ha sido un camino de rosas, pero gracias por haber estado en los momentos de euforia y haberme guiado en los de angustia.

Gracias, Carlos y Álex, por todo el apoyo en los experimentos, pero sobre todo por los buenísimos ratos en el laboratorio. Gracias, Sara, Tea, Sandra y demás compañeros del laboratorio celular, por haberme ayudado siempre que lo he necesitado y haberme hecho sentir una más. Gracias, Olaya, Nerea y Lorena, por haber decidido probar el mundo de la investigación con nosotras. Gracias, Begoña, por todo tu apoyo directo e indirecto.

Gracias a mis compañeros del Lally Lab en Dublín. Fue un placer trabajar (¡y disfrutar!) con todos vosotros. Gracias, Tríona, por dejarme pasar unos meses en tu grupo y enseñarme tanto. Fue una experiencia de investigación inmejorable.

Una no puede salir cuerda de una tesis si no tiene el apoyo de sus compañeros. Gracias a todos los que están y estuvieron. Gracias, Silvia, por ser mi tándem, por las risas y por los lloros compartidos. Y qué suerte poder llevarme amigos de esta experiencia, Álvaro, Bea, Diego, Jose, Nico, Patri...

Gracias a todos mis amigos. Gracias a la danza y a todas mis bailarinas.

Gracias a mi familia. Papá, mamá, gracias por haberme aguantado estos años en casa, gracias por pensar tanto en mí, espero no haberos preocupado demasiado en los momentos bajos. Gracias Bea y Day por ser tan buenos hermanos, por dejar claro que siempre puedo contar con vosotros. Gracias a mis sobris, Asier y Joel, porque solo veros me da fuerzas cuando flaqueo. Gracias, Pili y Ramón, porque sois como mis segundos padres y me acogéis como a una hija.

Gracias, Iulen, por haberme acompañado todos estos años, haberme animado cuando estaba baja, haberme animado aún más si cabe cuando estaba alta. Gracias por compartir tu entusiasmo conmigo, dudo que hubiera llegado a este momento sin ti. Y ahora a por la nueva aventura, que vendrá seguida de muchas más. Seguro.

Abbreviations

ABS	Acrylonitrile butadiene styrene
ATA	Ascending thoracic aorta
BAEC	Bovine aortic endothelial cell
BMS	Bare metal stents
C	Circumferential
C3D8H	Hybrid eight-node linear bricks
CFD	Computational fluid dynamics
CHP	Collagen hybridizing peptide
COH3D8	Eight-node 3D cohesive element
CPD	Cone-and-plate device
CVD	Cardiovascular disease
CZM	Cohesive zone model
DES	Drug-eluting stents
DIC	Digital image correlation
DMSO	Dimethyl sulfoxide
DTA	Descending thoracic aorta
EC	Endothelial cell
EDTA	Ethylenediaminetetraacetic
FDM	Fused deposition modelling
FE	Finite element
FSI	Fluid-structure interaction

GOH	Gasser-Ogden-Holzapfel
H&E	Hematoxylin and eosin
HAEC	Human aortic endothelial cell
HCAEC	Human coronary artery endothelial cell
HSB	Hue-saturation-brightness
HUVEC	Human umbilical vein endothelial cell
IAA	Infrarenal abdominal aorta
IM	Intima-media
L	Longitudinal
LDL	Low density lipoprotein
M	Media
MA	Media-adventitia
OS	Orbital shaker
ox-LDL	Oxidised low density lipoprotein
PBS	Phosphate-buffered saline
PDMS	Polydimethylsiloxane
PFA	Paraformaldehyde
PLA	Polylactic acid
PLM	Polarised light microscopy
PPFC	Parallel-plate flow chamber
PSR	Picrosirius red
PSS	Physiological saline solution
R	Radial
ROI	Region of interest
SEF	Strain energy function
SI	Shape index
SMC	Smooth muscle cell

TFM   Tissue freezing medium

TSL   Traction-separation law

WSS   Wall shear stress

List of Figures

List of Tables

Contents

Introduction

1.1 Cardiovascular diseases

Cardiovascular diseases (CVDs) such as ischemic heart disease, stroke, heart failure and many others (see Figure 1.1) remain the leading cause of death worldwide [1, 2], and their incidence is increasing globally [3]. Prevalent cases of CVD have nearly doubled, from 271 million in 1990 to 523 million in 2019, whereas the number of CVD deaths have steadily increased from 12.1 million in 1990 to 18.6 million in 2019 [3]. Age-standardised data suggests that this increase is heavily influenced by population growth and aging [3], leading to the assumption that cases will continue increasing, especially in areas where the share of older population is projected to double in 2050. CVDs are, however, not exclusively an "old people problem", as they were the cause of 6.2 million deaths occurring between the ages of 30 and 70 in 2019 [3]. CVD burden and mortality also show regional and national differences, reflecting the disparity not only in access to healthcare, but in the prevalence of CVD risk factors [4]. Proving this balance between both causes, middle-income countries show higher mortality due to CVD than higher- or lower-income countries [1].
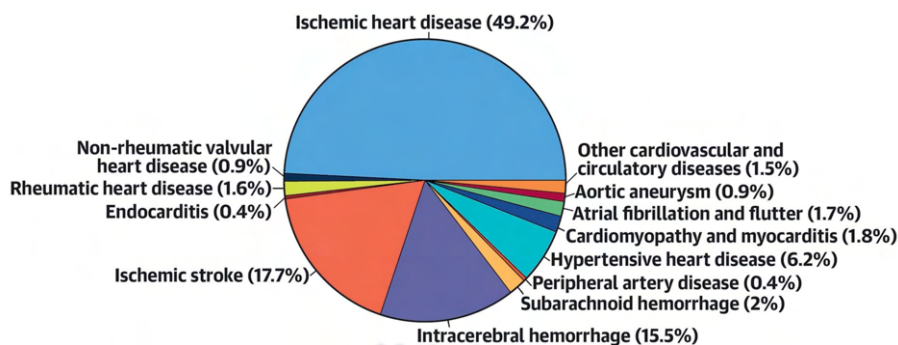
Figure 1.1. Proportion of CVD deaths by cause (part of the Central Illustration from ref. [3]). Ischemic heart disease involves acute myocardial infarction, chronic stable angina, chronic ischemic heart disease and heart failure. Data from 2019.

Because of their importance, research has long focused on unraveling the causes or triggers of these diseases. The main metabolic risk factors for developing CVD

include, in order of relevance, high blood pressure, high LDL (low density lipoprotein) cholesterol in blood, obesity in terms of a high body-mass index, hyperglycemia or high fasting plasma glucose in the blood and kidney dysfunction [3]. To these metabolic risks, we can also add the main behavioural risks that include a bad diet, smoking, alcohol abuse and low physical activity [3]. Other environmental risks such as air pollution are also linked to the development of CVDs [3]. The determination of these factors comes from extensive studies involving large amounts of subjects and observing overall numbers, trends and behavioural patterns. Reducing the incidence of these factors would indeed improve CVD numbers. Another complimentary approach is to study the mechanisms of the specific diseases, in order to be able to prevent and treat each one of the severe pathologies. Considering the numbers of prevalence shown in this section, it is clear that research that focuses in increasing the understanding of these diseases is paramount [2].

1.1.1   Motivation

In recent years, biomechanics has been a key driver for the investigation of the mechanisms of different CVDs [5–9]. Mechanical forces play a crucial role in regulating vascular physiology and function, and are instrumental in the development of blood vessels, maintenance of homeostasis, and progression of arterial disease [5]. More specifically, mechanical damage in different forms leads the development of several arterial diseases, like atherosclerosis [10], in-stent restenosis [11] or arterial dissection [12]. Overall, while there is still much to be learned about the precise details of these mechanisms of damage, the scientific community has made significant progress in understanding the fundamental principles underlying mechanical damage in the body. The aim of this thesis is to shed light on the impact of various damage mechanisms on the aforementioned CVDs. The following sections will provide a detailed account of the anatomy and physiological mechanical behaviour of arteries,. Subsequently, the three diseases that are the focus of this study—aortic dissection, atherosclerosis and in-stent restenosis —will be examined in detail, along with the approach that we will adopt to enhance our understanding of their underlying damage mechanisms.

1.2   Anatomy of the cardiovascular system. Focus on arteries

The cardiovascular system, also known as the circulatory system, is responsible for circulating blood throughout the body to transport nutrients, oxygen, hormones, and waste products [13]. The main components of the cardiovascular system are the heart, blood vessels, and the blood itself [13]. The heart is a muscular organ that pumps blood to the rest of the body. Blood vessels are the conduits through which blood flows

and is transported throughout the body. There are three main types of blood vessels: arteries, veins, and capillaries, see Figure 1.2. Arteries carry oxygenated blood away from the heart and to all the organs in the body, while veins carry deoxygenated blood back to the heart. Capillaries are the smallest blood vessels and are responsible for exchanging nutrients and waste products between the blood and the body's tissues. Finally, blood is the conducting medium. It is made up of red blood cells, white blood cells, platelets, and plasma. These particles are responsible for transporting oxygen, nutrients, hormones and waste products to the rest of the body, as well as helping to fight infections [13]. Overall, the anatomy of the cardiovascular system is complex, but it plays a critical role in maintaining the body's homeostasis and ensuring that all of the body's tissues receive the nutrients and oxygen they need to function properly. This thesis focuses on the study of various vascular diseases that occur in the arteries, in particular aortic dissection, atherosclerosis and in-stent restenosis, so more detail on the anatomy and function of these vessels will follow.
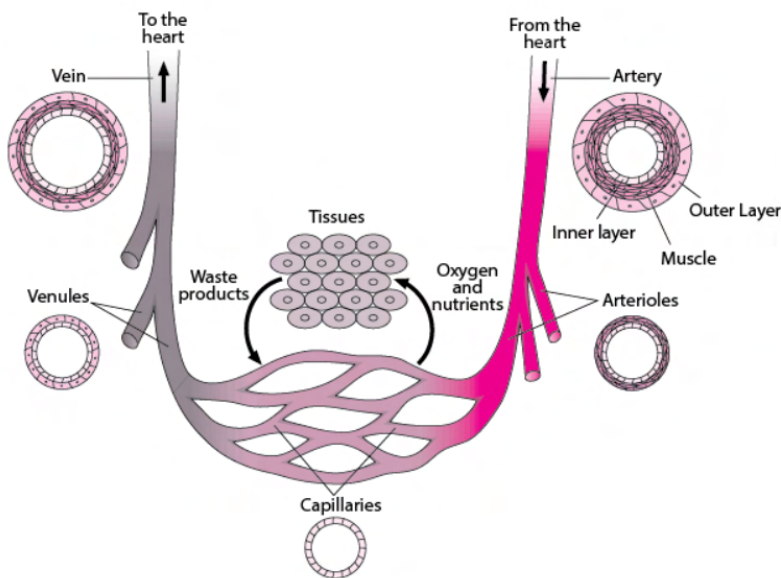
Figure 1.2. Outline of the different components of the circulatory system and their function [14].

Arteries are blood vessels that carry oxygenated blood away from the heart to the rest of the body. Their microstructure varies according to location in the body, age, species, disease, etc. [13]. They can be categorised in two main types, elastic and muscular arteries [13,15]. Elastic arteries are the largest arteries in the body and have a high proportion of elastic fibers in their walls. They are responsible for carrying blood away from the heart and distributing it to smaller vessels. The elasticity of these

arteries allows them to stretch and recoil in response to changes in blood pressure, helping to maintain a consistent flow of blood throughout the circulatory system. They are located close to the heart, with the aorta, common carotid and common iliac arteries being the main examples of elastic arteries [13,15]. In contrast, muscular arteries are smaller arteries that contain a higher proportion of smooth muscle cells in their walls. They are responsible for distributing blood to the various organs and tissues of the body. Muscular arteries have less elasticity, but their walls can contract and relax to regulate blood flow to specific areas of the body. Some examples of these arteries are the coronary, the cerebral, femoral or renal arteries [13,15]. Figure 1.3 shows the typical histology of a muscular and an elastic artery. Overall, elastic arteries are designed to handle high-pressure blood flow from the heart and distribute it to the body, while muscular arteries are designed to regulate blood flow to specific organs and tissues. In addition, some arteries such as the external carotid arteries show characteristics of both types and are called transitional arteries [13].

(a) (b)

(c) (d)
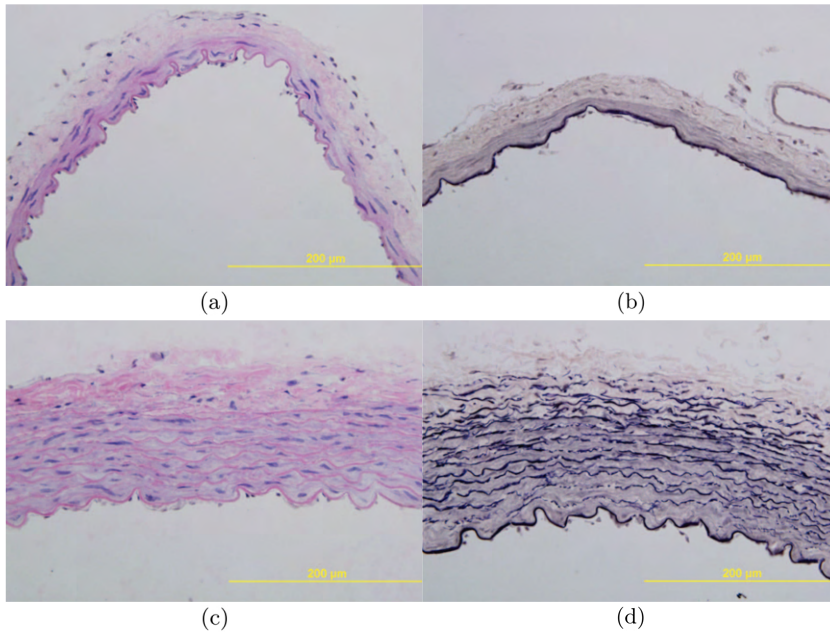
Figure 1.3. Representative histological images of a basilar artery (a and b), which is classified as muscular, and a common carotid artery (c and d), considered an elastic artery, from rabbits (Figure 1 from ref. [16]). (a) and (c) show a hematoxylin and eosin stain, where the nuclei of muscle cells is coloured dark purple and elastin and collagen are coloured pink. (b) and (d) show Verhoeff's elastin stain, which colours elastin in black. The difference in elastin content, which is the main component to give elasticity to the vessels, between both types of arteries is marked.

Regardless of type, the walls of all arteries have three distinct layers: the tunica intima, the tunica media, and the tunica adventitia [13, 15, 17], see Figure 1.4. The tunica intima or intima is the innermost layer of the artery and is in contact with the blood that flows through it. Its microstructure is similar in elastic and muscular arteries. It is composed of a single layer of endothelial cells, which acts as a barrier between the blood and the surrounding tissues. These endothelial cells rest on a thin basal membrane, called the basal lamina. This lamina consists mostly of type IV collagen, some adhesion molecules like laminin and fibronectin, and proteoglycans. It acts primarily as an adherent substrate where endothelial cells can grow [13]. In some arteries like the aorta or the coronaries, the intima also contains a subendothelial layer of connective tissue and axially oriented smooth muscle cells [13]. Overall, the intima in healthy young individuals is very thin and barely contributes to the mechanical integrity of the arteries [15]. With age and disease, the intima thickens and stiffens, increasing its contribution to the mechanical behaviour of the artery [15]. The tunica media or media is the middle layer of the arteries and is composed of smooth muscle cells and elastin and collagen fibrils [15, 17]. Vascular smooth muscle cells tend to be oriented helically, forming a small angle with the circumferential direction. This preferred orientation allows the vessels to regulate the diameter of the artery, which controls blood flow and blood pressure in medium and smaller arteries, and to contribute to the control of the distensibility of bigger and more elastic vessels like the aorta [13]. Due to its microstructure, the media is the main bear-loading layer in a physiological environment and shows different fibre packing in elastic and muscular arteries. In particular, muscle fibres in elastic arteries are separated by fenestrated elastic laminae, whereas the smooth muscle appears as a compact single layer in muscular arteries [13, 15, 17], see Figure 1.3. The tunica adventitia or adventitia is the outermost layer of the artery and is composed of connective tissue, collagen fibers, and some elastic fibers. It also contains nerves and the vasa vasorum, a network of small blood vessels that supply oxygen and nutrients to the outer layers of the vessels [13]. The collagen fibres in the adventitia are more aligned with the longitudinal direction of the vessels and their wavy configuration serves to reinforce the wall at higher levels of pressure, limiting acute over-distension and even rupture [13, 15]. The internal and external elastic laminae are fenestrated membranes of elastin that separate the tunica media from the intima and adventitia, respectively [15, 17]. These laminae are thicker in the muscular arteries [13].

Overall, the anatomy of the arteries allows them to carry blood under high pressure from the heart to the rest of the body. The muscular and elastic properties of the artery walls allow them to expand and contract in response to changes in blood flow and pressure, while the inner layer of endothelial cells provides a smooth surface for blood to flow through.
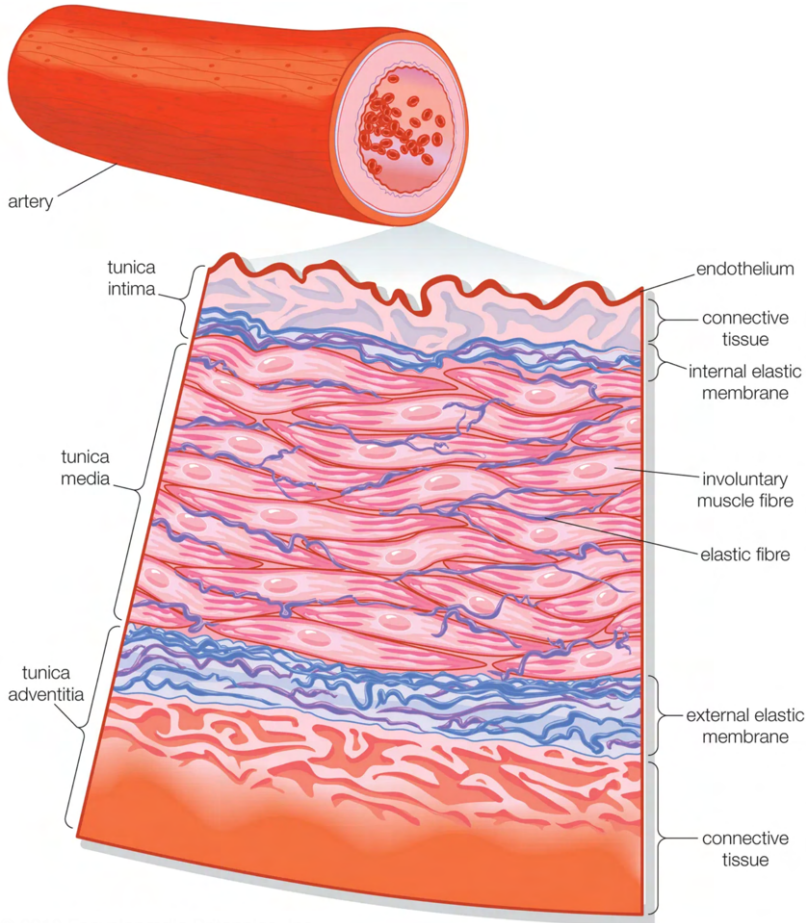
Figure 1.4. Outline of the three layers of an artery—tunica intima, media and adventitia—and their microconstituents [18].

1.3   Mechanical behaviour of the arteries

The mechanical behaviour of arteries is essential for maintaining healthy blood flow, preventing vascular damage and ensuring overall cardiovascular health. Dysfunctional mechanical behaviour of arteries can lead to conditions such as hypertension, atherosclerosis, aneurysms, and other vascular diseases. In this section, we will discuss the healthy mechanical behaviour of the arteries, linking the macroscopic properties with the microstructure detailed in Section 1.2. It is important to note beforehand, however, that arteries have an active and a passive mechanical behaviour [15]. Active

mechanical behaviour refers to the ability of the smooth muscle cells within the arterial walls to contract or relax, which is known as vasoconstriction and vasodilation, respectively. This active mechanical behaviour is important for regulating blood flow and pressure. On the other hand, passive mechanical behaviour refers to the inherent properties of the arterial walls, which include elasticity and compliance. These passive mechanical properties are important for maintaining blood flow and pressure throughout the body. In our case, we are interested in the intrinsic mechanical properties of the vessels and the effect of their microstructure in their mechanical response. Therefore, we will focus on the arteries' passive state, excluding their active behaviour from the scope of this work.

The mechanical properties of the vessels can be studied in vivo [19] and in vitro [20]. Studying them in vivo is ideal as they are subjected to all the actual stimuli that can affect their behaviour [15]. However, in these conditions, it is not possible to isolate the effect of one factor in their response, as the physiological environment is extremely complex, with nerves, hormones and many other factors influencing their behaviour. In contrast, in vitro studies provide a controlled experimental environment where the behaviour of arteries can be observed in response to specific stimuli that have been deliberately separated from other factors, without interference from other variables that might be present in vivo. In vitro studies can be a powerful tool for understanding the mechanisms underlying the physiological behaviour of arteries, although they may not perfectly replicate the in vivo situation.

Many different in vitro tests have been designed to observe and study the mechanical properties of vessels in different ways. Uniaxial tensile tests are a simple and common way that provide basic information of the behaviour of the artery wall. Although they are not sufficient to evaluate the complete behaviour of vessels, they provide good isolated information that can be observed in different directions, layers and vessels. The response in these tests is also widely linked and explained to their microstructure [21], therefore they are a good way to detail the basic mechanical behaviour of the arteries. Other common mechanical tests include planar biaxial testing [22–25] or inflation tests [26–29], which are procedures to study the mechanical properties of the tissue in two directions, see Figure 1.5.

Focusing the attention on the behaviour shown in uniaxial tests, the typical stress-strain curves show an exponential appearance, see Figure 1.6. The initial slope is associated with the elastic stretch of the elastin fibres in the vessels. As the wavy collagen fibres are recruited with further stretching [21], they give rigidity to the tissue, stiffening the material response in higher levels of strain and giving the curve the exponential look.

When comparing the mechanical response of the arteries in the main directions of the vessel, circumferential and longitudinal, we can generally observe the circumferential direction showing higher overall stiffness than the longitudinal one [31, 32]. This is less prevalent in the more elastic parts of the arteries, e.g., in the ascending and upper descending aorta [33, 34] or in the more proximal carotids [31]. This higher stiffness in the circumferential direction is due to the fact that the main orientation of the fibers is more aligned with this direction, therefore fibres are recruited faster
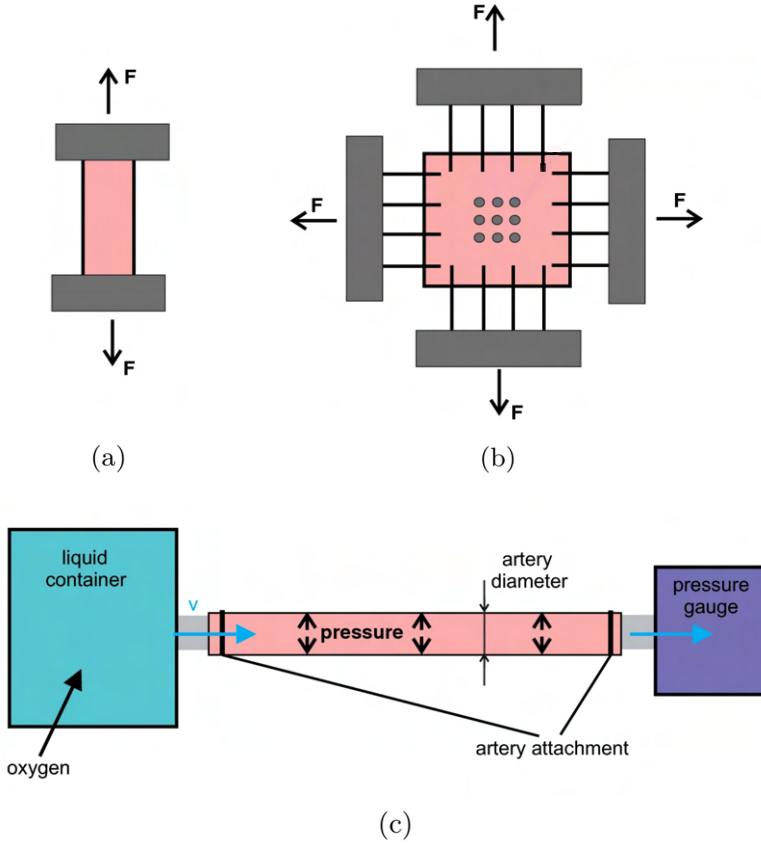
Figure 1.5. Outline of the different tests to study the mechanical properties of vessels (a) Uniaxial tensile test. (b) Biaxial test. (c) Inflation test (all adapted from Figure 3 from ref. [30]).

to give rigidity to the tissue. The mechanical response of each layer of the vessels has also been studied [32–35]. In the more elastic locations of the vessel where the anisotropy between the longitudinal and circumferential directions is not so predominant, like the upper descending thoracic aorta, the intima and adventitia show a more isotropic behaviour [33, 34]. It is the media that shows greater stiffness in the circumferential direction, as its fibers are mostly oriented in this direction. On the other hand, when moving distally through the aorta, the anisotropy becomes more prevalent in the whole vessel and in all layers of the vessel [32, 34]. The intima, however, is the most isotropic layer in all cases. The aorta is one of the most studied vessels, partly because of its large size and calibre and partly because of its tendency
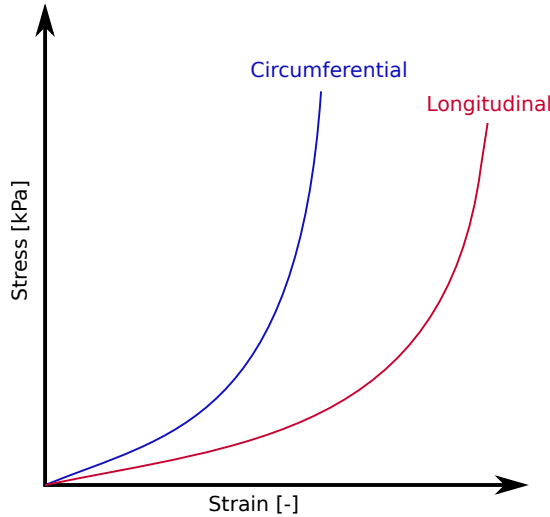
Figure 1.6. Typical exponential shape of a stress vs strain curve of an artery. The response in the circumferential direction (blue) is commonly stiffer than in the longitudinal one (red), as the collagen fibres responsible for the stiffening are preferably aligned towards the circumferential direction.

to develop diseases such as atherosclerosis, aneurysms and dissections. However, the mechanical response of other arteries has also been studied. Although this general behaviour remains, different vessels show different levels of stiffness in their mechanical response [31, 32, 34, 35].

The mechanical properties of vessels change with age. Large elastic arteries, such as the aorta, progressively stiffen throughout life. This progressive stiffening is largely due to changes in their structure, see Section 1.2. For example, it is known that elastic laminae fragment and break down over time and that the ratio of collagen to elastin concentration increases in the ageing aorta. In addition, with hypertension there is a thickening of the vessel wall. This change in vessel structure leads to significant changes in the elastic and viscoelastic properties of the vessel [22, 26, 36].

To sum up, the mechanical behaviour of the arteries in the circumferential and longitudinal directions has been broadly studied and the tendencies here described are widely accepted. However, the contribution of the radial component in the mechanical behaviour of arteries has been overlooked as it was assumed to not have an impactful effect. Although the stresses that appear in the radial direction are relatively small compared to the other two directions, they have a distinguishing characteristic, as the radial stress is compressive in contrast with the tensile of the other two directions [37].

1.4   Aortic dissection

Arterial dissection is a vascular pathology that occurs in the main vessels of the cardiovascular system, namely, the aorta, the carotid arteries and the coronary arteries [38]. This pathology is characterised by the propagation of a tear throughout the walls of a vessel [38, 39]. Due to this propagation, a false lumen can be created, which could imply a narrowing or even a collapse of the actual lumen [40], combined with the potential formation of blood clots, that could occlude more distal vessels. The dissection can also propagate further and reach the adventitial layer, where it can cause the rupture of the vessel with an often fatal outcome [38, 39, 41, 42]. In particular, acute aortic dissection involving the ascending part of the aorta has an in-hospital mortality of up to 50% in the first hours [43–45].

Although the specific initial cause is still unknown, two mechanisms have been suggested as triggering factors and are widely accepted: i) a tear in the intimal layer of the vessel wall, which can happen spontaneously, in an already damaged intima, or provoked by external trauma, e.g., in medical interventions and ii) the rupture of the vasa vasorum, causing a weakening of the vessel wall and an intramural haematoma that can progress through the wall [39], see Figure 1.7. Depending on the location and comorbidities, one of these two explanations has been found to be prevalent. For example, a study of 505 cases of dissected aneurysms in the aorta determined that there were signs of an initial intimal tear in 96% of cases [46], whereas spontaneous coronary artery dissection is characterised by the presence of an intramural haematoma [47]. The risk factors associated with the weakening or damaging of the intima so far are age, hypertension, smoking and congenital and genetic disorders, like bicuspid aortic valve syndrome or Marfan syndrome, among others [39, 48–50]. Nevertheless, current investigation of arterial dissection has focused on its propagation instead of its initiation, as patients arise once the pathology has started [51].

Dissection in the aorta in particular can happen throughout the entire vessel and, depending on the area in which it occurs, the outcome is frequently different [44, 45]. In fact, the current classifications of aortic dissections, the Stanford and the DeBakey Classification [52, 53], sort the dissections only considering the location of the aorta in which they appear, see Figure 1.8. Stanford type A dissections involve the ascending aorta, whereas Stanford type B dissections do not [40]. Similarly, the DeBakey Classification differentiates between dissections that involve (DeBakey types I and II) or do not involve (DeBakey type III) the ascending aorta. In those involving the ascending part, the DeBakey Classification also distinguishes between the dissections that propagate throughout the descending part of the aorta (type I) or those confined in the ascending part (type II) [53]. These classifications serve as a first determination of the diagnosis and the risks associated with the pathology. When comparing both classifications, we can observe that Stanford type A dissections involve DeBakey types I and II. As this initial classification can influence the first stages of treatment, the significance of differentiating the dissections in the ascending aorta using the DeBakey Classification has been emphasised [54].
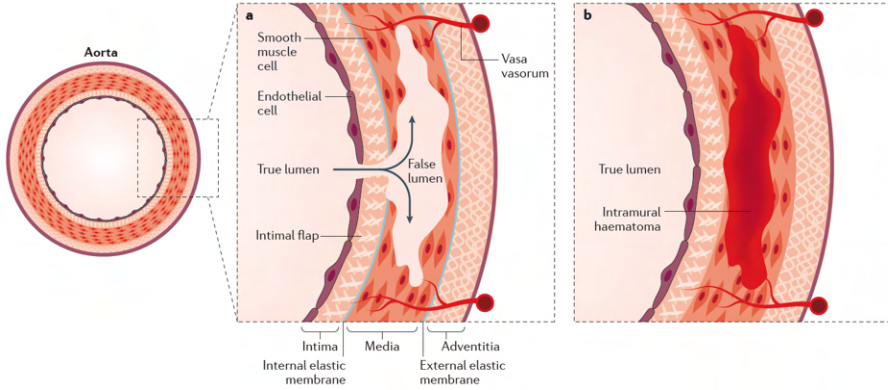
Figure 1.7. Aortic dissection and the two triggering mechanisms that have been observed (Figure 1 from ref. [39]). (a) shows the initiation of the dissection due to an intimal tear, whereas (b) shows the presence of an intramural haematoma as first step to develop a dissection.

Focusing on the different outcomes among locations, dissections that appear in the ascending part of the aorta, which account for around 60-70% of the cases [43, 48, 55, 56], tend to need surgical intervention due to their severity, as they can involve failure in other surrounding vessels (like the coronary arteries). On the other hand, dissections occurring in the descending thoracic or the abdominal aorta are more commonly medically treated as they are most likely to turn chronic, but they can also need endovascular intervention [39, 48]. It is, therefore, a pathology that highly depends on location.

In vitro-in silico evaluation of the dissection properties of the aorta   As discussed above, the mechanisms of arterial dissection are still to be understood. Whereas the initiation of the dissection can be affected by biological cues, the propagation of the tear is mostly a mechanical phenomenon. This thesis aims to enhance our understanding of the propagation by examining its mechanics, providing valuable insights into this damage phenomenon. To do so, we have defined a methodology to establish the dissection properties of the aorta and have studied them throughout the entire vessel, the different layers and the main directions. Dissection properties of arteries are frequently studied experimentally via delamination tests, such as the T-peel test [57] and the mixed-mode peel test [58]. So far, a study that performs both tests throughout different regions of the aorta, as well as dissecting several interfaces, is missing. This makes it difficult to extract conclusions in terms of vessel heterogeneity, as a standardised experimental procedure cannot be assured for different studies in literature [50]. Therefore, we will perform both dissection tests on healthy porcine aortas, dissecting three interfaces of the vessels, i.e., the intima-media (IM), the media-adventitia (MA) and the media (M) within itself, considering different re-
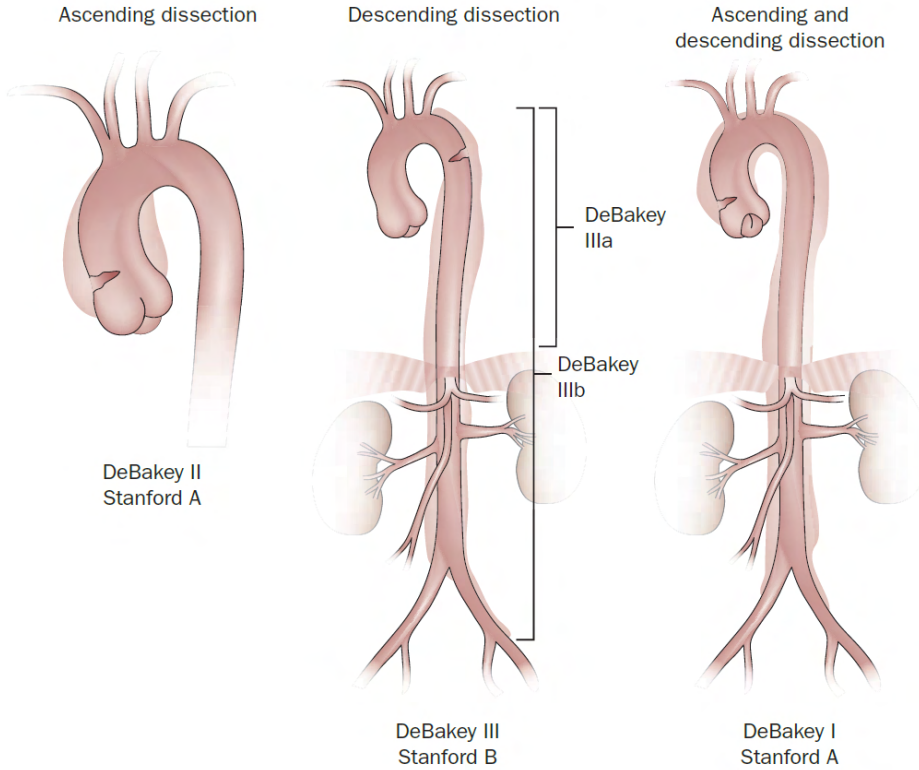
Figure 1.8. Stanford and DeBakey classifications (Figure 1 from ref. [53]). The image on the left depicts a dissection that is restricted to the ascending aorta, while the image in the center shows a dissection that is limited to the descending portion. On the right, there is an aortic dissection that involves both the ascending and descending segments of the aorta.

gions of the aorta, the ascending thoracic aorta (ATA), the descending thoracic aorta (DTA) and the infrarenal abdominal aorta (IAA).

The experimental tests will be subsequently modelled with cohesive zone models (CZMs) and the experimental values reproduced by fitting the dissection properties of the strips. These properties can be observed and compared to obtain conclusions regarding material behaviour and can also subsequently be used in computational models that reproduce arterial dissection, giving further understanding into the mechanisms of the disease. For these purposes, proper characterisation of biological tissue is key to understanding the effect of the biomechanical environment in the pathology.

1.5   Atherosclerosis

Nowadays, atherosclerosis is the principal etiology of CVDs [9] and therefore is the major cause of mortality worldwide [3, 59]. Despite its incidence, its mechanism is still not fully understood [9, 59]. This pathology consists in the progressive narrowing of blood vessels due to the deposition of an atheroma plaque in the vessel walls. The biggest risk of the formation of the plaque is that, under certain conditions, it can break and unleash a blood clot. This clot, also called thrombus, can travel throughout the circulatory system and finally occlude a smaller vessel, as can be seen in Figure 1.9. Especially if this occlusion happens in the heart (myocardial infarction) or the brain (stroke), the consequences can be fatal.
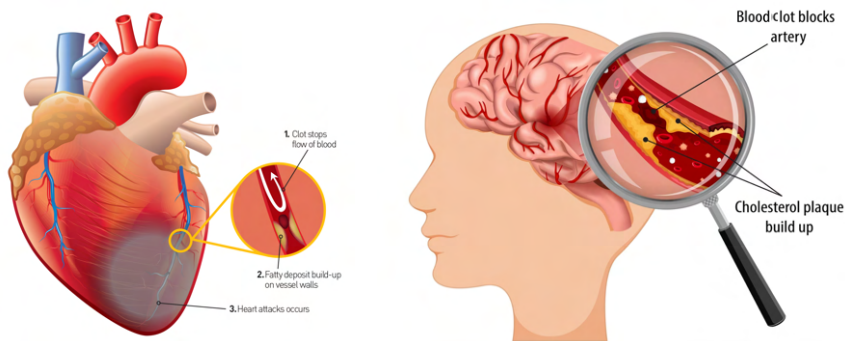
Figure 1.9. Possible outcomes of an atheroma plaque. Blood clots can result from the rupture of an atheroma plaque and may obstruct blood flow in vital vessels. This can lead to a myocardial infarction (on the left) [60] or a stroke (on the right) [61].

The process of atherosclerosis is quite complex and involves many biochemical and cellular mechanisms. Atherosclerosis commences with a dysfunctional endothelium. Toxins, mechanical damage or diabetes are some of the factors hypothesised to trigger this dysfunction. The damaged endothelium shows an increase in its permeability and consequently allows the leakage of macromolecules like low density lipoprotein (LDL) into the vessel wall [59, 62]. These molecules accumulate in the tunica intima. The damage also triggers the inflammatory response cascade, involving the recruitment of monocytes. Inside the endothelium, LDL oxidises, since it is no longer in the presence of the antioxidants in blood [59]. The oxidation of LDL inside the wall provokes endothelial cells (ECs) to express some adhesion molecules and release cytokines [62]. The cytokines act as signaling cues that further increase the immune response, that is, the recruitment of monocytes. These monocytes, helped by the adhesion molecules, enter the vessel wall to eliminate the alteration—the oxidised LDL (ox-LDL). They differentiate into macrophages and start ingesting the ox-LDL via phagocytosis [59]. The receptors of these immune cells do not receive any down-regulating signals and continue accumulating lipid until they transform into foam cells [9].

Meanwhile, the muscle cells from the medial layer, with a healthy contractile phenotype, are altered because of the presence of ox-LDL. They change their phenotype and become synthetic smooth muscle cells (SMCs), with no contractile function, and migrate from the medial to the intimal layer [59]. There, they surround the foam cells, generate an accumulation of extracellular matrix (mostly collagen) and form a fibrotic cap around the lipid core. The graphical scheme of the process is shown in Figure 1.10. This accumulation is the atheroma plaque, and as it increases, it will damage the vessel wall with more severity and enter its lumen.
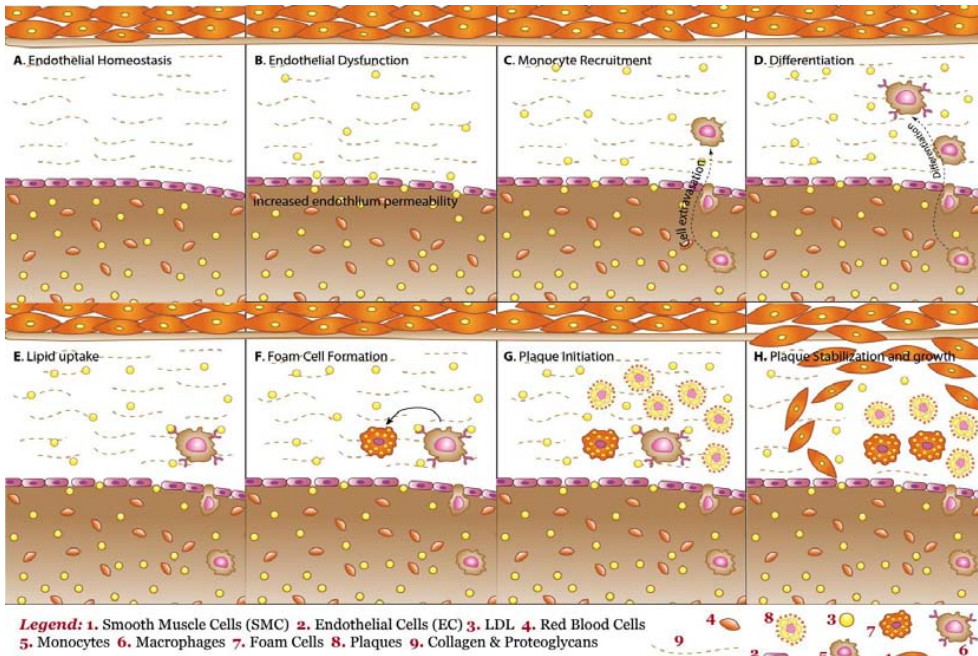
Figure 1.10. Process of formation of the atheroma plaque (Figure 1 from ref. [62]). A blood vessel functions properly in homeostasis (A). When some factors provoke a dysfunction in the endothelium, its permeability is increased, and molecules in blood flow (like LDL) enter the vessel wall (B). The presence of these molecules generates a recruitment of monocytes (C), that differentiate into macrophages inside the wall (D) and start digesting ox-LDL (E). When macrophages uptake too much lipid, they transform into foam cells (F), and stay inside the endothelium (G). The presence of these foam cells provokes a change in the phenotype of the muscle cells in the medial layer. They transform into smooth muscle cells and move to the intimal layer, where they surround the foam cells and generate collagen, stabilising the forming plaque (H).

Several factors have been studied and some are currently acknowledged to influence the apparition of the disease, like dyslipidemia or the increased presence of LDL in blood. Factors such as these are systemic, that is, they affect the whole circulatory

system equally. However, atherosclerosis most frequently appears in specific locations, such as the carotid bifurcation, the coronary arteries, the infrarrenal abdominal aorta and the popliteal arteries [9]. What these sites have in common is that they involve bifurcations and areas where blood flow is disrupted or altered. For this reason, current research is focused on the haemodynamics and biomechanics that trigger this disease.

The changes in blood flow that occur at these specific sites have been strongly associated with alterations in the permeability of the endothelium [63–66]. Under conditions of disturbed flow, such as those seen in areas of branching or curvature, endothelial cells (ECs) undergo a series of changes in their shape and function that can contribute to the development of atherosclerosis. By studying these changes at the cellular level, we can gain insights into the mechanisms that trigger the development and progression of this disease, which may lead to the development of new therapeutic strategies to prevent or treat atherosclerosis.

Studying the damage in the endothelium that can trigger the development of atherosclerosis   In this thesis, we will focus the study of atherosclerosis on the mechanical factors that can cause the initiation of the disease at the cellular level, that is, the process of damage in the endothelium. In particular, we will study the effect of different flow rates on the permeability of the endothelial layer. We will do so by designing and setting up a flow experiment where ECs will be cultured to create a confluent monolayer and be subsequently subjected to different flow rates. The integrity and permeability of the monolayer will be studied by analysing the morphology of the ECs as a response to flow. This line of work is already being investigated in literature, with some correlations found between flow patterns and EC morphology. Nevertheless, the novelty of our research lies in following the same protocol to perform different ranges of flow and in objectively quantifying the cellular response in each case. Due to our mechanical background, we are also interested in the effect, both combined and uncoupled, of other mechanical stimuli that the endothelium is subjected to in vivo. A full study of other stimuli is out of the scope of this part of the thesis. However, we will also work on the first steps to initiate this future line of research by designing a flow device capable of reproducing physiological and pathological strain patterns in the monolayer of ECs.

1.6   In-stent restenosis

Stenosis is the narrowing or blockage of arteries that reduces blood flow. The possible causes of this blockage are varied and severe. Atherosclerosis (see Section 1.5) is the most common cause of stenosis in arteries, but there can be other causes including congenital abnormalities like aortic coarctation, which is a constriction in the aorta (see Figure 1.11), inflammation or trauma, among others. The choice of treatment of stenosis depends on various factors such as the location, severity and underlying

cause, as well as the overall health of the patient. Nevertheless, stent implantation
is typically considered the primary treatment option for both coronary artery disease
and aortic coarctation [67–71].
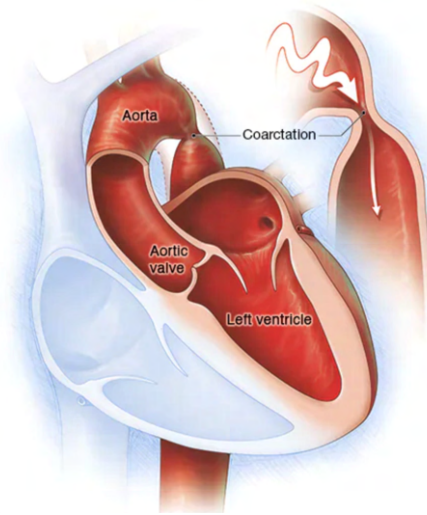
Figure 1.11. Schematic of an aortic coarctation, which is generally a congenital defect.
This pathology forces the heart to pump harder to move blood through the aorta [72].

Stent implantation or stenting consists in the deployment of a metallic mesh
or stent that reopens the vessel maintaining its integrity [73, 74], see Figure 1.12.
Bare metal stents (BMS) were introduced to clinical practice in 1987 [75], and by
1998, BMS implantation accounted for nearly 70% of coronary interventions [76].
Since their inception, the primary complications associated with coronary stent place-
ment have been stent thrombosis and in-stent restenosis. Stent thrombosis is a life-
threatening condition that results in the blockage of the stent by thrombus. On the
other hand, in-stent restenosis is the most common complication associated with coro-
nary stent placement, which can be influenced by various factors such as the patient,
lesion morphology or stent design [77]. In-stent restenosis consists in the proliferation
of neointimal tissue over the deployed stent [78–81], which can cause a subsequent
narrowing, see Figure 1.12. Despite the significant number of stents implanted in
patients over the past decades, there have been relatively few pathological studies
conducted to examine the behaviour of these devices after implantation [77], and
the mechanisms triggering this complex process are still not fully understood. To
mitigate the risk of restenosis, drug-eluting stents (DES) have been developed and
are now frequently employed in clinical practice [82–84]. However, despite the use
of these stents, the occurrence of restenosis cannot be considered negligible [84–86].
The clinical incidence of in-stent restenosis after BMS implantation is approximately
20%–35%, whereas the use of DES has led to a further decrease in the occurrence

to 1%–20% [69, 77, 85, 87, 88], though the extent of the observed reduction is heavily dependent on the angiographic and clinical characteristics of their use [69].

Figure 1.12. Process of a stent implantation and development of in-stent restenosis. A catheter with the balloon and stent is threaded through the blood vessels to the site of the blockage. Once it reaches the area, the balloon is dilated, expanding the stent with it. The balloon is subsequently deflated and removed, leaving the stent deployed and opening the vessel. After some time, tissue can grow over the stent, re-blocking the vessel (Figure 3 from ref. [89]).

Deployment of a stent can cause arteries to undergo excessive stretching and indentation injury to the areas that come into contact with the stent struts. Arterial injury after stenting has been experimentally shown to correlate strongly with neointimal hyperplasia [68, 90, 91], and this damage is widely agreed to be the cause of in-stent restenosis [73, 92–94]. The development of neointimal hyperplasia is the result of the combined effect of smooth muscle cell migration and proliferation, which is initiated by complex signaling cascades in response to stimuli originating from both within and outside of the vessel wall [95]. However, despite the progress made in understanding the molecular mechanisms that underlie neointimal hyperplasia, the specific triggers that initiate this process after stenting are still not fully understood.

On the quantification of the damage caused by stenting in arteries Our aim with this study is to elucidate the underlying mechanisms that lead to in-stent restenosis and to explore how the damage caused by the stent in the vessel can be accurately detected, quantified and ultimately reduced. In order to achieve this, we will use a novel tool called collagen hybridizing peptide (CHP), which has demonstrated the ability to bind to areas of arterial damage where collagen is present [96]. Provided that the damage that stents cause in vessels affects their collagen, CHP should be able to mark these injured sites. Quantifying stent-induced damage would significantly impact stent design, allowing the development of patient specific stents that reduced the risk of developing in-stent restenosis [94, 97–101]. Moreover, it would bring light to the understanding of the mechanisms of damage after stenting.

1.7   Structure of the thesis

This doctoral thesis aims to investigate various mechanisms of arterial damage from multiple perspectives. To achieve this objective, the thesis will be structured into independent chapters, each dedicated to a specific pathology and area of knowledge.

Each chapter will begin with a comprehensive literature review of the current state of research regarding the study of the damage mechanisms of the specific disease, followed by our objective and an outline of the research questions that will be addressed with our study. The research will be fully developed, presenting the methodology and results obtained. The concluding section of each chapter will summarise the key findings and highlight the contributions made to the field. In the final section of the thesis, we will present general conclusions based on the major findings and contributions of the research, and discuss potential future directions for further investigations. This structure will enable readers to easily navigate the thesis and gain a comprehensive understanding of the research presented.

In addition, the thesis will feature two appendices that provide supplementary information to support the research presented. The first appendix will provide an overview of the basics of continuum mechanics and its application to the modelling of vessels, providing context for the research. The second appendix will detail an experimental study that we have conducted to investigate the mechanical properties of vessels in the radial direction, an area that has been under-studied in the field (see Section 1.3). These appendices will serve to enhance the reader's understanding of the research and provide additional context for the findings presented.

Damage caused by dissection

In this chapter, the arterial damage in vessels caused by the propagation of a dissection will be studied in terms of material characterisation. The dissection properties of the vessels are still under investigation due to the complexity to extract conclusions of this behaviour with experimental tests. This is why we will combine such experimental tests with computational models to fully characterise the dissection behaviour of the aorta. A proper characterisation of the dissection properties can deepen the understanding of this disease and shed light on the progression of tears in vivo. In particular, two different peel tests have been performed on porcine aortas, considering different locations of the vessel, different delamination interfaces and directions. All these conditions have been performed in order to give a more complete understanding of the delamination behaviour of the aorta. Subsequently, the experiments have been computationally replicated and the dissection properties of the tissue obtained by fitting the computational results with the experimental data.

The experimental part of this work has been published in *Biomechanics and Modeling in Mechanobiology* [102], and part of the computational work has also been published in *Mathematics* [103].

2.1   State of the art

Arterial dissection is a complex process that entails damage propagation. Our understanding of the mechanics involved in arterial dissection is still limited, and there is a scarcity of quantified biomechanical data available on this topic [38]. Characterising dissection properties of vessels can shed light on the underlying mechanisms of the propagation of a tear in the tissue. While some in vitro dissection experiments have been conducted to investigate this behaviour, there has been relatively little focus on integrating these experiments with computational models in order to enhance the understanding of the experimental results. In this section, the experimental and computational studies on the mechanics of arterial dissection are discussed.

2.1.1 Experimental work

Several experimental methodologies have been developed so far to improve the understanding of the dissection and fracture behaviour of the vessels. Tensile tests and the determination of the ultimate tensile strength of the vessel wall in the two main directions—longitudinal and circumferential—had been used as a way of analysing failure properties of the vessels [104–109]. It was reported that aortas exhibit significantly higher ultimate stress in the circumferential direction than in the longitudinal direction [104–109]. Angouras et al. [104] observed that this failure stress, which is linked to the risk of vessel rupture, did not change with age. Additionally, Mohan and Melvin [106] found that dynamic loading increased almost two-fold the ultimate stress compared to quasi-static stretching. Purslow [108] observed that ultimate stress increased distally in different portions of porcine DTA. Peña et al. [107] observed a similar trend, where ultimate stress increased from the DTA to the IAA, and they could determine that this increase happened mainly due to the adventitia, as they performed failure tests of the individual layers of the aorta. Supporting this finding, Manopoulos et al. [105] found a significant difference between the failure stress of the intima-inner media and the outer media-adventitia, with the latter bearing notably higher ultimate stresses in human ATAs. While this test informs about the mechanical behaviour of arteries leading up to failure, it does not yield any insight into the mechanics involved in the propagation of a tear, which is the mechanism of arterial dissection.

Therefore, centering the focus on dissection, delamination tests were introduced for vascular tissue as a way of reproducing the propagation of a tear in vitro. In particular, a T-peel test, which involves a mode I of fracture, was proposed by Sommer et al. [57]. This test consists in the progressive separation of the layers of a specimen by normally pulling from the flaps of two layers, see Figure 2.1.a. In addition, a mixed-mode peel test was developed as a more physiological way of dissecting two layers, as it involves a mixed mode of fracture, more similar to the real scenario [58]. In this case, the layers are dissected by pulling from one flap in parallel to the plane of dissection, see Figure 2.1.b. Both peel tests are described in detail in Section 2.2.2. Additionally, Witzenburg et al. [110] conducted shear lap experiments on porcine aorta to investigate its shear properties. This was motivated by previous findings suggesting that stresses near an advancing dissection in the aorta comprise not only radial tension but also transmural shear [111]. More recently, FitzGibbon and McGarry [112] developed a dissection test to study tissue response to mode II fracture, a relevant mechanism in the in vivo conditions of the propagation of arterial dissection.

Several dissection studies have based their investigations in the first two peeling tests—the T- and mixed-mode peel tests—mostly on the aorta [57, 58, 104, 110, 113–121], but also in the carotid and coronary arteries [122, 123]. Regardless of the vessel, it has been observed that the delamination in the circumferential direction requires less force than in the longitudinal direction, although this trend often fails to reach statistical significance [57, 110, 113–122]. This effect of vessel anisotropy is suggested

(a)   (b)
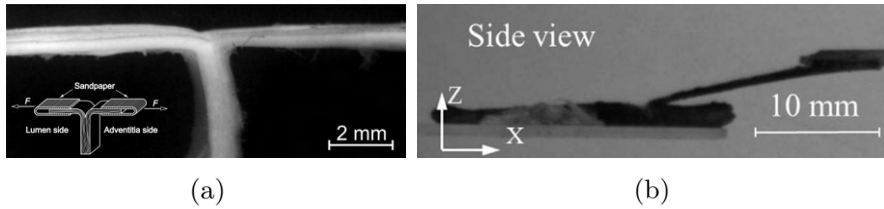
Figure 2.1. (a) Schematic and image of a T-peel test (Figure 6 from ref. [57]). (b) Image of a mixed-mode peel test (Figure 3 from ref. [58]).

to arise as the propagation of a tear in the circumferential direction happens between lamellar layers of muscle and connective tissue, whereas a tear propagated in the longitudinal direction has to break throughout the fibres [57, 122]. Unlike failure stress, dissection force decreases with age, which suggests that arterial dissection becomes easier as individuals get older [104, 113, 119]. Regarding gender differences, Sokolis and Papadodima [119] did not observe any variations, despite the fact that aortic dissections are more prevalent in men [124, 125] and the outcome of the disease is usually worse for women [124–126]. Therefore, it can be suggested that the inferior prognosis in women results from their different clinical features, which may lead to a delayed diagnosis after symptom onset [126].

So far, these dissection studies in the aorta have commonly focused on one specific location of the vessel [57, 58, 108, 117, 121] and have dissected either the medial layer within itself [113, 116, 119] or the two main interfaces (intima-media and media-adventitia) [114, 115], not finding noteworthy differences. Some studies have compared between healthy and diseased conditions in which dissection is likely to occur, like atherosclerosis [114, 115] or aneurysms [104, 118]. Especially in aneurysms, it has been found that the resistance to dissection diminishes in the affected tissue [104, 118]. Recently, Horný et al. [113] and Sokolis and Papadodima [119] evaluated the dissection behaviour of the human aorta considering the different locations throughout the vessel, only within the medial layer, and observed that diseccion force decreased when moving distally in the aorta.

However, the number of studies is still low and the conditions in each work sometimes vary, therefore the variation in the results is rather large and comparing data across different groups can be challenging [50]. To our knowledge, no study has reported yet the dissection behaviour through different locations of the aorta in both directions and between all interfaces, nor performing both dissection tests. Considering the contrasting progression and outcome of this disease in the different locations of the aorta, it is of great interest to perform such dissection study, and one of the objectives of this section of the thesis will be to achieve this goal.

2.1.2   Computational work

The development of computational models that reproduce experimental testing can greatly assist in the interpretation of results, as the models can enhance the understanding of the underlying phenomena. The reliability of experimental data and the validity of the models themselves are both critical to the value of this approach. Therefore, the computational work involved in defining the delamination tests that is going to be discussed in this section was mostly conducted by the same groups that carried out the experimental tests (described in Section 2.1.1). These groups possess the most comprehensive data and understanding of their experiments, and thus they were best suited to replicate their results using computational methods.

Some studies have analysed the behaviour of arterial tissue under mode I delamination [12,58,127] or mixed-mode along the medial layer [58], but none has compared the contributions of these two failure modes to the process of delamination of the layer interfaces. In these cases, a cohesive zone formulation has been used to model the propagation of tissue crack. Gasser and Holzapfel [127] used a cohesion law within the extended finite element (FE) method to simulate the controlled peeling experiments by Sommer et al. [57]. Subsequently, Ferrara and Pandolfi [12] applied an anisotropic cohesion law to reproduce the anisotropic behaviour observed in the peeling tests. Noble et al. [128] computationally investigated arterial perforation or dissection by an external body. Leng et al. [58] used a CZM to simulate the arterial wall delamination under shear mode dominated failure and the opening T-shaped delamination modes. FitzGibbon and McGarry [112] calibrated the mode II fracture energy based on measurements of crack propagation rates by a CZM. Additionally, some microstructure-based models of healthy [110] or aneurysmal ascending aorta [129, 130] have also been developed to further characterise and understand the pathological process. As a novel approach, Yu et al. [131] developed a computational model to reproduce the avalanche-like behaviour that occurs in the propagation of aortic dissections by individually modelling discrete interlamellar collagen fibres. Their results evidence that this avalanche behaviour comes from the local buildup of strain energy followed by a cascade of mechanical failures in the collagen fibres, that results in force drops in the propagation of the dissection (as will be observed more thoroughly in Section 2.2.5 and in the experimental results of this study). In spite of these computational studies, a methodology to combine T- and mixed-mode peel tests with CZMs in order to fit the normal and mixed delamination properties of different interfaces has not been presented yet in the literature.

2.1.3   Objectives of the study

Aortic dissections present different outcomes and severity depending on their location. Therefore, one key to understanding this disease comes from the study of the dissection properties of the artery and the variations throughout the vessel. This study aims to conduct peeling tests on various interfaces and locations of the aorta and es-

tablish a reliable methodology to derive dissection properties from the experimental results. To do so, entire porcine aortas, including the ATA, the DTA and the IAA have been harvested and peel tests performed to evaluate the dissection properties of three interfaces: the intima-media (IM), the media-adventitia (MA) and the media (M) within itself, in both vessel directions, longitudinal and circumferential, see Figure 2.2. Two different tests, the T- and mixed-mode peel tests, have been performed for each condition, and the experimental results are presented in terms of mean peeling force per width, dissection energy per reference area and separation distance at damage initiation.
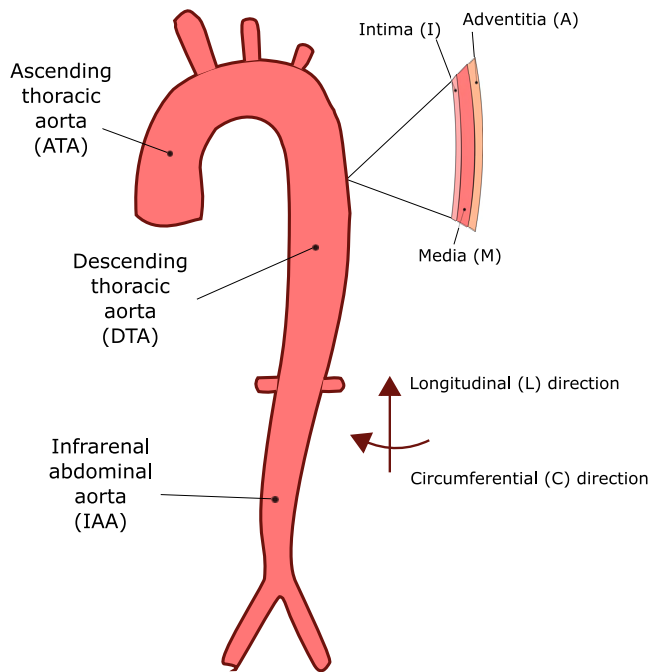
Figure 2.2. Outline of the different locations, directions and interfaces in the aorta that have been experimentally tested in this study.

Computational models of these two experimental tests have been subsequently performed in order to propose a methodology to calibrate the dissection properties of the porcine aorta, by fitting the experimental and computational results. With these properties, further computational models of the process of arterial dissection can be developed as a tool to help understand the underlying mechanisms of such a complex pathology.

2.1.4   Research question posed

- Do the dissection properties of the aorta depend on the location in the vessel?

- What interfaces are easier to propagate a tear?

- What are the dissection properties of the porcine aorta?

- Can we propose a methodology to obtain the dissection properties from the experimental data of the peel tests?

- Which FE approach is most suitable for developing a CZM that accurately replicates these experiments?

2.2   Experimental methodology

2.2.1   Origin and pre-processing of samples

For the experimental part of this study, a total of 9 healthy porcine aortas were harvested postmortem from female pigs. The swines were 3.5 ± 0.45 months old and weighed 45 ± 5 kg. They had been sacrificed for different studies that do not interfere with the aorta or the circulatory system, therefore no animal was killed specifically for these experiments. The experiments were approved by the Ethical Committee for Animal Research of the University of Zaragoza, with code PI36/20, and all procedures were carried out in accordance with the "Principles of Laboratory Animal Care" (86/609/EEC Norm). The animals were sacrificed under general anaesthesia through an intravenous injection of potassium chloride and sodium thiopental, and the aortas were harvested by skilled veterinarians. All 9 vessels were complete, including the three zones of study: ATA, DTA and IAA, except for 2 arteries, in which the portion of the IAA was missing. Once harvested, the whole arteries were kept frozen at -80 °C to assure a proper preservation, and thawed 24 hours before the tests at 4 °C. The specimens were cut in rectangular shapes of a dimension of 20 x 5 mm, approximately. The width, height and thickness of the specimens were subsequently measured. Table 2.1 shows the mean thickness of the samples according to location. Until testing, the rectangular samples were kept in ion-free physiological saline solution (PSS, 0.9 % NaCl) at 4 °C. All experiments were performed within 48 hours after the defrosting of the samples.

2.2.2   Experimental procedure

2.2.2.1   Sample preparation

In each location of the artery, a total of 12 specimens were obtained per porcine, 6 strips destined to each peel test. In these sets of 6 samples, there is one specimen

Table 2.1. Thickness of the specimens as function of location in the aorta.

Location	Thickness (mm)
ATA	2.17 ± 0.54 (n=108)
DTA	1.99 ± 0.46 (n=105)
IAA	1.12 ± 0.23 (n=78)

for each separation layer, i.e., IM, MA and M, all in both directions, circumferential and longitudinal, see Figure 2.3. An initial incision of around 5 mm in length was performed in order to assure that the separation occurred between the layers of interest. In case the initial incision was faulty or the dissection test was not successful, some extra specimens were cut to help complete the set where possible. With these conditions, and accounting for the aortas with no IAA, a minimum of 300 tests were conducted. The number of actual tests performed was higher due to the need to repeat some unsuccessful tests. After all tests and subsequent processing, a total of 291 tests were considered successful.

2.2.2.2 Peel tests

In the **T-peel test**, the two tongues of the specimen were gripped by two moving clamps. These clamps moved in opposite directions at a speed of 1 mm/min each, which entailed a total testing speed of 2 mm/min, separating the layers of the specimen in the direction normal to the interface plane. The test ended after 20 mm of separation or the complete dissection of the sample. An outline of the T-peel test is shown in Figure 2.4.a.

In the **mixed-mode peel test**, one side of the sample was glued to a clamp plate and completely fixed. This was always the intimal side as its surface is softer and allows for a better attachment. Therefore, it is only one flap that was gripped by a moving clamp, which moved at a speed of 1 mm/min in the parallel direction of the specimen, see Figure 2.4.b. Both speeds are low enough to assume a quasi-static state.

The T-peel and mixed-mode peel tests were carried out in the Instron BioPuls™ low-force planar-biaxial Testing System and the high precision drive Instron Microtester 5548 system adapted for biological specimens, respectively. Load cells of 10 N were used (Instron 2530-428), with an accuracy of 2.5 mN and a displacement resolution of 0.015 mm. The experiments were performed at room temperature and samples were either submerged or humidified with PSS to assure proper hydration throughout the experiments.
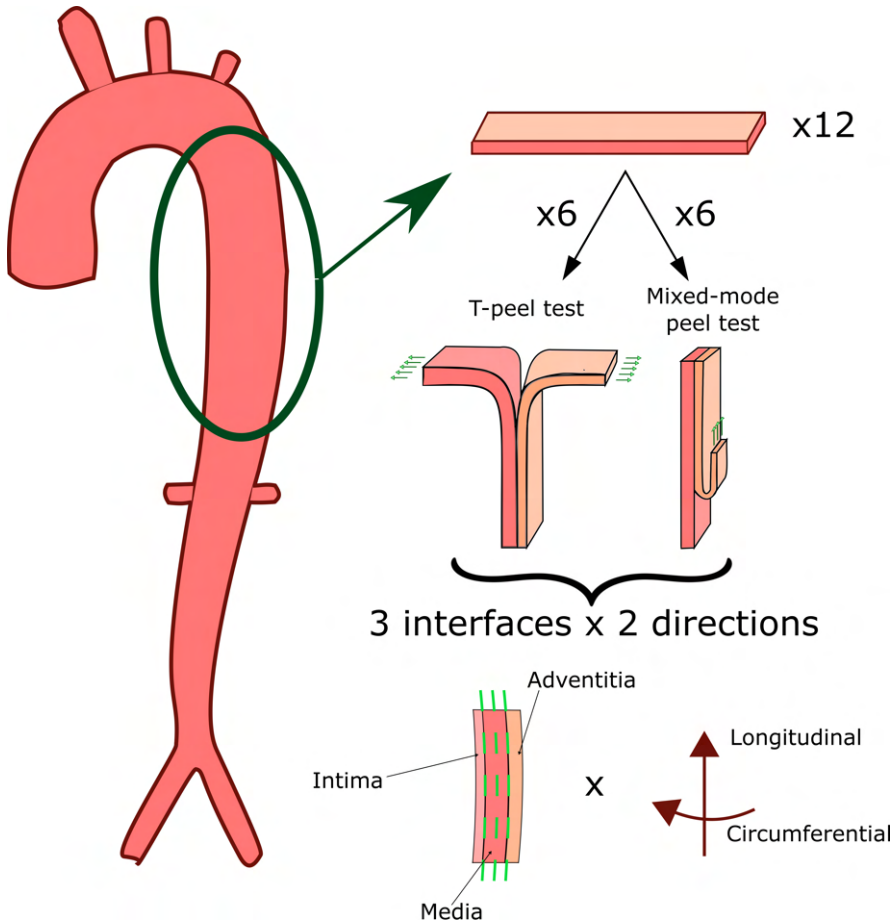
Figure 2.3. Outline of the distribution of samples obtained per location, the DTA in this case (circled in dark green). 12 rectangular samples are divided into two sets of 6, one for each peel test. These 6 samples per test account for the separation of the three main interfaces, depicted by the dashed light green lines (IM, MA and M) in both directions, circumferential and longitudinal.

2.2.3   Histology

After the peel tests, histologies were performed in the dissected tissue with two intentions: i) to check that the separation occurred between the layers of interest and ii) to examine the dissection interfaces. To do so, prepared samples were processed in the histological laboratory, in particular, in Servicios Científico Técnicos del CIBA (IACS-Universidad de Zaragoza). They were washed with PSS at room temperature, subsequently fixed in 10% buffered formalin and embedded in paraffin following stan-
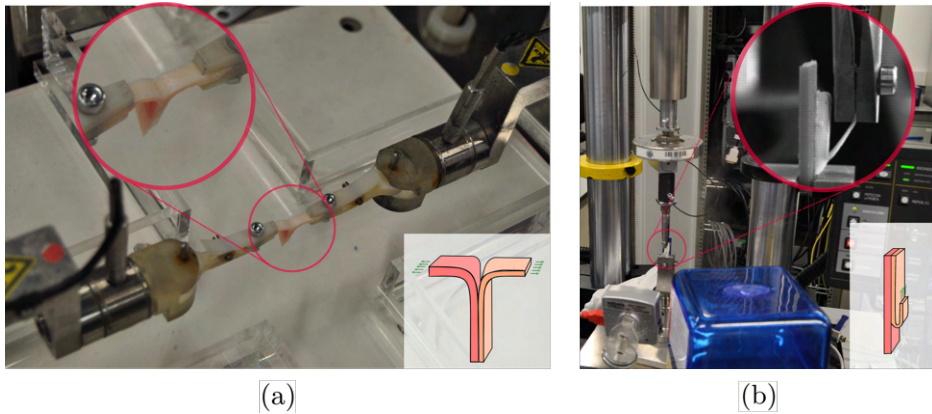
Figure 2.4. Experimental setup and descriptive outline of the experimental tests. (a) shows the dissection of a sample by means of the T-peel test in the Instron BioPuls™ low-force planar-biaxial Testing System. (b) shows the dissection via the mixed-mode peel test in the high precision drive Instron Microtester 5548 system.

dard procedures. The histology blocks were sectioned at 5 μm and stained with four different stains: haematoxylin and eosin (H&E), Masson's trichrome, orcein and picrosirius red. The information provided by observing the tissue with each of these stains is different and complementary:

- **H&E** stains cell nuclei in dark purple and cytoplasm and connective tissue—collagen and elastin—in pink. With this stain, the overall structure of the vessel can be observed, with a special focus on the orientation of the fibres and muscular cells.

- **Masson's trichrome** stains cell nuclei in dark purple, muscle fibres in red and connective tissue—collagen and elastin—in light green or light blue. This stain also allows to check the microstructure of the vessel, increasing the information regarding the muscle fibres.

- **Orcein** stains elastic fibres (elastin) exclusively in brown.

- **Picrosirius red** stains collagen fibres and enhances their birefringence, allowing to study their orientation with polarised light microscopy.

2.2.4   Mean peeling force/width, dissection energy and separation distance at damage initiation

The force vs displacement curves were extracted from the experimental peel tests. The data was later processed and the values of force were divided by the width of the specimen to avoid the effect of this dimension in the results. Mean force/width

and standard deviation of the tests was calculated throughout the separation of the specimens.

The dissection energy or critical energy release rate (G_c) for both peel tests was calculated following the proposed method by Sommer et al. [57]. Briefly, the dissection energy per reference area is the difference between the external work, W_{ext}, and the internal elastic energy, W_{elas}:

$$G_c = (W_{ext} - W_{elas})/L. \tag{2.1}$$

L is the initial length of the interface to be dissected, as shown in Figure 2.5.a and Figure 2.5.b. The external work is defined by

$$W_{ext} = 2Fl \tag{2.2}$$

in the T-peel test, and by

$$W_{ext} = F(L + l) \tag{2.3}$$

in the mixed-mode peel test, where F is the force applied to dissect the specimen per reference width and l is the length of the dissected specimen right before complete separation, see Figure 2.5.a and Figure 2.5.b. Assuming a linear relationship between the first Piola–Kirchhoff stress and the related stretch [57,116], the elastic energy can be defined as

$$W_{elas} = F(l - L). \tag{2.4}$$

The separation distance at damage initiation (δ_0) is obtained from the experimental curves following the approximation proposed by Wang et al. [121]. The displacement increments (Δd) associated with upward slopes of the force-displacement curves (not including the initial elastic part) are extracted, as shown in Figure 2.5.c, excluding those lower than the tolerance of the load cell (2.5 mN). The median value of these displacements per condition is considered the separation distance at damage initiation of the dissection, $\delta_0 = median(\Delta d)$.

2.2.5   Statistical analysis

Normal distribution of the data was checked using Shapiro-Wilk test [132]. The significant difference among the response to dissection for each condition was studied by means of an independent one-tailed t-test. In cases of non-normal distribution, the Mann-Whitney test was used as comparison method. $p < 0.05$ was established to indicate statistical significance. All data processing was performed with Matlab R2020a.

2.3   Experimental results

For both types of tests, the results are displayed in plots that collect the force/width vs interface separation curves of all the samples per condition, as well as the average
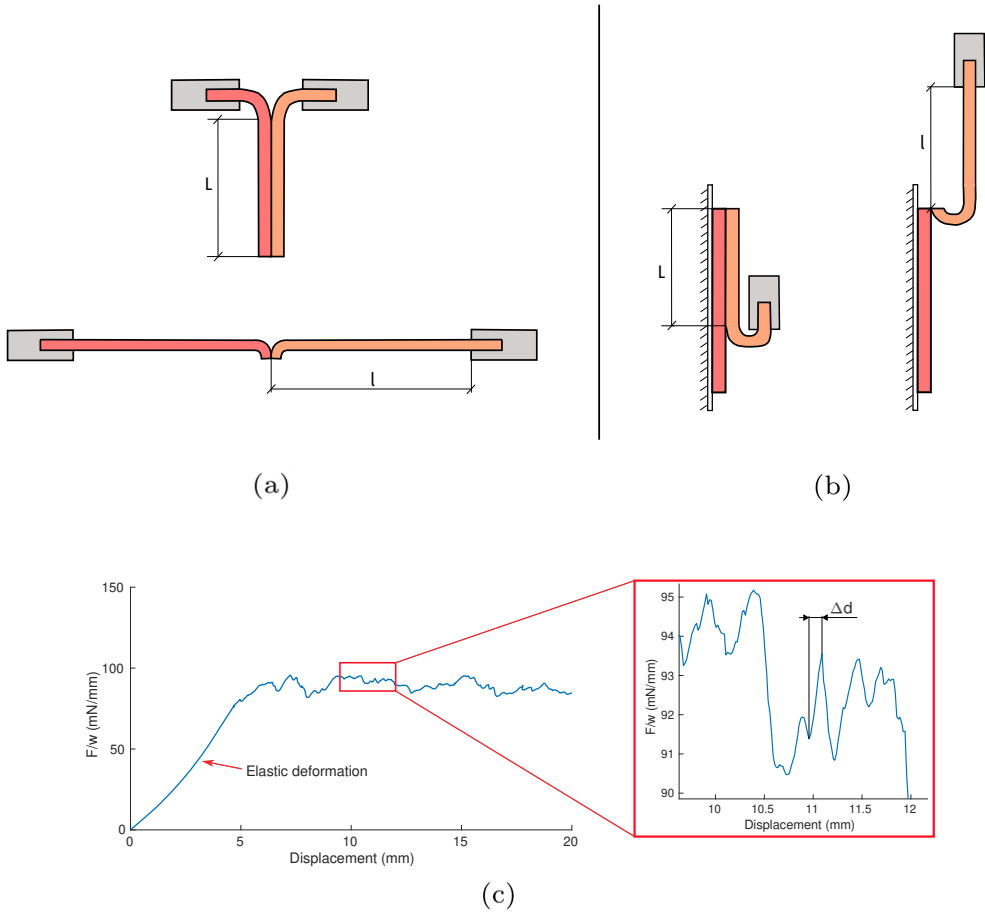
Figure 2.5. Outline of the considered dimensions to calculate the dissection energy in the T-peel test (a) and mixed-mode peel test (b). (c) shows an example of the obtention of displacement increments Δd in the force/width curves.

force/width throughout this separation. Moreover, mean and standard deviations of the dissection force/width and energy are shown in respective tables and bar charts.

In all specimens, the experiment starts with an elastic deformation of the tongues, with no separation yet of the layers, as can be seen in Figure 2.5.c. This phenomenon translates into a non-linear upward slope at the beginning of the force/width vs displacement curves. Once the specimens start to dissect, the force reaches a plateau phase, which accounts for the dissection force of that specimen. This plateau force is not constant, but shows an irregular stability that is produced by the phenomenon of stick-slip tearing [118]. This is the relevant information for this study and the part of the curves that will be displayed.

2.3.1 T-peel test

Figure 2.6 shows the force/width vs interface separation curves of all the specimens in the T-peel test throughout the entire separation. Table 2.2 and Figure 2.7.a detail the averaged force/width and standard deviation of each experiment, whereas Table 2.3 and Figure 2.7.b show the dissection energy per reference area. The results are displayed per location—ATA, DTA or IAA—orientation of the sample—longitudinal (L) or circumferential (C)—and per dissected interface—IM, MA or M. In terms of location, force/width and dissection energy are consistently higher for the ATA than for the other regions of the aorta. In terms of anisotropy, higher values of force/width and dissection energy in the peeling of samples in the longitudinal direction of the vessels can be observed in the ATA for the separation of the IM and MA, but not in the separation within the media. As for the differences among interfaces, IM separation tends to require less force/width and energy in all locations, and especially in the longitudinal direction in the DTA and IAA.

Table 2.2. Average force/width $\pm$ SD (mN/mm) of the T-peel tests. IM stands for intima-media, MA for media-adventitia and M for media. C and L are the circumferential and longitudinal directions, respectively. The number of samples per condition is also included.

F_m	IM		MA		M	
	C	**L**	**C**	**L**	**C**	**L**
ATA	58.72 $\pm$ 24.21 (n=9)	65.76 $\pm$ 21.67 (n=8)	69.27 $\pm$ 34.84 (n=8)	77.79 $\pm$ 24.15 (n=8)	62.18 $\pm$ 22.78 (n=8)	64.46 $\pm$ 29.01 (n=8)
DTA	44.69 $\pm$ 14.54 (n=8)	36.03 $\pm$ 18.99 (n=6)	43.22 $\pm$ 16.72 (n=8)	44.53 $\pm$ 16.72 (n=9)	49.47 $\pm$ 19.91 (n=8)	50.53 $\pm$ 16.13 (n=9)
IAA	39.73 $\pm$ 16.41 (n=6)	35.43 $\pm$ 17.14 (n=5)	49.41 $\pm$ 12.35 (n=5)	46.58 $\pm$ 17.44 (n=7)	43.85 $\pm$ 15.32 (n=7)	45.29 $\pm$ 18.61 (n=8)

Table 2.4 shows the separation distance at damage initiation for the T-peel tests. It has been reported that this separation distance can be related to fracture toughness [133]. However, no clear tendency can be found in these results.

Table 2.3. Average dissection energy $\pm$ SD (mJ/cm²) of the T-peel tests.

G_c	IM		MA		M	
	C	**L**	**C**	**L**	**C**	**L**
ATA	21.08 $\pm$ 8.16	24.86 $\pm$ 9.29	26.15 $\pm$ 15.28	30.44 $\pm$ 12.81	19.64 $\pm$ 6.90	21.76 $\pm$ 9.23
DTA	15.41 $\pm$ 5.96	12.24 $\pm$ 7.76	16.57 $\pm$ 4.84	15.58 $\pm$ 5.40	16.52 $\pm$ 5.77	17.27 $\pm$ 5.48
IAA	15.92 $\pm$ 7.32	15.48 $\pm$ 8.21	19.05 $\pm$ 3.42	21.60 $\pm$ 9.81	16.53 $\pm$ 7.00	15.79 $\pm$ 6.52
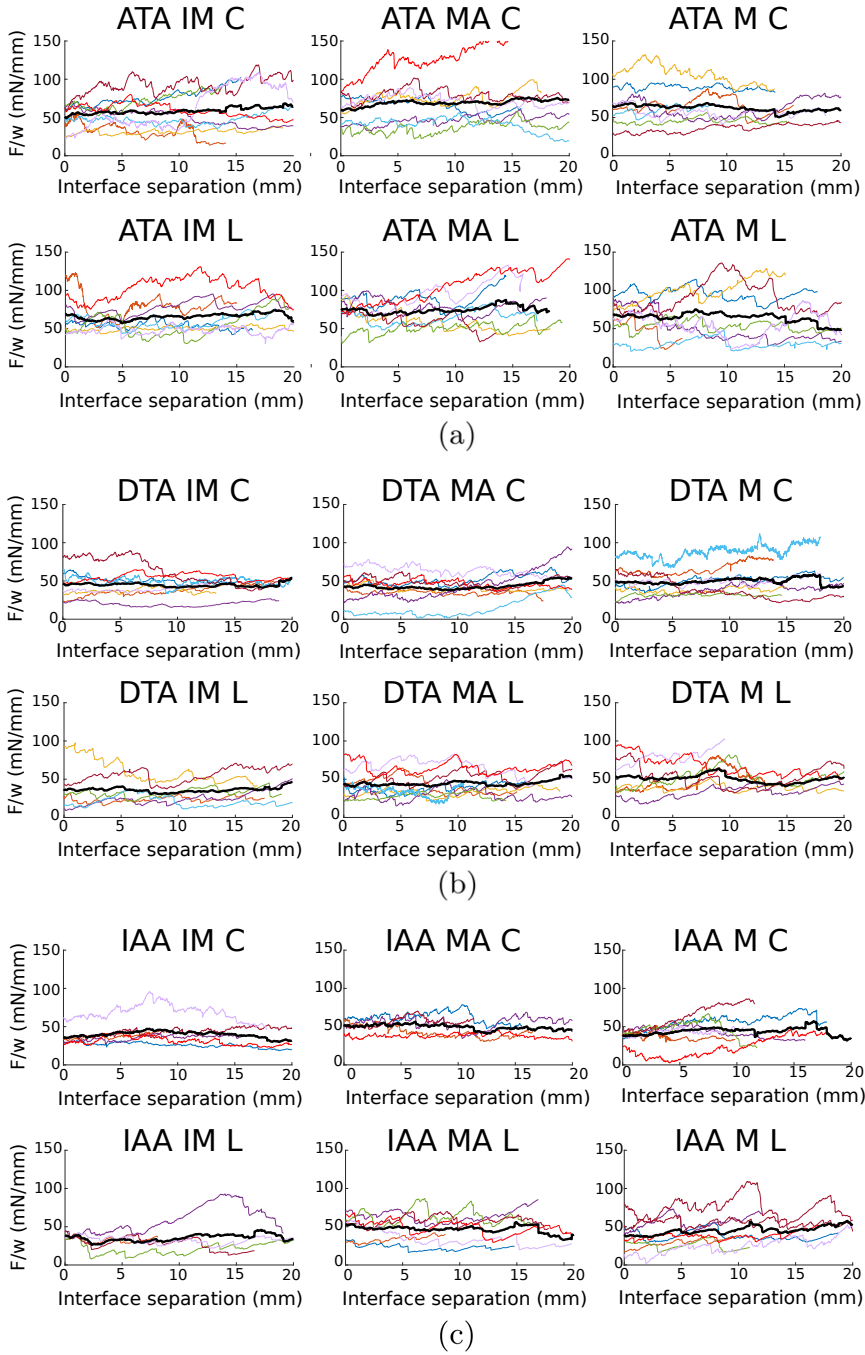
Figure 2.6. F/w (mN/mm) vs interface separation (mm) of the T-peel test performed in the specimens of the ATA (a), DTA (b) and IAA (c). For each region, the C direction is shown on top and the L one at the bottom. Separation of the IM is shown on the left, of the MA in the centre and the M on the right. Each individual is represented by one colour.
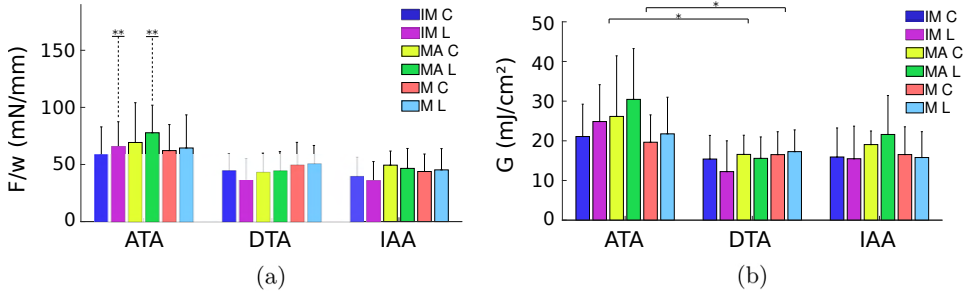
Figure 2.7. Averaged mean force/width and standard deviation (a) and dissection energy and standard deviation (b) of the T-peel test. * Statistically significant differences with a $p < 0.05$. ** Statistically significant difference, $p < 0.05$, in the separation of the specified interfaces between the ATA and the DTA, as well as the ATA and the IAA, shown this way for graphical purposes.

Table 2.4. Separation distance at damage initiation (mm) of the T-peel tests.

δ_0	*IM*		*MA*		*M*	
	C	**L**	**C**	**L**	**C**	**L**
ATA	0.0809	0.0995	0.1633	0.1839	0.1499	0.0666
DTA	0.0702	0.2037	0.1500	0.1324	0.0501	0.1361
IAA	0.1147	0.1991	0.1174	0.2004	0.0998	0.1669

2.3.2   Mixed-mode peel test

Figure 2.8 shows the force/width vs interface separation curves of all the specimens in the mixed-mode peel test throughout the entire separation. Table 2.5 and Figure 2.9.a detail the averaged force/width and standard deviation of each experiment, whereas Table 2.6 and Figure 2.9.b show the dissection energy per reference area. The force/width values obtained in this test were consistently higher than those obtained in the T-peel test. This increased force/width is common [134, 135] and is thought to happen because of the bend of the sample in the mixed-mode peel test, while other explanations suggest that the combination of different modes of fracture (modes I and II) has some effect in this increased dissection force [134]. In terms of location, dissection in the ATA required more force/width and energy than in other locations. In terms of anisotropy, dissection in the longitudinal direction required more force/width and energy than in the circumferential one in all locations, and the dispersion of results in the former was also generally higher. Regarding the differences among interfaces, IM separation required the least force/width and energy than other interfaces in all locations. In particular, the separation of the IM in the C direction was the easiest in all three locations.
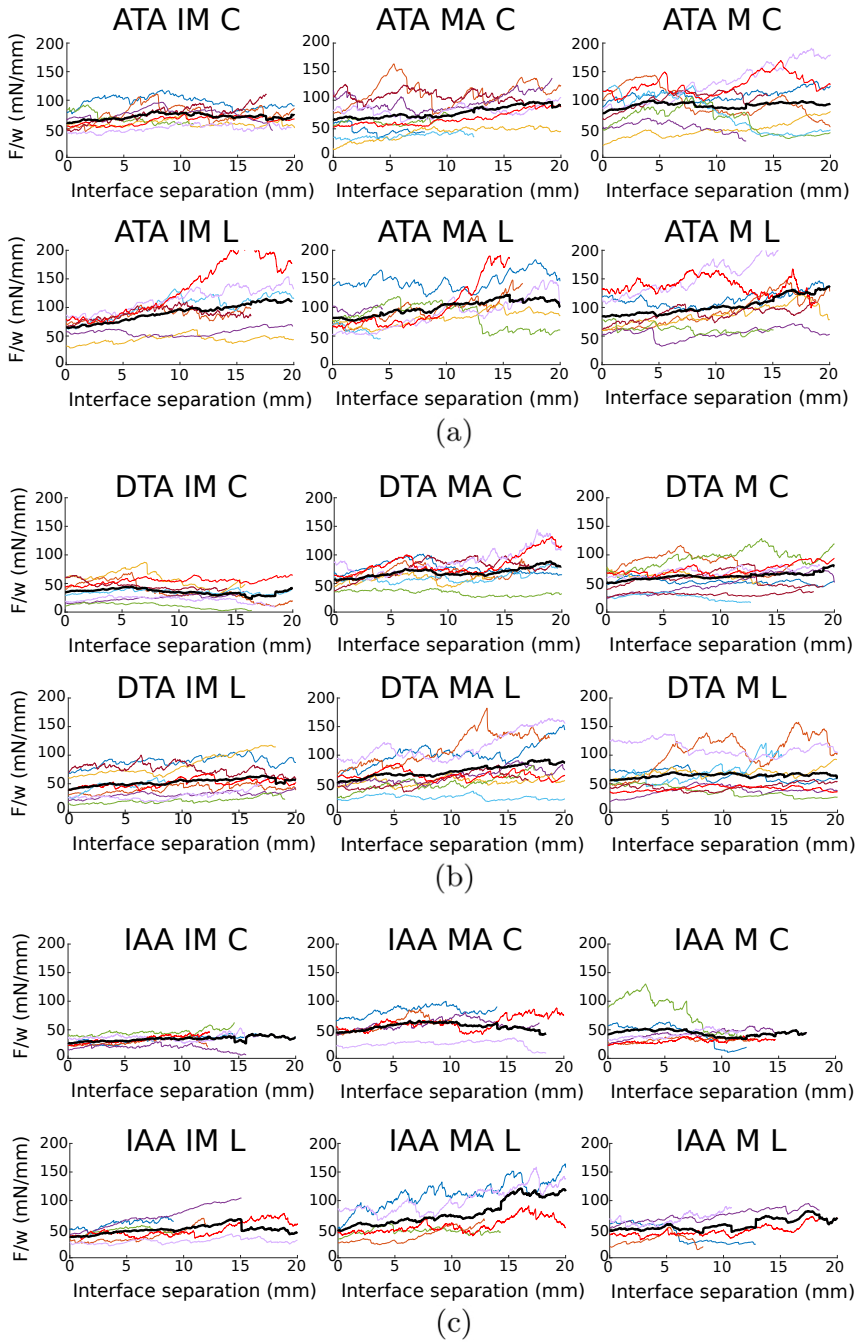
Figure 2.8. F/w (mN/mm) vs interface separation (mm) of the mixed-mode peel test performed in the specimens of the ATA (a), DTA (b) and IAA (c). For each region, the C direction is shown on top and the L one at the bottom. Separation of the IM is shown on the left, of the MA in the centre and the M on the right. Each individual is represented by one color.

Table 2.5. Average force/width $\pm$ SD (mN/mm) of the mixed-mode peel tests.

F_m	IM		MA		M	
	C	**L**	**C**	**L**	**C**	**L**
ATA	71.04 $\pm$ 16.92 (n=8)	90.69 $\pm$ 35.06 (n=7)	78.90 $\pm$ 28.80 (n=9)	100.16 $\pm$ 32.53 (n=8)	91.57 $\pm$ 37.77 (n=9)	103.03 $\pm$ 41.44 (n=8)
DTA	35.34 $\pm$ 18.47 (n=8)	52.95 $\pm$ 26.75 (n=9)	69.37 $\pm$ 21.62 (n=8)	72.32 $\pm$ 33.49 (n=9)	62.80 $\pm$ 23.38 (n=10)	64.50 $\pm$ 31.88 (n=9)
IAA	33.81 $\pm$ 8.25 (n=6)	49.10 $\pm$ 21.56 (n=6)	57.41 $\pm$ 21.58 (n=5)	79.29 $\pm$ 31.48 (n=5)	44.16 $\pm$ 16.95 (n=6)	57.90 $\pm$ 18.87 (n=5)
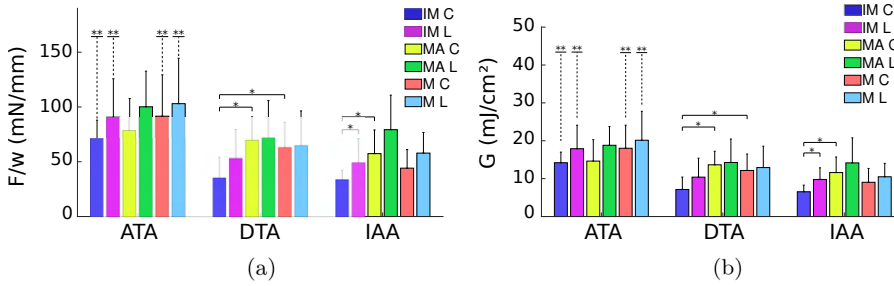
Figure 2.9. Averaged mean force/width and standard deviation (a) and dissection energy and standard deviation (b) of the mixed-mode peel test. * Statistically significant differences with a $p < 0.05$. ** Statistically significant difference, $p < 0.05$, in the separation of the specified interfaces between the ATA and the DTA, as well as the ATA and the IAA, shown this way for graphical purposes.

Table 2.6. Average dissection energy $\pm$ SD (mJ/cm²) of the mixed-mode peel tests.

G_c	IM		MA		M	
	C	**L**	**C**	**L**	**C**	**L**
ATA	14.20 $\pm$ 2.80	17.90 $\pm$ 6.20	14.64 $\pm$ 5.65	18.81 $\pm$ 4.94	18.02 $\pm$ 6.10	20.14 $\pm$ 7.64
DTA	7.14 $\pm$ 3.27	10.40 $\pm$ 5.01	13.66 $\pm$ 3.57	14.27 $\pm$ 6.19	12.16 $\pm$ 4.33	12.93 $\pm$ 5.65
IAA	6.54 $\pm$ 1.75	9.79 $\pm$ 3.07	11.61 $\pm$ 4.11	14.16 $\pm$ 6.61	9.04 $\pm$ 3.66	10.50 $\pm$ 3.54

Table 2.7 shows the separation distance at damage initiation for the mixed-mode peel tests.

2.3.3   Histology

Figure 2.10 shows different histologies performed on the delaminated interfaces of the DTA (a–c) and IAA (d–f) in the circumferential direction. The proper separation of the interfaces can be observed due to the distinct microstructural composition of the layers. Figure 2.10.a and Figure 2.10.d show the IM interface. The higher amount of connective tissue (elastin) in the intima, in light green, helps differentiate this

Table 2.7. Separation distance at damage initiation (mm) of the mixed-mode peel tests.

δ_0	IM		MA		M	
	C	**L**	**C**	**L**	**C**	**L**
ATA	0.1000	0.0572	0.0833	0.0550	0.0833	0.0495
DTA	0.1167	0.1001	0.0626	0.0831	0.1167	0.1167
IAA	0.0833	0.0999	0.0666	0.0341	0.0833	0.0526

layer from the media, which is characterised by the presence of muscle fibres (red).
The intima on the DTA is clearly visible, as well as the separation from the media
with the internal elastic lamina. This distinction is not as clear in the IAA, but the
intima can be differentiated by the higher amount of elastin (light green) on the outer
area. Regarding the media and adventitia, Figure 2.10.b and Figure 2.10.e, both
layers can be observed distinctively as the adventitial layer shows higher amounts
of connective tissue (collagen, in light green). The gaps on the adventitia are fat
tissue, also characteristic of this layer. Finally, Figure 2.10.c and Figure 2.10.f show
the separation of the media. The circumferentially oriented muscle fibres can be
perceived in the histologies.
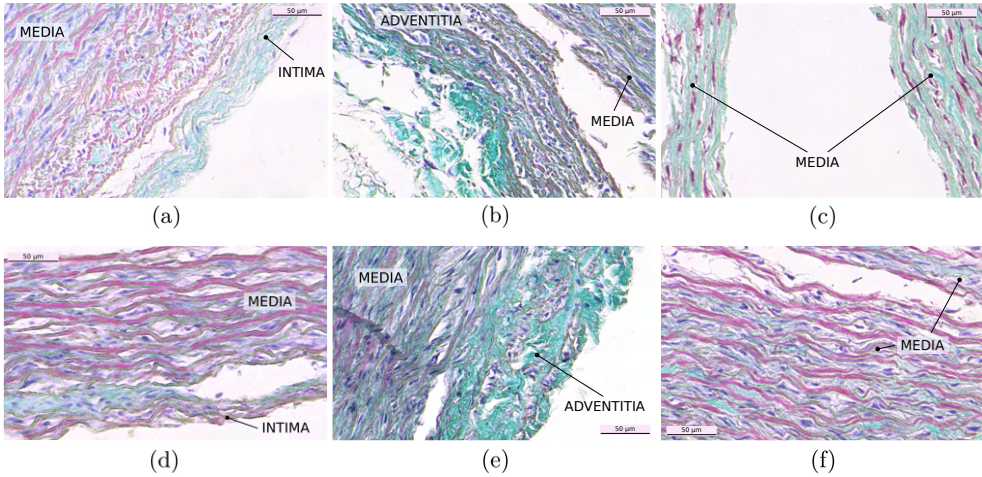
Figure 2.10. Masson's trichrome histologies of the three dissected interfaces with the T-peel test in the C direction. (a)–(c) show separations in the DTA and (d)–(f) in the IAA. IM separation is on the left column, MA separation is on the middle and M separation on the right. The different layers are indicated on the images. Scale bar is 50 μm.

2.4   Discussion of the experimental results

The experimental part of this study involved the performance of two dissection tests: the T-peel test, in which the separation happens in the perpendicular direction to the dissecting plane, and the mixed-mode peel test, in which the layers are separated in the direction parallel to the specimen. The T-peel test reproduces a mode I of fracture, whereas the mixed-mode peel test involves a mixed mode of fracture of modes I and II. However, both delamination tests are not the exact reproduction of the propagation of a tear in vivo [112, 136]. Nevertheless, many studies in literature that investigate the dissection behaviour of vessels have carried out these experiments and, therefore, the results can be properly compared and validated.

The discussion of results and comparison with other studies in literature will account for the differences found in location, interface and direction, but both tests will be discussed simultaneously as they showed similar trends.

2.4.1   Effect of location

The most notorious difference found in this study is the higher values of force/width and dissection energies that the specimens of the ATA present as opposed to the DTA and IAA for both tests. These values of force/width and energies have also been found slightly higher for the DTA than for the IAA, mostly in the mixed-mode peel test, although with no statistical significance. Therefore, this suggests that the resistance to dissection tends to diminish when moving distally, although type A dissections—those that involve the ascending aorta—are more frequent [48, 55, 56]. These results agree with the studies in literature that have performed T-peel tests on the medial layer of healthy porcine aortas, see Table 2.8. Myneni et al. [116] performed these delamination tests in specimens from the ATA and DTA. They obtained higher values of force/width for the specimens from the ATA than for those from the DTA in both directions, and the values are similar to those obtained in this study. Similarly, Leng et al. [58] performed T-peel tests on porcine IAAs. The values of force/width they reported are closer to the values in the DTA given by Myneni et al. [116], as what happened in our tests. Wang et al. [121] also performed T-peel tests on porcine DTAs and Noble et al. [117] on thoracic aortas (not specifying between ascending or descending) and the values of force/width they obtained were lower than those of the ATA obtained by Myneni et al. [116]. Compared to the data in this study, the ranges of values match, but the force/width here obtained in the T-peel test is slightly lower. Regarding dissection energy, the values obtained by Noble et al. [117] and Wang et al. [121] agree with those obtained in this study of the DTA (18.3-15.2 mJ/cm² and 18.4-10.6 mJ/cm², respectively).

The propagation of dissection through different locations of the aorta had been studied with other methodologies. Roach and Song [137] injected ink into the medial layer and controlled the pressure and volume needed to propagate tears in porcine aortas. They determined a uniform decrease of the tearing pressure and dissection

Table 2.8. Values of force/width obtained from T-peel tests on the medial layer of healthy porcine aortas. Table includes results from different studies as well as from this work—described as own research—for comparison. The values of force/width of Leng et al. [58] are estimated from their graphs, as they do not provide the value of an averaged force/width.

F_m	M		Source
	C	**L**	
ATA	86.0 ± 10.8	107 ± 31.6	[116]
	62.2 ± 22.8	64.5 ± 29.0	own research
DTA	57.5 ± 15.1	69.8 ± 17.9	[116]
	67.4 ± 11.7	76.7 ± 25.9	[117]
	46.0 ± 11.9	72.3 ± 22.3	[121]
	49.5 ± 19.9	50.5 ± 16.1	own research
IAA	around 60	around 60	[58]
	43.9 ± 15.3	45.3 ± 18.6	own research

energy while moving distally up to the upper abdominal aorta. However, when reaching the lower abdominal aorta, the energy increased dramatically. That decreasing tendency from the ATA to the upper abdominal aorta matches what was observed in this study.

The higher values of peeling force/width in the ATA have also been observed in healthy human aortas. Recently, Horný et al. [113] and Sokolis and Papadodima [119] studied the effect of location—among other parameters—in the dissection behaviour of the medial layer of human aortas via T-peel tests, obtaining these higher values of force/width in the ATA. Previously, Pasta et al. [118] had performed T-peel tests on the medial layer of the human ATA and obtained higher values of force/width in the delamination than Kozuń [114] and Sommer et al. [57], who performed the same tests on the human thoracic—presumably the descending region—and infrarenal abdominal aorta, respectively. Nevertheless, the specific values obtained in these studies do not completely match and cannot be directly compared to those of this work as they focused on human vessel. Apart from species, the differences between human and porcine tissue studies also arises due to age variations [113, 119, 138]. Human samples in most studies come from aged subjects, whereas the swines in the present study were comparably young, and dissection resistance has been shown to diminish with age [113, 119].

2.4.2   Effect of direction

Regarding vessel anisotropy, in the studies that performed T-peel tests in the medial layer of aortas, force/width for specimens in the longitudinal direction of the vessel is generally higher and the dispersion is larger than for those in the circumferential

direction [57, 58, 113, 116–118, 121], although this tendency has not always shown a statistical significance. This happens because the dissection within the medial layer in the circumferential direction normally separates muscular fibres and lamellar structures, whereas the dissection in the longitudinal direction has to propagate throughout these structures. Sommer et al. [57] observed the rougher surface of the longitudinal dissections compared to the circumferential ones with the help of histologies. In this study, this difference has not been found so predominantly, but is more prevalent in the results of the mixed-mode peel test, with even one statistically significant difference in the IAA, in the IM separation.

As for the separation distance at damage initiation, no clear differences are found throughout the experiments and the range of values agrees with literature [121]. Wang et al. [121] also did not find differences in this parameter regarding the different directions on healthy tissue, but did when compared to purified elastin. In particular, δ_0 was lower—although not statistically significant—in the dissection of purified elastin. This distance thus is less likely to vary notably unless substantial differences are imposed in the specimens.

2.4.3   Effect of dissected interface

Regarding the differences among interfaces, the main observation has been the easier propagation of a tear in the IM in terms of lower values of force/width and dissection energy in the DTA and IAA, more predominantly in the mixed-mode peel test. The results per interface in the ATA are fairly homogeneous. Tong et al. [122] performed T-peel tests differentiating the dissection among layers in the human carotid bifurcation, while Kozuń et al. [114, 115] did the same on human thoracic aortas. In the three studies, the separation in the IM implied less dissection energy than the separation of the MA. This could be explained by less internal structures being dissected when these two different layers are separated, which are clearly set apart by the internal elastic lamina, making the dissection interface less rough and easier to split. Also, the smaller dissection energy and force/width to separate the intimal and medial layers accounts for the easier and favoured propagation of an initial dissection, while it slows down when it translates to the medial layer.

2.4.4   Effect of individuals

The possibility that the differences found in this study arise from testing different individuals and not different locations, interfaces or directions has also been evaluated, with no significant or prevalent tendencies found. It can only be pointed out that some aortas were more difficult to test than others, meaning that when tests failed in one aorta, they were more likely to keep failing in the same aorta. And also that, in some aortas, the differences between directions and interfaces were more marked and closer to the tendencies generally found in literature. However, the number of full sets of samples is not enough to extract conclusions on this hypothesis.

2.4.5   Limitations of the experimental results

The results here presented are not directly suitable yet to clinical practice and it is important to discuss some limitations. The main one is that this study has been performed in healthy porcine tissue. An already damaged endothelium or a degenerated media can be a trigger for aortic dissection [39, 43]. Additionally, dissection is a common outcome of other pathologies like aneurysms [104]. Comparative studies between healthy and pathological tissue have shown the difference of dissection behaviour among them [114, 115, 118], as well as the the change in properties when the tissues are degraded [117, 121], or even the differences with age [113, 119]. Moreover, porcine aorta has been shown to provide different resistance to dissect than human aorta, in terms of peeling force/width and energy, therefore human models would require human tissue characterisation. Another limitation is the number of samples, as n=9 may not be enough to completely avoid individual characteristics. Also, the aortas were not fresh and therefore their mechanical behaviour could have been affected by the freezing/unfreezing process.

As per the histological study of this work, its purpose was to assure the separation of the layers of interest as observed via visual inspection. It would have been interesting to perform histologies in samples in the longitudinal direction to observe the differences in the dissected surfaces when compared to the circumferential. Furthermore, as the T- and mixed-mode peel tests involve different modes of rupture, performing histologies to samples from the mixed-mode peel test could have also brought some light onto the different mechanisms of damage that can occur in aortic dissection in vivo [139].

2.4.6   Key experimental findings

- The aorta has a location-dependent behaviour in terms of dissection properties. In particular, the vessel wall is easier to dissect when moving distally.

- The different layers to dissect require different levels of dissection energy and force. In particular, the separation of the intima and media is the easiest to propagate.

- Although less prominent, the anisotropy also plays a role in the dissection behaviour of the aorta, where tears in the circumferential direction tend to propagate more easily than in the longitudinal direction.

Therefore, these results suggest that dissection properties should be characterised in terms of location, direction and interface of the vessel.

2.5   Computational modelling

This section will provide a detailed description of the computational models developed to reproduce the experiments. With the reproduction of the delamination tests with a computational model, the dissection properties of the vessel can be obtained and the behaviour to dissection fully characterised [58, 103, 121]. To replicate the propagation of a tear from the in vitro tests, we will employ CZMs, which have been used in other research studies (see Section 2.1.2). With the development of these models, we propose a methodology to obtain the dissection properties of vessels from two types of peel tests. To develop these models, the formulation of fracture behaviour must be properly defined. Moreover, mechanical models require the elastic properties of the materials to ensure proper simulations. Al these factors will be detailed in this section, apart from the actual numerical implementation.

2.5.1   Elastic properties of aortic tissue

The elastic properties of the tissue have been extracted from experimental data of uniaxial tensile tests performed on the same tissue on which the peel tests were performed. The stress-strain curves from these tests were fitted with a hyperelastic material model to reproduce the behaviour of the tissue. Subsequently, the parameters of the fitted model were employed to transfer this elastic behaviour to the computational model.

2.5.1.1   Uniaxial tensile tests

From each aorta and location (see Section 2.2.1), two extra rectangular strips, one in the longitudinal and one in the circumferential direction, were cut with a dimension of 5 mm of width and 25 mm of length. Simple uniaxial tension tests were performed in these samples in a high precision drive Instron Microtester 5548 system using a 10 N load cell with a minimum resolution of 0.005 N. After flattening and securing the tissue specimen in the grips, the zero load point was established to eliminate any weight effects and the pre-tension used to flatten the specimens during load cell measurements. A non-contact Instron 2663-281 video-extensometer was used to measure the strain during the tests. Three cycles of loading and unloading were applied (reaching the stress levels of 60, 120 and 240 kPa) at 30%/min of strain rate, which can be considered quasi-static [31]. Five preconditioning cycles at all load levels were applied. The tissue was kept from dehydration with the help of a humidifier. The engineering stress (first Piola Kirchhoff stress tensor $\mathbf{P}$) is computed as $P_i = \frac{F_i}{t_i \, w_i}$, where F_i is the load registered by the Instron machine and t_i and w_i are the initial thickness and width of each strip in circumferential and longitudinal directions. Only the elastic properties of the tissue are of interest, therefore only the experimental data at the second loading level (120 kPa) after preconditioning is considered.

2.5.1.2 Material model

The Gasser-Ogden-Holzapfel (GOH) model presented by Gasser et al. [140] is used to reproduce the elastic response of the aorta. It is a nonlinear, anisotropic, hyperelastic model that incorporates the contributions of the individual constituents of the tissue (e.g. collagen fibers, elastin fibers, smooth muscle cells) to its overall behaviour. In particular, the model takes into consideration the existence of two families of collagen fibres that are oriented helically, with the same but opposite angle of orientation, see Figure 2.11.

This model proposes the application of a generalised structure tensor $\mathbf{H} = \kappa \mathbf{1} + (1 - 3\kappa)\mathbf{M}_0$, where $\mathbf{1}$ is the identity tensor and $\mathbf{M}_0 = \mathbf{m}_0 \otimes \mathbf{m}_0$ is a structure tensor defined using unit vector $\mathbf{m}_0$ to specify the mean orientation of fibres. The strain energy function (SEF) of the GOH model is as follows:

$$\Psi = \mu \left(I_1 - 3\right) + \sum_{i=4,6} \left[\frac{k_1}{2k_2} \left(exp\left\{ k_2 \hat{E}_i \right\} - 1 \right) \right], \qquad (2.5)$$

where $I_1 = tr\bar{\mathbf{C}}$ represents the first invariant of the Cauchy-Green tensor ($\mathbf{C} = \mathbf{F}^T\mathbf{F}$), $\mathbf{F}$ is the deformation gradient [141] and

$$\hat{E}_i = \kappa I_1 + (1 - 3\kappa)I_i - 1 \quad i = 4, 6 \qquad (2.6)$$

where

$$I_4 = \lambda_\theta^2 \cos^2(\theta) + \lambda_z^2 \sin^2(\theta), \qquad I_6 = \lambda_\theta^2 \cos^2(-\theta) + \lambda_z^2 \sin^2(-\theta). \qquad (2.7)$$

In (2.5), μ and k_1 are stress-like parameters and k_2 and κ are dimensionless. $\mu > 0$ accounts for the stiffness of the vessel matrix, excluding the effect of the fibres. $k_1 > 0$ represents the stiffness of the fibres themselves. $k_2 > 0$ impacts the exponential
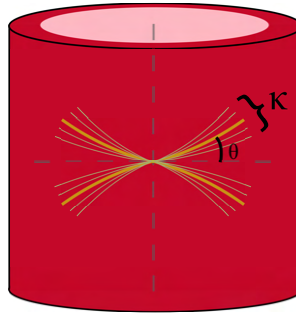
Figure 2.11. Representation of the two families of fibres accounted for in the GOH model. θ is the angle of the main orientation of the families with the circumferential direction and κ represents the dispersion of the fibres.

performance of the response curve, which comes mostly from the recruitment of fibres to work in the loading direction. $\kappa \in [0, 1/3]$ is a dispersion parameter—the same for each collagen fibre family—, in which a value of 0 implies totally aligned fibres with the preferred orientation, whereas a value of $1/3$ indicates a completely isotropic behaviour of the tissue. In (2.7), θ represents the orientation angle of the main collagen fibres.

2.5.1.3   Numerical fitting

The elastic properties of the aorta were fitted with the uniaxial tension tests data by using a Nelder and Mead type minimisation algorithm [142] defining the objective function

$$\chi^2 = \Sigma_{i=1}^n \left[\left(P_{\theta\theta} - P_{\theta\theta}^{\Psi} \right)_i^2 + \left(P_{zz} - P_{zz}^{\Psi} \right)_i^2 \right] \tag{2.8}$$

using HyperFit software.[1] The tissue was assumed incompressible [143], i.e., $\det(\mathbf{F}) = \lambda_1\lambda_2\lambda_3 = 1$, where $\mathbf{F}$ represents the deformation gradient tensor and λ_i, $i = 1, 2, 3$, the stretches in the principal directions. $P_{\theta\theta}$ and P_{zz} are the First Piola-Kirchhoff (engineering) stress data obtained from the tests, and

$$P_{\theta\theta}^{\Psi} = \frac{\partial \Psi_{\text{iso}}}{\partial \lambda_{\theta}} \ \text{ and } \ P_{zz}^{\Psi} = \frac{\partial \Psi_{\text{iso}}}{\partial \lambda_z} \tag{2.9}$$

are the First Piola-Kirchhoff stresses for the ith point for a homogeneous pure uniaxial state Ψ. The normalised root mean square error, $\varepsilon \in [0, 1]$, was computed for the fitting of the material model, following

$$\varepsilon = \frac{\sqrt{\frac{\chi^2}{n-q}}}{\varpi}, \tag{2.10}$$

where

$$\varpi = \sum_{i=1}^n \frac{P_i}{n} \tag{2.11}$$

is the mean value of the measured engineering stresses, n is the number of data points, q is the number of parameters of the SEF and, therefore, $n - q$ represents the number of degrees of freedom.

The elastic mechanical data obtained by uniaxial tests experiments in each direction, longitudinal and circumferential, were fitted using the SEF represented in (2.5). The material constants resulting from the fitting to the SEF are shown in Table 2.9. The low value obtained of $\varepsilon = 0.0652$ demonstrates the goodness of the fitting.

Plots of the fitted stress-stretch behaviour for the longitudinal and circumferential directions, together with the underlying experimental data are depicted in Figure 2.12 for the constitutive law in (2.5).

---

[1]www.hyperfit.wz.cz

Table 2.9. Material parameters obtained from the uniaxial stress-stretch curves. θ represents the angle with respect to the circumferential direction of the vessel.

μ (kPa)	k_1 (kPa)	k_2 (-)	κ (-)	$\theta(°)$	R^2	ε
18.0606	504.9060	44.8462	0.24299	35	0.9893080	0.0652
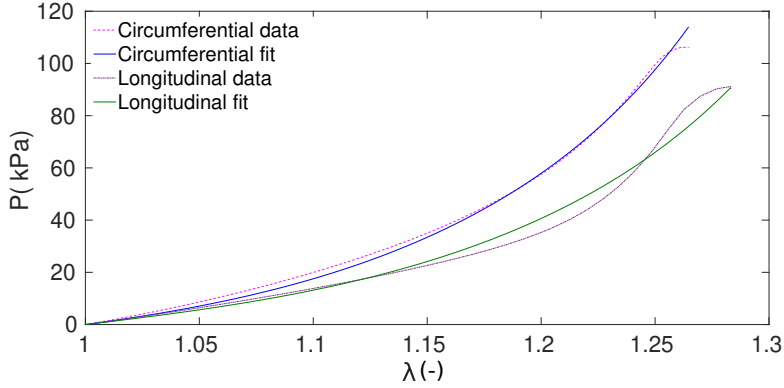
Figure 2.12. Experimental data of uniaxial tension tests and computational fitting obtained with the proposed constitutive law.

2.5.2 Fracture properties of aortic tissue

In order to model the fracture behaviour of the interface between the arterial layers, we propose a traction-separation law (TSL) that relates the interfacial traction **t** (normal and shear) with interfacial displacement $\boldsymbol{\delta}$ [144]. The components of the traction stress vector (τ_n, τ_s, and τ_t) represent the normal and the two shear tractions along the interface and the related displacements are δ_n, δ_s, and δ_t.

The elastic behaviour of the interface is defined by:

$$\boldsymbol{\tau} = \begin{pmatrix} K_{nn} & 0 & 0 \\ 0 & K_{ss} & 0 \\ 0 & 0 & K_{tt} \end{pmatrix} \boldsymbol{\delta} = \mathbf{K}\boldsymbol{\delta}. \tag{2.12}$$

A triangular TSL was considered to model cohesive properties of the tissue, see Figure 2.13. The initial interface displacement $\delta_{0_{n,s,t}}$, the tissue maximum strength $\tau_{n,s,t_{max}}$ and the energy release rate (the energy dissipated by the cohesive zone) $G_{0_{n,s,t}}$ define the mechanics of the cohesive zone following

$$K_{ii} = \frac{\tau_{i_{max}}}{\delta_{0_i}} \qquad G_{0_i} = \frac{\delta_{r_i} \cdot \tau_{i_{max}}}{2}, \tag{2.13}$$

where $i = n, s, t$.
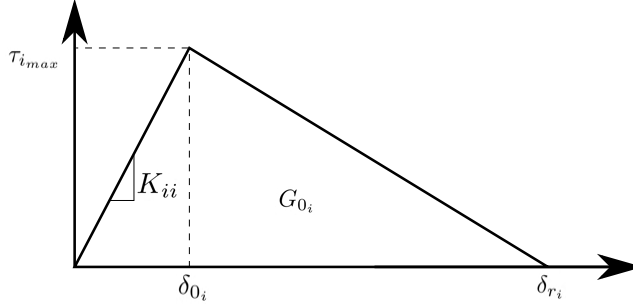
Figure 2.13. Traction-separation law considered. The cohesive strength $\tau_{i_{max}}$, the initial (reversible) interface displacement δ_{0_i}, the maximum cohesive displacement, δ_{r_i}, the dissection energy G_{0_i} and the cohesive stiffness K_{ii} are parameters to be defined.

The evolution of damage can be defined by specifying either the effective displacement at complete failure, $\delta_{r_{n,s,t}}$, related to the effective displacement at the initiation of damage, $\delta_{0_{n,s,t}}$, or the energy dissipated due to failure $G_{0_{n,s,t}}$.

Damage law is defined in the context of Continuum Damage Mechanics Theory [145]. Damage is assumed to initiate when the maximum nominal stress ratio reaches a value of one:

$$max\left\{\frac{\tau_n}{\tau_{n_{max}}}, \frac{\tau_s}{\tau_{s_{max}}}, \frac{\tau_t}{\tau_{t_{max}}}\right\} = 1. \tag{2.14}$$

$D \in [0, 1]$ is a scalar variable that represents the damage of the material and combines the effects of all the mechanisms. D monotonically progresses from 0 to 1 upon further loading after the initiation of damage. In the context of linear softening, the evolution of D is computed as

$$D = \frac{\delta_m^f(\delta_m^{max} - \delta_m^0)}{\delta_m^{max}(\delta_m^f - \delta_m^0)}, \tag{2.15}$$

where δ_m is computed as

$$\delta_m = \sqrt{\langle\delta_n\rangle^2 + \delta_s^2 + \delta_t^2}, \tag{2.16}$$

and δ_m^f is the displacement at complete failure relative to the displacement at damage initiation, δ_m^0, and δ_m^{max} refers to the maximum value of the displacement reached during the loading history. The Macaulay brackets ($\langle x\rangle = 0$ if $x < 0$ or $\langle x\rangle = x$ if $x > 0$) are used to enforce that there is no damage initiation at pure compressive deformation or stress.

Finally, the stress of the traction-separation model is computed according to:

$$\tau_n = \begin{cases} (1 - D)\tau_n & \text{if } \tau_n' > 0 \\ \tau_n' & \text{otherwise} \end{cases} \tag{2.17}$$

$$\tau_s = (1 - D)\tau_s' \tag{2.18}$$
$$\tau_t = (1 - D)\tau_t' \tag{2.19}$$

where τ_n', τ_s' and τ_t' are the effective stress components of the undamaged material computed by the elastic traction-separation law.

2.5.3   Numerical implementation

This damage model will be solved by developing FE models. In particular, the software Abaqus/Standard v6.14 will be used, which has some in-built cohesive formulations to solve this type of delamination. Two different approaches have been studied to reproduce our experiments, which involve using either cohesive surfaces or cohesive elements. In both cases, the formulation and parameters to be fitted are the same (see Figure 2.13). However, on the one hand, the cohesive surfaces approach gives these properties directly to the two interfaces in contact that are going to be separated, which also have implemented the hyperelastic material behaviour. On the other hand, the cohesive elements approach involves placing a layer of thin elements with cohesive properties exclusively between the two interfaces that are intended to be separated. The models developed following both approaches, their similarities and differences, are going to be detailed in this section.

2.5.3.1   Cohesive surfaces

Both the T-peel test and the mixed-mode peel test were reproduced with cohesive surfaces. The FE geometry was specific for each experimental strip, and their specific dimensions were obtained by averaging the experimental measurements per condition, see Table 2.10. The ratio of thickness per layer was obtained from other studies from literature [34, 146, 147], see Table 2.11. The total length of the strips in all models was of 20 mm. Variations in this dimension were observed to not affect the results of the models. The corresponding interfaces to be separated were defined with the cohesive contact model previously presented and the models were meshed with hybrid eight-node linear bricks (C3D8H), see Figure 2.14. A mesh sensitivity analysis was performed in both models to achieve the compromise between accuracy and computational time. A refined mesh in the contact area was needed in order to get appropriate results, see Figure 2.14. The final number of elements of each specimen is included in Table 2.10. The symmetry of the problem was taken into account and only half of the width of the specimens was modelled.

Regarding the boundary conditions, in the T-peel test, the non-separated end of the strip was fixed to prevent its movement as solid rigid, and in both flaps at the other end the same displacement was imposed in opposite directions, causing delamination at the interface of the layer. As for the mixed-mode peel test, the inner surface of the intima of the specimen was fixed and a displacement loading parallel to the strip length was applied to the free end of the other layer, causing the desired delamination at the interface.

Table 2.10. Dimensions and number of elements of each model.

Specimen		Width (mm)	Thickness (mm)	Number of elements
T-peel test	**IM**	4.0	1.70	50,340
	MA	4.0	2.00	54,700
	M	4.0	2.10	57,040
Mixed-mode peel test	**IM**	5.0	1.57	25,265
	MA	4.8	2.30	20,370
	M	5.0	2.00	27,962

Table 2.11. Thickness ratio of the layers as function of location in porcine aorta [34, 146, 147].

Location	Thickness ratio of layer		
	Intima	**Media**	**Adventitia**
ATA	14%	64%	22%
DTA	12%	60%	28%
IAA	18%	49%	33%

(a)   (b)
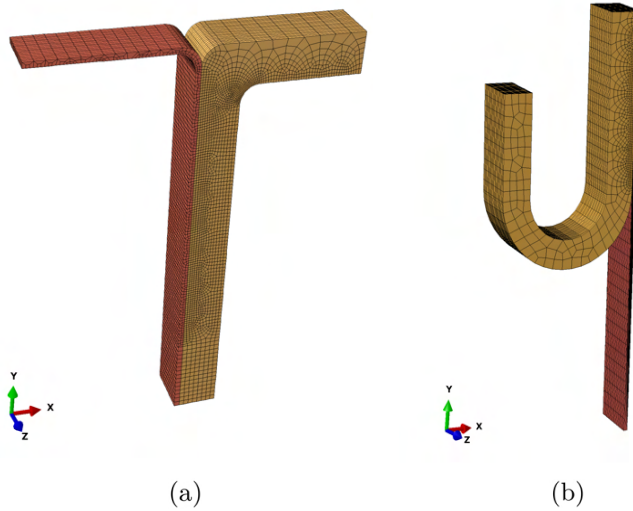
Figure 2.14. FE models of the T-peel test (a) and mixed-mode peel test (b) using cohesive surfaces. Both models represent the IM separation. The thinner copper-coloured parts represent the intimal layer and the thicker brass-coloured parts, the media and adventitia.

An iterative trial-error procedure was performed to fit the delamination proper-ties of aorta layers. The mechanical data in terms of the dissection force/width vs. displacement curve from the T-peel and mixed-mode peel tests was compared in each iteration. The displacements applied in the free surfaces were prescribed and the

cohesive properties updated in order to fit the mean force recorded during the tests. The hyperelastic material model (see Section 2.5.1) was implemented via the in-built material model in Abaqus. The preferred fibre directions were included manually in the input files. A static implicit analysis was carried out for all models, as the strips are pulled apart slow enough to exclude inertial effects.

The T- and mixed-mode peel tests were used to identify the normal cohesive material parameters that model purely normal failure at the interface of IM, MA and M (δ_{0_n}, δ_{r_n}, $\tau_{n_{max}}$, K_{nn} and G_{0_n}). A cohesive zone was introduced in the two surfaces of the interface to analyse, where tissue delamination was expected.

2.5.3.2   Cohesive elements

The general approach of creating CZMs with cohesive elements is very similar to that of cohesive surfaces. In this case, only the T-peel test was reproduced with cohesive elements, and a parameter sensitivity analysis was performed with this model. The geometrical parameters are the same as the previous case, and the mesh elements now combine the hybrid eight-node linear bricks (C3D8H) with eight-node 3D cohesive elements (COH3D8) in the cohesive layer between interfaces, a thin layer of 0.001 mm of thickness, see Figure 2.15. The boundary conditions of the T-peel test are the same in this case than in the previous one. However, in these models we could determine that a one element thick plane strain model gave the same results as the full 3D model, notably reducing the computational time. Being a one element thick model, we were able to still introduce the orientation of the collagen fibres in the width of the specimen. In this plane strain base model, the total number of elements is 2303, with 143 type COH3D8 elements and 2160 type C3D8H elements, see Figure 2.15.

Using this model, the impact of various parameters on the dissection force was examined, specifically focusing on the influence of the length of the flaps or incision size, the total thickness of the sample and the thickness ratio between flaps, the different material parameters of the GOH material model and modelling different material properties per layer [34]. A static implicit analysis was performed in all cases.

2.6   Calibrating the dissection properties of the porcine aorta using cohesive surfaces

The studied output of the computational models is the force/width (mN/mm) required to separate the simulated interfaces, which is the data we obtain from the experimental tests (Section 2.3). In this case, the fitted tests were a set of samples from the DTA. The normal values of cohesive properties δ_{0_n}, δ_{r_n}, $\tau_{n_{max}}$, K_{nn} and G_{0_n} were calibrated by an iterative fitting of the experimental measurements of the T- and mixed-mode peel tests. In each iteration, the values of peak and mean force of the computational modelling were compared to the experimental data until their
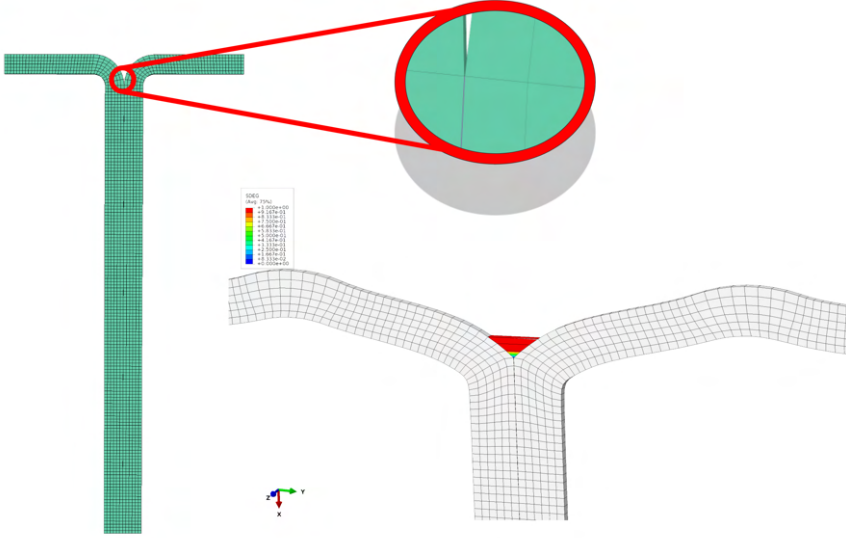
Figure 2.15. Mesh of the base cohesive element model. The cohesive element layer of 0.001 mm of thickness is zoomed in and it lies between the two interfaces to separate. The cohesive elements can be observed more clearly when the layers are being separated (right).

difference was below 10%. Several iterations were needed to identify the sets of constants ($\tau_{n_{max}}$, K_{nn} and G_{0_n}) that minimised the differences between the value of load vs. displacement curve obtained by the experimental T-peel and mixed-mode peel tests and that obtained by the FE model. These parameters are presented in Table 2.12 and Table 2.13, respectively. The ranges of force achieved in the simulation could mostly be fitted by modifying parameters directly related to the initiation and development of damage $\tau_{n_{max}}$ and G_{0_n}. The parameter related to the cohesive behaviour K_{nn} had a reduced impact in the level of force and was found to account for the convergence of the models.

Table 2.12. Normal cohesive material parameters obtained by fitting of the T-peel test and used to model normal failure at the interface.

	Interface	δ_{0_n} (mm)	δ_{r_n} (mm)	$\tau_{n_{max}}$ (kPa)	K_{nn} (mN/mm3)	G_{0_n} (mN/mm)
IM	Longitudinal	0.023	0.070	230	10,000	8
	Circumferential	0.014	0.100	200	14,000	10
MA	Longitudinal	0.019	0.086	185	10,000	8
	Circumferential	0.020	0.063	160	8,000	5
M	Longitudinal	0.013	0.092	130	10,000	6
	Circumferential	0.010	0.100	80	8,000	4

Figure 2.16 shows the experimental data of the T-peel tests and the numerical fit obtained with the cohesive surfaces models. The initial elastic part of the curves is well reproduced in all cases except for the MA separation in the circumferential direction. This part of the tests is mainly affected by the modelling of the material and the preferred fibre directions (see Section 2.5.1). Due to convergence issues, this test could not be computed for a clamp displacement of more than 2 mm per side. Damage properties shown in Table 2.12 are consistently lower in the circumferential direction than in the longitudinal direction in each interface. This is in accordance with the dissection in the circumferential direction reportedly being easier, as it can propagate separating lamellar layers and not tearing them [57]. Furthermore, damage properties are notably smaller in the dissection within the medial layer compared to the dissection of both interfaces. The stiffness of the cohesive contact K_{nn} is similar in all cases. The values of the interface displacement, δ_{0_n}, are one order of magnitude below the experimental data calculated of the separation distance at damage initiation, see Table 2.4.
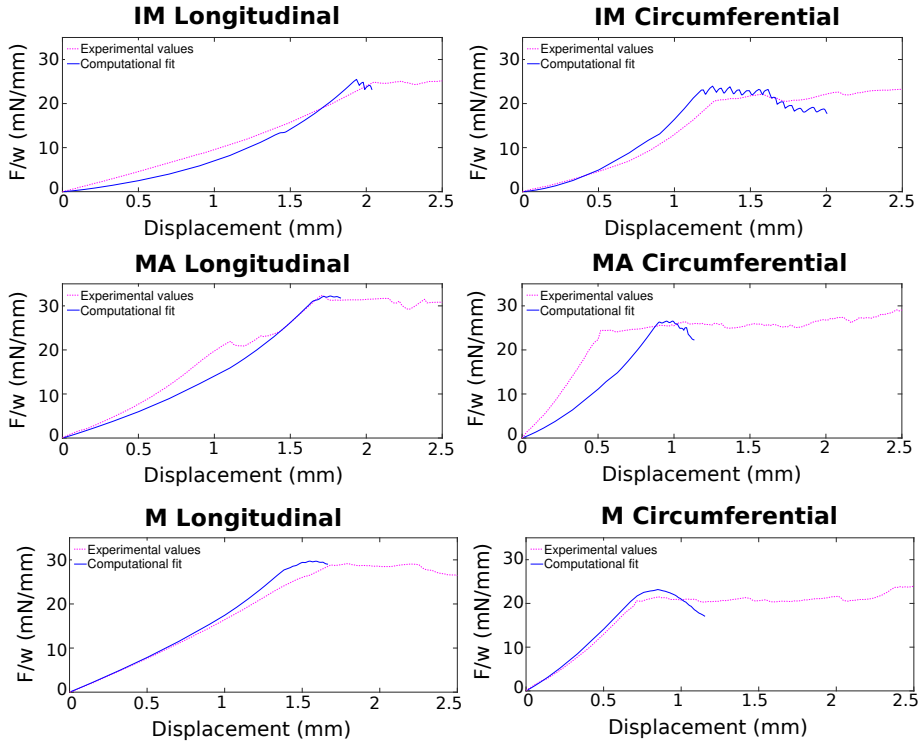
Figure 2.16. Correlation between force/width vs. displacement experimental (pink dashed lines) and computational (blue straight lines) curves of the T-peel test of the interfaces IM, MA and M for longitudinal and circumferential directions.

Table 2.13. Normal cohesive material parameters obtained by fitting of the mixed-mode peel test and used to model normal failure at the interface.

	Interface	δ_{0_n} (mm)	δ_{r_n} (mm)	$\tau_{n_{max}}$ (kPa)	K_{nn} (mN/mm3)	G_{0_n} (mN/mm)
IM	**Longitudinal**	0.040	0.100	800	20,000	40
	Circumferential	0.034	0.073	550	16,000	20
MA	**Longitudinal**	0.078	0.104	1250	16,000	65
	Circumferential	0.088	0.107	1400	16,000	75
M	**Longitudinal**	0.081	0.100	1300	16,000	75
	Circumferential	0.075	0.100	1200	16,000	60

Figure 2.17 shows the experimental data of the mixed-mode peel tests from a set of samples from the DTA and the numerical fit obtained with the cohesive surfaces models. In this case, the initial elastic part of the curves is well reproduced in all cases. The modelling of the mixed-mode peel test allowed for higher convergence, up to 10 mm of clamp displacement. All fitted parameters in this test shown in Table 2.13 are consistently higher than those obtained for the simulation of the T-peel test. The dissection of the IM provided the lowest damage parameters, in accordance with this separation presenting the lowest dissection forces. For the IM and M dissections, the longitudinal direction presented higher values in its properties than the circumferential direction. The effective displacement at complete failure, δ_{r_n}, is of around 0.1 mm in all cases, and is similar to the experimentally obtained, see Table 2.7. The cohesive parameter K_{nn} is the same in all cases, except for the IM separation in the longitudinal direction.

The experimental forces to be fitted are predominantly higher in the mixed-mode peel test than in the T-peel test, with the exception of the separation of the intima-media in the circumferential direction. The dissection parameters obtained in all simulations of the mixed-mode peel tests are notably higher—sometimes one order of magnitude—than those obtained in the T-peel tests. The main parameter that affects the reaction force of the simulations was $\tau_{n_{max}}$ and therefore is the one that varies most throughout the simulations. Ferrara and Pandolfi [12] had checked the relevant influence of this parameter in the numerical results of a dissection process. The marked difference between the parameters obtained in both types of simulations is not convenient. The negligible impact of the tangential components of the cohesive model in the mixed-mode peel test simulations lead to the assumption that not all the damage phenomena are being captured in the simulations, which could lead to these differences. Moreover, the rupture stress obtained in the uniaxial tension tests was of 1090 and 660 kPa for the circumferential and longitudinal directions, respectively. The values of $\tau_{n_{max}}$ obtained in the mixed-mode peel test models are more similar to these fracture stresses. This could also imply that the low values of these parameters in the T-peel test could be due to the specimens experiencing damage in the tissue and not the specific separation of layers.
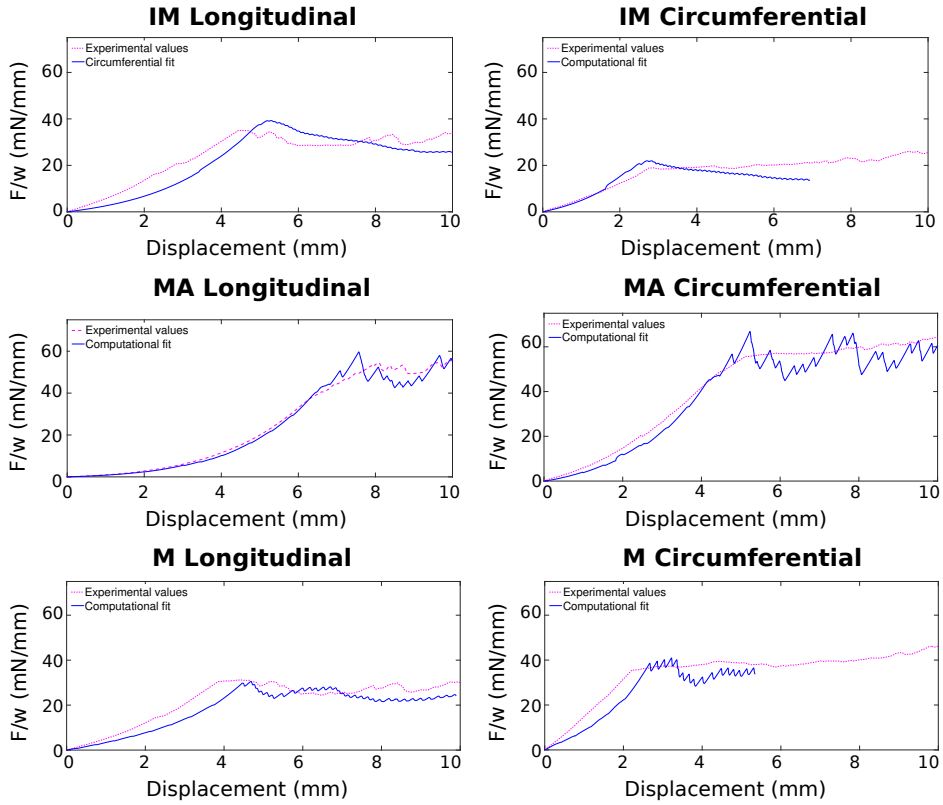
Figure 2.17. Correlation between force/width vs. displacement experimental (pink dashed lines) and computational (blue straight lines) curves of the mixed-mode peel test of the interfaces IM, MA and M for longitudinal and circumferential directions.

When compared to literature, Leng et al. [58] reproduced with CZMs these same two tests for the separation of the medial layer of a porcine abdominal aorta. They established a $\tau_{n_{max}}$ of 440 kPa for both tests, which lies in the same order of magnitude of our results for the T-peel test. The energy rate they obtain however is higher—220 and 186 mN/mm for the mixed-mode and T-peel test, respectively.

The complexity of the numerical models here presented entails some convergence issues. The simulation of contact and damage has always been challenging, even more when combined with hyperelastic anisotropic material models. Carrying out these computations with a static implicit analysis ensures a more accurate and stable solution, but it also hinders a full convergence of the models. As a future development, the cohesive model could be modified to include a more real contribution of shear stresses in the dissection properties of the tissue. An anisotropic damage model with a different dependence on the separation direction could probably provide a more uniform fitting for the T-peel and mixed-mode peel tests. Moreover, the process

of delamination has an important viscous factor and adding this in the formulation would likely render more valid results.

   To sum up, in this part of the study, we have provided a calibrated methodology to obtain delamination properties of arteries. The characterisation of these properties is relevant to achieve a better understanding of the mechanical behaviour of vessels in general and of the process of aortic dissection in particular. Furthermore, numerical studies about in vivo aterial dissections can benefit from this type of data to reproduce with more accuracy the physiology and pathology of the cardiovascular system.

2.7   On the development of CZMs based on cohesive elements

Using cohesive elements, we created an optimised CZM reproducing the T-peel test with a short computation time. This has enabled us to analyse how various experimental and modelling factors impact the dissection force obtained during the T-peel test. Starting from the evaluation of the effect of the width of the experiment, which led us to define a plane strain model, we have evaluated other geometrical and test-related variables, such as the effect of the size of the initial incision, the total thickness of the sample and the thickness ratio between the flaps. Apart from these, we have also studied the effect of the modelling parameters of the material and cohesive formulation. In this section, we will show and discuss the results of these evaluations. It must be noted that these analyses have been performed by modifying exclusively the studied parameter, leaving the rest of the conditions of the simulation fixed.

2.7.1   Effect of geometrical parameters

Figure 2.18 shows the computational dissection force/width of the simulations in the analysis of the influence of geometrical parameters. The effect of a variable will be considered relevant when the mean dissection force differs more than 5%. The total width of the sample shows to have no impact on the results, which is expected as we are studying the force/width precisely to avoid its effect. In this analysis of the width, we can also observe how the plane strain model gives the same results as a full 3D model. In terms of incision size, the simulation was carried longer as there were some variations at the start of the delamination. When examining the stable plateau dissection force, it is noteworthy that the initial incision size has no effect on the outcome. This information is valuable in determining an experimental protocol. The total thickness of the sample, however, does affect the dissection force. In particular, higher thicknesses result in greater dissection forces, while lower thicknesses lead to lower dissection forces. This finding implies that, when developing computational models for dissection tests, it would be necessary to create a separate model for each location of the aorta, as its thickness varies along its length (Table 2.1). Ultimately,

the thickness ratio between the flaps that are being separated does not impact the dissection force. This allows for the development of a basic, generalised model using a 50-50 thickness ratio, which tends to exhibit good convergence.
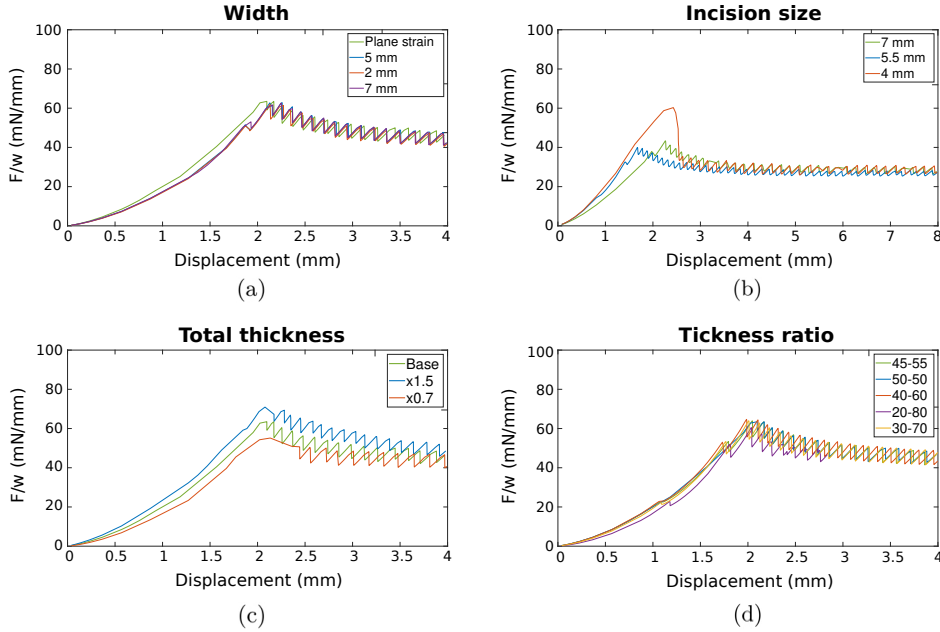
Figure 2.18. Analysis of the effect of the geometrical parameters of the strips. Width (a), incision size (b) and thickness ratio (d) have no effect on the dissection force (F/w), whereas the total thickness of the specimen (c) does affect this dissection force.

2.7.2 Effect of elastic modelling parameters

The effect of the material formulation of the GOH model was analysed by varying the model parameters within the ranges that have been reported in the literature [34,148]. Figure 2.19 shows an overlook of all the different tested combinations. It can be seen how the initial part of the curves, i.e., the elastic deformation of the specimen, is highly affected by the parameters of the hyperelastic model, but the dissection force to separate the interfaces remains unaltered. Figure 2.20 shows a closer look of all the varied parameters, where their specific effect on the initial slope can be discussed. When varying μ, Figure 2.20.a, which accounts for the stiffness of the isotropic matrix, we can observe how it indeed affects the most initial slope of the elastic deformation, when only the matrix is giving mechanical support as collagen fibres have not fully stretched from their wavy configuration. In fact, the last part of the initial upward slope, which is more affected by the stiffness of the fibres as they are already recruited, shows the same slope among these cases. In contrast, we can

see how this last slope differs when we vary k_1, Figure 2.20.c, the stiffness of the fibres, whereas the initial part of the slope in this case remains the same. κ accounts for the coherence of alignment of the fibres with the defined angle. As our base model is a sample in the circumferential direction, and fibres are mostly aligned in this direction, Figure 2.20.b shows how decreasing the value of κ, i.e., making the fibres more aligned, results in a stiffening of the elastic part. Moreover, Figure 2.20.d shows the effect of the parameter k_2, which affects the exponentiality of the curves, and we can see how an increase in this value, causes a more exponential initial part of the curves. Changing the orientation of the sample, from the circumferential to the longitudinal direction, did not affect either the dissection force. Lastly, we investigated the impact of incorporating the layer-specific elastic properties of the vessel into the models, and determined that it had no significant effect on the dissection force.
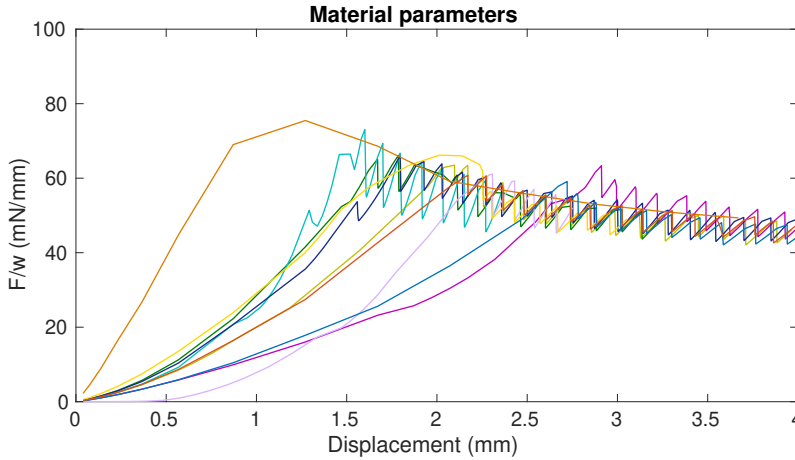
Figure 2.19. General overlook of the effect of different parameters of the GOH material model in the dissection force. The plateau dissection force remains unaltered for all cases.

2.7.3 Studying the impact of the cohesive and damage parameters

To finish this computational study with cohesive elements, we observed the effect of the cohesive and damage properties on the dissection force, see Figure 2.21. With this analysis of our model, we can obtain essential information that will enable us to iteratively fit the cohesive and damage parameters and replicate the data from experimental tests. We could observe that the dissection energy, G_{n_0}, is the parameter that most affects the dissection force (Figure 2.21.a), whereas the cohesive strength, $\tau_{n_{max}}$, has a smaller effect (Figure 2.21.b and Figure 2.21.c). This finding differs with the cohesive surface models, in which the cohesive strength had a bigger effect in the
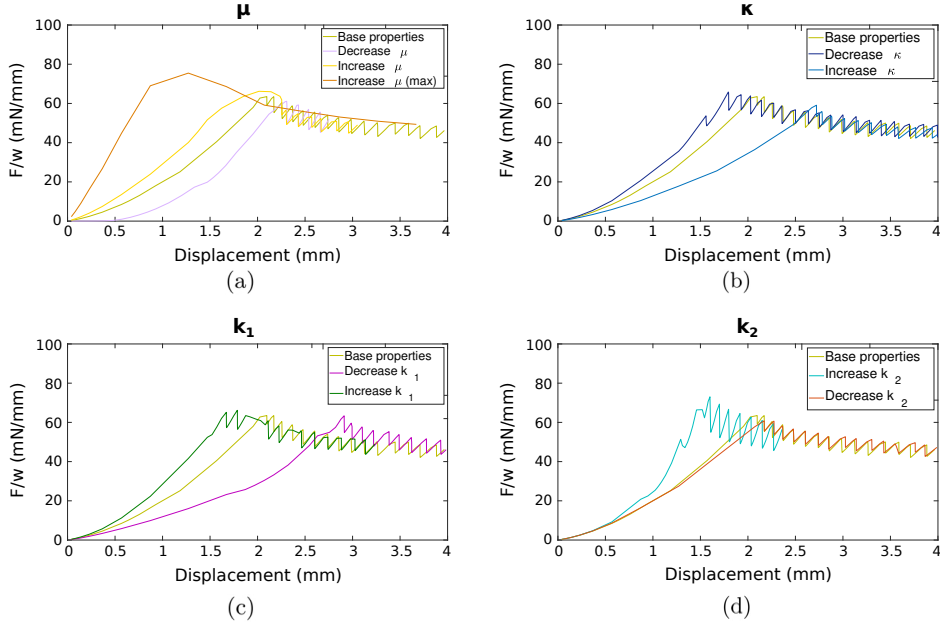
Figure 2.20. Analysis of the effect of the material parameters of the GOH hyperelastic model. The material parameters do not affect the dissection force, but have a strong impact in the initial part of the curves, where the specimens are suffering elastic deformation.

results than the dissection energy (see Section 2.6). We can also observe that $\tau_{n_{max}}$ has some impact on the stiffness of the initial elastic deformation. An increase in $\tau_{n_{max}}$ results in a slightly stiffer initial slope, while a decrease in $\tau_{n_{max}}$ softens the initial curve. Changing the stiffness of the cohesive contact on its own, K_{nn}, did not affect the curves, only the convergence of the models, as what happened with the cohesive surface models. When varying $\tau_{n_{max}}$ without changing K_{nn} or G_{n_0}, the cohesive displacement, δ_{0_n}, also varies proportionally (see (2.13)). We observed the effect of modifying both $\tau_{n_{max}}$ and K_{nn}, keeping δ_{0_n} constant (Figure 2.21.c). No differences between this case and the previous in which δ_{0_n} changes with $\tau_{n_{max}}$ were found (Figure 2.21.b).

2.8   Overall computational conclusions

The application of CZMs to simulate delamination tests can aid in determining the dissection properties of vessels. In this study, we have suggested two methodologies for constructing these models based on experimental tests, which allowed us to give a preliminary characterisation of the dissection properties and to enhance our understanding of the dissection results regarding the cohesive and damage formulations.

(a)

(b)   (c)
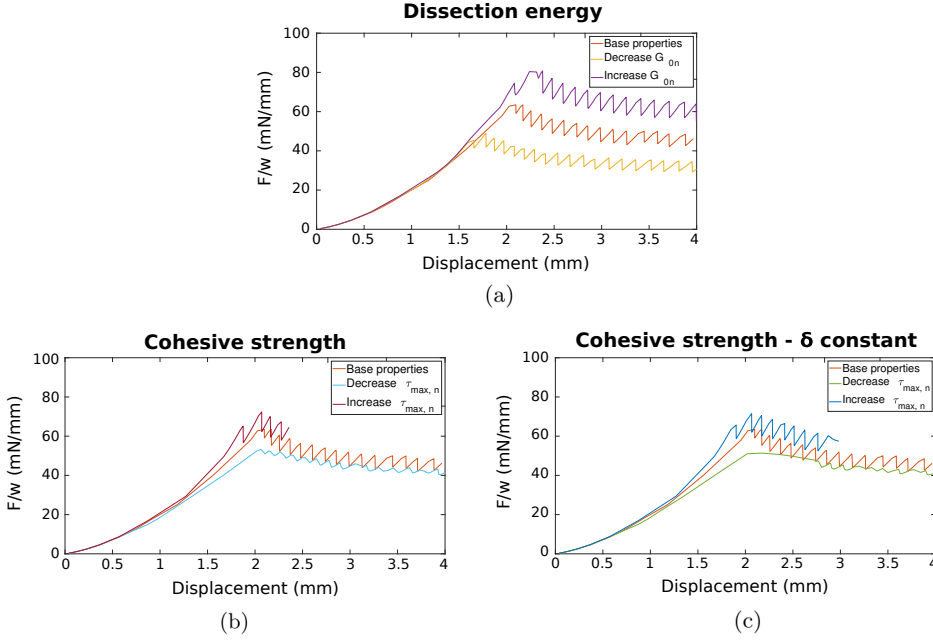
Figure 2.21. Analysis of the effect of the cohesive and damage parameters. Dissection energy (a) has the biggest effect on the dissection force, whereas cohesive strength (b–c) has a smaller impact.

However, due to the intricate physical processes involved in the contact and damage formulation, the findings presented here are not conclusive but rather a preliminary approximation of what further research may uncover.

2.9   Key computational findings

- CZMs based on cohesive elements show higher convergence than those based on cohesive surfaces. Combining the cohesive and the hyperelastic formulation on the same elements (cohesive surfaces) seems to hinder convergence of the models.

- Formulating a simple TSL in the normal direction does not fully capture the complex damage mechanism that happens in a combined mode of rupture, such as in the mixed-mode peel test. A mixed cohesive formulation should be included to reproduce more complex modes of rupture.

- The width, incision size or thickness ratio of the samples does not affect their resistance to dissection. This implies that the variations observed in dissection

force during the experiments were not due to differences in these parameters and is also valuable information when creating general models.

- The elastic mechanical properties of the tissue do not affect the dissection force in the T-peel test. This suggests that performing additional experiments to characterise the material during peeling tests may be unnecessary, as a standard characterisation would suffice for the models.

- If a unified CZM is to be reproduced for a vessel, only locations where the total thickness of the samples is different should require specific models.

Damage caused by haemodynamics

In this chapter, we study one of the mechanisms of damage in the endothelium of the vessels that arises from different mechanical stimuli caused by haemodynamics. In particular, we focus our work on the perturbations in the permeability of the endothelium, which are directly related to endothelial cell morphology. Therefore, this study is performed at the cellular level, in particular by performing flow tests on ECs. Since this was a completely new research line for our group, this chapter includes all the steps needed to setup and establish the experiments, starting at the design of the flow chamber devices—to reproduce both, stress and strain stimuli—, following with the different tests needed to define a working protocol, and ending with some experiments and the development of image analysis tools to process the results.

3.1   State of the art

Wall shear stress (WSS) has been acknowledged for decades to have a direct influence on the development of atherosclerosis [149–151]. However, the specific factors of this variable (e.g., its magnitude or directionality) and how they contribute to the development or protection against this disease are not clearly understood [152]. It is then of great interest to continue analysing the effect of this stimulus on different EC types in order to help bring light to this mechanism.

WSS is the tangential stress that ECs in the intimal layer of the vessels perceive due to blood flow [153]. This stress is orders of magnitude lower than other mechanical stimuli in vessels, like pressure, and so its effect comes from the activation of biologic signaling at the cellular level rather than from affecting macroscopic mechanical integrity [153]. The careful evaluation of sites prone to develop atherosclerosis in vivo has led to the determination of the existence of athero-prone and athero-protective flow patterns [154, 155]. Specifically, steady laminar flow generating a high shear stress is found to be athero-protective [154], whereas disturbed and oscillatory flow is considered athero-prone [155]. These different flow patterns cause different

WSS values and profiles to which ECs respond differently. High and unidirectional WSS is linked with aligned and elongated healthy ECs, which are less permeable to macromolecules and have less monocyte adhesion [156]. This behaviour is considered athero-protective. ECs can also respond in terms of gene expression and phenotype to this mechanical stimulus [157]. Conversely, ECs in sites with oscillatory and low WSS show a cobblestone morphology and with no distinct preferential orientation, forming a permeable monolayer [156] and showing an athero-prone behaviour. In these sites, leaky ECs also present an inflammatory phenotype [158]. These morphological responses to different flow patterns have also been observed in vivo [159, 160]. Therefore, it is well established that flow patterns affect EC morphology, which directly affects the permeability of the endothelium and the propensity to develop atherosclerosis. Therefore, we want to focus this new line of research on WSS response in terms of cell morphology (shape and alignment of ECs), as a good approach to investigate the initiation of this disease as a disruption of the endothelium. Moreover, in order to achieve a better and complete understanding of this physiological response of ECs, it is interesting to combine WSS with other mechanical stimuli that occur in vivo, like cyclic stretch, in order to bring new insight into the role of the damaged endothelium in the initiation of atherosclerosis.

Flow chamber devices are well established tools used for the study of EC response in vitro, as they allow to generate specific and controlled flow conditions on a layer of ECs [156]. In this section, we will present and comment the different types of devices that are commonly used to perform flow tests on ECs and the results in terms of EC morphology that have been obtained using these devices.

3.1.1   Flow chamber devices

There are three main types of flow devices commonly used to study the effect of flow parameters on ECs. These are parallel-plate flow chambers, cone-and-plate devices and orbital shakers [152]. Their operating mechanism, advantages and disadvantages are discussed below. Some remarks regarding devices reproducing stretch will be included at the end of this section.

3.1.1.1   Parallel-plate flow chamber

The parallel-plate flow chamber (PPFC) is the most common in vitro device for flow studies on ECs [156]. It consists in a chamber or channel in which fluid can flow at certain and controlled rates to generate the desired values of WSS in the monolayer. ECs are seeded and left to create a monolayer in the substrate of the chamber, normally a glass slide or coverslip, see Figure 3.1.

One of the main advantages of these devices is their simplicity, both in design and operation [156]. Their simplicity also entails a bigger versatility to reproduce different flow patterns by making uncomplicated modifications to the basic designs. These devices also allow the retrieval of ECs after the experiment for subsequent analyses
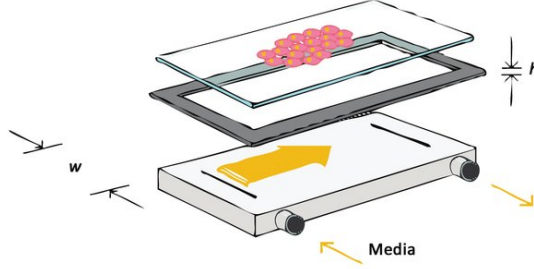
Figure 3.1. Outline of a parallel-plate flow chamber (Figure 2 from ref. [161]). w and h represent the width and the height of the chamber where the culture media flows. Cells are seeded on the glass slide represented on top.

or data collection or their immediate fixation after the tests [162], the continued sampling of the flow medium to obtain information about secreted metabolites [163] and the possibility to live image the response of the monolayer with the appropriate equipment [164]. However, one limitation of these devices is that the WSS generated can present areas of non-uniformity, especially near the walls or the reservoirs [165]. In these areas, ECs exposed to these altered WSS values could release different factors that could cause unexpected behaviour of the monolayer of ECs [152]. If this effect wants to be avoided, a careful study of the WSS patterns on the device should be performed and ECs seeded and confined in a section with a uniform WSS pattern [165].

The most straightforward flow pattern that can be reproduced in these systems is steady laminar flow. With no disruptions in an uncomplicated rectangular cross-section geometry, the velocity profile (u) of the flow can be described as a parabolic function of the height position (y) [166]:

$$u(y) = \frac{1}{2\mu} \frac{dP}{dz} \left[\left(\frac{h}{2} \right)^2 - y^2 \right], \tag{3.1}$$

where μ is the viscosity of the fluid, $\frac{dP}{dz}$ is the pressure gradient parallel to the plates and h is the height of the channel. By integrating in the height of the channel, WSS in the monolayer of cells, $\tau_{monolayer}$, can be obtained as a function of the flow rate (Q) and the geometry of the cross section [166]:

$$\tau_{monolayer} = \mu \frac{\partial u}{\partial y} \bigg|_{y=0} = \frac{6\mu Q}{wh^2}, \tag{3.2}$$

where w is the width of the channel. This equation is valid for a fully developed, laminar, Newtonian fluid in a channel with a high aspect ratio (w/h) [156]. A high aspect ratio ensures that most ECs in the monolayer are subjected to homogeneous WSS [166]. As per (3.2), the WSS that ECs are subjected to in these devices can be

easily modified by changing the dimensions of the cross-section of the channel or the flow rate.

The flow rate is usually generated in these devices with peristaltic pumps [156]. Their mechanism of action is called peristalsis, which is the movement of fluid due to traveling contracting waves [167]. They drive fluid by the rotation of a rotor with several rollers over a flexible tubing that hosts the fluid [156]. By alternatively compressing and releasing the tubing, the fluid is displaced. Due to this compression-release pattern, peristaltic pumps generate pulsatile flow. In order to achieve a steady flow with these pumps, a fluid damper can be placed between the pump and the device.

These pumps present several advantages for cell experiments, the main one being the fact that the fluid is never in contact with the pump itself, so they do not compromise the sterility of the experiment. Moreover, they are relatively inexpensive and their recirculation system allows the use of less volume of culture medium. They provide versatility in the range of flow rates to generate, by changing the rotation speed or the tubing diameter. And finally, they can rotate—and thus move the fluid— in both directions, allowing the generation of oscillatory flow [156]. This feature is interesting as steady laminar flow is not the only flow pattern that happens in vivo. On the one hand, blood flow due to heart contraction has a pulsatile nature [155]. And on the other hand, sites with disturbed and oscillatory flow have been widely correlated with the development of atherosclerosis [168]. However, to achieve a controlled oscillatory or pulsatile flow, these pumps should be linked with a computer software system, with a flow probe to feed information to the system [156], increasing the overall price of the setup.

If a flow disturbance wants to be reproduced, the solution in PPFCs is as easy as including a perturbation in the length of the channel, see Figure 3.2.a. PPFCs including this disturbance are commonly called vertical-step flow systems [168]. In these devices, a step is included to reproduce a recirculation area, similar to the one generated after the plaque or in a bifurcation, sites prone to the development of atherosclerosis [168], see Figure 3.2.b. By including this step, two areas of interest are found in only one experiment: the recirculation area above mentioned and a fully developed flow area, usually localised downstream the recirculation area.

3.1.1.2 Cone-and-plate devices

Another way of generating WSS on a monolayer of ECs are the cone-and-plate devices (CPDs). They have the same functioning principle of a viscosity rheometer, where an inverted conical piece rotates above a flat surface, forcing the fluid between them to flow azimuthally in concentric circles and, thus, produce WSS on the bottom plate where ECs are seeded [170, 171], see Figure 3.3. By computationally controlling the rotation of the cone, pulsatile flow can also be reproduced with these devices [172].

These devices present some advantages over PPFCs [156]. Because of their geometry, they lack the effect of walls and inlets in WSS distribution. Also, small deviations in their dimensions do not cause major changes in WSS values. The flow profile in them is independent from hydrostatic pressure gradients. The volume of fluid they

(a) (b)
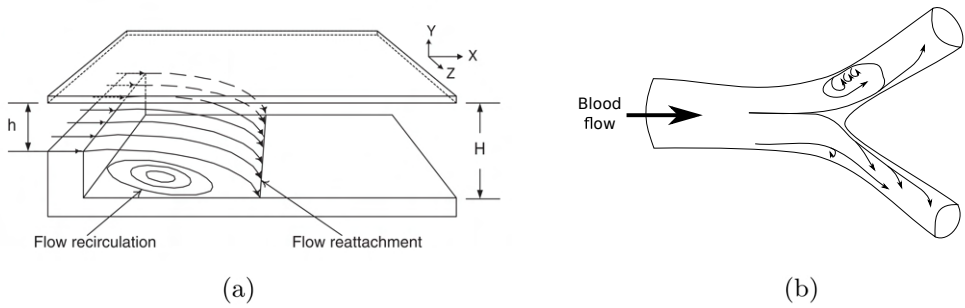
Figure 3.2. (a) Scheme of a vertical-flow step device (Figure 9 from ref. [168]). (b) Flow pattern after a bifurcation of a vessel (adapted from Figure 3 from ref. [169]).
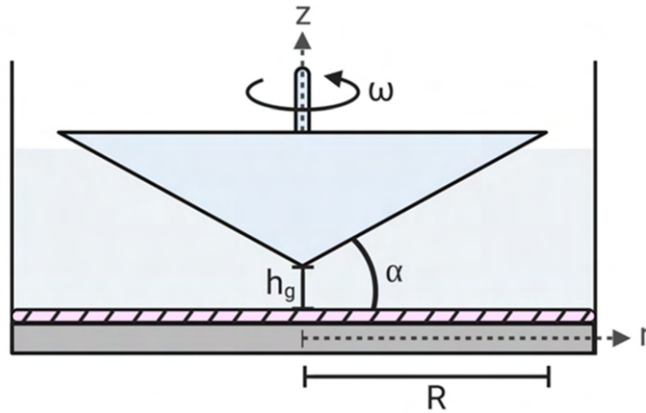
Figure 3.3. Outline of the cone-and-plate device (Figure 7 from ref. [156]). By regulating the geometrical parameters of the device, the WSS applied at the bottom plate can be uniform and modified as required.

require is small and therefore metabolite detection is easier. Moreover, ECs can be more easily accessed to if some contact techniques are required, such as atomic force microscopy [166]. They also present several disadvantages, such as the difficulty to allow live imaging of the experiments, the significant evaporation of the fluid if it is exposed to an open environment and the accumulation of secreted molecules that can affect cell behaviour [156].

3.1.1.3 Orbital shakers

Orbital shakers (OSs) have long been used for mixing or agitating samples, but they are increasingly being used as a way to generate multidirectional patterns of WSS [152,173]. They basically consist of a flat platform that produces an in-plane circular

movement. A monolayer of ECs is cultured in common lab equipment and placed on this platform, thus a circular wave of culture medium is generated over the monolayer of ECs, see Figure 3.4 [174]. WSS magnitude and directionality can be controlled by adjusting the viscosity and depth of the fluid over the ECs, the well radius, the orbital radius and the angular velocity [175, 176]. However, the calculation of this WSS pattern is complex, in part due to the frequent apparition of a wave because of the free surface of the fluid [176]. It is well established that ECs seeded in the centre of the wells are exposed to a different WSS profile than ECs on the edges [177] (Figure 3.4.b), and so different factors can be excreted by ECs in different areas, affecting their behaviour [177, 178]. A way to avoid this problem is by segmenting the well and seeding ECs exclusively in the area where the profile of WSS is homogeneous [178], increasing the complexity of use of these devices. However, ECs in the centre of the wells are exposed to multi-directional flow, a profile that is currently being related to the apparition of atherosclerosis [179, 180] and that is difficult to reproduce with other methods [174].

(a)   (b)
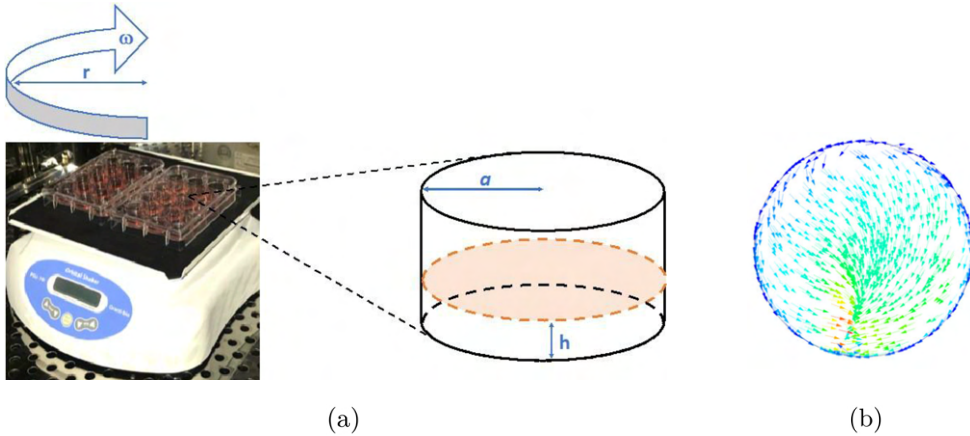
Figure 3.4. (a) Image of an orbital shaker with two 12-well plates on it (Figure 1 from ref. [174]). (b) Pattern of WSS in the bottom of a cultured plate in an OS at one time step. Arrows indicate WSS direction and colours represent its magnitude (Figure 1 from ref. [173]).

3.1.1.4 Flow devices to reproduce cyclic stretch

Some groups have developed devices to study EC response to WSS and cyclic stretch simultaneously. These devices are usually an adaptation of the systems described above to include the possibility to stretch in a controlled way the substrate where the monolayer of ECs is seeded. Several studies have developed channel devices in which the substrate can be deformed following different methodologies [181–185], with devices similar to PPFCs. Other studies have chosen to adapt CPDs and make the

substrate plate a flexible membrane to allow cell stretch [186]. In addition, other devices have been designed as compliant silicone tubes mimicking blood vessels that deform with the pressure caused by the pulses of flow [187–190]. Most of these devices allow the study of both stimuli coupled and uncoupled, allowing a more comprehensive view of EC response.

3.1.2   EC response to WSS

All the devices detailed above are the main in vitro tools used to evaluate the response that ECs show to different WSS patterns. ECs react to this stimulus by changing their morphology, but also their phenotype, secreting different metabolites, changing their molecule adhesion, etc. Due to the nature of our study, we will focus this review on the current understanding of changes in morphology, but will also discuss slightly about changes in EC phenotype.

When subjected to laminar, steady and unidirectional WSS, ECs elongate and align with the direction of flow [149, 172, 191–196], see Figure 3.5.a. This has been studied to be a time-dependent response [192, 193, 196]. In particular, bovine aortic endothelial cells (BAECs) have shown to initially respond to this steady pattern of WSS by enhancing their attachment to the substrate and surrounding ECs. Afterwards, they show characteristics of motility as they realign, to finally thicken their intercellular junctions and increase their amount of microfilaments like actin when they are disposed in their final configuration [192], see Figure 3.5.b. EC response has also been shown to depend on WSS magnitude [196–199]. Low enough values of WSS do not cause ECs to elongate and align with the direction of flow, and this WSS threshold form which ECs start to modify their morphology and their time-dependent response is suggested to differ according to cell type [196]. ECs that come from arteries respond to WSS ranging from 1 to 8 Pa [192, 194, 195, 199–201], whereas vein ECs (such as HUVECs) respond to WSS values an order of magnitude lower, 0.1-0.8 Pa [172, 202, 203]. The specific threshold for each cell line, however, is not firmly determined, although the ranges are in line with their physiological environment in the body.

Following a more physiological approach, when the pulsatility of the flow is included, ECs show they can discriminate between different types of pulsatile flow environments [193]. In particular, ECs subjected to always positive pulsatile WSS showed a more elongated shape than when subjected to steady flow. For a low-amplitude type of pulsatile flow that changes direction but maintains a positive average WSS, ECs also elongated but to a lesser extent; whereas in a fully oscillatory flow with a mean WSS of 0 Pa, ECs remained in a polygonal shape and did not exhibit alignment [193]. When reproducing more complex flow patterns calculated from in vivo environments, ECs were observed to respond differently to flow patterns in areas less likely to develop atherosclerosis, showing an elongation and coherent alignment, as well as secreting proteins to reduce inflammation [205], than to flow patterns from areas prone to develop this disease, where ECs maintained a cobblestone shape and developed a

(a)

(b)
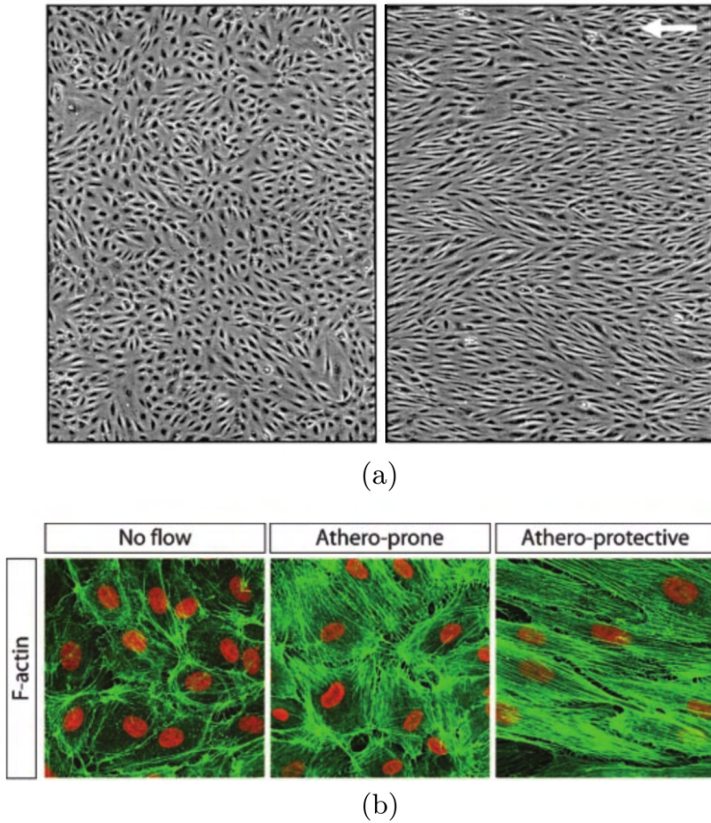
Figure 3.5. ECs response to flow. (a) BAECs in the static control (left) show a random orientation and have a rounder shape than when subjected to steady flow (right), as BAECs elongate and align with the direction of flow, shown with the white arrow (Figure 2 from ref. [172]). (b) F-actin stained HUVECs after being exposed to different flow patterns. HUVECs that were not subjected to flow show a cobblestone configuration and fewer actin filaments. When exposed to athero-protective flow patterns, HUVECs elongate and align, increasing their amount of microfilaments. When subjected to athero-prone flow conditions, HUVECs keep a cobblestone shape with no preferred orientation, but they also increase their amount of microfilaments (Figure 3 from ref. [204]).

proinflammatory phenotype [204], see Figure 3.5.b. On another note, studies showed that ECs subjected to turbulent flow, caused by a disturbance, maintained a more polygonal and disorganised shape [149, 162, 206], even compared to steady WSS with the same average magnitude [191], suggesting that EC response to WSS depends on its direction and not only on its magnitude.

Following this hypothesis, more recent studies have started to evaluate EC response to multidirectional flow with OSs [173, 177]. This is an interesting approach

as in areas predisposed to the development of cardiovascular pathology, blood flow changes its main axis throughout the cardiac cycle, i.e., is multidirectional [179, 207]. Dardik et al. [177] compared the behaviour of BAECs and HUVECs subjected to the complex flow generated by an OS and to the more studied steady flow generated by a PPFC. They found that ECs in the periphery of the wells in the OS, where WSS is higher, steady and unidirectional, elongated and aligned with the direction of flow, similarly to ECs in the PPFC. ECs in the centre of the OS presented a cobblestone morphology with no preferred orientation, more similar to the ECs in the static control, see Figure 3.6. However, ECs in the OS exhibited a significant increase in cell density when compared to PPFC and static control cells. When studying the two main areas of the OS in detail, they found that ECs in the centre of the well showed higher levels of proliferation and apoptosis, whereas ECs in the periphery showed a decrease of cell density compared to the static controls. This study suggested that ECs in the centre of the well were activated and prone to develop atherosclerosis. Chakraborty et al. [202] found similar behavioural patterns in HUVECs on OSs. Additionally, they defined a new flow metric to account for the directionality of the oscillatory fluid that proved to correlate well with cell proliferation and shape index, supporting the dependency of EC behaviour with WSS direction. Similarly, Arshad et al. [173] performed a comprehensive analysis of the orientation of cell nuclei throughout the surface of an OS, as they computed the complex flow patterns in their experiments with computational fluid dynamics (CFD). They observed that human aortic endothelial cells (HAECs) nuclei alignment depended strongly not only on WSS magnitude but also direction.
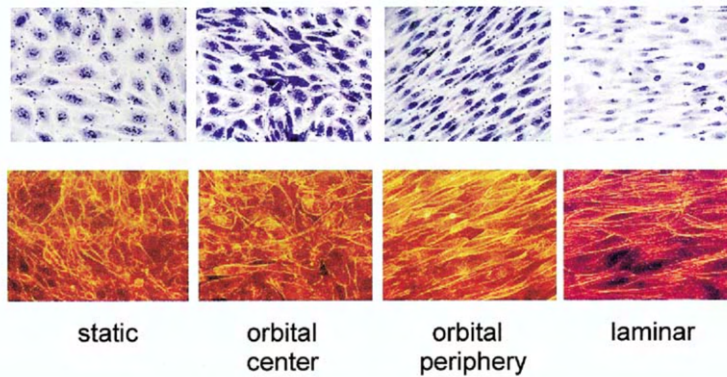
Figure 3.6. Shape of ECs (top) and F-actin (bottom) when subjected to flow in an OS and a PPFC. ECs in static conditions (left) show a random orientation and cobblestone shape, similar to those in the centre of an OS (centre left), where WSS is low and multidirectional. In this area, ECs showed higher density and higher proliferation and apoptosis rates. ECs in the periphery of the OS (centre right) elongate and align with flow, similarly to ECs subjected to steady laminar flow in PPFCs (right) (Figure 2 from ref. [177]).

3.1.3   Objectives of the study

As already discussed, alterations in the permeability of the endothelium are a prerequisite for the growth of an atheroma plaque. Therefore, it is crucial to fully understand the mechanisms that trigger this dysfunction in the permeability, which is correlated to EC shape and orientation. Although studies about EC morphology as a response to different flow patterns are numerous, there are still gaps in this knowledge that could help in the understanding of the triggering mechanisms of atherosclerosis. In particular, flow experiments are usually performed with HUVECs or aortic ECs—whether human, porcine, from rabbit—, whereas atherosclerosis happens mostly in the coronary and the carotid arteries. More studies with different flow parameters in cell types from these sites, such as human coronary artery endothelial cells (HCAECs), would bring a closer insight into the actual behaviour of atherosclerotic sites. Moreover, ECs in the body are subjected to a myriad of stimuli combined, for example cyclic stretch due to the pulsatile nature of blood flow. Studies that couple stress and strain stimuli are still scarce and needed.

It is then the main objective of this work to start and develop a research line destined to study how ECs change their shape and orientation—i.e., the permeability of the monolayer—when subjected to different mechanical stimuli. To do so, four main areas have been addressed in this work: i) the design of the flow chamber devices to reproduce different flow conditions and different strain stimuli, ii) the tuning of the flow system and experiment conditions, iii) some preliminary in vitro flow tests with ECs (HUVEC and HCAEC) and iv) the image analysis tools developed to obtain the desired information from the tests. The tasks and procedures were carried out in the laboratories of the Applied Mechanics and Bioengineering (AMB) group of the Aragon Institute of Engineering Research (I3A).

3.1.4   Research questions posed

- Can we design and manufacture a flow device capable of reproducing physiological and pathological flow and strain conditions simultaneously?

- How do different types of endothelial cells respond to different flow parameters in terms of shape and orientation?

- Do HCAECs respond to flow at different levels of WSS than HUVECs?

- Can phase-contrast images of ECs be segmented automatically?

- Can we objectively quantify the shape and orientation of ECs from microscope images?

3.2   Design of the flow chamber device

3.2.1   Requirements, initial device and modifications

Before addressing the design of the device, the conditions that it should reproduce must be defined. The first requirement is that the design of the device must be versatile enough to allow the integration of the strain stimulus with few modifications. With the strain device in mind, the overall dimensions must be adequate for it to fit in the biaxial testing machine (outer dimensions not exceed 60 mm) that is planned to be used afterwards for the implementation of strain in the two main directions (axial and transversal). In terms of the flow conditions, we want cells to be subjected to a wide range of shear stresses, reaching values below and above the physiological level, as well as the possibility to include different flow patterns in the channels. Regarding the particular range of WSS values that we want to include in the study, the higher level of WSS that we want to subject cells to is up to 1 Pa, as we will use HCAECs and the physiological WSS in the human coronary arteries reaches 0.68 Pa [208].

For the design of the flow chamber device, we used as baseline a commercial device that had been worked with before in the lab to culture monolayers of different ECs and epithelial cells. It consists of three squared channels 2 mm wide, 2 mm high and 35 mm long, with cylindrical inlets and outlets of 2.3 mm in diameter. The overall dimensions of the device are 15 mm wide, 40 mm long and 6 mm high. It is made of polydimethylsiloxane (PDMS), due to its studied biological properties (non-cytotoxicity and transparency, mainly [209, 210]). The mould to generate these PDMS devices is made of a biocompatible resin and manufactured with a 3D printer using stereolitography by the company Beonchip. Finally, it is attached via plasma treatment to a microscope slide, where cells will adhere and grow, see Figure 3.7.

| (a) | (b) |
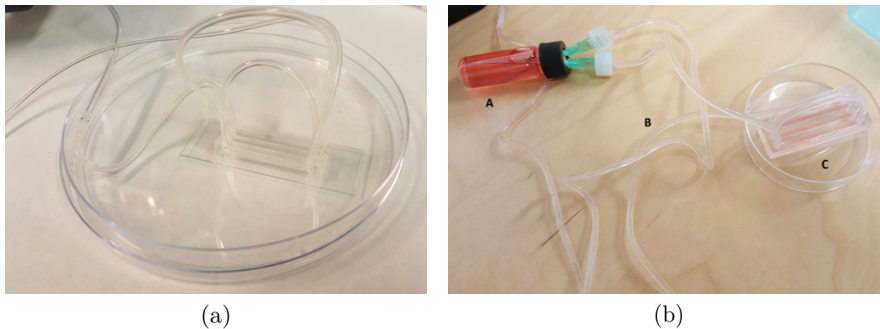
Figure 3.7. (a) Initial device and tubing. The three squared channels are connected among each other with the tubing system. These tubes come from the peristaltic pump, which will provide the desired flow rate to generate a certain value of WSS. (b) The initial device, C, with the tube montage required for the tests, B, and the fluid deposit of 5 ml, A. MesoEndo Cell Growth Medium (Sigma-Aldrich) is already through the whole system.

To supply the flow to the system, a peristaltic pump is available to be used in the lab, an appropriate pumping system according to the advantages discussed in Section 3.1.1.1. In particular, the pump available is a Watson-Marlow, model 323S, with a 318MC pumphead, see Figure 3.8. The head's maximum speed is 110 rpm. The flow rate supplied with this speed depends on the diameter of the tube around the head. With the widest available tubes, the maximum flow rate achievable is 10 ml/min.
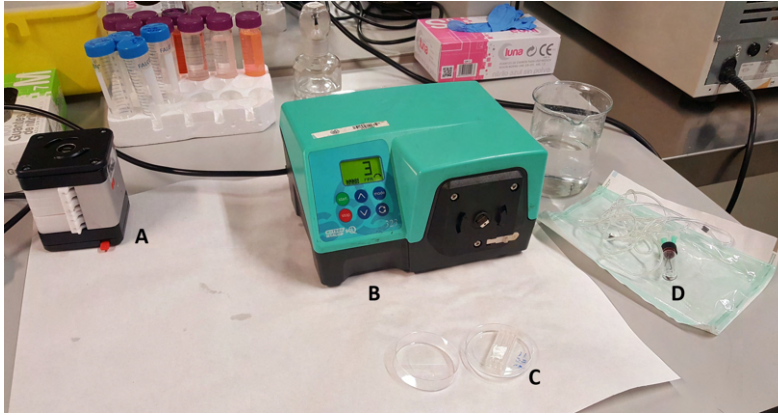
Figure 3.8. Whole flow system. B and A are the peristaltic pump and the pumphead, respectively. C is the initial flow device and D indicates the set of tubes and the fluid deposit for the experiments.

Considering these initial conditions and equipment, several simulations were computed to determine the possibilities to generate the desired flow parameters. These simulations were run in the commercial software Comsol, following a fluid-structure interaction (FSI) approach. This methodology considers the deformation that the fluid causes in the solid due to the pressure it exerts on it. The calculus is then updated with the deformed geometry of the solid and the whole system is recalculated, until the equilibrium is reached. Therefore, for FSI simulations, both the PDMS and the culture medium had to be fully characterised. Both material characterisations are described below (Section 3.2.1.1 and Section 3.2.1.2). In parallel, several trials were carried out in the laboratory to check the commercial device and some test parameters (such as outlet pressure, needed for the simulations), see Figure 3.7.b.

With these FSI simulations, we obtained that the highest possible flow rate generated a WSS of only 0.9 Pa, see Figure 3.9. As the tests required higher levels of WSS, this initial device would not be valid for the study.

Following these restrictions, the need for an updated design of the device emerged. The goal is for it to be able to reproduce a wide range of WSS reaching up to 1 Pa. The only geometrical restrictions are the diameter of the inlets and outlets, since it coincides with that of the laboratory tubes, and that the overall dimension of the device does not exceed 60 mm to fit the biaxial machine.
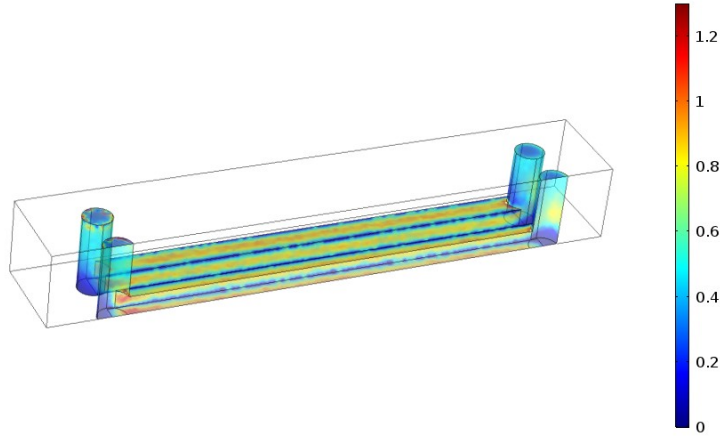
Figure 3.9. Representation of the initial flow device in Comsol. Only half of the geometry is simulated due to the symmetry of the device. Scale colour bar shows WSS (Pa) when it is subjected to the maximum flow rate of 10 ml/min.

As per (3.2), WSS in PPFCs such as our device directly depends on flow rate and is inversely affected by the cross-sectional area of the channel. Considering the operational restriction to increase flow rate, WSS will be increased by reducing the cross-sectional area. The width of the channels was decided to be maintained in order not to reduce the area where cells are seeded and to ensure that the effect of the walls is avoided in the central part of the channels. With the aim of generating two different values of WSS per test, an inverse step was designed to reduce the cross-sectional area in the final half of the channels, as shown in Figure 3.10. This inverse step reduces the height of the last half of the channel to 1 mm. Moreover, the total length of the channels and therefore the device was reduced to 30 and 35 mm respectively, to allow better manipulation and less volume of PDMS. With these modifications, WSS reaches 1 Pa with a flow rate of 4.5 ml/min in the area below the inverse step, see Figure 3.10.b, a comfortable operation rate for the system.

3.2.1.1   PDMS characterisation

For the FSI simulations, the mechanical properties of the PDMS that conforms the device are needed. The characterisation of the material was carried out following the standard ASTM D638-14 Tensile Properties of Plastics [211], which defines the procedure to determine the modulus of elasticity and Poisson's ratio of plastics via tensile testing. A total of 8 test specimens were machined according to the standard. The tests were carried out in the Tissue Characterisation Laboratory, in the Aragon Institute of Engineering Research (I3A), using the uniaxial testing machine Instron

(a) (b)
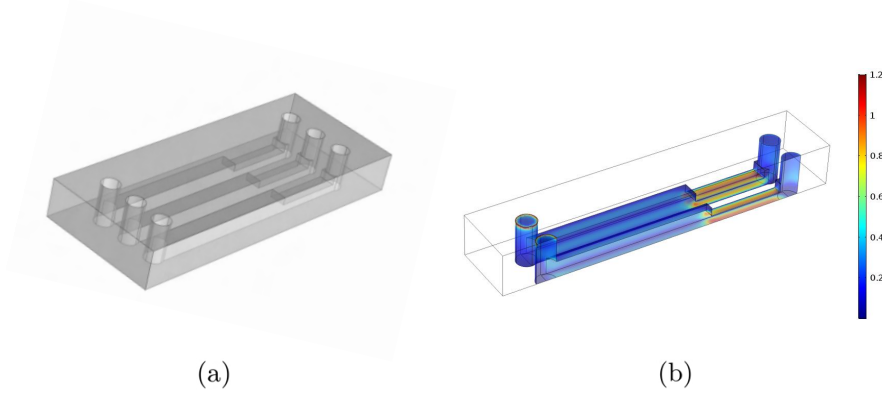
Figure 3.10. Representation of the final geometry of the device in Comsol. The geometry remains symmetrical (a), so only half the device is simulated (b). There are two areas with distinct WSS (Pa), shown in the colour bar. WSS of 1 Pa reached in the downstream area with a flow rate of 4.5 ml/min. Flow direction is from left to right.

5848. A video-extensometer was used during the tests to measure both the axial and transverse strain simultaneously. Figure 3.11 shows the specimen between both clamps, with the four dots in the center that will be tracked by the video-extensometer to calculate the axial and transverse strains.

(a) (b)
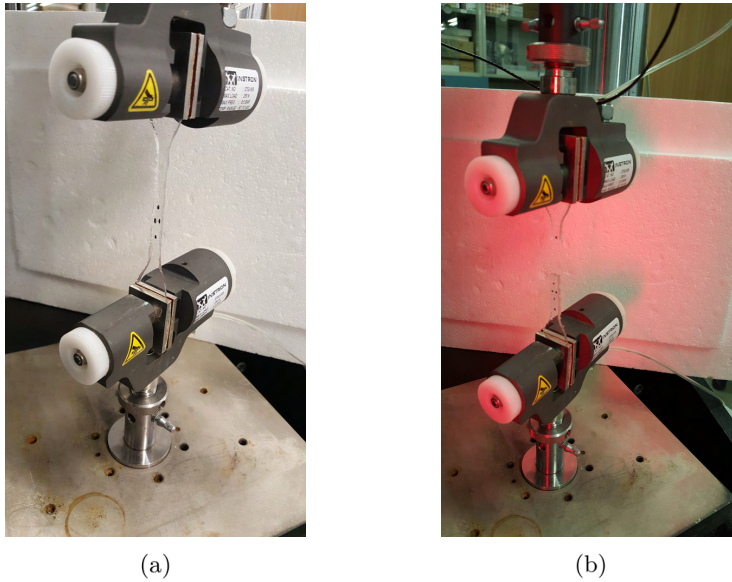
Figure 3.11. Uniaxial test performed to the PDMS specimens, following ASTM D638-14 [211]. (a) Disposition before the beginning of the test. (b) End of the uniaxial test.

The procedure is as follows: a preload of 0.2 N is applied at a crosshead speed of 0.1 mm/min, according to the standard. Afterwards, the test speed is set to 5 mm/min, with a working bench of 10 N to show precision at small strains. Once the tests are finished, the data are imported and processed to obtain the desired information. Due to the compliance of the material, the tests produced large deformations in the specimens. Therefore, the initial linear portion had to be localised to calculate Young's modulus. Following the Spanish standard UNE-EN ISO 527-1 [212], the strain interval between 0.05% and 0.25% was the portion chosen as the initial linear segment, and thus, where the slope was calculated to obtain the elastic modulus, see Figure 3.12.
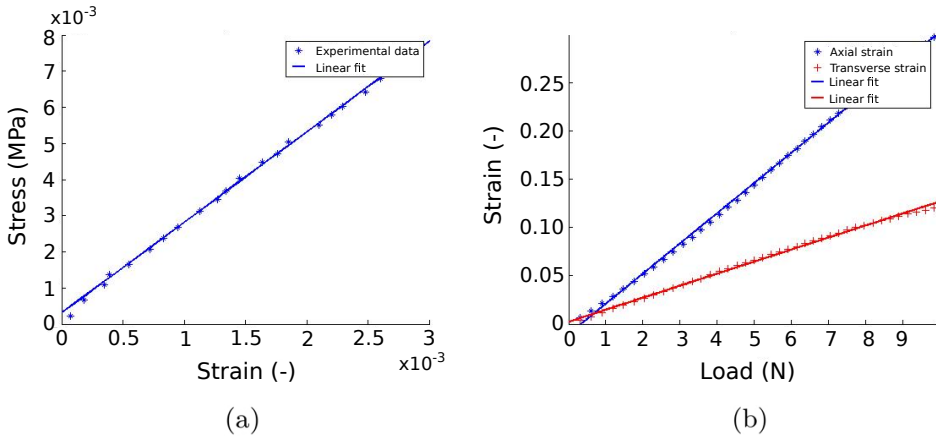
Figure 3.12. Postprocessed results of the uniaxial test of a representative specimen. (a) Experimental data and numerical fit of the axial stress-strain curve. This linear fit at small deformations allows the obtention of Young's modulus. (b) Experimental data and numerical fit of the axial and transversal strain represented vs the load. With these fits, Poisson's ratio is calculated.

After processing all data, a variability in the results was found. These differences split the results into two groups, which matched two slightly different polymerization processes. Two specimens were machined out of a material that was cured overnight at 60°C right after mixing the PDMS with the crosslinking agent. The remaining mixture was kept at -20°C and, once needed for the other batch of specimens, cured at the same conditions as the initial batch. This intermediate freezing process significantly affected the material properties. Considering this variation and in order to homogenise the mechanical properties, the protocol of PDMS fabrication for the devices was decided to include at least an overnight storage at -20°C.

After the calculation of Young's modulus and Poisson's ratio, these are transformed into the Lamé parameters, following (3.3) and (3.4). With these, the hyperelastic model used to reproduce PDMS behaviour was the Neo-Hookean model. Table 3.1 shows the mechanical parameters that characterise PDMS.

$$G = \frac{E}{2 \cdot (1 + \nu)} \tag{3.3}$$

$$\lambda = \frac{\nu \cdot E}{(1 + \nu) \cdot (1 - 2 \cdot \nu)} \tag{3.4}$$

Table 3.1. Young's modulus, Poisson's ratio and Lamé parameters that reproduce the behaviour of PDMS.

E (kPa)	ν (-)	G (kPa)	λ (kPa)
2585.08	0.39	927.16	3449.69

3.2.1.2   Culture medium characterisation – Addition of Dextran

Along with PDMS properties, the rheology of the culture medium is also needed for the numerical study. The medium used for these tests is MesoEndo Cell Growth Medium (212-500) from Sigma-Aldrich. It is suitable for most types of ECs, including the more delicate HCAECs to be used in this study. The parameters of interest for the simulations are the density and the dynamic viscosity of the fluid. Supplier specifications of the product do not include these characteristics. Therefore, the rheological analysis has to be performed separately.

On the one hand, the density of the product is easily measured in the laboratory by precisely weighing a certain known volume. Its dynamic viscosity, on the other hand, needs a viscosimeter or rheometer to be obtained. The viscosity measurements were carried out in the Service of Rheological Characterisation of Fluids at the University of Zaragoza. There, a rheometer with a cone-plate sensor that allows more accurate measurements for low viscosity fluids (of around 1 mPa · s, the viscosity of water) and less sample quantity is used. In particular, each measurement required 0.5 ml of sample.

Initially, the culture medium with no alterations was measured. The fluid presented a dynamic viscosity of around 1 mPa · s (or 1 cPs), see Figure 3.13.a. This value is way below blood's viscosity, 4.5 mPa · s [213] and a higher viscosity can help in the generation of higher WSS values (see (3.2)).

Therefore, the dynamic viscosity of the culture medium was increased. This was achieved by the addition of Dextran D4876 (MW 150,000 by Sigma-Aldrich), a soluble compound that has been broadly used for that purpose [173, 189, 214, 215]. It is reported to not alter cell behaviour, specifically in the morphological parameters of interest of this study [173, 216, 217]. The quantity of Dextran needed to obtain a dilution with blood viscosity was estimated with values reported from literature [218] and subsequently checked with the rheometer. The addition of Dextran cannot be performed easily in sterile conditions, therefore the solution must be subsequently filtered with a 0.2 μm Nylon filter to remove any possible contamination that may have occurred during the mixing process. Although this step is crucial for the experimental

tests, it was also performed in the study of rheological properties in case the filtering affected the dynamic viscosity. The final solution includes 4.93% (w/v) of Dextran and presented a dynamic viscosity of 3.9 mPa · s, .
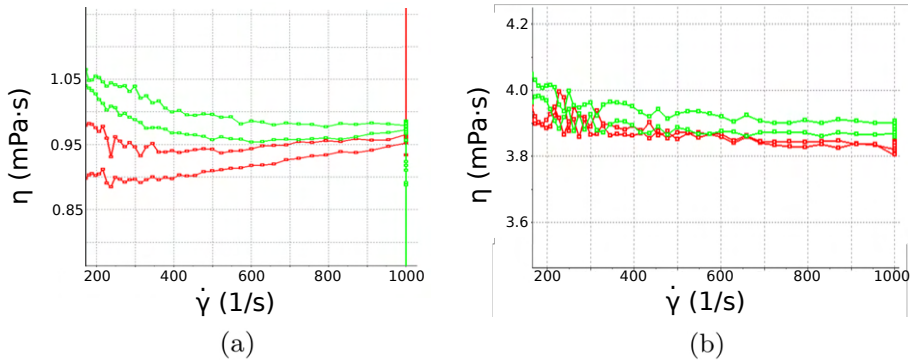
Figure 3.13. Viscosity vs shear rate of MesoEndo Cell Growth Medium (a) and of the prepared solution with 4.93 % of Dextran (b). Measurements of two different samples are shown in both cases. The final flatness of the curves indicates that the fluids can be considered Newtonian. The curves of the pure culture medium (a) show alterations at lower shear rates, as the viscosity of this product was around the threshold sensitivity of the rheometer.

3.2.2   Mould design and fabrication

With the final geometry of the device established, we moved to the design of the mould. This step was performed in SolidWorks. All mould trials were manufactured in a 3D printer using fused deposition modelling (FDM) technique, in the Design Engineering and Manufacturing Department of the University of Zaragoza, as it provided more flexibility and promptness for the trials. Several prototypes were tried to ensure the required dimensions of the flow device (anticipating moulding shrinkage), as dimensional variations can be crucial in the performance of the device, see (3.2). A draft angle of 15° to facilitate demoulding was included in the design of the mould after checking in the FSI simulations that this angle did not imply any changes in the test conditions. The design of the new mould is represented in Figure 3.14.a.

The possibility of manufacturing the final mould using FDM and acrylonitrile butadiene styrene (ABS) as material was considered. However, the moulds fabricated with this technique presented higher roughness, which translated to the device and its channels, as can be seen in Figure 3.14.b. The effect of this roughness in EC behaviour in the device was supposed to be negligible [219], but we found alterations in cell behaviour. Therefore, the final mould geometry was sent to Beonchip to be elaborated with the same resin as the initial moulds, Figure 3.15.
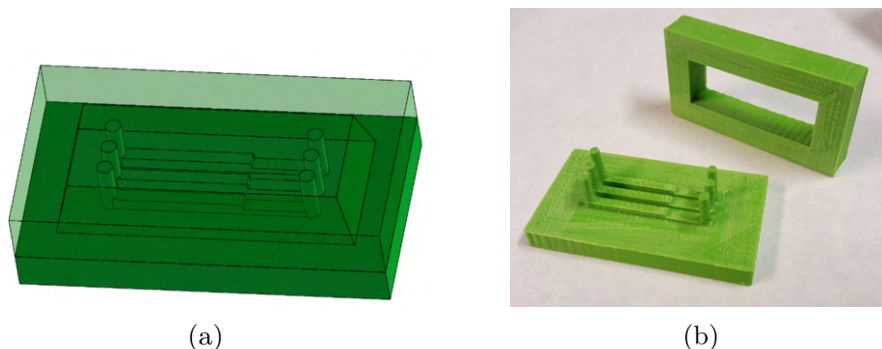
Figure 3.14. (a) Final and assembled geometry of the mould in Solid Works. Female part represented translucent to allow visualization of the channels. (b) ABS mould showing high roughness. Sandpaper was used to reduce this roughness.
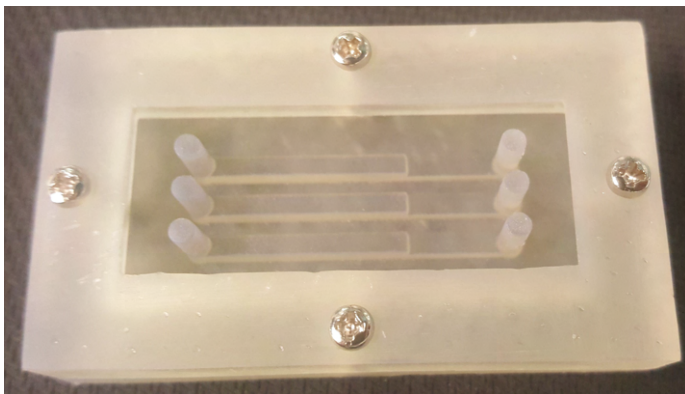
Figure 3.15. Final mould made of a biocompatible resin by stereolitography, used for the fabrication of the final devices.

3.2.3   Fabrication of the device

The fabrication of the microfluidic device involved the preparation of the PDMS and its curing in the mould. PDMS was supplied from Dowsil as a Silicone Elastomer Kit. This kit included the silicone elastomer base and the curing agent. These two components were mixed in proportion 10:1 in weight, following the manufacturer's instructions. The blend was then stirred and kept at -20°C, as commented in Section 3.2.1.1.

Once prepared, the PDMS was poured into the mould and the air bubbles were removed in a vacuum chamber. Afterwards, it was left to cure at 60°C overnight. Finally, the device was removed from the mould and bonded to the microscope slide using plasma treatment and a supportive overlay of PDMS. The final device is shown

in Figure 3.16. This is the device that was used in the flow experiments with ECs. It is mandatory to sterilise the devices once ready before any contact with living cells. This sterilisation was carried out in the autoclave.
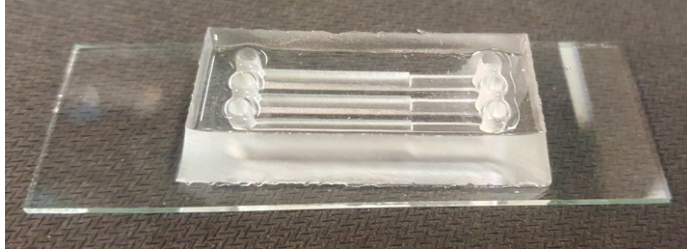
Figure 3.16. Final flow device. The cross-sectional area reduction can be seen in the right part of the three channels. Culture medium will flow from left to right.

3.2.4   Modifications for the strain device

From this redesign of the flow device, the modifications needed to include a strain stimulus that maintained the possibility to apply flow to ECs were studied. This part of the work was performed with the help of a student developing her Bachelor's thesis. Similar than with the flow device, the operational requirements were initially defined. The strain values to be implemented vary from 2% to 10%, a range that includes physiological—higher end—and pathological—lower end—strain conditions [220, 221]. Moreover, the strain must be achieved homogeneously in the base of the channels, so that all ECs are subjected to the same mechanical environment. As already commented, the strain will be applied with a biaxial machine, in particular the Instron BioPuls™ low-force planar-biaxial Testing System, see Figure 3.17. This system has four servo-electric actuators, two in the transverse direction and two in the longitudinal direction, allowing both uniaxial and biaxial strains in the device. The maximum applicable load on each axis is 50 N and the clamps provide a minimum and maximum length of 15 and 60 mm, respectively. Its use ensures the mechanical requirement on the one hand, as it can apply controlled displacements, and the biological requirement on the other, as its configuration allows the placement of a methacrylate cabinet covering the system to maintain the temperature and humidity conditions for ECs during the experiments.

In the flow chamber, the substrate where ECs are cultured is a glass slide. However, for the study of deformations, a flexible membrane is needed. As ECs will be cultured attached to it, the material chosen for the compliant membrane must be bio-compatible. For simplicity and availability, PDMS will be tested as substrate. To make this membrane, PDMS was poured into a cleaned and conditioned Petri dish, carefully distributed and cured following the same procedure as the device. PDMS contraction after curing (of around 1.1%) must be taken into account to obtain the
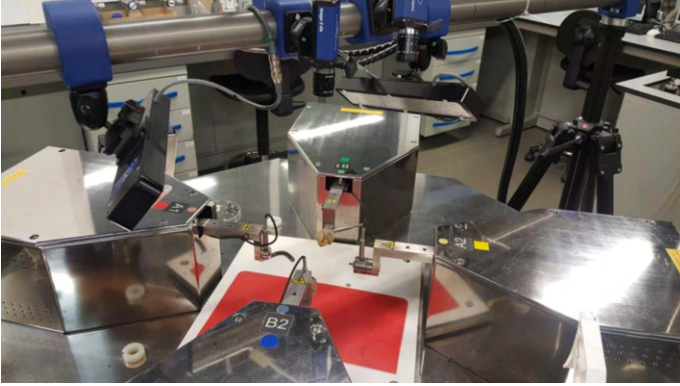
Figure 3.17. Instron BioPuls™ low-force planar-biaxial Testing System that will apply the strain in the flow device.

desired thickness. After curing, the substrate can be cut with the required shape and the device mounted and attached using a thin layer of PDMS as adhesive.

3.2.4.1   Model validation via Digital Image Correlation

Before studying with FE models the dimensions of the substrate, the validation of the computational model has to be performed, so as to make sure that the computational results match the real strains in the device. Using the flow device with a base thickness of 1.6 mm, a uniaxial tensile test was carried out, applying a continuous displacement of 5.6 mm/min in the longitudinal direction of the channels. The real time deformation was recorded using a Digital Image Correlation (DIC) system, specifically the LaVision StrainMaster system. To do so, the bottom side of the PDMS substrate was sprayed to create a pattern of random dots to be tracked by the system and create the deformation maps. The images obtained were processed with the open code Ncorr for Matlab. Subsequently, the test was reproduced by means of an FE analysis with Comsol Multiphysics, developing a 3D model of the entire geometry of the device. The mechanical analysis was considered stationary due to the low speed of the application of the load.

In contrast with the previous FSI model, the deformations in this case were larger and the accurate reproduction of the mechanical behaviour of PDMS was crucial for the model. Therefore, a more complex hyperelastic material model was chosen to reproduce PDMS behaviour in larger deformations. In particular, we chose the two-parameter compressible Mooney-Rivlin approximation to fit the data of the uniaxial tests obtained in Section 3.2.1.1, and the constants of the constitutive model are shown in Table 3.2. For the device mesh, a fine mesh of 27,334 tetrahedral domain elements, 6482 contour elements and 934 edge elements (Figure 3.18) was defined. Due to the symmetry of the device, only half of the geometry was simulated.

Table 3.2. Parameters of the Mooney Rivlin hyperelastic model to reproduce the behaviour of PDMS.

C_{01} (kPa)	C_{10} (kPa)
-105.31	414.97
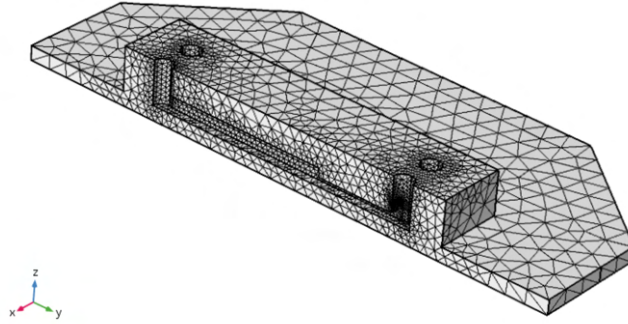
Figure 3.18. Mesh of the FE model to reproduce the experimental uniaxial test.

A displacement of 5.725 mm was applied at both ends in accordance with the experimental test, whereas the rest of the contours were allowed free displacement. To validate the numerical simulation, the deformation field at the base of the FE model is compared with the experimental measurements (DIC) at the end of the test, see Figure 3.19. At first glance, both experimental and computational devices showed higher strains near the grip ends and a more homogeneous distribution in the centre. These sites, however, are subjected to edge singularities and will not be studied or compared. As an initial check, a random selection of points was selected and the deformations measured with the DIC obtained. In all cases examined, the FE model achieved a relative error below 2% when compared to the experimental results obtained at the central points. These findings suggested that the FE model exhibits promise for accurately representing the system under consideration.

To validate the computational results, the analysis of the strain profile on a centre line along the longitudinal axis, which matches the centre line of the centre channel, was compared. This region showed a similar distribution in the experimental and numerical results with a mean error of 4.3% (Figure 3.20), a low enough value to consider the FE model validated.

3.2.4.2   Modifications and final strain device

With the validated FE model, the shape and thickness of the substrate were studied to obtain the optimum geometry for our requirements—achievement of certain strains and homogeneity of the strain distribution along the channels (see Section 3.2.4). The thickness of the membrane has the highest impact in this homogeneity, being
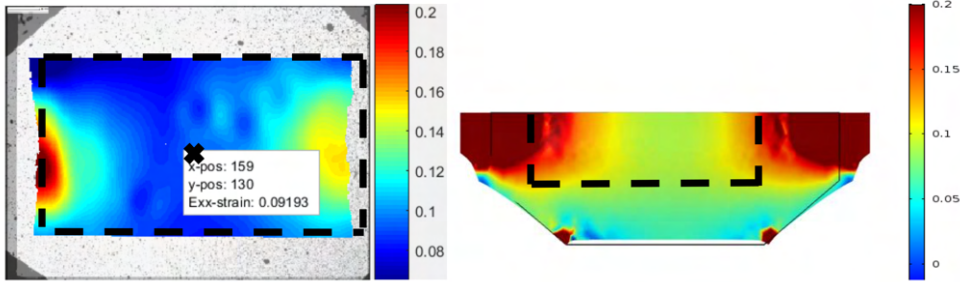
Figure 3.19. Deformation fields: experimental (left) and numerical simulation (right). The dashed line shows the same region of interest (ROI) to facilitate comparison.
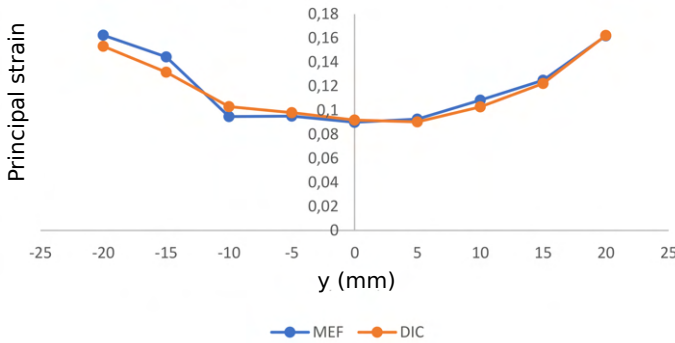
Figure 3.20. Deformations in the centre line of the device for the experimental and computational device.

the higher thicknesses the ones that show a more homogeneous distribution of strain. Moreover, lower thicknesses have a higher risk of rupture in the areas near the grips. However, thickness is also limited by the load cell of the biaxial unit, as higher thicknesses require higher loads to achieve the desired levels of strain. Accounting for this compromise, the optimal thickness for the substrate was stated to be 1.6 mm.

Regarding the shape of the substrate, two different layouts that allow an easy clamping for the application of biaxial deformations were studied, see Figure 3.21. To test both geometries, the maximum displacement before rupture was applied and the achieved strain in the channels in both directions obtained. With the second geometry, the maximum deformation possible in the longitudinal direction could not reach 10%, so the first shape was initially selected for the device.

With these two parameters of the system fixed, FSI simulations of the device showed differences in strain among the central and the side channels. As ECs in all
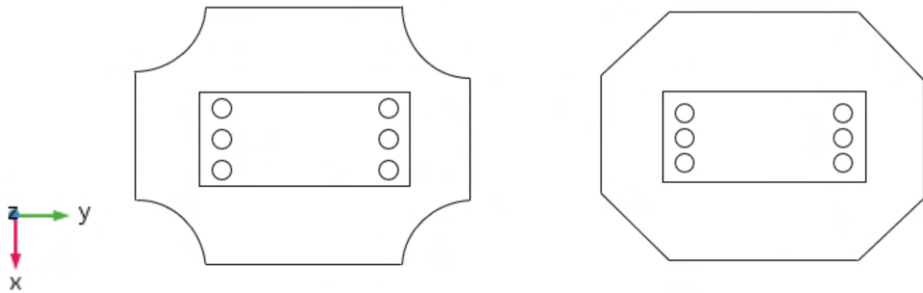
Figure 3.21. Two tested shapes of the PDMS base for the strain device. These shapes are designed to allow an easy grip by the clamps.

channels are required to be subjected to the same stimuli, this issue was solved by reducing the number of channels to two. This implied a reduction in the amount of information per test, but the homogeneity of the mechanical stimuli is a critical requirement. With only two channels, the overall dimensions of the device were reduced and the same strains could be obtained with lower displacements. Therefore, for simplicity in manufacturing, the second shape of the base was now valid and finally selected for the device, see Figure 3.21. Moreover, the width of the channels was increased to 2.3 mm (from the previous 2.0 mm), the size of the tubing and entrances, in order to increase the area of cells to be studied. Finally, to enhance the quality of the images obtained in the microscope, a material reduction was defined in the area above the channels. The configuration of the final device is shown in Figure 3.22 and the mould for it in Figure 3.23.

With the model of this final device, the application of the biaxial strains was analysed and an acceptable homogeneity was observed throughout the channels, with the highest deviation in strain being 1.3% for the case of applying 10% strain. The maximum stresses reached in all cases were not near the rupture stress of PDMS, observed in the lab to be around 6 MPa.

3.3   Flow tests

This section describes all the steps that were performed in the cell laboratory, including the tuning of the flow system and all the protocols followed in the flow tests. It is crucial to follow every procedure carefully, as sterility is easily compromised. It should be noted that every operation here described that involves EC manipulation and exposure must be conducted inside a laminar flow hood.
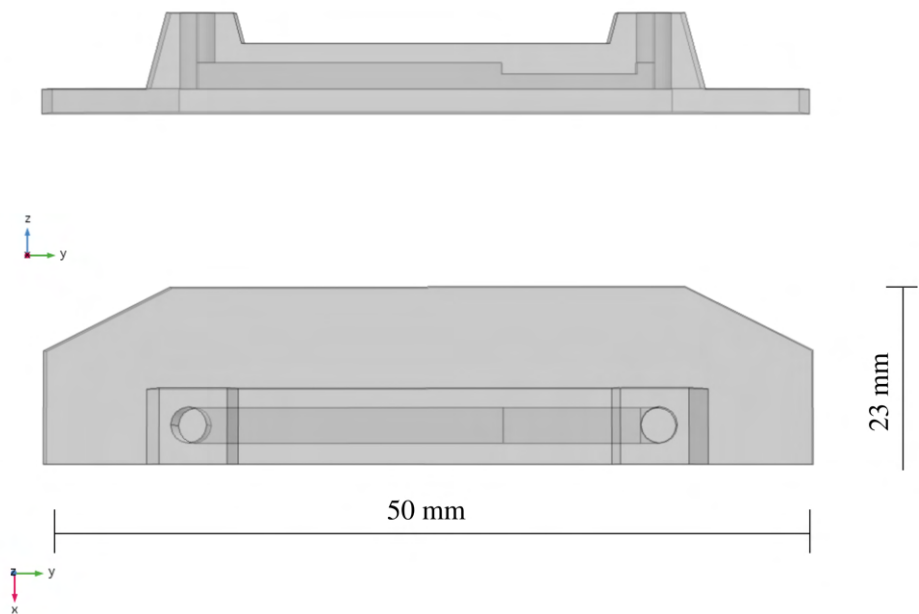
Figure 3.22. Final configuration of the strain device. The 1.6 mm thick base shows flat chamfers and the device now only has two channels.
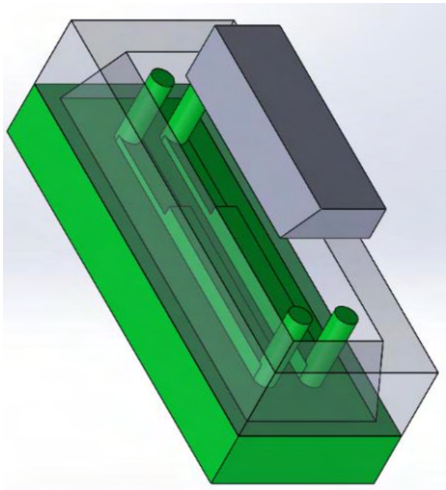
Figure 3.23. Mould to fabricate the strain device. An extra piece is mounted in the system to make the material reduction above the channels. This piece also includes a draft angle.

3.3.1   Setup of the experiments

The flow tests were tuned and carried out with the flow device described in Section 3.2.3. As this line of research is new to the group, a careful design and tuning of cell experiments had to be performed in advance. This initial setup was performed with HUVECs, as their cost is lower and are less sensitive that other ECs such as HCAECs. Some parts of the protocol were standard, mostly those related to cell handling, so they did not have to be optimised. However, cell density when seeding, the adhesion protein used in the substrate or the flow pump were the three main factors to optimise for our flow tests. They will be discussed in detail below, along with the protocol to handle ECs and prepare them for flow tests.

3.3.1.1   Cell handling and seeding density

Before use, HUVECs were previously cryopreserved in vials in liquid nitrogen, each vial containing 1 ml of an aggregate of cells, usually between 500,000 and 1 million, culture medium and dimethyl sulfoxide (DMSO). Once needed, a cryovial was submerged in a 37°C water bath. Right before the cells were completely thawed, it was removed from the heat and its content was resuspended in fresh culture medium and introduced in a flask. The flask was afterwards placed in the incubator, which maintains an atmosphere of 37°C and 5% CO_2, for cell growth. Whilst left to grow, cell medium had to be refreshed every 24 to 48 hours. Once ECs reached high confluence, they were seeded in the flow device.

To obtain the cells that were attached in the flask, they had to be trypsinized. For this, it was first necessary to remove the medium by aspiration. Cells were subsequently rinsed with phosphate-buffered saline (PBS) to remove any trace of culture medium, as it can inhibit the action of trypsin. Subsequently, the solution of trypsin and ethylenediaminetetraacetic acid (EDTA), from Lonza, was poured into the flask, ensuring a full coverage of the surface of cells. The flask was afterwards left for at least 2 minutes at room temperature to make ECs detach from the flask. If ECs were not detaching properly, the flask could be placed in the incubator for a minute to enhance the effect of trypsin. Once this detachment was verified by visual checking in the optical microscope, the flask was filled with cell medium to prevent further action of the trypsin that could irreversibly damage the cells. This solution was placed in a Falcon tube and centrifuged for 5 minutes at 1200 rpm to generate a pellet of cells in the bottom of the tube. The supernatant was later aspired and the remaining pellet of cells was resuspended in culture medium by gently pipetting to break up the clumps.

Once cells were resuspended, they could be counted in a haemocytometer. This step is crucial in order to know the cell density injected in the channels of the device. The procedure works as follows: 10 μl of the solution with the cells and the medium was injected between the haemocytometer and the coverslip. The surface of the device is patterned with a squared grid, as shown in Figure 3.24. Using the optical microscope, ECs inside the grids marked with an L (Figure 3.24) were counted and

averaged per L-marked grid. This number was afterwards multiplied by 10,000 and
the result was the number of cells per ml in the solution.

Figure 3.24. Overview of the haemocytometer (or Neubauer chamber), which allows count-
ing the number of cells in suspension. The glass slide is placed over the central part of the
device. The surface of the device has a grid that can be observed in the microscope. Cells
in the four lateral squares labeled 'L' are counted to obtain cell number per ml.

Cell density injected in the flow chamber was crucial for the development of a
proper monolayer of ECs to cover all the surface without overlapping, see Figure 3.25.
The evaluation of the generation of a confluent monolayer started by trying a seeding
concentration of 100,000 cells per squared centimeter [149,193,222], or 180,000 cells for
all three channels—1.8 cm^2 is the overall seeding surface in our device. After several
iterations, the optimum cell density was established at 200,000 cells per squared
centimeter or around 350,000 cells for all channels.

| (a) | (b) | (c) |
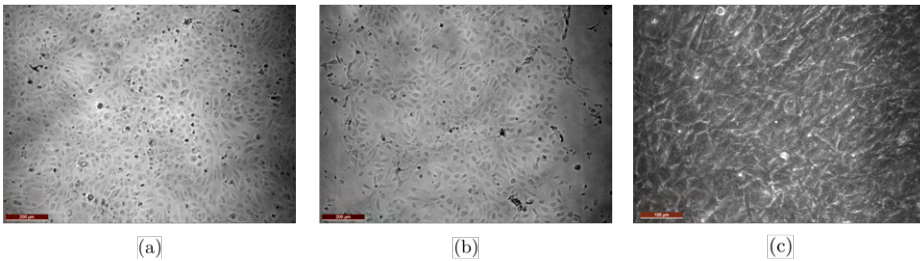
Figure 3.25. Examples of the different types of monolayers that can be obtained due
to appropriate or inappropriate cell density. (a) A confluent homogeneous monolayer of
HUVECs. (b) A monolayer of HUVECs that could not cover the entire surface (see sides of
the image). (c) An overlapped layer of HUVECs.

3.3.1.2   Adhesion protein

Before seeding, the substrate of the flow chamber had to be treated to enhance cell
adhesion, as glass is highly hydrophobic. This was done by initially giving the surface

an oxygen plasma treatment for 60 seconds and subsequently incubating an adhesion protein in the flow chamber, which enhanced the hydrophilicity of the surface. In this adhesion study, three different commonly used proteins were tested with our device and HUVECs. These adhesion proteins are collagen, fibronectin and Matrigel™. Collagen and fibronectin are proteins usually found in the body, whereas Matrigel™ is a solubilised basement membrane created by Corning™ that reproduces a physiologically relevant environment for cell culture [223]. Regarding the other two proteins, rat tail type I collagen and human fibronectin also from Corning™ were used. The concentrations used of each protein are detailed in Table 3.3, and were selected following available protocols or other studies from literature [177, 224].

Table 3.3. Coating concentration of each of the three tested adhesion proteins.

Protein	*Collagen*	*Fibronectin*	*Matrigel*
Concentration	100 μg/ml	50 μl/cm^2	5 μg/cm^2

After including the dilution of protein in the channels of the device, it was incubated for 1h at 37 °C to enhance its effect. After this time, the solution in the channels was aspired and the device was carefully washed with PBS to remove any traces left. Afterwards, the defined amount of cells (Section 3.3.1.1) was pipetted into the channels and the seeding was left to culture in the humidified incubator overnight. The flow tests could be performed when a confluent monolayer of ECs in the channels was formed.

For this adhesion study, the maximum flow rate for 24 hours, i.e., 4.5 ml/min, implying 0.3 and 1 Pa of low and high WSS, was applied with the peristaltic pump (Section 3.2.1) as these are the most aggressive conditions of our tests. Phase-contrast images throughout all the channels were obtained right before applying flow, at 16 hours and at the end of the tests, 24 hours later. From these images, cell density was obtained by counting the number of cells in each image and the best adhesion treatment was determined as the one that caused the least cell reduction and where the highest number of cells could be found at the end of the experiments. The results regarding cell density are detailed in Figure 3.26.a. From these data, we can conclude that fibronectin showed to be the best adhesion treatment for our experiments, agreeing with the qualitative observation of the images (Figure 3.26.c).

Apart from these three adhesion proteins, in this study we verified the adequacy of the material of the substrate. Therefore, we also tested the adhesion of ECs using a PDMS substrate and compared that to the glass slide (Figure 3.26.b). In this case, we observed that PDMS was a better substrate for EC adhesion and fibronectin coating than a glass slide, therefore we decided to change our flow device and provide it with a PDMS base.

(a)   (b)

(c)
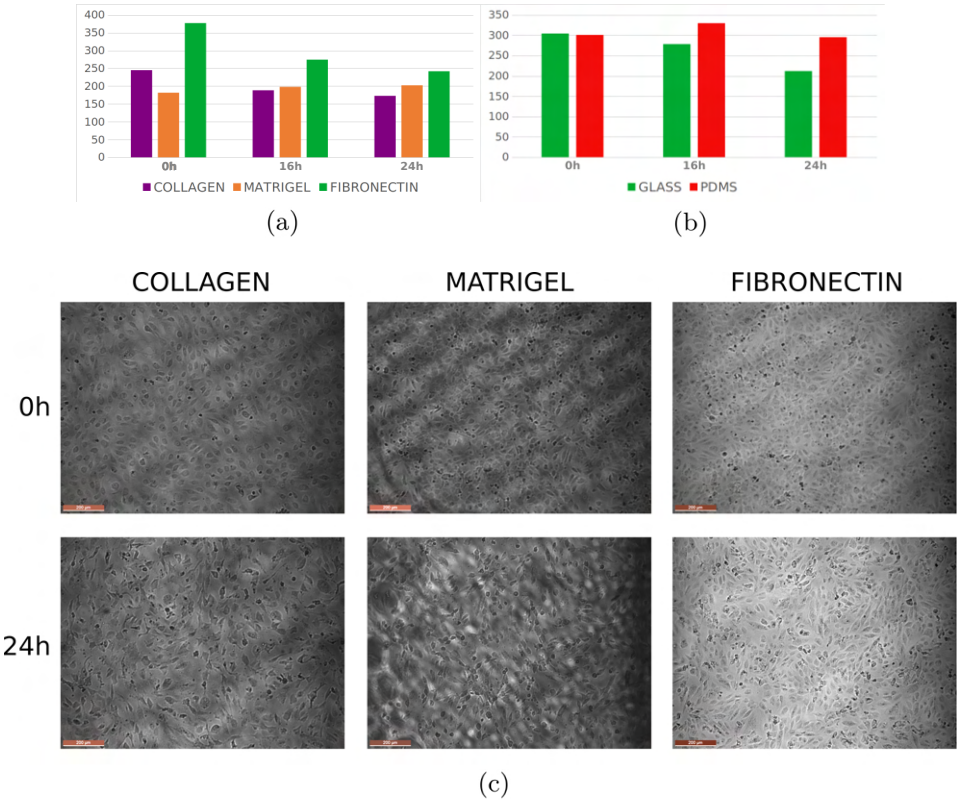
Figure 3.26. Results of the adhesion study. (a) Cell count (cels/mm^2) for the evaluation of the three adhesion proteins. (b) Cell count (cels/mm^2) for the evaluation of substrate material. In this case, tests were performed with fibronectin as adhesion protein. (c) Representative images of the results comparing adhesion protein, at the beginning (top) and at the end (bottom) of the experiments.

3.3.1.3 Flow pump

The tuning of the peristaltic pump, see Figure 3.27.a., and some experimental tests were performed with the help of a student, as part of her Bachelor thesis. Some initial measurements were performed with the flow pump to obtain a coarse linear relationship between pump speed and flow rate, see Figure 3.27.b. From this starting point, a finer tuning was performed to obtain the specific pumphead speed needed to get our required flow rates (2.5 ml/min, 3.5 ml/min and 4.5 ml/min). This tuning was performed with plain PBS, PBS with 4.93% of Dextran as the culture medium and this last solution at 37 °C, to ensure that these changes in fluid viscosity or temperature did not affect the flow rate the pump provided. The results obtained for this calibration are shown in Table 3.4.
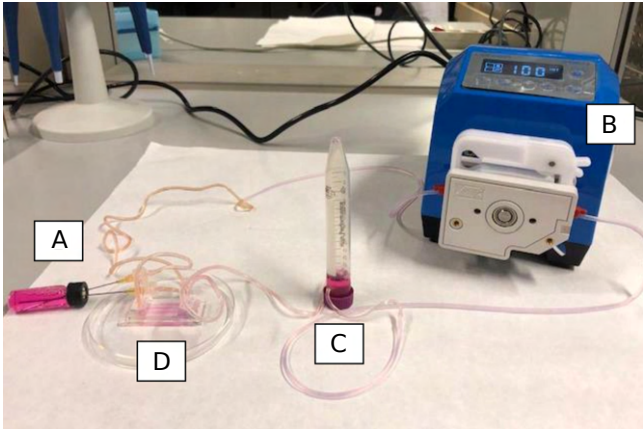
(a)
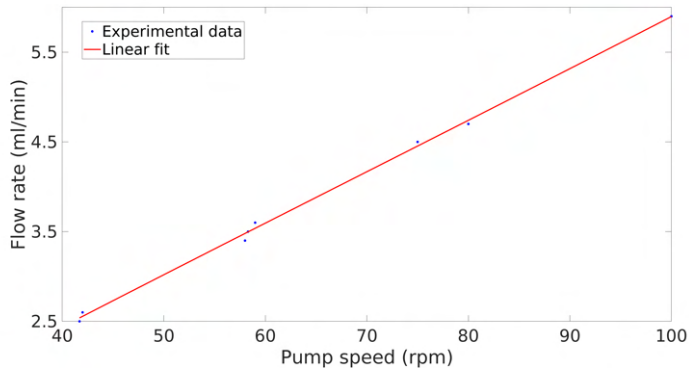
(b)

Figure 3.27. (a) Experimental setup of the G100-1J peristaltic pump. Culture medium flows from the reservoir, A, to the pumphead of the peristaltic pump, B. Afterwards, we include a damper, C, to avoid the pulsatility generated by the pump and make the flow in the device, D, steady. (b) Coarse linear fit between the pumphead speed and the flow rate.

Table 3.4. Flow rates (ml/min) obtained with certain pumphead speeds (rpm) with different fluid conditions.

Pumphead speed (rpm)	PBS	PBS + dextran	PBS + dextran at 37ºC
41.7	2.4	2.5	2.6
58.3	3.5	3.5	3.6
75.0	4.5	4.4	4.5

In parallel, we performed the setup of the pressure pump OB1 from Elveflow, see Figure 3.28. This pump could be controlled with the computer, allowing the generation of more complex flow patterns, like oscillatory or pulsatile flow, interesting for further studies. Generally, pressure pumps move flow from one reservoir to another by applying a pressure change. If recirculation of fluid is required, flow direction would have to be reversed as it would flow from the second reservoir to the first. In our case, we need flow to maintain the same direction to generate positive pulsatile patterns, for example. However, due to the time length and the high demand of flow volume our experiments require, we also need to include a recirculation of flow. The Mux Injection system from Elveflow is a solution for this problem. It is an injection valve with six inputs and two interchangeable configurations that allows, by a specific placement of the tubing, to maintain flow direction in the devices while changing the reservoir that is providing the system and with a fast switch time (100 ms). Additionally, a flow sensor is required for the software to be able to control the setup guided by flow rate. The system was assembled and several trials were performed with different flow patterns set in the software. Due to the high dimensions of this entire system, it does not fit an incubator, so the tests with cells would have to be performed in a heating cabinet with a tampon solution to account for the lack of CO_2 in the culturing environment.
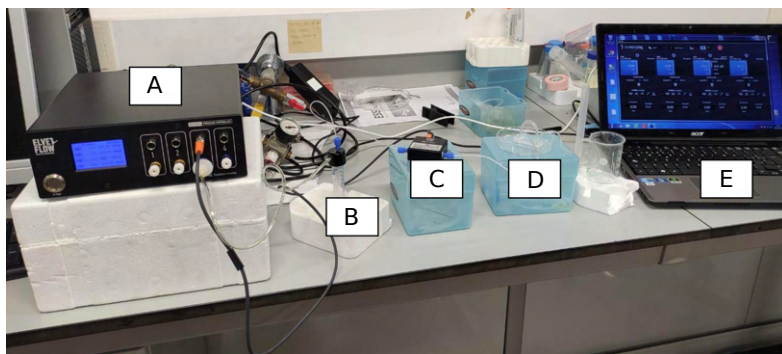
Figure 3.28. Calibration setup for the OB1 pressure pump. A pressure probe comes from the pump, A, into the reservoir, B. When pressure is applied, culture medium leaves the reservoir and flows through the flow sensor, C, and moves to the flow device, D. The pressure pump and the flow sensor are connected to the computer, E, for a careful control of the conditions of the setup.

3.3.2   Procedure of the flow tests

Before performing the flow tests, the tubing system was previously sterilised in the autoclave and the confluent monolayer of ECs was cultured in the flow chamber following the specifications detailed in Section 3.3.1.1 and Section 3.3.1.2. The entire

system consisted of a peristaltic pump, a set of tubes, a 5 ml bottle filled with cell medium, a fluid damper and the flow chamber device assembled on a PDMS base (Section 3.3.1.2).

Firstly, control images of the cells along the three channels were taken in the phase-contrast microscope to be later compared with the disposition of the cells once subjected to flow. Afterwards, the tubes were connected to allow a progressive feeding of the system. The flow rate was initially low to facilitate visual checking of any possible leaks and to avoid ECs to be drastically pushed by a high shear. Once the system was proven watertight, the flow rate was set to the test value and the kit was kept in the humidified incubator for 24 hours, a sufficient time-frame for cells to respond to flow [193]. Throughout this time, images of the cells were taken at 2-4-8-16-24 hours to obtain their time dependent response. The time interval between images was shorter at the beginning of the experiments as it is when ECs change more evidently their morphology [193]. The flow rates selected for the experimental tests due to the WSS values they generate are shown in Table 3.5.

Table 3.5. Flow rates (ml/min) used in the experimental tests and WSS generated in both areas of the flow device.

Flow rate	High WSS (Pa)	Low WSS (Pa)
1.25 ml/min	0.28	0.08
2.5 ml/min	0.55	0.16
3.5 ml/min	0.77	0.23
4.5 ml/min	1	0.30

After the 24 hours, the system was moved again to the phase-contrast microscope to obtain the final images of the cells under flow conditions. Finally, the kit was carefully disassembled and the tubing system was thoroughly checked and set aside for sterilisation and reutilisation. Cells were finally fixed for immunostaining. This fixation consisted in emptying and washing the device after the tests, to afterwards include a 4% paraformaldehyde (PFA) in PBS solution. It was then left at room temperature for 15 minutes. Finally, the solution was removed and the fixed ECs were kept submerged in PBS at 4°C.

3.4   Image analysis

Once the flow test was finished, the grayscale microscope images of the cells throughout the experiment had to be processed. From them, we wanted to study cell response in terms of morphology, therefore the information that we extracted is the shape index (SI) of the cells and their orientation. The SI provides information about the circularity of the cells. A value of SI of 1 means a perfect circle, while a value closer to 0 implies a more elongated shape, as can be inferred from (3.5). These two factors were calculated with Matlab R2020a. However, the quality of the images was

not optimal and cell contours could not be automatically segmented in the software. Therefore, a preprocessing was needed, which was also carried out in Matlab. After this step, the images were analysed and the results of the flow tests obtained.

$$SI = \frac{4 \cdot \pi \cdot area}{(perimeter)^2} \qquad (3.5)$$

3.4.1   Image preprocessing

This section discusses the final preprocessing employed to improve the quality of the images for the posterior cell morphology analysis. The whole process involved defining multiple iterations and functions to arrive at this optimised solution, as the images captured by each microscope varied and achieving uniformity across all images posed a challenge.

First, a contrast enhancement was implemented to sharpen the edges with the function *imadjust*. Afterwards, the images were inverted to achieve a darker background by using *imcomplement*. Subsequently, the background of the images was estimated with the help of the function *imopen* and subtracted. This step is carried out to mitigate differences in brightness between the centre and the borders of the images, see Figure 3.29.b and c. In order not to lose the information of one of these two areas, this homogenisation in brightness is necessary. Figure 3.29 shows the initial image and the ones resulting after this preprocessing.

From this processed image, the next step was the binarization with the function *imbinarize*, which is essentially the transformation of a grayscale image into a black and white one. For this, it was necessary to establish a threshold to determine the level of gray that is black or white. However, only by establishing a threshold, these images were still not properly binarized, as lighter areas represent background in some places of the image and cells in others. Since this is quite a common problem, certain methods include the so called adaptive threshold, which establishes a local threshold in the neighbourhood of each pixel. With this method, the binarization of the images was fairly accurate, see Figure 3.30.a. Afterwards, residual noise from the images was erased establishing a minimum amount of pixels per item, with function with *bwareaopen*.

The holes that can be seen in the particles were filled with function with *imfill* and the cells that were in the border of the image and therefore not shown whole were removed with function *imclearborder*. In order to make sure that two cells were not overlapped and counted as one in the binarization, the function *imerode* was used to separate the borders of the particles, avoiding undesired overlaps. Finally, to overcome an over erosion, *imdilate* was used afterwards to expand the borders of the cells but making sure that single cells were still visible as unique particles, see Figure 3.30.b.

(a)

(b)

(c)
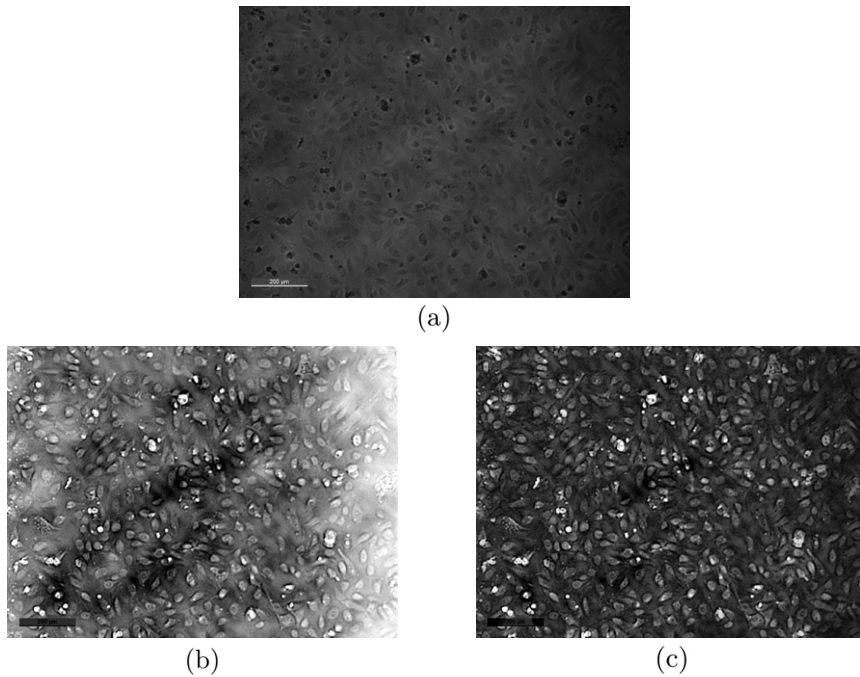
Figure 3.29. (a) Initial phase-contrast image. Note the differences in brightness in the entire image. (b) The inverted image, showing ECs in a lighter shade than the background. The differences in background brightness are carried to this step. (c) The inverted image after removing the background. Note that the brightness of the image is now quite homogeneous.

(a)

(b)
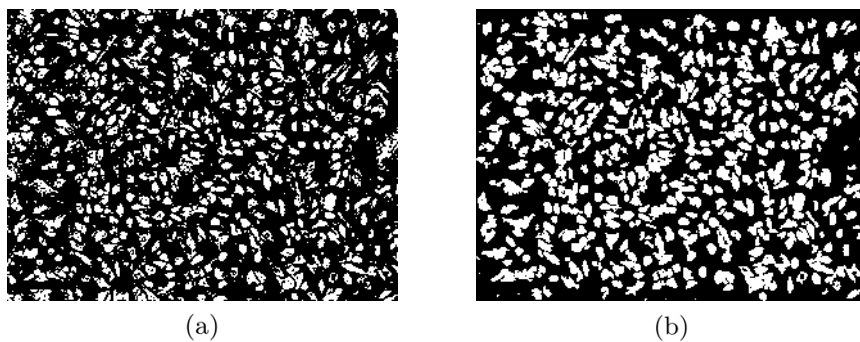
Figure 3.30. Both steps in binarization. (a) Initial binarized image after applying the adaptative threshold. (b) Final binarized image.

3.4.2   Particle analysis and measurement

The binarized and processed images were then analysed to obtain cell contours. In order not to count the extra residual noise of the images, a minimum area limit was set, so that all the small white dots that can be seen in Figure 3.30.b were not analysed as cells. Despite our efforts in the previous step, some cells were still overlapped in the images and the binarized result was a bigger white particle. As the known watershed function did not prove good effect in our images to separate the two objects, we set an upper area limit to block the detection of these overlapped cells. In Figure 3.31, a representative example of the cell contour detection is shown.
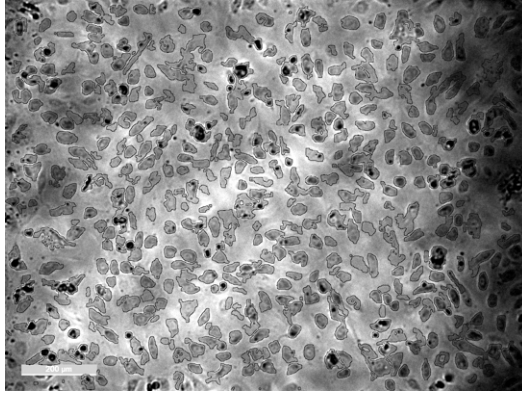
Figure 3.31. Representative image of the cell contours detection. The detected contours are drawn over the initial image, before any processing.

With the initial analyses, we consistently observed fairly low values of SI, even for the apparently rounded cells. It was observed to happen due to the high number of small spikes that are drawn in the detected contours. These spikes caused a higher perimeter value that did not involve a higher area, artificially reducing the values of SI (see (3.5)). Therefore, we chose to analyse the roundness of the particles, see (3.6). This measurement considers the area and the length of the mayor axis of the ellipse that best fits that cell, therefore avoiding the over-measurement of the perimeter. This parameter also takes the value of 1 for a perfect circle and 0 for a line.

$$Roundness = \frac{4 \cdot area}{\pi \cdot (major\ axis)^2} \tag{3.6}$$

3.4.3 Nuclei segmentation

Due to the image processing protocol causing some loss of information with some cells not being properly detected, we evaluated, as an alternative procedure, the possibility of obtaining cell shape and orientation from staining the nuclei of ECs. Therefore, two flow tests (n=6) with the highest flow rate of 4.5 ml/min (see Table 3.5) were performed on HUVECs stained with Hoechst. Hoechst dyes stain the DNA inside cell nuclei and, thanks to its high cell membrane permeability, it can be used on living cells. Images were taken at the beginning of the test, at 16 hours and at the end, both phase-contrast and fluorescence, see Figure 3.32. The purpose of this analysis was to compare the changes in shape and orientation observed in both types of images and thereby validate the use of stained nuclei and fluorescence images.
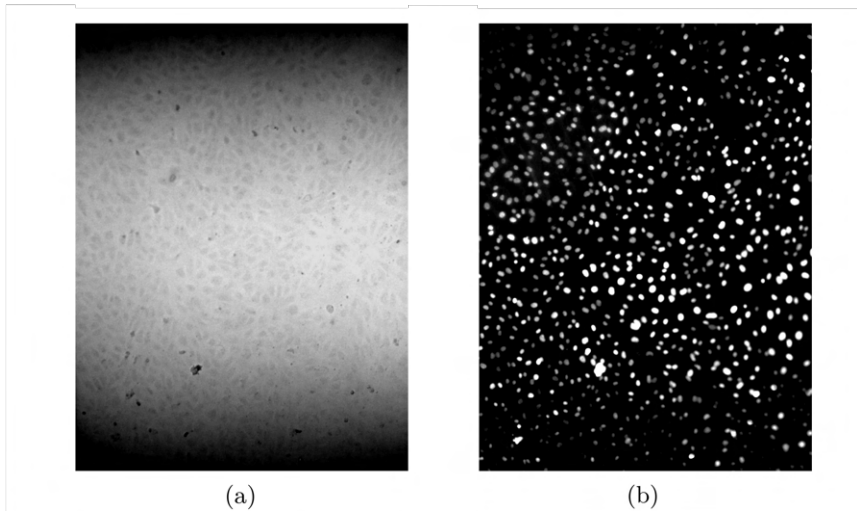
Figure 3.32. Phase-contrast (a) and fluorescence (b) images of the same spot in the device at the beginning of the test.

The image processing for the fluorescence images required less steps than the one detailed previously (Section 3.4.1). In particular, the fluorescence images were merely contrast enhanced (*imadjust*) before binarization. After binarizing the images (*imbinarize*), the remaining holes were filled (*imfill*) and the nuclei in the borders of the images erased (*imclearborder*). Afterwards, particle analysis was performed in the open software Fiji [225], differing from the phase-contrast images (Section 3.4.2), in which this analysis was performed in Matlab. Due to the clearer contours in these images, a watershed algorithm could be directly applied to separate the overlapped

particles. Similarly than with phase-contrast images, a pixel size limit was set to ensure that only the nuclei were being segmented.

Some significant elongation in terms of a reduction of the roundness factor was observed in the first time interval when analysing both, cell and nuclei contour, and in both areas of high and low WSS, see Figure 3.33. In the last time interval, from 16 hours to the end of the experiment, the roundness of both, cells and nuclei increased significantly. This is probably due to cell loss, but this effect will be discussed in the following section. In these tests, two different WSS levels were applied to cells, see Table 3.5. The roundness at the beginning of the experiments was similar in both WSS areas for cells and nuclei. However, the roundness in both cases showed significant differences in the area subjected to low and high WSS. In particular, cells subjected to a lower value of WSS elongated more (lower value of roundness) than those subjected to the higher WSS, and this can be observed in both, cell shape and nuclei. This difference can also be due to more cell loss in this aggressive environment. In terms of orientation, the results between whole cells and nuclei differed in some cases, see Figure 3.34. A change in cell orientation was observed in whole cells, in both levels of WSS (Figure 3.34.a). Cell nuclei, however, did not reproduce this cell orientation (Figure 3.34.b). The possibility to observe the orientation of the whole cells only by observing the nuclei was expected, as Ghim et al. [226] observed a reorientation of nuclei. However, they found a consistent discrepancy of 10-20° between the direction of the nuclei and the overall direction of porcine aortic endothelial cells.
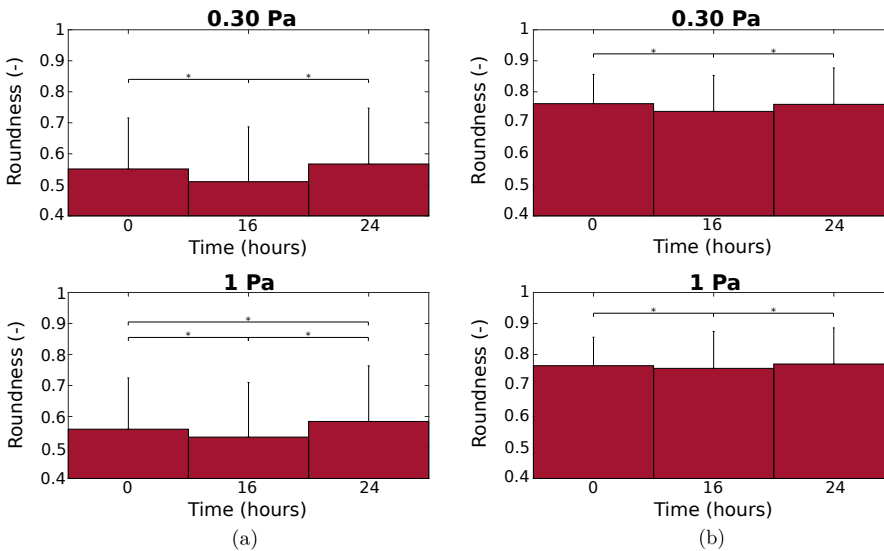
Figure 3.33. Roundness of cells (a) and nuclei (b) for the two different levels of WSS studied. * indicates a statistically significant difference (p<0.05).
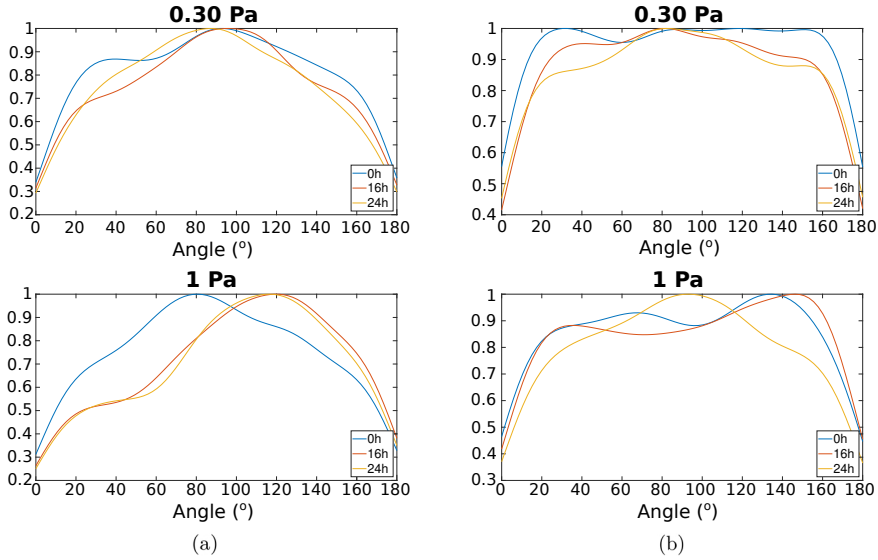
Figure 3.34. Histograms of cell (a) and nuclei (b) orientation for the two different levels of WSS studied.

3.5 Preliminary results of the flow tests

Following all the protocols that have been described above, flow tests with steady laminar flow were performed on HUVECs (passages 3-6) and on HCAECs (passages 3-7). The objective of these initial tests was to obtain the WSS threshold from which ECs start to respond to flow, and to observe whether it varied with cell type. These tests could give us valuable insight into the need to use the specific cell type of the area to be studied, as well as giving a clearer differentiation on the response threshold. Due to their different origin, the flow ranges studied for HUVECs were smaller, as ECs from vein are physiologically subjected to low values of WSS [227]. Therefore, for the experiments with HUVECs and steady flow, flow rates of 1.25, 2.5 and 3.5 ml/min were studied, generating WSS values ranging from 0.08 to 0.77 Pa (see Table 3.5). On the other hand, on the experiments with HCAECs, the flow rates studied were 2.5, 3.5 and 4.5 ml/min, causing a WSS that ranged between 0.16 and 1 Pa (Table 3.5), in order to include the higher ranges of WSS that happen in coronary arteries [208].

3.5.1 HUVECs subjected to steady flow

Figure 3.35 shows the results of HUVEC roundness for the different values of WSS. HUVECs in static conditions show a relative randomness and no clear conclusions can be extracted from them. In these conditions, HUVECs showed an already elongated shape at the beginning of the experiments, observed in the low initial value of
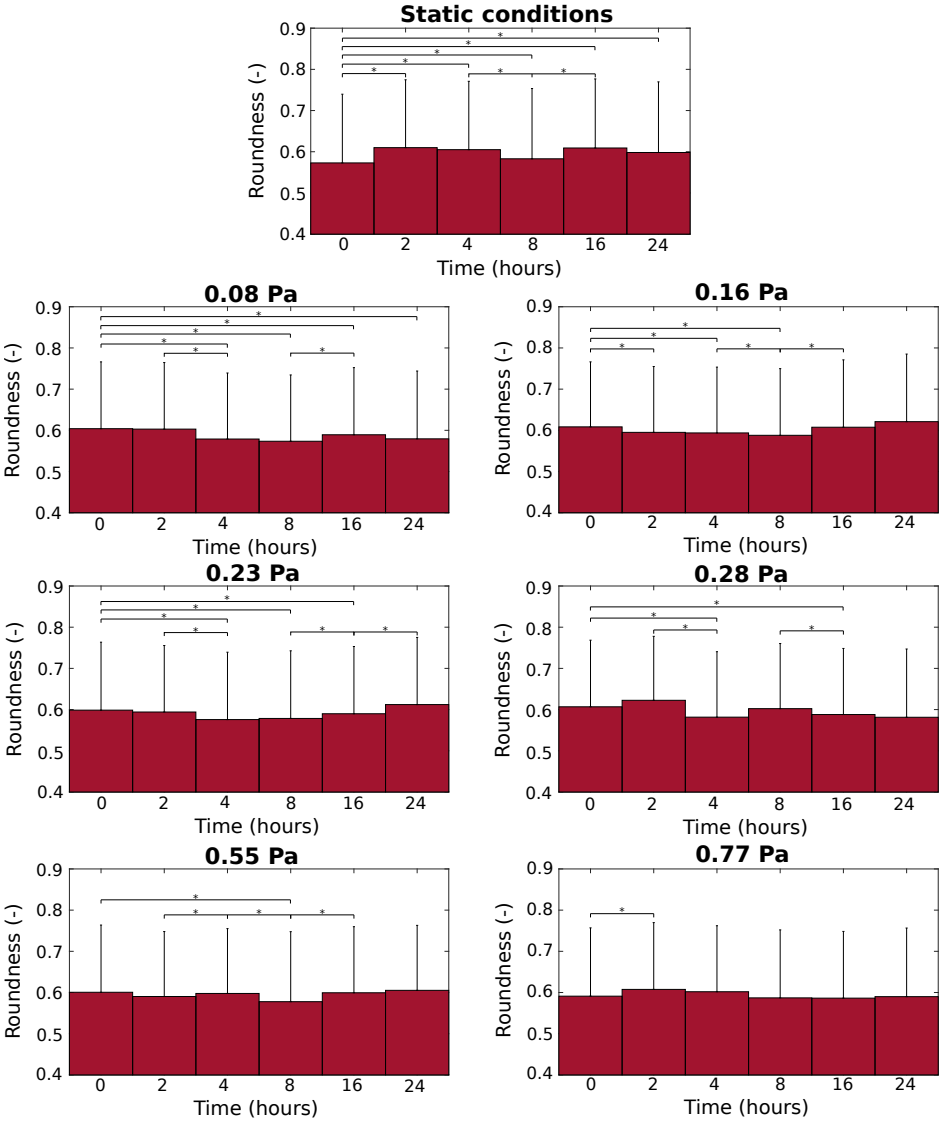
Figure 3.35. Median and standard deviation of the roundness of HUVECs (passages 3-6) throughout different levels of WSS (n=6 for all conditions). * indicates a statistically significant difference (p<0.05). Median instead of mean is represented in an attempt to reduce the skewness that apoptotic round cells cause in the data.

roundness. After this moment, HUVECs show changes in their roundness throughout the experiment without a clear tendency. We can observe, however, that the changes in the values of roundness are small, and so are in all the tested conditions. Other

studies in literature studying HUVECs and measuring their SI or roundness reported higher initial values [172], indicating a more circular starting shape which allows ECs to change their shape more notably throughout the tests. Despite this initial already elongated shape, further elongation can be seen consistently as a reduction in the roundness value in the first 8 hours of most levels of WSS studied (from 0.08 Pa to 0.55 Pa). Therefore, the WSS threshold from which HUVECs start to elongate seems to be below 0.08 Pa. Further flow tests with lower flow rates could be performed in order to obtain the WSS to which HUVECs do not change their shape. In the highest level of WSS, 0.77 Pa, HUVECs started more elongated than other cases and no further elongation was observed during the experiment.

(a)   (b)
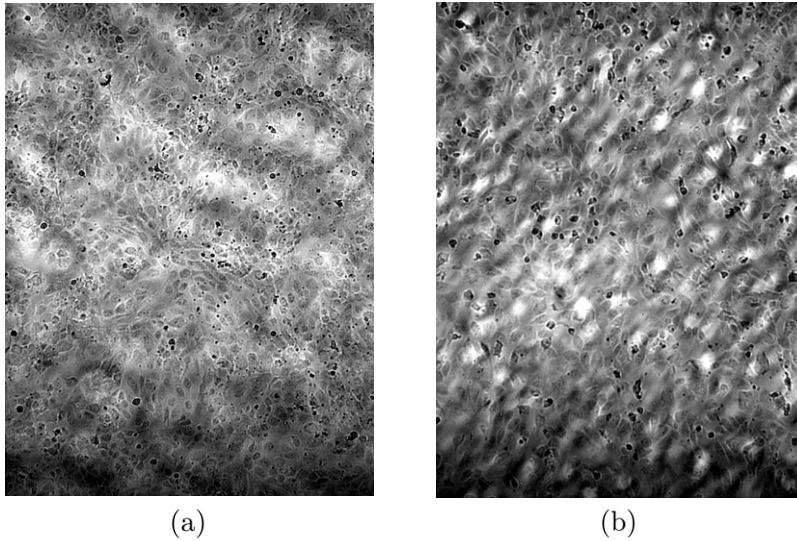
Figure 3.36. Monolayer of HUVECs at the beginning (a) and 20 hours into the flow test (b). The initial confluent monolayer is lost in that time span and HUVECs recover their initial cobblestone configuration, rendering the results invalid from this point in time.

In almost all cases, HUVEC roundness increases at 20 hours of flow. By qualitatively observing the images, this increase corresponds to a moment of relevant cell loss and the monolayer being compromised, see Figure 3.36. In this new distribution in the channels, the monolayer is no longer confluent and some HUVECs regain a more cobblestone shape. Apart from that, other HUVECs become apoptotic, resulting in rounding before finally detaching. Due to this two factors, the results are considered invalid once the monolayer is compromised, normally around 16 hours after the beginning of the tests. The median of the roundness factor is evaluated instead of the mean (Figure 3.35) as the data distribution is somewhat skewed towards the higher end (the rounder shapes) due to these outliers. This disruption of the monolayer also

happens in the highest levels of WSS studied (0.77 Pa), where HUVECs are not able
to withstand such high shear rate and some cells detach almost at the beginning of
the tests, translating into an increase of the overall roundness of ECs. The generation
and preservation of a confluent monolayer of ECs throughout flow studies is one of
the main challenges of these experiments. Davies et al. [191] also reported cell loss
when ECs were subjected to flow for over 8 hours.
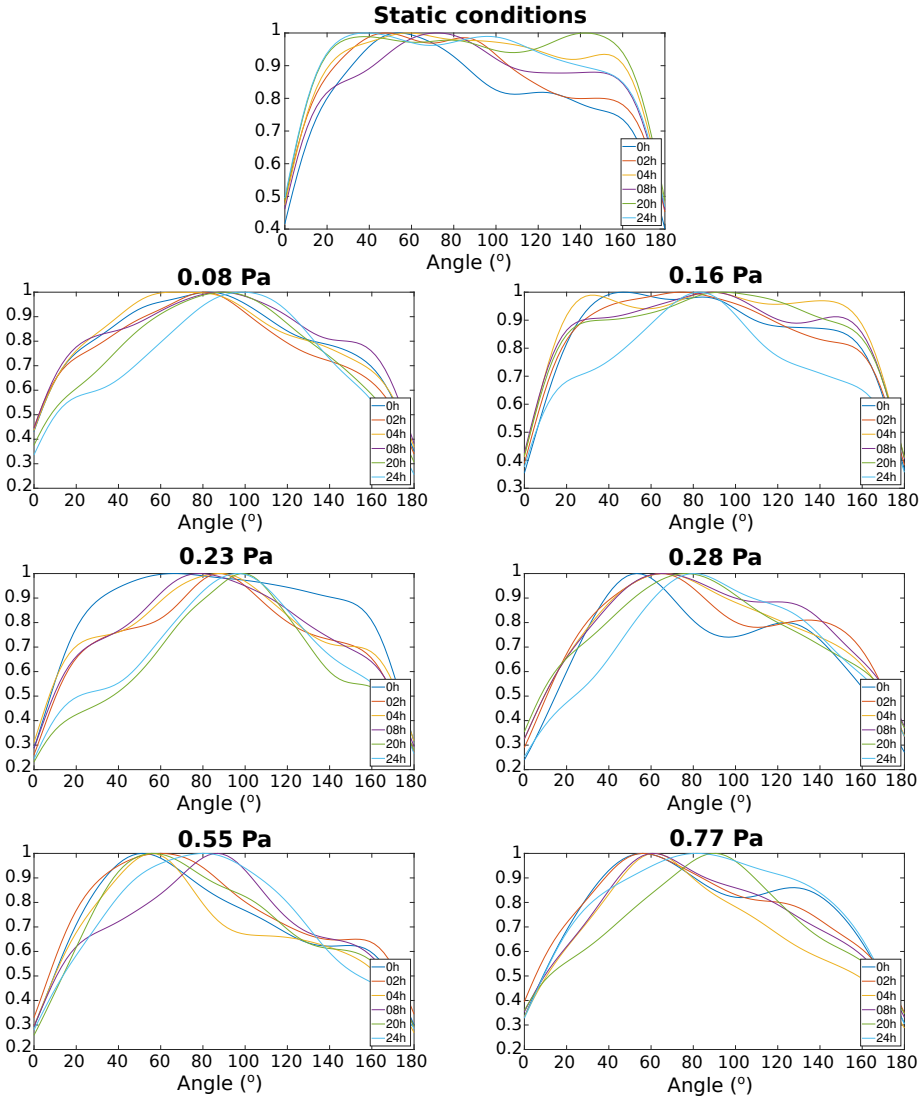
Figure 3.37. Normalised histogram of orientations of HUVECs (passages 3-6) in the
different levels of WSS (n=6 for all conditions). The 90° angle is the direction of flow.

Figure 3.37 shows the normalised histograms of HUVEC orientation in all tested conditions and throughout the time lapse of the experiments. An angle of 90° represents alignment with flow. When HUVEC were not subjected to flow, Figure 3.37.a, the histogram shows a flat distribution of the different angles, which represents a random orientation of HUVEC. However, when subjected to even the smallest values of WSS, HUVEC reorient with the direction of flow (90°) throughout the tests. In the case of the three lowest WSS values, Figure 3.37.b–d, HUVECs showed an initial preferred orientation of 90°. As they became subject to flow, this preferred direction coinciding with the direction of flow became more pronounced, i.e., more cells were aligned with this direction. In the case of the three highest WSS values, Figure 3.37.e–g, the orientation of HUVEC at the beginning of the experiment was around 50-60°. By the end of the experiments, this orientation shifted to an alignment with flow (90°). Therefore, although cells were lost halfway through the experiment, the remaining ones maintained their orientation with flow.

3.5.2   HCAECs subjected to steady flow

Following the same protocol than with HUVECs, steady flow tests were performed on HCAECs. Since these ECs come from arteries, the physiological WSS they are subjected to in vivo is higher [208], therefore the tests were designed to reproduce higher levels of WSS by applying flow rates of 2.5, 3.5 and 4.5 ml/min or WSS values from 0.16 to 1 Pa, see Table 3.5. These tests were carried to 32 hours of flow, as other studies on ECs coming from arteries measured cell shape throughout the experiments and observed that EC response did not change from this timepoint [193].

Figure 3.38 shows the results of HCAEC roundness for the static conditions and all the levels of WSS studied. In some cases, the images from the first hours of flow are missing due to microscope unavailability. Similar to what happened with HUVECs, HCAEC response in static conditions in terms of roundness shows a randomness from which other conclusions cannot be obtained. In the four lowest levels of WSS—0.16, 0.23, 0.30 and 0.55 Pa—, a significant elongation can be observed in the first 8 to 16 hours of the study. However, this elongation is lost afterwards due to the loss of the confluent monolayer, see Figure 3.39. When subjected to a WSS of 0.77 Pa, HCAECs show an elongation in the first 8 hours although it cannot be considered statistically significant. In the highest level of WSS—1 Pa—, it was very complicated to maintain a confluent monolayer when such a high flow rate was applied and HCAECs detached more easily since the beginning of the experiments, invalidating the results obtained, Therefore, we observed how HCAECs elongated with lower values of WSS than expected. This threshold that we were expecting to find, thus, could not be determined with these experiments.

When compared to the results obtained with HUVECs, HCAECs have an overall more elongated shape which can be observed in their lower values of roundness, at the beginning and throughout the tests (Figure 3.38). However, HCAECs have also responded to the lower values of WSS, like HUVECs, which is not consistent with
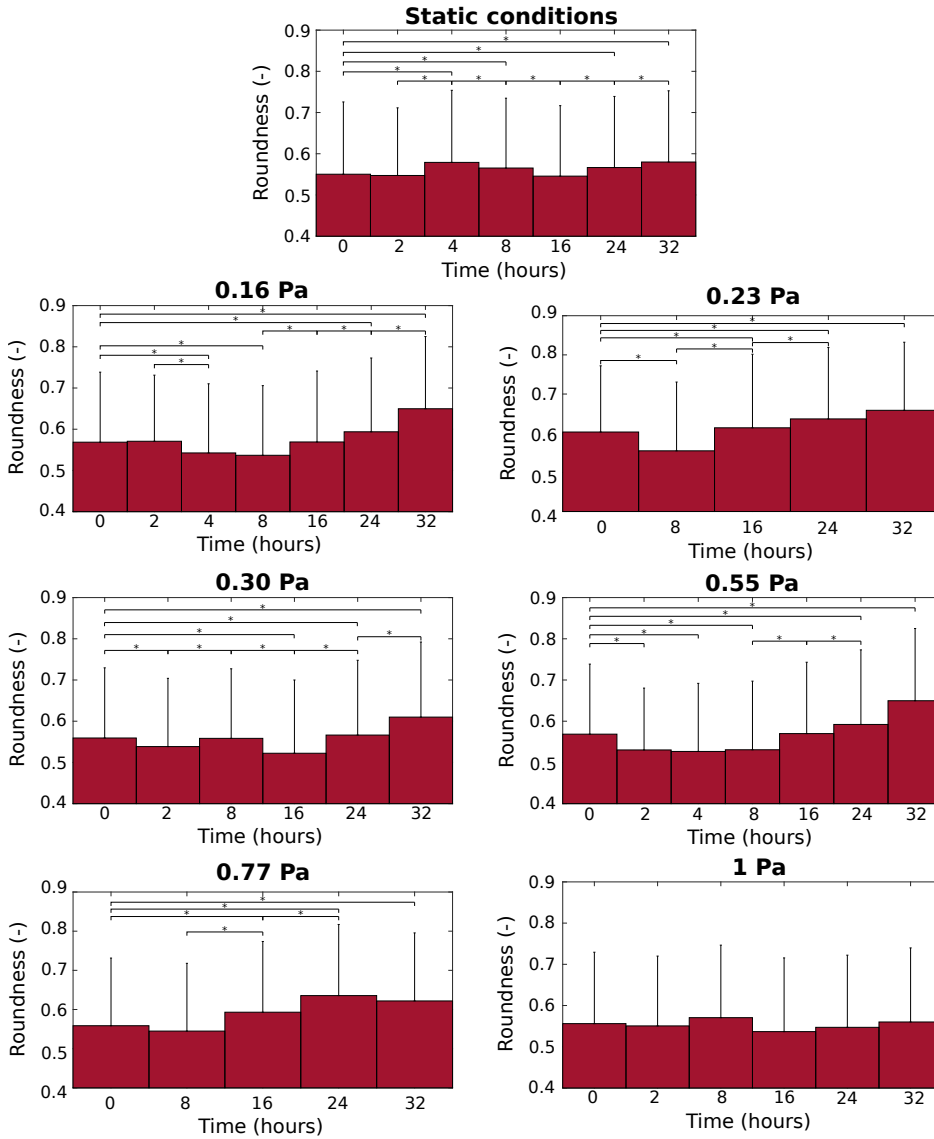
Figure 3.38. Median and standard deviation of the roundness of HCAECs (passages 3-7) throughout different levels of WSS (n=6 for all conditions, except for the 3.5 ml/min test—0.23 Pa and 0.77 Pa—, in which n=3). * indicates a statistically significant difference ($p < 0.05$). Median instead of mean is represented in an attempt to reduce the skewness that apoptotic round cells cause in the data. Overall values of roundness of HCAECs are lower than those of HUVECs.
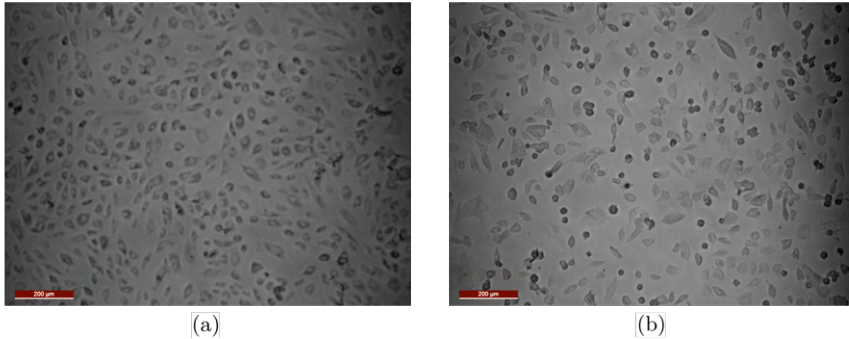
Figure 3.39. Monolayer of HCAECs at the beginning (a) and 16 hours into the flow test (b). The initial confluent monolayer is lost, invalidating the results from this point in time.

their stress stimulus under in vivo conditions. These results suggest the possibility that any type of EC could provide similar results in flow tests.

In terms of cell orientation, Figure 3.40 shows the normalised histograms of the orientations throughout the experiments and in the different conditions. Similarly than with HUVECs, the orientation of HCAECs was random in the static conditions and in all levels of WSS, they tend to align with the direction of flow with time. This alignment is clearer in the three lower levels of WSS were the monolayer is mostly maintained. However, in the higher levels of WSS, although most HCAECs are finally lost, the remaining ECs tend to maintain their orientation with flow, similar to what happens with HUVECs.

3.6   Key findings

- We have been able to develop a flow chamber device to study the behaviour of ECs subjected to flow that is easily adaptable to apply a combined stimulus of WSS and cyclic stretch. Several experiments have been performed with the flow device and ECs. However, no tests have been performed yet with ECs and the strain device.

- The optimum protocol for flow tests on HUVECs was clearly defined. In particular fibronectin over a PDMS substrate was shown to provide the best adhesion characteristics for a monolayer of HUVECs.

- A computer controlled pressure pump was set up to reproduce more complex flow patterns, including flow pulsatility.
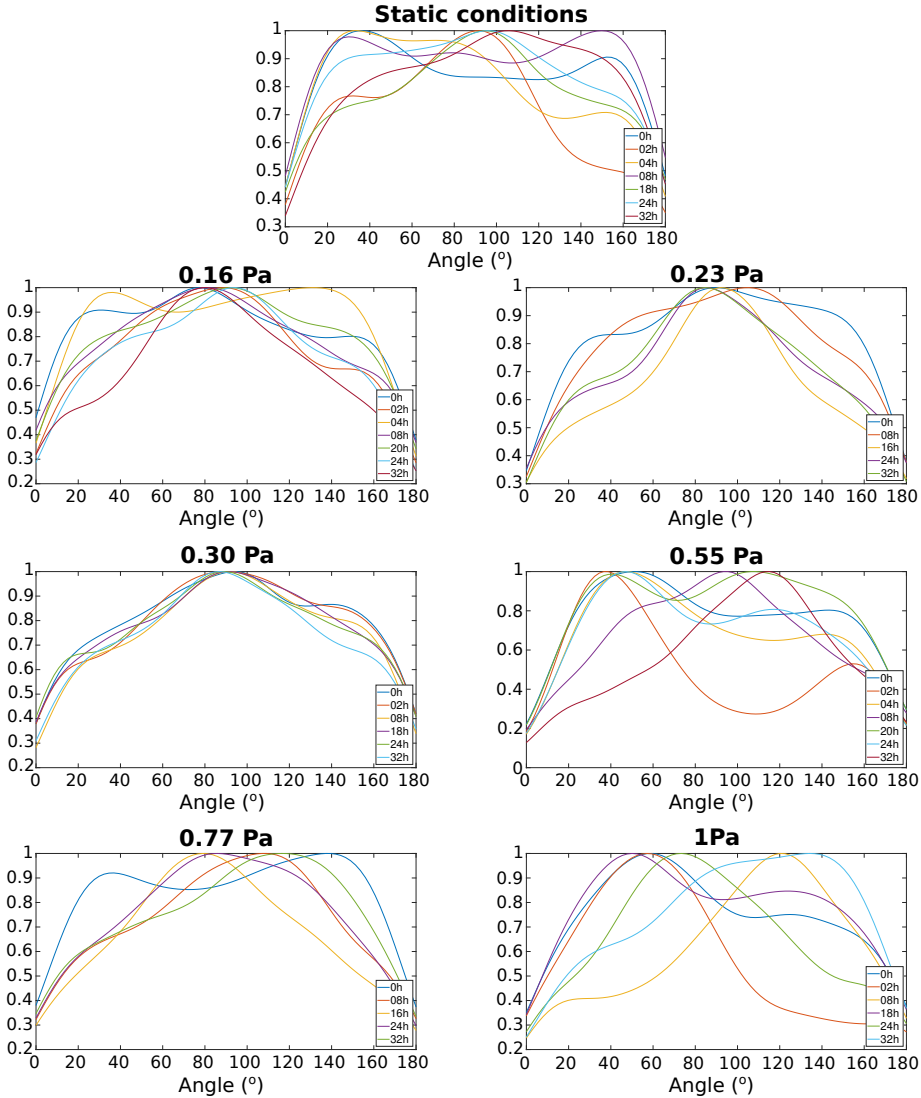
**Figure 3.40.** Normalised histogram of orientations of HCAECs (passages 3-7) in the different levels of WSS (n=6 for all conditions, except for the 3.5 ml/min test—0.23 Pa and 0.77 Pa—, in which n=3). The 90° angle is the direction of flow.

- EC nuclei showed elongation when cells were subjected to flow, showing good agreement with the response of whole cell morphology. The orientation of nuclei, however, did not replicate the orientation of cells.

- Phase-contrast images were automatically segmented succesfully with an image processing in-house code developed in Matlab.

- HUVECs and HCAECs showed response to flow in terms of morphology at low values of WSS. In particular, both types of ECs elongated during the first hours of the experiments and oriented with the direction of flow in all cases.

- No clear evidence of different levels of response was found between HUVECs and HCAECs, suggesting that any type of EC would be valid to obtain generalised results in flow tests.

- The critical factor of flow tests is the preservation of a confluent monolayer throughout the entire experiments. ECs are delicate and a monolayer can be easily compromised when the shear rates of the flow are relatively high.

- The preliminary findings obtained from the cell experiments represent the first step towards future work in this area aimed at achieving more conclusive results. The optimisation process carried out in this study will serve as a basis for these future investigations.

Damage caused by stent indentation

In this chapter, we explore a novel approach to understand and quantify the mechanical damage caused by stents in arteries that can lead to in-stent restenosis. Specifically, we use collagen hybridizing peptides, which are synthetic and fluorescent strands of peptide similar to collagen that can bind to damaged and denatured collagen in vascular tissue. To simulate the effect of stent struts on arteries when expanded, we have devised an indentation test that mimics a single repeating unit of indentation. By observing and quantifying any damage to the collagen caused by this indentation, we intend to gain deeper insights into the underlying mechanisms of damage that trigger in-stent restenosis.

4.1   State of the art

In-stent restenosis is a complex phenomenon that involves a range of biological and mechanical factors, including inflammation, thrombosis and mechanical injury caused by the stent itself. In an attempt to understand the mechanical environment that stents cause after expansion, several computational models have reproduced the expansion of a stent and analysed the stresses in the tissue [228–232]. More recently, mechanobiological models have emerged to relate mechanics to the generation and progression of in-stent restenosis. These are divided in agent-based models [233, 234], cellular automata methods [235, 236] and continuum models [95, 237–239]. Computational models such as these, however, need experimental data to validate and refine their assumptions and predictions.

In the search for experimental ways to understand the mechanical damage that occurs in stented vessels, collagen hybridizing peptides (CHPs) have emerged as a new potential tool for its assessment. Essentially, CHPs are synthetic peptides that can bind to places where collagen is damaged and fluoresce, allowing observation of these sites in the microscope [96, 240]. The actual mechanism of these peptides relies on the triple helix structure of collagen in the vessels. With damage or tissue remodelling, this structure of the collagen can be denatured, unfolding the triple helical chains. CHPs are able to bind to these denatured helices of collagen through

hydrogen bonding [241], see Figure 4.1.a. In simple terms, CHP is a single strand that can bind to collagen helices that lack some of the three strands, thus it has negligible affinity to intact collagen [242]. Due to its neutral and hydrophilic nature, CHP is also inert towards non-specific binding [243]. Considering the abundancy of collagen in arteries, CHP has already been successfully used in these vessels to detect chemical or heat-induced damage in their collagen [240, 244, 245], as well as mechanical damage induced by over-stretching the tissue [96], see Figure 4.1.b. These earlier studies using CHP support the possibility that, provided that stent induced damage involves damage in collagen, CHP could be a good marker to detect and quantify damaged areas in stenting and offer the possibility to link these areas to in-stent restenosis, moving one step forward towards a better understanding of the specific damage stimulus driving in-stent restenosis.

4.1.1   Objectives of the study

Considering the potential of this novel peptide for localising damaged areas, it is the objective of this study to determine whether CHP is capable of detecting and quantifying the mechanical damage that stents cause in vessels. To achieve this aim, indentation tests have been performed in porcine aortic tissue, which has subsequently been treated and evaluated with CHP. In these tests, three factors have been studied: (1) the effect of indentation level, or strain to which the tissue is stretched; (2) the effect of stent design by using two different size indenters; and (3) the effect of recoil or whether this damage is reversible in any way. The indentation tests have been reproduced numerically to give further insight into the mechanical stimuli present in the vessels and to link these with CHP results.

4.1.2   Research questions posed

- Is CHP a good marker for the type of damage that stenting causes in arteries?

- Can we quantify with CHP different levels of damage in indented tissue?

- What are the mechanical stimuli that favour the apparition of collagen damage in an indented tissue?

- Is there a threshold level of indentation that does not cause damage to the collagen in the tissue?

- Is collagen damage caused in vessels by an indentation reversible?

(a)

(b)
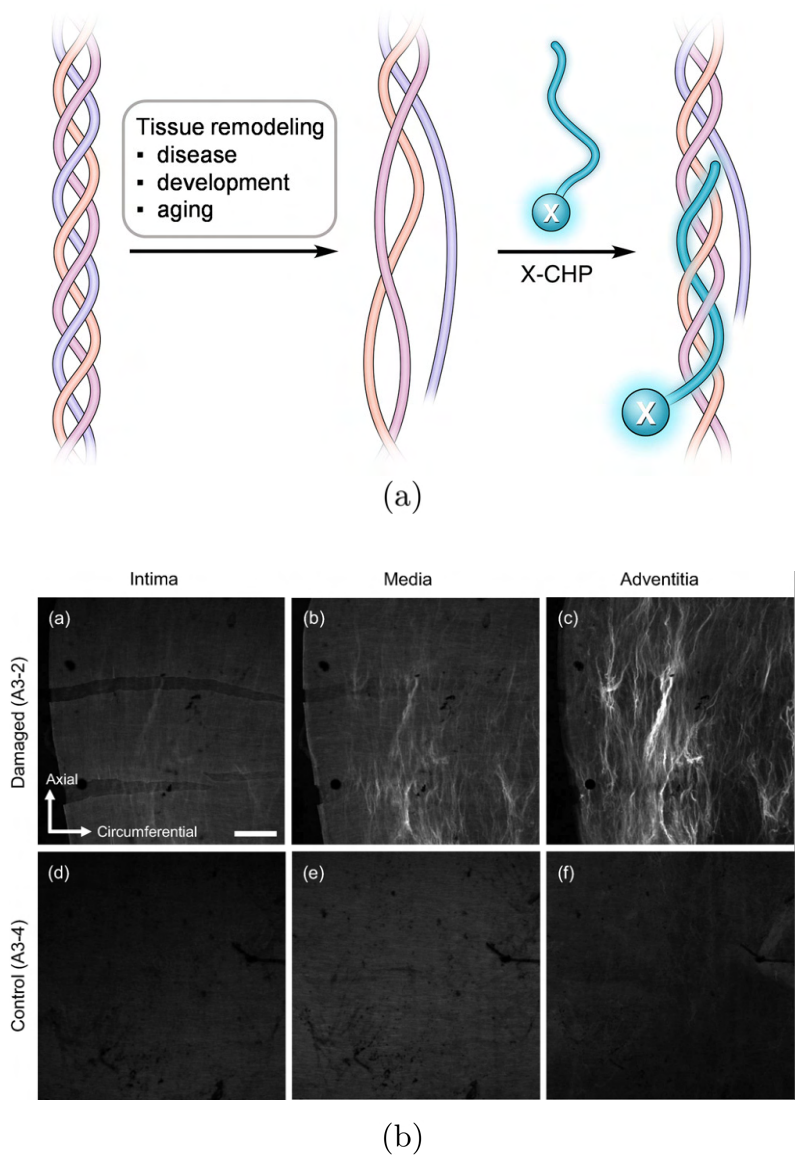
Figure 4.1. (a) Schematic of the mechanism of CHP binding with denatured collagen (Figure 1 from ref. [242]). (b) CHP marking damaged over-stretched middle cerebral arteries (top) and control samples (bottom) from sheep (Figure 4 from ref. [96]).

4.2   Materials and methods

4.2.1   Study design

The damage caused in the vessels by stenting was reproduced in vitro with indentation tests. These tests represent one of the repeating units or struts of the stent, as can be seen in Figure 4.2. The in vitro indentation consisted in the controlled displacement of a round-shaped nitinol wire (Fort Wayne Metals) towards the tissue, see Figure 4.2. In these tests, three different conditions were studied: i) the effect of indentation level, by displacing the indenter three different distances defined to assure some damage [68, 97, 246], ii) the effect of stent design or indentation pressure, by indenting the tissue the same amount with wires of two different diameters and iii) the effect of recoil, by allowing the tissue to recover after the indentation. Each of these conditions was tested in different vessels, with a minimum of three successful samples each. One same condition—the maximum level of indentation with the biggest wire and no recoil—was tested in the three different vessels to account for possible individual variations. The overview of the tests is displayed in Table 4.1.
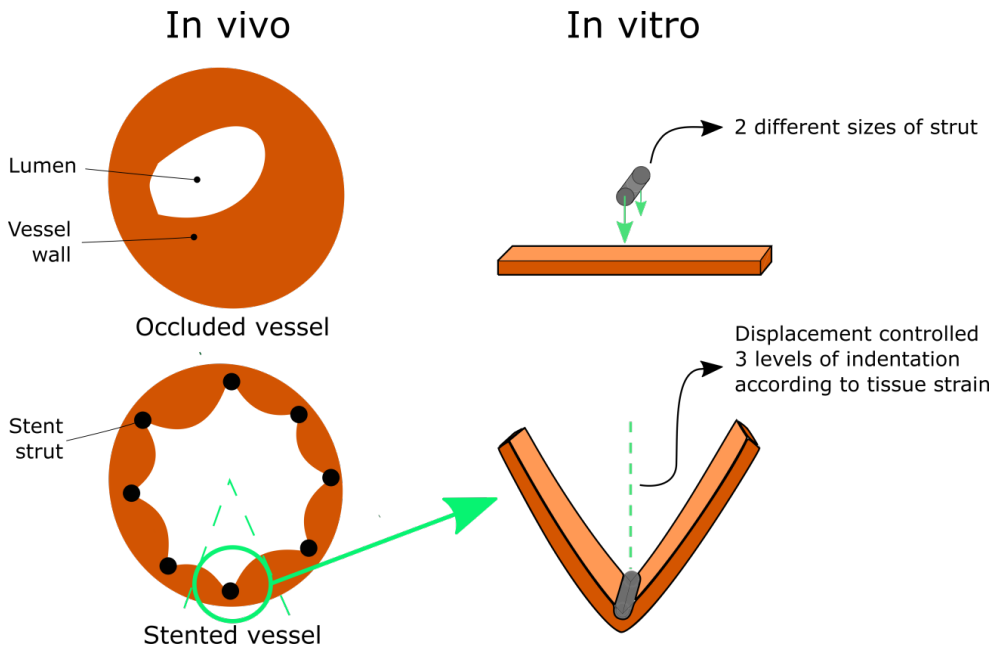
Figure 4.2.   Outline of the indentation that occurs in vivo when stenting (left) and its replication with the indentation tests in vitro (right). A repeating unit of the stent (circled in light green) is represented by the indentation tests in vitro, by displacing a certain distance an indenter towards the tissue, with the intimal side on top.

Table 4.1. Testing conditions of each of the tested aortas. Aorta 1 was used to evaluate the effect of indentation level; aorta 2 the effect of stent design; and aorta 3 the effect of recoil.

	Indentation level (% of tissue strain)			*Strut diameter*		*Allow tissue relaxation*	
	40%	**80%**	**120%**	**203 μm**	**305 μm**	**Yes**	**No**
Aorta 1	**x (n=4)**	**x (n=3)**	**x (n=4)**		x		x
Aorta 2			x	**x (n=6)**	**x (n=5)**		x
Aorta 3			x		x	**x (n=6)**	**x (n=6)**

4.2.2 Design and fabrication of the indentation system

An indentation system was designed with SolidWorks based on a previous system [247] and 3D printed in polylactic acid (PLA). Briefly, the benchtop device consisted of a holder where the samples were gripped with the help of clamps and screws, and an indenter piece with three guides to place the nitinol wire, according to the three levels of indentation to test. The indenter piece, and subsequently the wire, was kept tightened and prevented from bending during the indentation with the aid of a supporting stainless steel jig that gave rigidity to the system, see Figure 4.3.

4.2.3 Experimental tests

4.2.3.1 Obtention and preprocessing of samples

3 porcine aortas were obtained from a local abattoir. The aortas were stored in tissue-freezing medium (TFM; RPMI-60 Media, 1.8 M DMSO and 0.1 M Sucrose) for proper preservation [248], placed in a Mr. Frosty supplier cryosystem (containing isopropyl alcohol; VWR) and cryopreserved at - 80°C. Before testing, the descending thoracic aortas were thawed and TFM was washed from the vessels with PBS. Rectangular samples in the circumferential direction were obtained, 4 mm wide and around 20 mm in length (10 mm for the distance between grips + 5 mm extra per side to grip the sample). Thickness of the samples was subsequently measured.

4.2.3.2 Indentation tests

Control samples in each vessel were separated (n=6 per vessel). For the samples to be tested (n=6 per condition, final number of successful tests shown in Table 4.1), three specimens were gripped in each indentation system, with the intimal side on top, mimicking the orientation of stenting in vivo. The wire was placed in the desired level and tightened, and the samples were indented at a controlled and slow pace to ensure
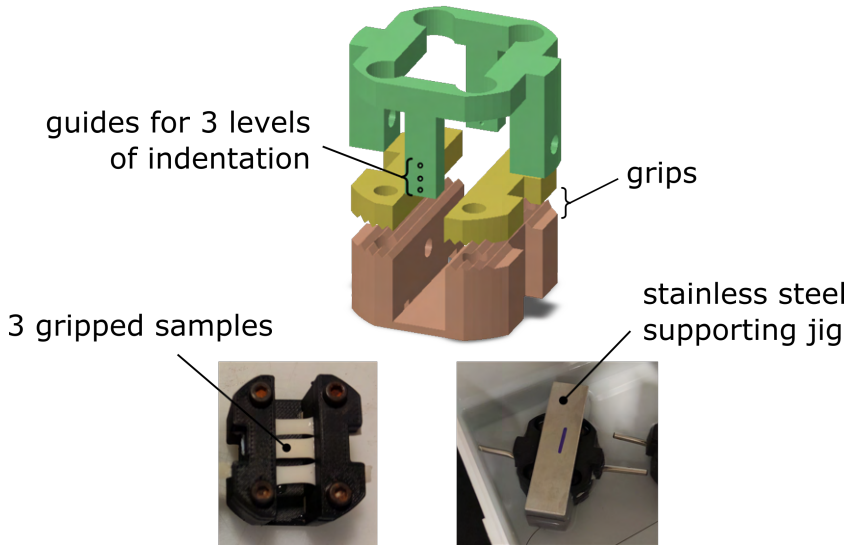
Figure 4.3. Design of the indentation system, set of three samples gripped to the base of the PLA device and indentation test with the support of a stainless steel jig, to prevent the bending of the wire.

a quasi-static indentation. Samples were left indented for 1h in 37°C PBS, and were subsequently fixed with 10% formalin (while maintaining the indentation) for 24h at room temperature. When studying the effect of recoil, the indenter was removed after 1h and the sample was left to recover for another hour before fixing. Samples were kept in 50% ethanol at 4°C after fixation and before histological processing.

4.2.3.3   Histological processing and CHP

Samples were cut after fixation to check two planes of interest with histology. In particular, the radial-circumferential (R-C) plane and the longitudinal-circumferential (L-C) plane were separated, see Figure 4.4. The R-C plane would give interesting information mostly in the indenter area throughout the thickness, whereas the L-C plane would show the change in collagen fibres on the same layer and their response in the area along the indenter. Next, control and tested samples were dehydrated, embedded and sliced at 7 μm, following standard histology protocols. Hematoxylin and eosin (H&E) and picrosirius red (PSR) stains were performed on the samples. H&E stain was chosen to observe the overall structure of the vessel, as it stains cell nuclei in dark purple and connective tissue (collagen and elastin) in pink. PSR stains collagen in red and allows for a careful observation of its orientation with polarised light microscopy (PLM), as it enhances the intrinsic birefringence of collagen. H&E

and PSR stained samples were observed in the brightfield microscope. Additionally, PSR stained samples were analysed with PLM, using two angles of incidence 45° apart, enough to cover all orientations, see Figure 4.5.
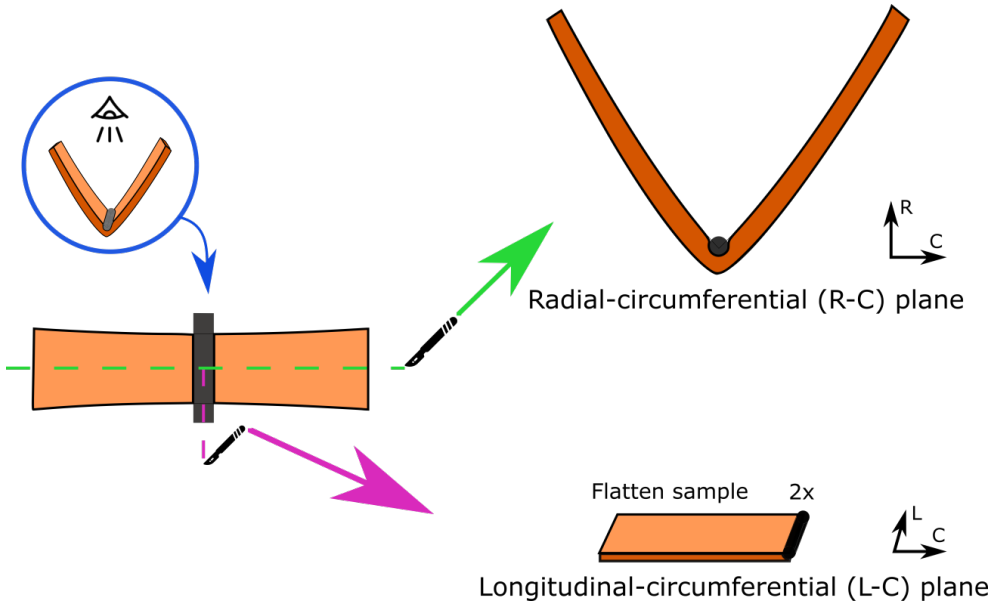
Figure 4.4. Planes of interest for histological studies in the tested samples. After fixing, the indenter was removed and the samples were cut in half following the green dashed line. One half was kept as is and was used to study the radial-circumferential (R-C) plane. The other half was again cut along the indentation site, following the pink dashed line. The two remaining pieces were carefully flattened and were used to study the longitudinal-circumferential (L-C) plane. Control samples were only cut once in half, following the light green line, obtaining one piece for each plane of interest.

CHP (3Helix) was also used in histological preparations of the tissue. In detail, 0.3 mg of CHP were dissolved in 5mL of PBS to obtain a 20 μM concentration of the peptide, vortexed and centrifuged to assure a homogeneous solution, following the suggested protocol. The solution was heated at 80°C for 5 minutes to denature the strands of CHP that had bound together, and subsequently brought to room temperature with the help of an ice bucket to avoid CHP from damaging the collagen in the tissue due to an overheating. The solution was immediately pipetted onto the histological preparations to ensure minimal deadtime. The slides with CHP were incubated overnight at 4°C, gently washed with PBS afterwards and coverslipped using Pertex as mounting solution. The washing step was critical as the tissue would easily detach from the glass slide after several hours of incubation and float away or fold in itself, losing the sample. CHP slides were then imaged with a fluorescence microscope, maintaining the same exposure time for all samples. It was determined
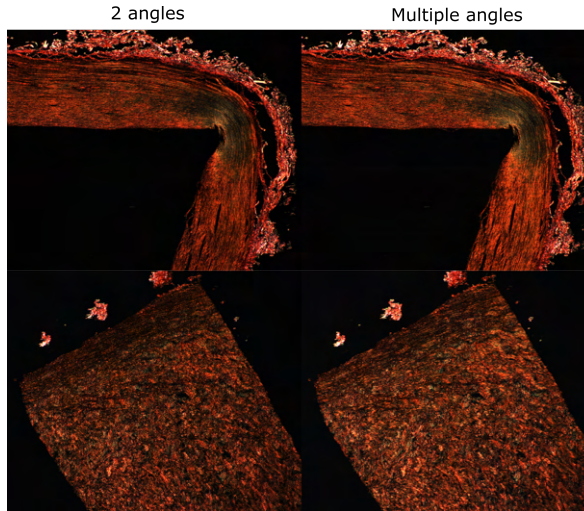
Figure 4.5. Images of PLM obtained with two angles of incidence $45°$ apart and multiple angles of incidence. The obtained images show the same brightness and no families of collagen fibres are missing in the two-angle image, therefore the two-angle approach is enough to obtain all the information from the PLM images.

that only one slice per condition was sufficient to observe damage with CHP, as the brightness of the images was observed to not vary throughout the thickness of the samples, see Figure 4.6.

4.2.3.4 Quantification of CHP

CHP images of the tissue were collected focusing on three areas of interest: the area right below the indenter or **strut area**, the area right next to the indenter or **mid area** and the area away from the indenter where the tissue has been homogeneously over-stretched or **stretch area** (see outline of the areas in Figure 4.9.a). A qualitative analysis was performed in these images to locate the highly affected areas, mostly by comparison within other areas in the same sample. Moreover, a quantification methodology was developed and performed to evaluate collagen damage avoiding subjective measurements, following the steps proposed by Converse et al. [96]. The quantification was performed in the R-C plane images. The quantification process consisted in averaging the brightness of all the control samples and defining that averaged value as a non-damaged brightness level. To evaluate the images of the tested samples, tissue was considered damaged when a pixel value was 1.75 times the non-damage brightness level. This factor was obtained as the smallest factor with which control images showed no damage ($<1\%$ damaged pixels). Quantification areas were defined and measured homogeneously across all samples. For the **strut area**, a square of 185 μm of side right below the indenter was evaluated; for the **mid area**, the
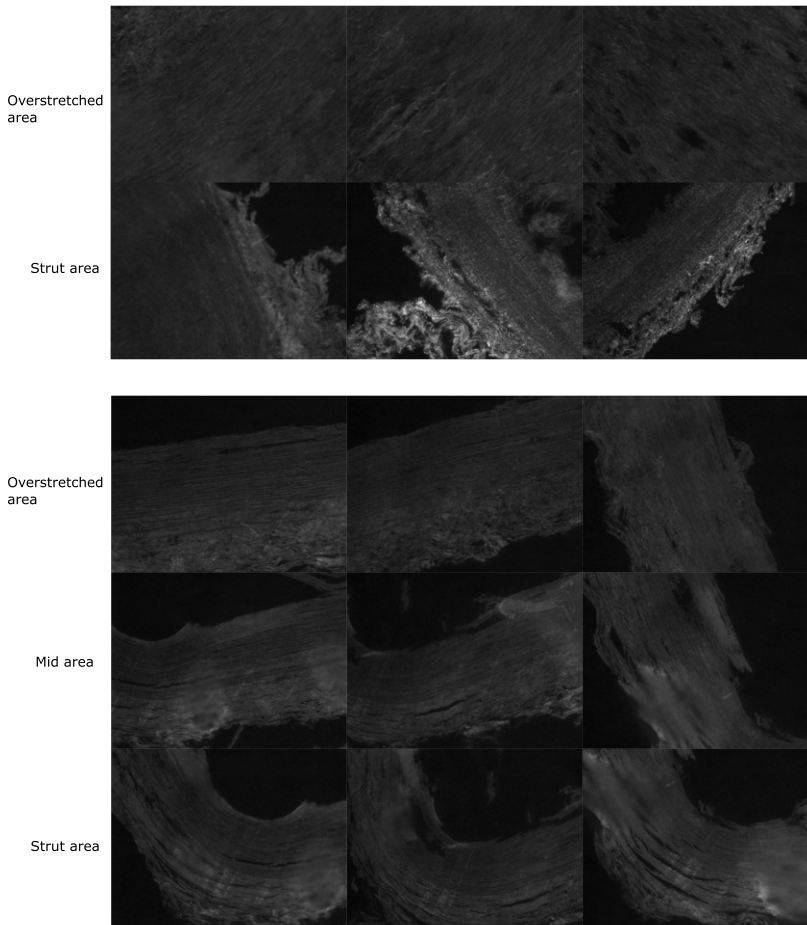
Figure 4.6. CHP images of the same samples throughout the thickness of the tissue (columns), in the L-C plane (top) and the R-C plane (bottom) and in different areas of the tissue (rows). The levels of brightness are constant, therefore one slice per sample is enough to observe collagen damage detected by CHP.

last portion of tissue in direct contact with the indenter was identified and a rectangle of 185 x 370 μm was placed from that point and away from the indenter, with the short side placed through the thickness; for the **stretch area**, a square of 325 μm of side was centrally placed in the over-stretched sample. The percentage of damage was finally quantified as the number of pixels in those regions with brightness over the established threshold in relation to the total number of pixels in those regions. In all cases, only evident artefacts such as folds or clear overstains were avoided when selecting the areas to quantify.

4.2.4   Computational model

An FE model of the experimental tests was developed in Abaqus/Standard v6.14 to assess the mechanical stimuli present in the samples during the experiments. The test was simulated as plane strain with one-element thickness. The displacement of the indenter was applied as a boundary condition and the gripped ends of the sample were fixed, as in the in vitro indentation. The three layers of the vessel were included and the anisotropic hyperelastic material model used was the GOH model [127], see Section 2.5.1. The preferred fibre directions were included manually in the input files. The material parameters of each layer were obtained from literature [34] and are shown in Table 4.2. Full incompressibility was assumed and the model was meshed with hybrid eight-node linear bricks (C3D8H).

Table 4.2. Parameters of the GOH material model used, differentiating per layer. θ is the preferred angle of orientation of the fibres with respect to the longitudinal direction of the vessel. The distribution of thickness of the different layers is also included [34].

Layer	% thickness	μ (kPa)	k_1 (kPa)	k_2 (-)	θ (º)	κ (-)
Intima	18	10	168	2.609	54.0	0.188
Media	49	15	85	1.376	72.3	0.156
Adventitia	33	5	128	4.285	66.1	0.181

4.3   Results

4.3.1   H&E and PSR – Collagen reorientation

Figure 4.7 shows the representative images of the samples stained with H&E and PSR for all tested conditions and the control, for both the R-C plane (a) and the L-C plane (b). PSR stained images are shown in brightfield on the left and PLM on the right, allowing a better observation of collagen fibres and their orientation. From these images, the orientation was analysed with OrientationJ [249], a plugin for the open access software Fiji [225]. From this analysis, a colour map in HSB (hue-saturation-brightness) mode was obtained, where the different orientations are displayed in different colours. The data regarding the angles of orientation were collected and represented in a histogram, shown on the right. An angle of 0° indicates the horizontal direction of the images. Regarding the R-C plane, Figure 4.7.a, the samples that were fixed while indented are quite self-explanatory. In their histograms, the angles shown represent the orientation of the sample due to the indentation, meaning that most fibres are aligned in the circumferential direction (the direction along the sample). Conversely, the indented sample allowed to recover (bottom) appears more similar to the control sample (top). In the histogram, in both control and relaxed samples, the main orientation is 0° or the circumferential direction of the

vessel. It is interesting to note how angles other than 0° are less frequent in the relaxed sample, implying fibres were recruited during the indentation and did not recover their original direction during relaxation. Regarding the L-C plane, Figure 4.7.b, a change in orientation in the area near the indenter (right side of the images) can be observed in the images and the histogram of all the tested samples. The fibers, which originally ran predominantly in the circumferential direction (0°), as can be seen in the control sample and in the area away from the indenter, were observed to reorient themselves towards the indenter. As they approached the indentation site, their alignment shifted to angles closer to 90°.

The realignment of fibres in the direction of the indenter in the L-C plane is further displayed in Figure 4.8. The main direction of fibres with respect to the circumferential (horizontal) direction is included in the area near the indenter (250 μm from the end, on the right) and in an area away from the strut (1.5 mm from the same end, on the left), as well as the coherence of this direction. This evaluation shows a consistent reorientation of the collagen fibres near the strut towards the longitudinal direction (90°), or the direction of the indenter, with angles that range from around
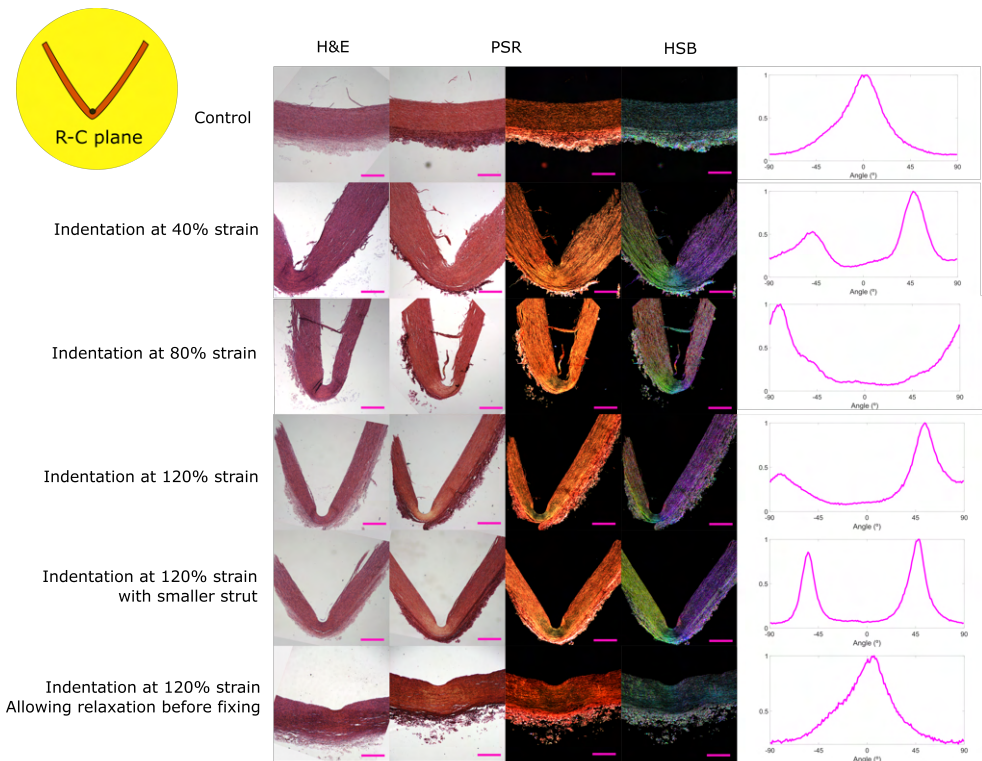
(a)
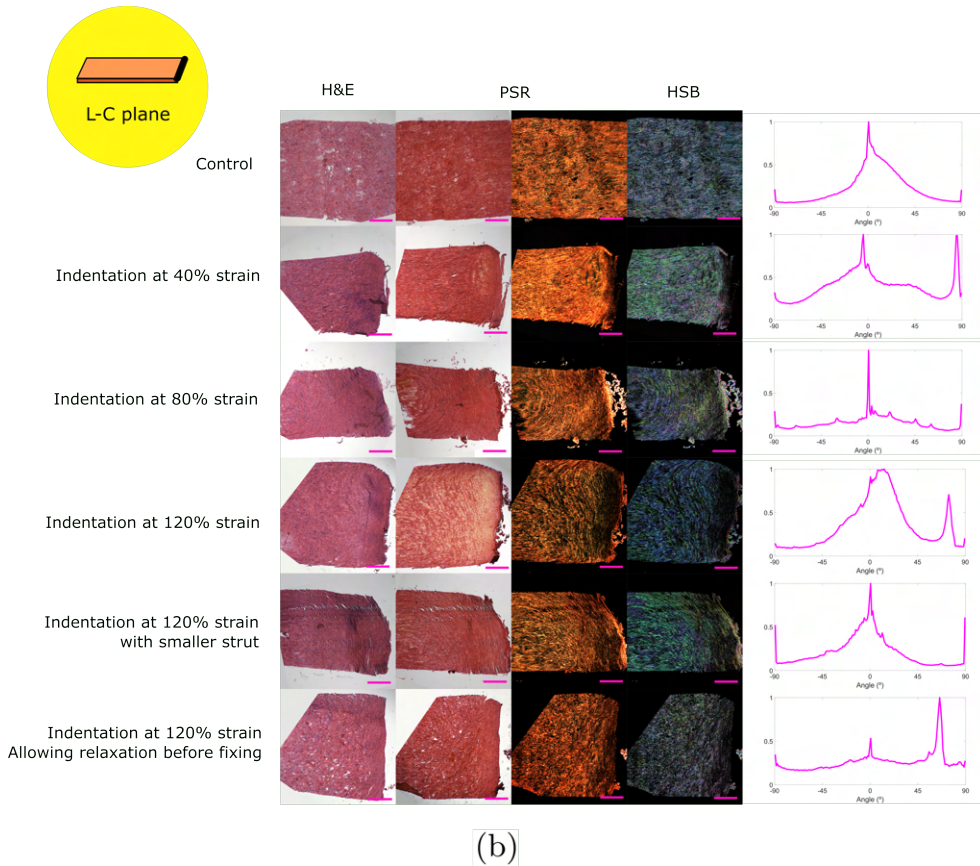
Figure 4.7. Representative images of control and tested samples stained with H&E and PSR, in the R-C plane (a) and in L-C plane (b), showing the indentation site on the right. PSR images are shown in brightfield (second column) and in PLM (third column). From these polarised light images, the study of orientation was carried out with OrientationJ (ImageJ), and a colour map representing the different orientations in different colours is shown in the fourth column. On the right, the histogram with the angles of orientation of the images is displayed. Images were acquired at 4x and the scale bar is 500 μm.

39° to over 89°; as opposed to the original orientation of the fibres (angles closer to 0° or the circumferential direction) observed away from the indenter and in the control samples, which range from a little over 0° to around 15°. In between these areas, there is a transition area in which the fibres are progressively changing its orientation towards the indenter direction. The coherence of alignment is higher in the areas away from the indenter.
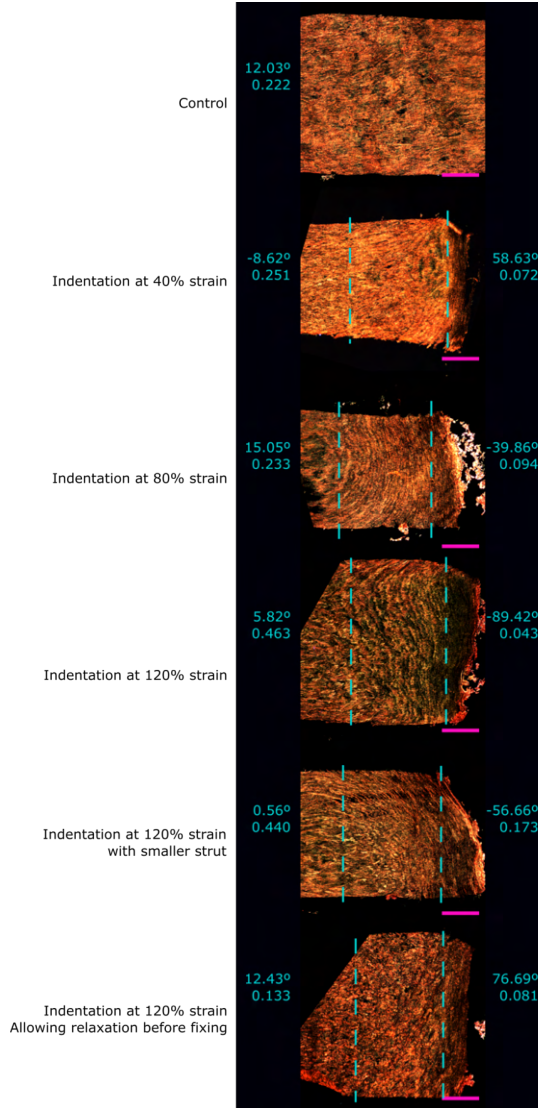
Figure 4.8. Measurements in the L-C plane of the preferred fibre direction and coherence of this orientation (the amount of fibres that are actually aligned in that direction, a ratio that ranges from 0 to 1, where 1 represents full alignment). The area near the indenter was measured up to 250 μm from the indented end, and the information is displayed on the right. In addition, an area away from the indenter, in particular 1.5 mm away from the indented end, was also evaluated and is displayed on the left. The main orientation angle and coherence of the control sample was evaluated for the whole image. Scale bar: 500 μm.

4.3.2   CHP – Collagen damage

Figure 4.9 shows the representative images of the CHP treated samples of the indentation tests and control, in both planes, the R-C (a) and the L-C (b). Brightness in the images represents sites where CHP joined damaged strands of collagen.

(a)
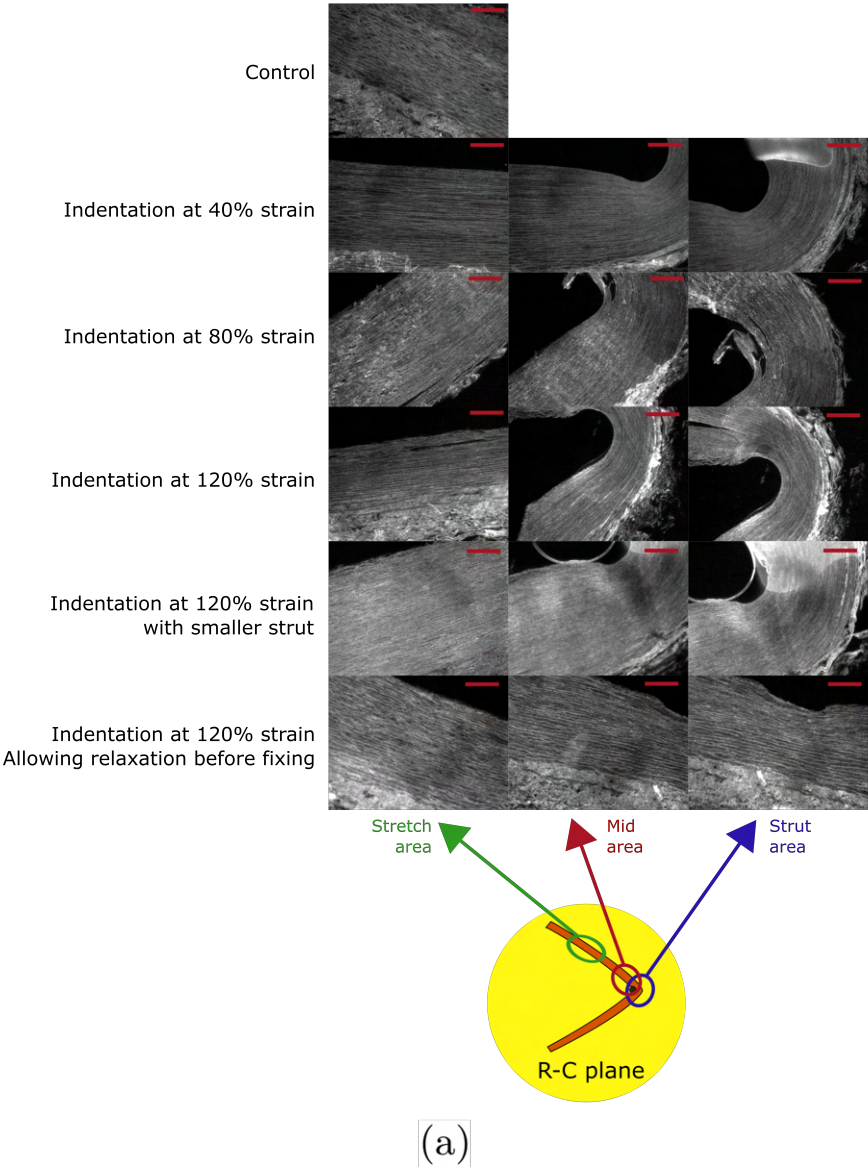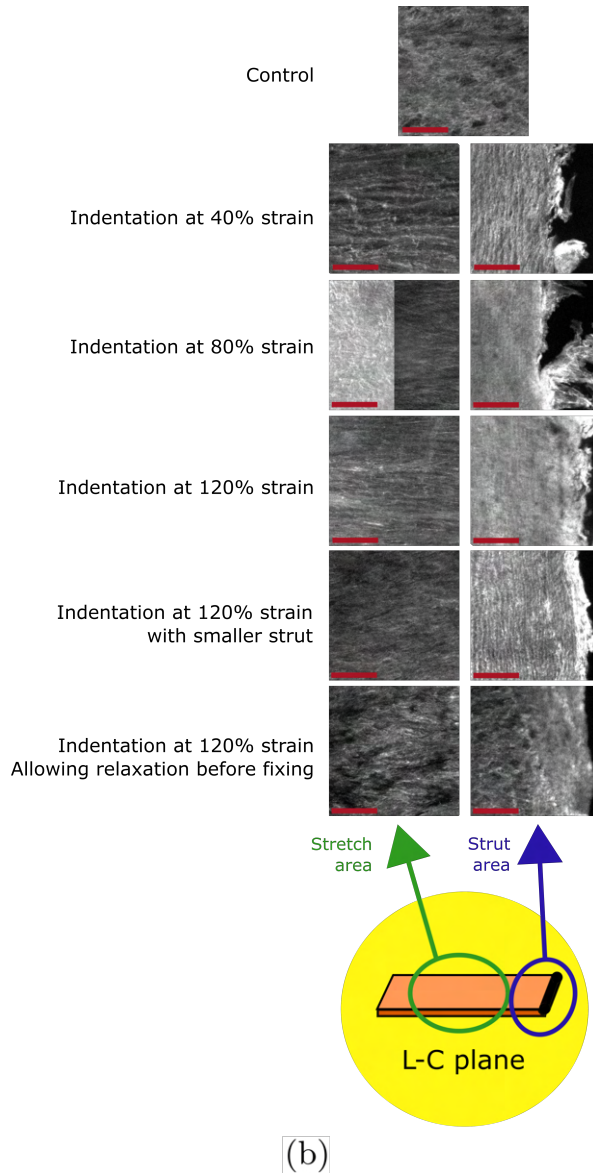
Figure 4.9. Representative fluorescence images of control and tested samples treated with CHP, in the R-C plane (a) and in L-C plane (b). The different areas are specified in the outline below the images. All images were obtained at the same exposure time and have been enhanced with the same parameters. Images were acquired at 10x and the scale bar is 250 μm.

In the R-C plane, Figure 4.9.a, the strut area, mid area and stretch area were imaged. Right under the indenter, in the strut area, the samples seem to be less damaged, whereas the most brightness appears in the mid area, next to the indenter. Moreover, the sample with the lowest indentation level shows the least brightness in general. In the sample allowed to recover after indentation, the sites of damage are not differentiated as clearly, as the brightness throughout the sample is quite homogeneous. In the L-C plane, Figure 4.9.b, the difficulty to flatten the samples and get clean slices for histology led to fewer images and of only two areas, the strut area and the stretch area. The layer analysed is mostly the inner media, but due to the difficulty in handling these samples, control in depth and different layers could not be performed. In the sample of indentation at 80% strain, only two images were obtained from the stretch area, therefore one could not be assumed as representative for the condition and both images are shown. In this plane, the strut area is consistently brighter and thus more damaged that the stretch area. In the stretch area, over-stretched and damaged fibres of collagen can be observed. All images have been brightness and contrast enhanced the same amount for displaying purposes. The subsequent quantification was performed on the raw images.

Notably high variability within samples was found, and the trends discussed above were observed more dramatically in some images of tested samples that could not be labelled as representative. Figure 4.10 shows some of these cases in which damage in certain sites is easier to differentiate. In particular, the R-C plane image shows that the region directly below the indenter appears to be less damaged or darker compared to other parts of the tissue. In contrast, the surrounding area is brighter, indicating notable collagen damage, which is more pronounced in the inner layers of the vessel. In the L-C plane, the damaged fibres of collagen can be clearly seen in the stretch area of the tissue, whereas the strut area is distinctly brighter and the fibres of collagen can be clearly seen in alignment with the indenter direction.

Table 4.3 shows the results of the damage quantification in the tested images. Damage percentage below 1% is considered non-damaged tissue, as per the definition of the methodology (Section 4.2.3.4). This quantification supports the qualitative observation that the mid area suffers in general more collagen damage than the strut area and sometimes the stretch area. Moreover, the quantification gives further insight in the apparent recovery of certain amount of damage when the tissue is left to relax after the indentation. Furthermore, the smallest level of indentation caused no damage in the stretch area of the tissue, suggesting the existence of a threshold of strain from which the collagen in the tissue starts to damage. The results were verified to confirm that the high variability was caused by variations in the images and not due to any inconsistency in the methodology.
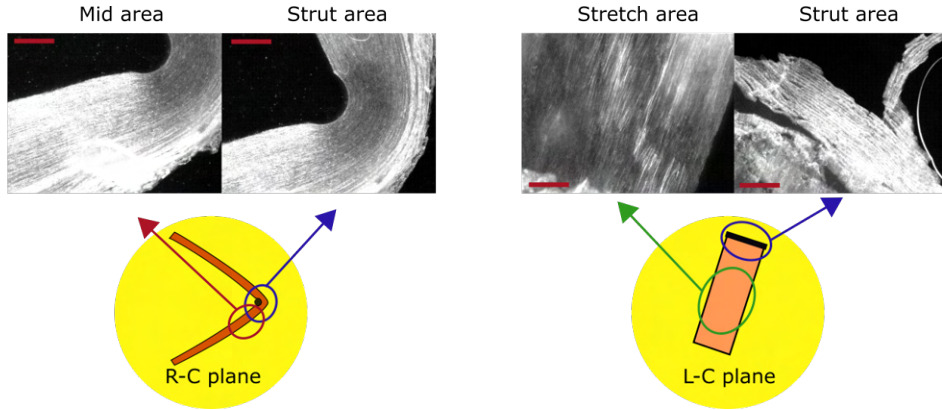
Figure 4.10. Fluorescence images of tested samples treated with CHP in both planes. All images come from samples indented at 120% strain level. In the L-C plane, the orientation of the sample in the images is the one shown in the outline below them. Images were obtained at the same exposure time and have been enhanced with the same parameters. Images were acquired at 10x and the scale bar is 250 μm.

Table 4.3. Results of the damage quantification in the tested images treated with CHP, in the R-C plane and including the three areas of interest. Mean and standard deviation of the damage quantification of all images is displayed.

	Strut area	*Mid area*	*Stretch area*
Indentation at 40% strain	$1.28 \pm 1.61\%$	$9.89 \pm 23.35\%$	$0.04 \pm 0.07\%$
Indentation at 80% strain	$23.98 \pm 32.44\%$	$20.87 \pm 40.30\%$	$25.57 \pm 41.90\%$
Indentation at 120% strain	$4.70 \pm 17.00\%$	$4.88 \pm 9.78\%$	$9.93 \pm 19.15\%$
Indentation at 120% strain with smaller strut	$5.01 \pm 7.83\%$	$23.34 \pm 38.57\%$	$11.13 \pm 23.28\%$
Indentation at 120% strain allowing relaxation before fixing	$5.09 \pm 11.12\%$	$1.35 \pm 3.04\%$	$0.21 \pm 0.25\%$

4.3.3 Numerical estimation of the mechanical stimuli in the indentation tests

The mechanical stimuli that the tissue is subjected to during the indentation tests are shown in Figure 4.11. In particular, maximum principal stress (Figure 4.11.a) and strain (Figure 4.11.b) values are shown for the case of highest indentation level (120% of tissue strain). Stress levels shown in the entire sample highlight the load that the adventitia bears, whereas the values of strain shown in a close-up view of the indenter show the higher levels of strain that the tissue is subjected to in the mid area.

(a)

(b)
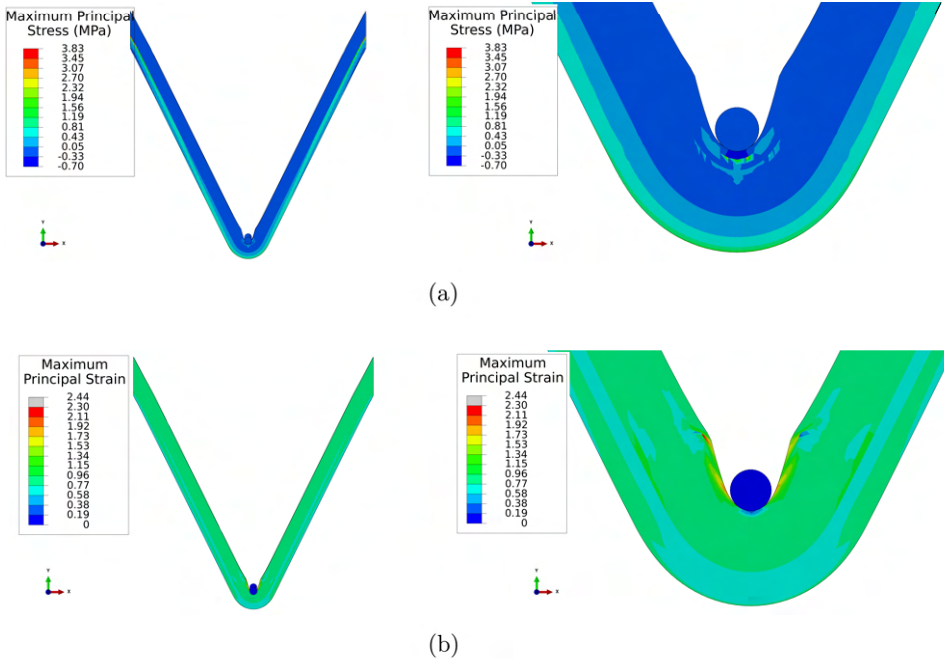
Figure 4.11. Plots of maximum principal stress (a) and strain (b) in the sample indented at 120% strain of the tissue.

4.4   Discussion

This study aimed to be an assessment of the validity of CHP to detect the type of damage that stents cause in blood vessels. With the results presented, the viability and potential of these peptides for this purpose has been shown. CHP fluorescence is higher in specific areas of the tissue subjected to indentation, supporting its specificity in the detection of damaged tissue in this type of injury.

The most damaged area during an indentation was observed to be the section right next to the indenter (see Table 4.3, Figure 4.9.a and Figure 4.10), which is an area where higher levels of strain are localised by comparison to the results obtained in the computational model (Figure 4.11). This points to strain as the most significant mechanical marker to correlate with tissue damage and restenosis-prone sites, in addition to the highly explored stresses [92, 231, 232, 237, 250]. In contrast, the compressed area right below the indenter showed qualitatively less collagen damage. However, this less aggressive damage due to compression seemed not to be reversible (Table 4.3). The sites that show notable damage correlate well with the areas which preferentially develop in-stent restenosis, as remodelled tissue that grows over the stent struts is postulated to come from areas that surround them and not from below [81, 237, 250].

Regarding the impact of the conditions examined in this study, in terms of the different levels of indentation, the results suggest that there is a threshold in indentation depth from which the collagen in the tissue starts to be injured, as the lowest level of indentation here tested showed little to no damage (see Table 4.3). The number of tests and levels of indentation, however, has not been enough in this study to determine this threshold. In terms of strut size, no clear difference was found, possibly due to the mechanical stimuli in the tissue being similar in both cases. Zahedmanesh and Lally [94] also observed in their computational studies that no differences in long-term stresses were found when the same stent with two different thicknesses were used to achieve the same final vessel diameter. In terms of recoil, collagen damage was found to be somewhat reversible (Table 4.3). This supports the assumption that the initial over-expansion of the stent in a vessel would not be the most critical stage for in-stent restenosis, but the final diameter to which the vessel remains expanded. This premise agrees with the clinical observation that for the same stent design but with different strut sizes and, thus, different recoil and final diameter, stents with thinner struts and more recoil cause less restenosis [94, 251].

The reorientation of collagen fibres with the indentation was also an interesting output of this study. Collagen fibres aligned along the length of the indenter at all levels of indentation, and this reorientation was also found to be permanent to some extent (Figure 4.8). In particular, the samples with the highest level of indentation visually presented the biggest area of reoriented fibres along the indenter, again showing the correlation between indentation depth and tissue response. Supporting these results, Ghazanfari et al. [252] studied collagen orientation after stenting pulmonary arteries and observed that collagen aligned with the stent struts in the areas right below the stents and appeared disorganised between struts. The fibres aligned with the indenter would not bear the indentation load, causing the tissue to soften. Geith et al. [253] also performed some indentation tests on porcine coronary arteries and they observed changes in collagen and tissue relaxation after the indentation.

Significant variability was found in the results of damage in the tests. The use of CHP in histology samples inherently brings some variability due to the challenges in applying the exact same amount of peptide over the same area of each sample. Consequently, some samples were clearly over or under-stained. This effect could be minimised by submerging full samples in a solution of these peptides instead of covering histological samples [96]. With this methodology, the difficulty of handling the samples that happened mostly in the L-C plane would also be reduced. Finally, as the vessels were obtained from an abattoir. Tissue could not be tracked prior to harvesting and diet or environment could have altered the tissues from one animal to another.

Collagen damage after stenting is yet to be linked to the development of in-stent restenosis. Other mechanical factors, such as penetration injury or the rupture of internal layers of the vessel, have been correlated with the proliferation of neo-intimal tissue [68]. Although this aggressive stenting injury is a strong stimulus for this proliferation, over-stretched tissue with no penetration injury also showed growth of neo-intimal tissue [68]. This supports the possibility that other types of tissue

constituent damage, such as collagen damage, could also trigger the development of in-stent restenosis.

Despite these limitations, this work serves as baseline for damage quantification after stenting. CHP has shown potential in the detection and quantification of damage due to indentation. In order to verify that this translates to stent induced damage, the authors consider that the next step would include the in vitro over-expansion of a stent in an artery, to assess the pattern of CHP with respect to stent placement. With favourable results, it would be interesting to move to animal models to link collagen damage with actual sites of in-stent restenosis. From there, the final step would be to obtain a curve that relates mechanical stimuli with potential to develop in-stent restenosis. Achieving this would support the design of patient-specific stents that would prevent or drastically reduce the development of in-stent restenosis.

4.5   Key findings

- We have proved that CHP can detect the type of damage caused by an indentation in an artery. This is the first step to understand the damage mechanisms in stenting. The final outcome of this line of research would be to link damaged sites due to indentation with the development of in-stent restenosis.

- In our indentation tests, we observed that strain played a greater role than stress in the generation of collagen damage. Specifically, the region immediately adjacent to the indenter consistently exhibited greater damage compared to other areas within the indented tissue. Our FE models indicated that these sites experienced localised higher strains.

- The fibres of collagen of the vessel reorient in the direction of the indenter, and they maintain their reorientation once the indentation is removed.

- Collagen damage due to indentation is reversible. This finding supports the hypothesis that the final opening diameter once the stent is stable is more critical in injury development compared to the momentary higher diameter to which the stent is initially over-expanded.

CHAPTER 5

Conclusions

Following the style of the entire document, the conclusions and future lines will be detailed according to the three pathologies studied. The conclusions here presented are general, since more specific findings were detailed at the end of every chapter.

5.1   General conclusions

Chapter 2: Damage caused by dissection

- Overall, we have defined a methodology that includes experimental tests and their reproduction with finite element models to obtain the dissection properties of vessels. This methodology can be applied to all types of vessels and all directions and interfaces within them. It is necessary to ensure homogeneous testing conditions so that a general cohesive zone model can replicate multiple scenarios.

- A series of computational models have been developed to reproduce the mechanism of dissection in the various layers of the aorta. These models can be used to computationally investigate dissection phenomena in clinically relevant problems.

- We could observe that the dissection behaviour of porcine aorta varies throughout different locations. Therefore, the dissection properties of vessels appear to be reliant on the microstructure of the vessel, as these sites exhibit variations in their microstructure.

- The intima-media interface was generally found to be the easier to dissect of the three studied interfaces. With the help of computational models, we could observe that this likely comes from the inherent microstructure of the interface and not from the different thicknesses of the layers.

- Our computational models suggest that the elastic properties of vessels do not affect the force needed to dissect them.

- Despite the fact that the porcine and human aorta exhibit comparable microstructure and mechanical behaviour, it is not feasible to extrapolate the results obtained in this study to human vessels due to the influence of age and

the potential existence of an intrinsic pathology in the dissection properties of the vessels.

- A more complex damage model including anisotropic cohesive behaviour or the viscosity of the cohesive contact would better reproduce the experimental results of the mixed-mode peel tests.

Chapter 3: Damage caused by haemodynamics

- We have been able to observe endothelial cell response to steady laminar flow in terms of elongation and alignment. Even when subjected to the lowest values of wall shear stress, endothelial cells showed a significant elongation and changes in their orientation, from random to preferentially aligned with the direction of flow, in the first hours of the experiment.

- We have developed an image analysis program that is able to extract cell contours from phase-contrast images of endothelial cells. This program can be further used in many applications that obtain this type of images from endothelial cells, by simply adjusting a few parameters in the code.

- A strain device was designed and tested as a way of applying strain stimuli coupled with flow. With a PDMS substrate, which is biocompatible and pliant, a two-channel device was computationally studied to be able to reproduce homogeneus strain stimuli in its channels. The computational model was validated with experimental testing and a digital image correlation system.

- No apparent difference in morphological changes was found between HUVECs and HCAECs, although their haemodynamic environment in vivo is completely different.

- Cell adhesion was found to be the most challenging part of the flow tests on endothelial cells. Although we performed an adhesion study to optimise this feature, in some experiments, after 16 hours of exposure to flow, the monolayer of endothelial cells became non-confluent. Despite this, some conclusions could still be drawn from cell response to flow during the first hours of the experiment.

Chapter 4: Damage caused by stent indentation

- We have developed indentation tests for arterial tissue that reproduce one repeating unit of the stent struts when it is expanded in vivo. From these experiments, we have been able to asses the validity of collagen hybridizing peptide as marker for the type of damage that stents cause in vessels.

- The level of indentation that the tissue is subjected to directly affects the generation of collagen damage in the tissue. In particular, we studied three levels of indentation, which were related to the levels of strain the tissue underwent

(40%-80%-120%), and little to no damage was found in the lowest level of indentation.

- The damage in collagen caused by indentation is somewhat reversible. This finding supports the hypothesis that the stimulus that causes this collagen damage in the vessel is not the initial over-expansion of the stent, but rather the final diameter of the stent after it is deployed.

- It seems that collagen damage is primarily induced by strain rather than stress in our indentation tests. This could be observed from the computational reproduction of the indentation tests. With these models, we could observe that the area right next to the indenter, which was usually the most damaged area in our tests, was subjected to higher local strains.

- Collagen fibres in indented tissue align with the indenter, and this realignment of fibres is maintained after the indentation is removed. These aligned fibres do not bear the indentation load, which overall results in the softening of the tissue.

5.2   Future lines of work

Chapter 2: Damage caused by dissection

- Reproduction of the mixed-mode peel test with a cohesive elements finite element model. The first trials have been performed already and, unlike in the cohesive surfaces models, the damage properties in the tangential directions affect the final results of the simulations. With these models, the normal dissection properties could be fitted with the T-peel test and validated with the mixed-mode peel test, by keeping them fixed and only calibrating the tangential properties.

- Perform histologies of the mixed-mode peel test to observe if some conclusions about the mode of the propagation of the tear can be obtained from the analysis of the dissected surfaces.

- With the dissection properties fitted in all the sets of experimental data, a neural network that predicts the dissection properties by inputting the experimental curve from a peel test could be developed. This tool would allow researchers that perform experimental peel tests to skip the step of developing cohesive zone models, which can be a complex and hindering task, and give them directly the dissection properties of vessels from their experimental results.

Chapter 3: Damage caused by haemodynamics

- Different flow stimuli could be applied to the monolayer of endothelial cells, like pulsatile flow or the addition of a perturbation in the flow to generate disrupted flow downstream, similar to the flow patterns when an atheroma plaque is starting to be developed in vivo.

- The study of the effect of physiological and pathological strain stimuli in the morphology of endothelial cells, initially uncoupled with the flow, to observe the isolated response of the monolayer, and subsequently coupled with flow, which would resemble the in vivo environment.

- Convolutional neural networks to automatically segment the phase-contrast images could be developed as a next improvement on the image analysis phase. Doing this segmentation with neural networks would allow to not include the apoptotic cells and other artefacts that could be distorting the results. A significant amount of images should be manually segmented to be used as training data of the neural networks.

Chapter 4: Damage caused by stent indentation

- In order to link collagen damage with stenting, an over-expansion of a stent in a vessel in vitro that assures tissue injury could be performed to observe and correlate collagen hybridizing peptide highlighted areas with stent placement.

- Provided that the previous experiment gave successful results, stent implantation in animal models and subsequent evaluation with collagen hybridizing peptide could help in the correlation of collagen damaged areas after stenting with areas prone to start developing in-stent restenosis, bringing research one step closer to designing patient-specific stents that drastically reduced the propensity to develop in-stent restenosis.

- Development of a computational model of the damage process calibrated with the results obtained in this experimental study. Such model would help in the understanding of the damage process that occurs in the vessel when it is indented.

5.3   Original contributions

5.3.1   Publications within the scope of this thesis

- Ríos-Ruiz, I., Martínez, M. A. & Peña, E. (2022). Is location a significant parameter in the layer dependent dissection properties of the aorta? *Biomech Model Mechanobiol* **21**, 1887–1901. doi: 10.1007/s10237-022- 01627-9

- Ríos-Ruiz, I., Cilla, M., Martínez, M. A. & Peña, E. (2021). Methodology to Calibrate the Dissection Properties of Aorta Layers from Two Sets of Experimental Measurements. *Mathematics* **9**(14), 1593. doi: 10.3390/math9141593

5.3.2   Publications out of the scope of this thesis

- Cabeza-Gil, I., Ríos-Ruiz, I. & Calvo, B. (2021). Experimental evaluation of the injection force exerted in intraocular lens delivery with syringe-type injectors. *J Mech Behav Biomed Mater* **124**, 104793. doi: 10.1016/j.jmbbm.2021.104793

- Cabeza-Gil, I., Ríos-Ruiz, I. & Calvo, B. (2020). Customised Selection of the Haptic Design in C-Loop Intraocular Lenses Based on Deep Learning. *Ann Biomed Eng* **48**, 2988–3002. doi: 10.1007/s10439-020-02636-4

5.3.3   Congress contributions

- **VIII Jornada de Jóvenes Investigadores del I3A**. Poster presentation entitled *Design of a microfluidic device to simulate the formation of the ateroma plaque*, 6 Jun 2019, University of Zaragoza (Spain).

- **25th Congress of the European Society of Biomechanics**. Oral communication entitled *In silico-in vitro study of flow parameters in permeability of coronary endothelial cells*, 7–10 Jul 2019, Technische Universität Wien (Austria).

- **IX Jornada de Jóvenes Investigadores del I3A.** Poster presentation entitled *Experimental Study of the Dissection Properties of Porcine Aorta*, 11 Dec 2020, University of Zaragoza (Spain).

- **26th Congress of the European Society of Biomechanics**. Oral communication entitled *Adding myocardial mechanics in a 3D fluid-structure interaction model of the left coronary bifurcation*, 11–14 Jul 2021, online at Politecnico Milano (Italy).

- **1st IACM Conference on Mechanistic Machine Learning and Digital Twins for Computational Science, Engineering & Technology.** Oral communication entitled *Deep learning approach to determine the biomechanics of intraocular lenses. One step closer to patient customization*, 26–29 Sep 2021, online at UC San Diego (USA).

- **X Jornada de Jóvenes Investigadores del I3A**. Poster presentation entitled *Adhesion Study of a Monolayer of Endothelial Cells*, 21 Oct 2021, University of Zaragoza (Spain).

- **X Reunión del Capítulo Español de la Sociedad Europea de Biomecánica**. Oral communication entitled *Modelos computacionales para la determinación de las propiedades de disección de la arteria aorta*, 25–26 Oct 2021, Universidad de Granada (Spain).

- **Second Colloquium of the Spanish Theoretical and Applied Mechanics Society**. Poster presentation entitled *Determination of aortic dissection properties with cohesive zone models*, 28–29 Mar 2022, Universidad de Sevilla (Spain).

- **27$^{\text{th}}$ Congress of the European Society of Biomechanics**. Oral communication entitled *Characterising dissection in aortic tissue: Effect of location and dissected layer*, 26–29 Jun 2022, University of Porto (Portugal).

- **11$^{\text{th}}$ European Solid Mechanics Conference**. Oral communication entitled *Computational models to determine dissection properties of the aorta*, 4–8 Jul 2022, NUI Galway (Ireland).

- **XI Reunión del Capítulo Español de la Sociedad Europea de Biomecánica**. Oral communication entitled *Estudio de disección en la aorta: Influencia de las capas y la localización*, 24–25 Oct 2022, University of Zaragoza (Spain).

CHAPTER **6**

Conclusiones

Siguiendo el estilo de todo el documento, se detallarán las conclusiones y líneas futuras según las tres patologías estudiadas. Las conclusiones aquí presentadas son generales, puesto que los hallazgos más concretos se detallaron al final de cada capítulo.

6.1   Conclusiones generales

Capítulo 2: Daño causado por disección

- En general, hemos definido una metodología que incluye ensayos experimentales y su reproducción con modelos de elementos finitos para obtener las propiedades de disección de los vasos. Esta metodología puede aplicarse a todo tipo de vasos y a todas sus direcciones e interfaces. Es necesario asegurar condiciones de ensayo homogéneas para que un modelo cohesivo general pueda replicar múltiples escenarios.

- Se han desarrollado una serie de modelos computacionales para reproducir el mecanismo de disección en las diversas capas de la aorta. Estos modelos pueden utilizarse para investigar computacionalmente los fenómenos de disección en problemas clínicamente relevantes.

- Pudimos observar que el comportamiento de la disección de la aorta porcina varía en función de la localización. Por lo tanto, parece que las propiedades de disección de los vasos dependen de la microestructura del vaso, ya que estas localizaciones muestran diferencias en su microestructura.

- La interfaz íntima-media fue generalmente la más fácil de diseccionar de las tres interfaces estudiadas. Con la ayuda de modelos computacionales, pudimos observar que esto probablemente se debe a la microestructura inherente de la interfaz y no a los diferentes espesores de las capas.

- Nuestros modelos computacionales sugieren que las propiedades elásticas de los vasos no afectan a la fuerza necesaria para diseccionarlos.

- A pesar de que la aorta porcina y humana presentan microestructura y comportamiento mecánico comparables, no es factible extrapolar los resultados obtenidos en este estudio a los vasos humanos debido a la influencia de la edad

y de la posible existencia de una patología en las propiedades de disección de los vasos.

- Un modelo de daño más complejo que incluya un comportamiento cohesivo anisótropo o la viscosidad del contacto cohesivo reproduciría mejor los resultados experimentales de las pruebas de delaminación en modo mixto.

Capítulo 3: Daño causado por hemodinámica

- Hemos podido observar la respuesta de las células endoteliales al flujo laminar constante, en términos de elongación y alineación. Incluso al ser sometidas a los valores más bajos de tensión cortante, las células endoteliales mostraron una elongación significativa y cambios en su orientación, pasando, en las primeras horas del experimento, de aleatoria a preferentemente alineada con la dirección del flujo.

- Hemos desarrollado un programa de análisis de imágenes que es capaz de extraer los contornos celulares a partir de imágenes de contraste de fase de células endoteliales. Este programa, con un simple ajuste de algunos parámetros en el código, se puede utilizar en muchas aplicaciones que obtengan este tipo de imágenes de células endoteliales.

- Se diseñó y probó un dispositivo de deformación para aplicar estímulos de deformación acoplados con flujo. Con un sustrato de PDMS, que es biocompatible y flexible, se estudió computacionalmente un dispositivo de dos canales para poder reproducir estímulos de deformación homogéneos en sus canales. El modelo computacional se validó con pruebas experimentales y un sistema de correlación de imágenes digitales.

- No se encontraron diferencias aparentes en los cambios morfológicos entre las células endoteliales HUVECs y HCAECs, aunque su entorno hemodinámico in vivo es completamente diferente.

- La adhesión celular resultó ser la parte más delicada de los ensayos de flujo en células endoteliales. Aunque realizamos un estudio de adhesión para optimizar esta característica, en algunos experimentos, después de 16 horas de exposición al flujo, la monocapa de células endoteliales perdió su integridad. A pesar de esto, se pudieron obtener algunas conclusiones de la respuesta celular al flujo durante las primeras horas del experimento.

Capítulo 4: Daño causado por la indentación de stents

- Hemos desarrollado ensayos de indentación en tejido arterial que reproducen la expansión de una varilla del stent in vivo. A partir de estos experimentos, hemos podido evaluar la validez del *collagen hybridizing peptide* como marcador del tipo de daño que los stents causan en los vasos sanguíneos.

- El nivel de indentación al que se somete el tejido afecta directamente a la generación de daño en el colágeno del tejido. En particular, estudiamos tres niveles de indentación, relacionados con los niveles de deformación que experimentó el tejido (40% - 80% - 120%), y observamos poco o ningún daño en el nivel más bajo de indentación.

- El daño en el colágeno causado por la indentación es reversible. Este hallazgo apoya la hipótesis de que el estímulo que causa este daño en el colágeno del vaso es el diámetro final del stent después de su colocación y no la sobredilatación inicial del stent.

- En nuestras pruebas de indentación, parece que el daño en el colágeno es principalmente inducido por la deformación en lugar de por la tensión. Esto se pudo observar a partir de la reproducción computacional de los ensayos de indentación. Con estos modelos, pudimos observar que el área justo al lado del indentador, que suele ser la zona más dañada en nuestras pruebas, estaba sometida a mayores deformaciones locales.

- Las fibras de colágeno en el tejido indentado se alinean con el indentador, y esta realineación de fibras se mantiene después de retirar la indentación. Estas fibras alineadas no soportan la carga de indentación, lo que en general provoca el ablandamiento del tejido.

6.2 Líneas futuras

Capítulo 2: Daño causado por disección

- Reproducir el ensayo de delaminación en modo mixto mediante un modelo de elementos finitos con elementos cohesivos. Las primeras pruebas ya se han realizado y, a diferencia de los modelos de superficies cohesivas, las propiedades de daño en las direcciones tangenciales afectan a los resultados finales de las simulaciones. Con estos modelos, se podrían ajustar las propiedades de disección normales con el ensayo en T y validarlas con el ensayo en modo mixto, manteniendo fijas las propiedades normales en este último caso y solo calibrando las tangenciales.

- Realizar histologías de los ensayos de delaminación en modo mixto para observar si se pueden obtener algunas conclusiones sobre el modo de propagación de la disección a partir del análisis de las superficies separadas.

- Con las propiedades de disección ajustadas en todos los conjuntos de datos experimentales, se podría desarrollar una red neuronal que predijera las propiedades de disección, dando como entrada la curva experimental de ensayo de delaminación. Esta herramienta permitiría a los investigadores que realizan estos ensayos experimentales omitir el paso de desarrollar modelos computacionales,

que pueden ser complejos y limitantes, y darles directamente las propiedades
de disección de los vasos a partir de sus resultados experimentales.

Capítulo 3: Daño causado por la hemodinámica

- Se podrían aplicar diferentes estímulos de flujo a la monocapa de células endoteliales, como flujo pulsátil o la adición de una perturbación en el flujo para generar un flujo turbulento aguas abajo, similar a los patrones de flujo que se dan en una placa de ateroma in vivo.

- Realizar el estudio del efecto de los estímulos de deformación fisiológicos y patológicos en la morfología de las células endoteliales, inicialmente desacoplados del flujo, para observar la respuesta aislada de la monocapa, y posteriormente acoplados con el flujo, lo que se asemejaría al entorno in vivo.

- Se podrían desarrollar redes neuronales convolucionales para segmentar automáticamente las imágenes de contraste de fase. Hacer esta segmentación con redes neuronales permitiría no incluir las células apoptóticas y otros artefactos que podrían distorsionar los resultados. Se deberían segmentar manualmente una cantidad significativa de imágenes para usarlas como datos de entrenamiento de las redes neuronales.

Capítulo 4: Daño causado por la indentación del stent

- Realizar la sobreexpansión de un stent en una arteria in vitro para asegurar el daño en el tejido y observar y correlacionar las áreas marcadas por el *collagen hybridizing peptide* con la localización del stent, para relacionar el daño del colágeno con el uso de stents.

- En caso de que el experimento anterior fuera exitoso, se podría realizar la implantación de stents en animales y posteriormente evaluar el daño del colágeno con el *collagen hybridizing peptide*, lo que ayudaría a correlacionar las áreas de daño tras la implantación del stent con áreas propensas a desarrollar restenosis intrastent, acercando la investigación a la posibilidad de diseñar stents personalizados que reduzcan drásticamente la propensión a desarrollar restenosis intrastent.

- Desarrollar un modelo computacional del proceso de daño calibrado con los resultados obtenidos en este estudio experimental. Este modelo ayudaría a comprender el proceso de daño que ocurre en la arteria cuando se indenta con un stent.

Appendices

A brief introduction to continuum mechanics

This appendix presents brief information about the fundamental kinematics used in this thesis. There are a significant amount of numerical models in literature defined to reproduce the nonlinear mechanical behavior of the arteries. In this thesis, we have mainly used the Gasser-Ogden-Holzapfel (GOH) model [140]. This model defines a new strain energy function (SEF) within the general framework of hyperelasticity and is grounded in the fundamental principles of continuum mechanics.

A.1 Deformation gradient tensor

Let Ω be the body of interest, with initial and deformed configurations at time t denoted by Ω_0 and Ω_t, respectively, as shown in Figure A.1. The motion of a point $\mathbf{P} \in \Omega$ is given by a trajectory denoted by φ. Thus, point $\mathbf{P}$ in the reference position is transformed into $\mathbf{p}$ due to φ. Then, φ transforms the reference position of a material point $\mathbf{X} \in \Omega_0$ to a spatial position $\mathbf{x} \in \Omega_t$, where $\mathbf{x} = \varphi(\mathbf{X}, t)$. Likewise, it is possible to go back from the spatial position of $\mathbf{p}$ to $\mathbf{P}$ using the inverse of φ, denoted by $\varphi^{-1}(\mathbf{x}, t)$, since it is assumed that φ has a unique inverse function and continuous derivative with respect to time and space.

Now, assuming that $\mathbf{P}$ and $\mathbf{Q} \in \Omega_0$ (material configuration) are very close points with an initial infinitesimal length of $dL = ||\mathbf{Q} - \mathbf{P}||$, and form the unit direction $\mathbf{a}_0 = \frac{\overline{PQ}}{||\mathbf{Q} - \mathbf{P}||}$, the relative vector of $\mathbf{Q}$ with respect to $\mathbf{P}$ is calculated as $\mathrm{d}\mathbf{X} = dL \cdot \mathbf{a}_0$. Having a motion φ, the motion $\mathrm{d}\mathbf{x}$ is obtained with their corresponding $\mathbf{p}$ and $\mathbf{q} \in \Omega_t$ (spatial configuration), following:

$$d\mathbf{x} = \mathbf{F} \cdot d\mathbf{X}, \tag{A.1}$$

where $\mathbf{F}$ is the deformation gradient tensor which defines the motion map φ and is defined as

$$\mathbf{F}(\mathbf{X}, t) = \frac{\partial \varphi(\mathbf{X}, t)}{\partial \mathbf{X}} = \frac{\partial \mathbf{x}}{\partial \mathbf{X}}. \tag{A.2}$$
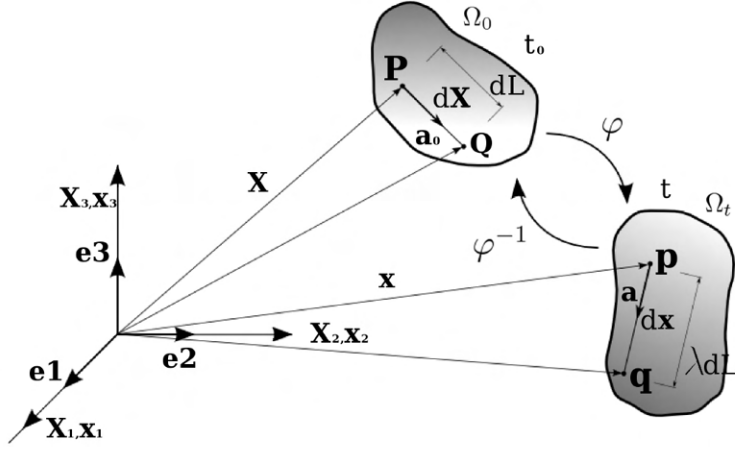
Figure A.1. Schematic of the deformation of a solid that includes the representation of a length element from the material configuration (Ω_0) to the spatial configuration (Ω_t).

Similarly, the vector $\mathbf{a}$ in the spatial configuration that comes from the vector $\mathbf{a}_0$ in the material configuration at time t is defined as the push-forward of $\mathbf{a}_0$:

$$\mathbf{a}(\mathbf{X}, t) = \mathbf{F}(\mathbf{X}, t) \cdot \mathbf{a}_0, \tag{A.3}$$

with $\lambda = ||\mathbf{a}|| = \sqrt{\mathbf{a} \cdot \mathbf{a}}$ being the stretch in the direction of $\mathbf{a}$, we have:

$$\lambda^2 = \mathbf{F} \cdot \mathbf{a}_0 \cdot \mathbf{F} \cdot \mathbf{a}_0 = \mathbf{a}_0 \cdot \mathbf{F}^T \cdot \mathbf{F} \cdot \mathbf{a}_0 = \mathbf{a}_0 \cdot \mathbf{C} \cdot \mathbf{a}_0. \tag{A.4}$$

The so-called right Cauchy-Green tensor $\mathbf{C} = \mathbf{F}^T \cdot \mathbf{F}$ is defined, where its eigenvalues correspond to the square of the principal stretches.

In order to define the volumetric transformation, the Jacobian determinant is introduced:

$$J = det(\mathbf{F}) = (det(\mathbf{C}))^{\frac{1}{2}}. \tag{A.5}$$

It is important to note that J must always be positive, since every infinitesimal volume is positive by definition.

In order to model the mechanical response under deformations that cause volume variations as well as purely shear deformations, the deformation gradient tensor can be decomposed multiplicatively as follows:

$$\mathbf{F} = J^{\frac{1}{3}} \mathbf{I} \cdot \overline{\mathbf{F}}. \tag{A.6}$$

The volumetric part is represented by $J^{\frac{1}{3}} \mathbf{I}$, where $\mathbf{I}$ is the second-order identity tensor, and $\overline{\mathbf{F}}$ represents the isochoric contribution, such that $\det(\overline{\mathbf{F}}) = 1$. Similarly to what

was previously mentioned for a body Ω, the isochoric part of the right Cauchy-Green deformation tensor can be defined as follows:

$$\overline{\mathbf{C}} = \overline{\mathbf{F}}^{T} \cdot \overline{\mathbf{F}} = J^{-\frac{2}{3}}\mathbf{C}. \tag{A.7}$$

As a result, the isochoric part of vector $\mathbf{a}$ and its corresponding isochoric stretch can be expressed as follows:

$$\overline{\mathbf{a}} = \overline{\mathbf{F}} \cdot \mathbf{a}_0 = J^{-\frac{1}{3}}\mathbf{a}, \tag{A.8}$$

$$\overline{\lambda} = ||\overline{\mathbf{a}}|| = J^{-\frac{1}{3}}||\mathbf{a}||. \tag{A.9}$$

A.2   Stress

Considering the body Ω under the influence of external and internal forces, Figure A.2 illustrates a cut plane passing through the previously mentioned point $\mathbf{X}$ in the reference configuration Ω_0 and point $\mathbf{x}$ in the spatial configuration Ω_t at time t.
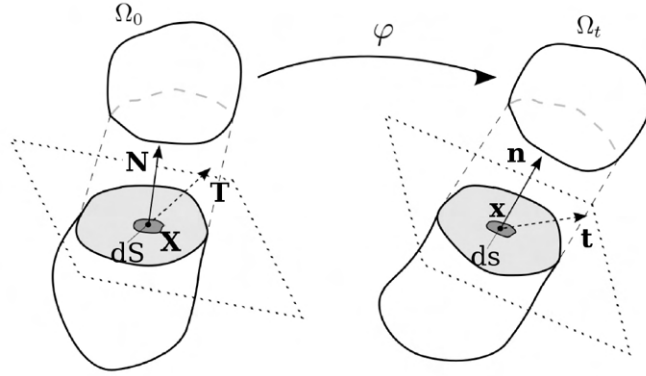
Figure A.2. Traction vectors associated to an infinitesimal surface.

Taking an infinitesimal surface in both configurations, denoted as $dS \in \Omega_0$ and $ds \in \Omega_t$, around the point of interest and within the cut plane, the resultant force acting on the point can be defined as $d\mathbf{f} = \mathbf{t}ds$, where $\mathbf{t}$ represents the Cauchy traction vector. Alternatively, $d\mathbf{f}$ can be defined in terms of the reference configuration by using vector $\mathbf{T}$ and dS instead of $\mathbf{t}$ and ds, resulting in $d\mathbf{f} = \mathbf{t}ds = \mathbf{T}dS$, where $\mathbf{T}$ is the first Piola-Kirchhoff traction vector.

To determine the values of the Cauchy traction vector $\mathbf{t}$ and the first Piola-Kirchhoff traction vector $\mathbf{T}$ with respect to a cut plane having a normal vector $N \in \Omega_0$ and $n \in \Omega_t$, Cauchy's theorem is applied in each configuration.

$$\mathbf{t} = \sigma \cdot \mathbf{n}, \tag{A.10}$$

$$\mathbf{T} = \mathbf{P} \cdot \mathbf{N}. \tag{A.11}$$

The symmetric spatial tensor σ is called the Cauchy stress tensor, and the tensor $\mathbf{P}$ is called the first Piola-Kirchhoff stress tensor. (A.11) relates the spatial values to the material configuration.

Thus, a relation between the Cauchy stress tensor and the first Piola-Kirchhoff stress tensor can be obtained, following

$$\sigma \cdot \mathbf{n} ds = \mathbf{T} dS = \mathbf{P} \cdot \mathbf{N} dS. \tag{A.12}$$

Therefore, it is possible to express $\mathbf{P}$ as a function of σ by using Nanson's formula $ds = J\mathbf{F}^{-T} dV$ to introduce the volumetric ratio J to define ds. This leads to the expression $\mathbf{P} = J\sigma \mathbf{F}^{-T}$.

Subsequently, the second Piola-Kirchhoff stress tensor, which is commonly used, can be defined as a function of the Cauchy stress tensor:

$$\mathbf{S} = J\mathbf{F}^{-1} \cdot \sigma \cdot \mathbf{F}^{-T}, \tag{A.13}$$

$$\sigma = J^{-1}\mathbf{F} \cdot \mathbf{S} \cdot \mathbf{F}^{T}. \tag{A.14}$$

The above equation is obtained by expressing the Kirchhoff stress tensor in terms of the Cauchy stress tensor as $\tau = \mathbf{F} \cdot \mathbf{S} \cdot \mathbf{F}^{T}$ (push-forward of $\mathbf{S}$) and using the fact that $\tau = J\sigma$. Therefore, it is possible to express the first Piola-Kirchhoff stress tensor in terms of the second Piola-Kirchhoff stress tensor as $\mathbf{P} = \mathbf{F} \cdot \mathbf{S}$.

A.3   Hyperelasticity for fibrous soft tissues

In order to develop constitutive laws for mechanical behaviour, SEFs (Ψ) are defined as functions of the deformation ($\mathbf{F}$). These SEFs can be expressed as functions of the right Cauchy-Green tensor or the stretch invariants. Using this approach, stress values can be obtained in terms of the aforementioned tensors, such as $\mathbf{P}$, $\mathbf{S}$, or σ. For hyperelastic models, specifically,

$$\mathbf{P} = \frac{\partial \Psi(\mathbf{F})}{\partial \mathbf{F}} = 2\mathbf{F} \cdot \frac{\partial \Psi(\mathbf{C})}{\partial \mathbf{C}}, \tag{A.15}$$

and applying the correlations to obtain $\mathbf{S}$ and σ:

$$\mathbf{S} = 2\frac{\partial \Psi(\mathbf{C})}{\partial \mathbf{C}}, \tag{A.16}$$

$$\sigma = J^{-1}2 \cdot \mathbf{F}\frac{\partial \Psi(\mathbf{C})}{\partial \mathbf{C}} \cdot \mathbf{F}^{T}. \tag{A.17}$$

A.3.1   Tangent operator

The nonlinear behaviour of hyperelastic materials necessitates the calculation of the elasticity tensor or tangent operator C to linearise the mechanical response. This enables the use of iterative methods to approximate the nonlinear solution of the original problem. The tangent operator C is the derivative of the stress with respect to the strain in the reference configuration:

$$C = 2\frac{\partial \mathbf{S}(\mathbf{C})}{\partial \mathbf{C}}. \tag{A.18}$$

Assuming the presence of a scalar-valued strain energy function Ψ, and according to (A.16), we can obtain:

$$C = 4\frac{\partial^2 \Psi(\mathbf{C})}{\partial \mathbf{C} \partial \mathbf{C}}, \tag{A.19}$$

which corresponds to a fourth-order tensor with 81 components, but due to the symmetries of the stress tensor $\mathbf{S}$ and elasticity tensor $\mathbf{C}$, the number of independent components can be reduced to 36.

A.3.2   Decoupling formulation

If we assume quasi-incompressibility of the tissue, we can express the SEF in a decoupled form. This involves dividing the SEF into two parts: the volumetric part Ψ_{vol} and the isochoric part Ψ_{ich}. Additionally, assuming anisotropy of the tissue, we can define $\mathbf{a}_{0i}$ of (A.4) as the preferential directions of the fibers. As a result, Ψ_{ich} must be split into two terms: the isotropic part Ψ_{iso} and the anisotropic part Ψ_{ani}. The anisotropic partdepends on the fiber directions $\mathbf{a}_{0i}$ and is a summation of n terms for n preferential fiber directions. Therefore:

$$\Psi = \Psi_{vol}(J) + \Psi_{ich}(\overline{\mathbf{C}}) = \Psi_{vol}(J) + \Psi_{iso}(\overline{\mathbf{C}}) + \Psi_{ani}(\overline{\mathbf{C}}, \mathbf{a}_{0i}). \tag{A.20}$$

By using the decoupled form of the SEF given in (A.20), and considering (A.16), the second Piola-Kirchhoff stress tensor can be decomposed into purely volumetric and purely isochoric parts as follows:

$$\mathbf{S} = 2\frac{\partial \Psi_{vol}(\mathbf{C})}{\partial \mathbf{C}} + 2\frac{\partial \Psi_{ich}(\mathbf{C})}{\partial \mathbf{C}} = \mathbf{S}_{vol} + \mathbf{S}_{ich}. \tag{A.21}$$

By decomposing the deformation gradient tensor according to (A.6) and using (A.20) and (A.21), we can express the elasticity tensor in a decoupled form as follows:

$$C = 4\frac{\partial^2 \Psi(\mathbf{C})}{\partial \mathbf{C} \partial \mathbf{C}} = 2\frac{\partial \mathbf{S}(\mathbf{C})}{\partial \mathbf{C}} = C_{vol} + C_{ich}. \tag{A.22}$$

APPENDIX B

Effect of the radial component in the mechanical integrity of the healthy aorta

Understanding the physiological behavior of arteries in the radial direction is essential for establishing a baseline against which pathological changes can be identified and analysed. Pathological conditions, such as arterial stiffening due to aging, atherosclerosis, or other diseases, can alter the radial behaviour of arteries, leading to impaired arterial function and increased cardiovascular risk. Therefore, investigating the radial behaviour of arteries is critical for comprehending their healthy mechanical properties and how they may be altered in various pathological conditions. In this thesis, the study of the influence of the radial component of the aorta will be carried out by performing experimental tests on porcine aortic tissue in the three main directions of the aorta—circumferential, longitudinal and radial—, in order to analyse and compare the results obtained in all directions and contribute to the comprehensive understanding of the healthy behaviour of the vessel.

B.1   State of the art

As commented in Section 1.3, the mechanical behaviour of arteries in the longitudinal and circumferential direction is well studied and established. However, little work has been done on studying the radial tensile strength of arteries. Previous studies had analysed the radial elastic properties of arteries, either under compression in dog aorta [254], rabbit aorta [255], porcine aorta [256] or dog carotid [257] or under tensile in porcine aorta [258]. When performing inflation tests in dog aorta, Vaishnav et al. [254] observed that the stress in the radial direction increased proportionally with

the intravascular pressure. However, Chuong et al. [255] and Dobrin et al. [257] made an interesting observation in their research on the behaviour of the aorta and carotid arteries during compression tests. Contrary to linear behaviour, they found that these arteries stiffened with increased compression pressure in the radial direction, which is similar to the stiffening observed during tensile testing of porcine aortas in the same direction [258]. Furthermore, Dobrin et al. [257] studied the compression response of healthy and elastase and collagenase treated canine carotid. They observed that the response to compression of these vessels is affected mostly by elastin and not by collagen. Moreover, Walraevens et al. [256] performed compression tests on healthy and calcified porcine aorta, obtaining that calcified tissue has a higher stiffness than healthy tissue at a certain strain level. When studying the tensile response of porcine aortas, MacLean et al. [258] determined the Young's modulus in the radial direction and it was notably different from the modulus in the circumferential and longitudinal directions. In neither case were stress vs. strain curves in the radial direction reported and compared with those in the other directions, nor in different locations of the vessels to account for the heterogeneity of the microstructure of vessels. Therefore, a comprehensive study that evaluates the importance of the radial component on its own and in contrast with the other directions throughout different locations is still lacking.

In terms of the in vitro testing, the unconfined compression test is the most commonly used method to determine the mechanical behaviour of materials subjected to compression, such as arterial tissue in the radial direction. Moreover, given the nature of the arteries, which have a small thickness in the radial direction compared to the other two, the unconfined compression test is a good candidate for the mechanical characterisation of the radial component [256]. In this test, specimens are mounted between two metal plates of the same size as the specimen. It is a relatively simple test that allows for both static and dynamic loading conditions and allows characterisation in the radial direction of the artery under both compression and tension if a suitable restraint is used, e.g., glue.

B.1.1   Objectives of the study

Arterial tissue in vivo experiences longitudinal and circumferential stretching during blood pressure, and this stretch generates a radial compression of the tissue. Therefore, compression tests in this direction would be physiologically relevant to fully determine the mechanical behaviour of arteries. Moreover, the mechanical behaviour in the radial direction of vessels is a key factor in some vascular diseases. For example, aortic dissection is an intramedial splitting caused by a radial tear across part of the vessel wall connecting the lumen to the middle layers of the wall [50]. The compression of the lipid core in an atheromatous plaque due to radial deformation of the fibrous cap substantially increases the risk of rupture of the plaque and thus the occurrence of an ischaemic event [259]. Therefore, knowledge of the properties in the radial direction should also be determined. A proper and full characterisation of the

mechanical behaviour of the arteries is the best starting point to further understand the different mechanisms that take place in the diseased state.

The objective of this study is to investigate the mechanical behaviour of the aorta in the radial direction under tension and compression tests, and to determine the impact of the aortic region on the radial properties of the artery. Our hypothesis is that the radial response of the aorta is more complex than previously described, exhibiting a non-linear behavior in response to both compression and tension. We will demonstrate that conventional models such as the Neo-Hookean model are insufficient to accurately replicate the observed behaviour of the aorta in the radial direction. Given that porcine aortas are commonly used as animal models in cardiovascular studies, our investigation will focus on analysing the mechanical behaviour of porcine aortas.

B.1.2   Research question posed

- Is the mechanical response of the aorta in tensile and compression in the radial direction linear or non-linear?

- Does location in the aorta have an influence in the radial mechanical properties of the vessel?

- Can the radial component be disregarded in favour of the mechanical strength in the longitudinal and circumferential directions?

B.2   Materials and methods

B.2.1   Sample preparation and experimental procedure

9 porcine aortas were harvested postmortem from approximately 3.5 ± 0.5 months-old female pigs, sacrificed for other studies that did not interfere with the aorta or the circulatory system. The experiments on these swines were approved by the Ethical Committee for Animal Research of the University of Zaragoza and all procedures were carried out in accordance with the "Principles of Laboratory Animal Care" (86/609/EEC Norm). After artery harvesting and cleaning by removing excess connective tissue, they were kept frozen at -80°C until testing. Once defrosted, samples were preserved in Krebs-Ringer at 4°C until preparation of testing samples was carried out. Each aorta was subdivided into three parts: ascending thoracic (ATA), descending thoracic aorta (DTA) and infrarenal abdominal aorta (IAA). From each location, at least one circumferential and longitudinal rectangular strip of 5x25 mm and one cylindrical disc of 8 mm of diameter were cut with a scalpel and a cylindrical punch with the appropriate dimensions, see Figure B.1.a. The stress free dimensions (length, with, thickness and diameter) were measured using an electronic Mitutoyo Digimatic micrometer.

Simple tension tests of the circumferential and axial rectangular strips (5x25 mm) were performed in an Instron Microtester 5548 system using a 10 N load cell with a minimal resolution of 0.005 N. A non-contact Instron 2663-281 video-extensometer was used to measure the strain during the tests. To avoid specimen drying, the strips were immersed in Krebs–Ringer solution. Three loading and unloading stress cycle levels were applied corresponding to approximately 60, 120 and 240 kPa of uniaxial stress at 30%/min of strain rate [34] under load control. Five preliminary cycles at all load levels were applied in order to precondition the samples.

For radial tests, the cylindrical discs were fixed between two plates using a cyanoacrylate adhesive (Loctite, Dusseldorf, Germany). The plates were attached to a uniaxial mechanical testing machine (Instron Microtester 5548), see Figure B.1.b. The lower plate was fixed and the upper plate was displaced in the radial direction. The experiment involved applying three levels of tension and compression, with the first level being 5% strain in tensile and -5% strain in compression, the second 10% in tensile and -10% in compression and the third 20% in tensile and -20% in compression at a rate of 30%/min of strain under displacement control. Five preliminary cycles at all load levels were also applied in order to precondition the samples.

(a)   (b)
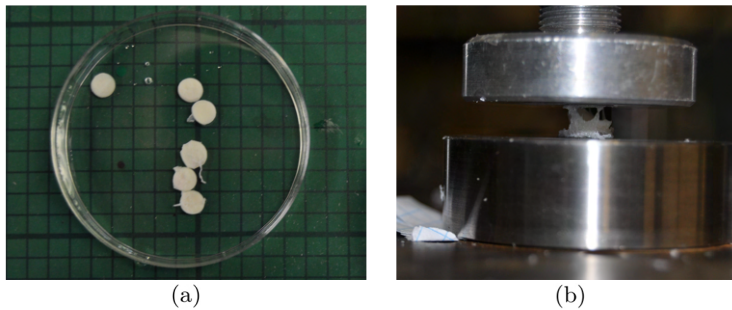
Figure B.1. Disk radial samples for the compression test from one artery (a) and setup of a sample in the uniaxial testing machine (b), where the adhesive can be appreciated as the plates are separated after the compression test.

B.2.2   Data processing

Force and displacement data was obtained from each test and processed using Matlab R2020a and transformed into stress-stretch curves. The engineering stress (first Piola Kirchhoff stress tensor **P**) in the direction of the stretch was computed as $P_{\theta\theta,zz} = \frac{F_{\theta,z}}{t_{\theta,z} w_{\theta,z}}$ and $P_{rr} = \frac{F_r}{\pi r^2}$, where F is the load registered by the Instron machine, $t_{\theta,z}$ and $w_{\theta,z}$ are the initial thickness and width in circumferential and longitudinal directions respectively and r is the radius of the cylindrical disc. Mean and standard deviation of the curves in each direction was calculated for all locations (ATA, DTA and IAA) and directions. Only cases where the impact of glue was visibly affecting the results were excluded from the analysis of the radial component, see Figure B.2.
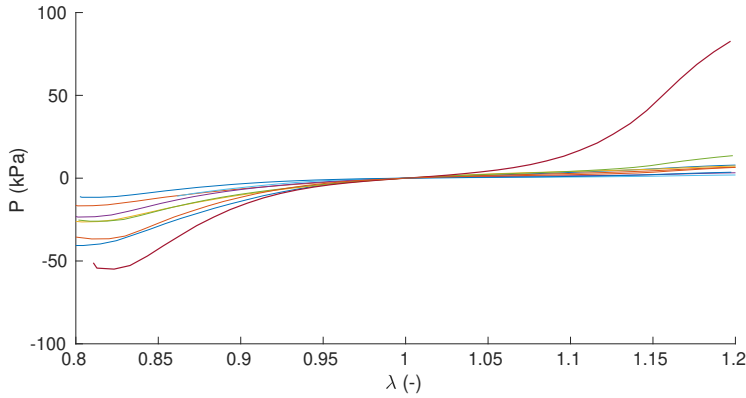
Figure B.2. Representation of some curves of the compression test in the radial direction. The dark red line comes from a sample in which the glue has affected the results. It can be especially appreciated in the tensile response of the tissue, as the effect of glue strongly stiffens the tissue response.

B.3 Results

Figure B.3 shows the complete tensile-compression test in the radial direction of a representative sample for each location of the aorta. Each strain level has 5 cycles of loading-unloading. Higher stresses are reached in the ATA for tensile and compression in all three levels of strain. However, the curves in compression appear more exponential in the other two locations of the aorta, implying a higher non-linear behaviour in these locations. Hysteresis can also be notably observed in the 20% strain cycles of the DTA and IAA.
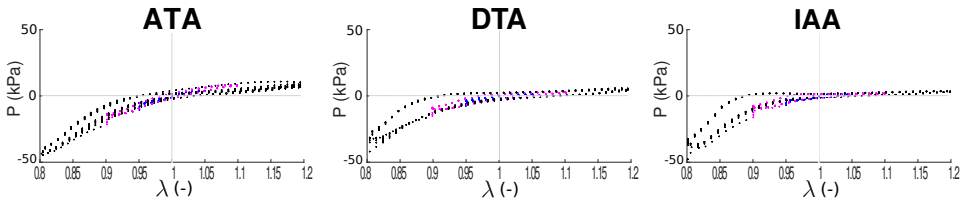
Figure B.3. Results of a representative sample of the complete tensile-compression tests in the radial direction in all three locations of the aorta, ATA, DTA and IAA. Blue markers represent the data from the first 5% strain cycle, pink markers from the 10% strain cycle and black markers from the 20% strain cycle.

In order to get a clearer comparison between areas, Figure B.4 shows three representative loading curves of the three studied locations of the aorta. The 20% strain cycle was chosen to better observe differences and tendencies.
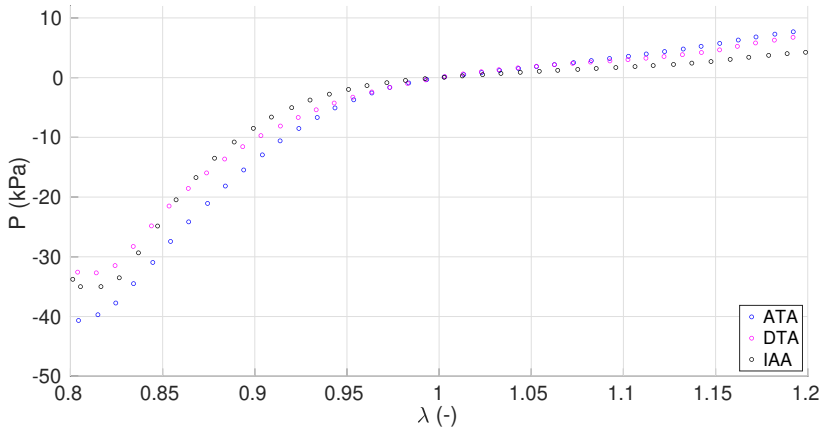
Figure B.4. Representative loading cycle in tensile and compression in the radial direction in all three locations of the aorta, ATA (blue), DTA (pink) and IAA (black).

Figure B.5.a shows the last loading cycle of representative samples in the three directions and in each location of the aorta. The increased anisotropy when moving distally can be observed in the circumferential and longitudinal curves of the IAA. Figure B.5.b zooms on the tensile response of the aorta in the first 20% strain in the three studied directions.
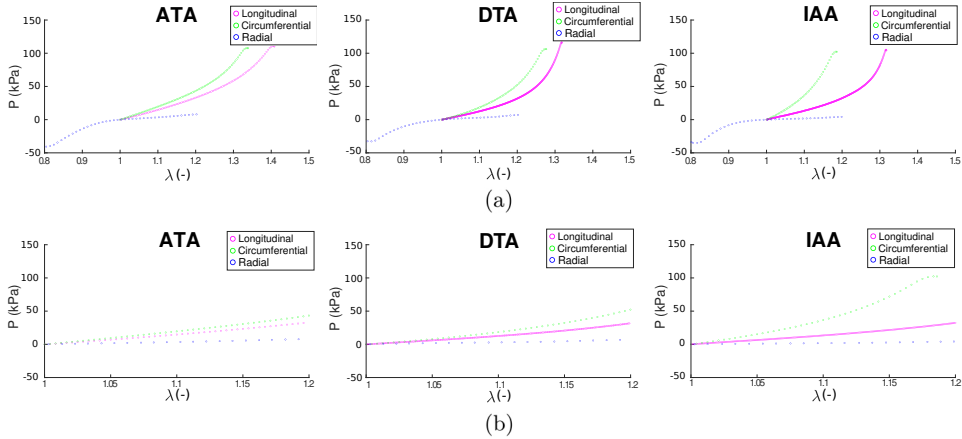
Figure B.5. (a) Results of representative samples of the last loading cycle in all directions—longitudinal (pink), circumferential (green) and radial (blue)—in the three locations of the aorta, ATA, DTA and IAA. (b) Zoom of the same results in the first 20% strain in tensile.

Figure B.6 shows all the curves of the last loading cycle of the 120 kPa (circumferential and longitudinal directions) or 20% strain cycles (radial direction) and their mean and standard deviation, differentiating between directions (columns) and locations (rows).
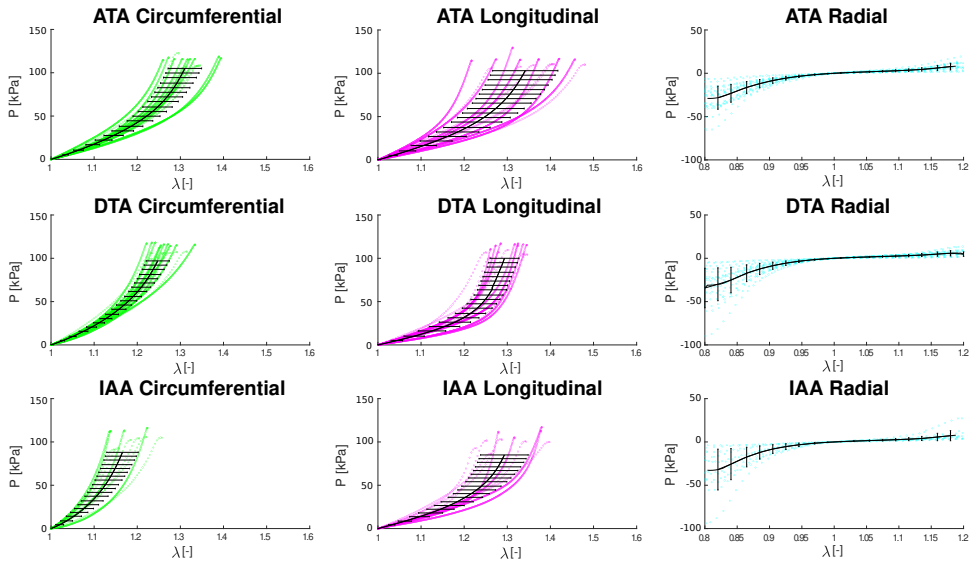
Figure B.6. Mean and standard deviation of the last loading curve of the 120 kPa or 20% strain cycles of all tested samples in the three directions and three locations of the aorta, ATA, DTA and IAA. n=14 for ATA C, n=13 for ATA L, n=21 for ATA R, n=18 for DTA C, n=16 for DTA L, n=22 for DTA R, n=10 for IAA C, n=10 for IAA L, n=12 for IAA R.

Table B.1 shows the Young's modulus calculated from the last cycle of the tensile-compression test in the radial direction. Because the stress-strain curves were nonlinear in all directions of testing, the slopes of these curves were calculated at strain increments of 0.8% for comparison between different directions of testing.

Table B.1. Young's modulus (kPa) for different levels of tensile and compression strain.

Location	Compression strain			Tensile strain		
	-17%	**-10%**	**-1%**	**1%**	**10%**	**17%**
ATA	249.38	168.02	48.78	37.01	32.75	78.75
DTA	298.77	172.84	45.56	34.98	25.38	49.00
IAA	387.72	171.11	43.96	34.50	29.13	74.38

B.4   Discussion of the experimental results

In this study, we have performed tensile-compression tests in the radial direction of porcine aortas, in addition to the more common uniaxial tensile tests in the circumferential and longitudinal directions. The purpose of these experiments is to shed light on the mechanical behaviour of healthy arteries in the radial direction, as this aspect has been relatively understudied. Knowledge of this physiological behaviour can help in understanding other pathological mechanisms that arise in several cardiovascular diseases [258].

The first observation we have made from our compression-tensile tests is that the mechanical response in the radial direction is non-linear. This non-linearity is more apparent in compression than in tensile, see Figure B.3, Figure B.4 and Table B.1. This difference can be explained by the fact that the compression stiffness of vessels in the radial plane is affected by their fibres in the circumferential-longitudinal plane due to the Poisson effect, whereas in tensile stress, the mechanical response is primarily attributed to the isotropic matrix and the limited number of collagen and elastin fibers oriented radially [260]. The non-linear behaviour in compression [255, 257] and in tensile [258] in the radial direction of arteries had already been observed in literature. In particular, MacLean et al. [258] calculated the Young's modulus of the upper and lower thoracic porcine aorta throughout the tensile test, up to 50% strain. The ranges of Young's modulus we obtain (Table B.1) are in accordance with their data, although they lay in the lower range of their results, which show a high variability. Moreover, they report a higher increase and generally higher Young's moduli in the DTA when increasing the strain level than in the IAA, whereas we have found generally higher moduli in the IAA than in the DTA. Furthermore, we have observed that the tensile stiffness in the ATA is greater than in either of the two other areas under study, see Table B.1 and Figure B.4. When observing the compression behaviour, however, it is the IAA where a higher increase in stiffness is found when increasing compression strain, see Table B.1. Moreover, the dispersion of results was also higher in this location, see Figure B.6. These differences highlight that there is a location-dependent behaviour in the radial direction of the aorta in both compression and tensile, adding to the location-dependent behaviour previously studied in the other two directions.

Upon examining the full characterisation of the tissue, as shown in Figure B.5, we have noted that the response in the radial component is not as insignificant as previously assumed, particularly in the initial levels of strain. In fact, as shown in Figure B.5, the initial 1% of tensile strain exhibits a consistent slope across all three directions, indicating that they possess similar stiffnesses. This finding suggests that for low levels of tensile strain, the elastic modulus of vessels in the longitudinal and circumferential directions could serve as an estimate of the modulus in the radial direction. These comparable values of tensile stiffness in the three directions at lower levels of strain were also found by MacLean et al. [258]. It should be noted that this relationship does not extend to the compression modulus, as the stiffness in the radial

direction changes even at lower levels of strain during compression (Table B.1).

Our experimental data of the compression tests can be compared with the results obtained by Walraevens et al. [256], who performed compression tests on abdominal aortic tissue. We have observed lower levels of stress in our experiments. In particular, they report a compression engineering stress of around 30 kPa when compressing the tissue 10%, whereas in our study we have obtained a mean compression stress of around 10 kPa, with the highest value of a specific sample reaching 20 kPa. Nevertheless, they report a Young's modulus of around 150 kPa at 10% compression strain, whereas we obtain a Young's modulus of 171.11 kPa. Our findings are consistent with previous studies in the literature. However, further research is warranted to more thoroughly characterise and comprehensively understand this behaviour.

Through this study, we have demonstrated that the radial response of arterial tissue is multifaceted, dependent on location, and distinct in compression and tension. These findings highlight the need for more advanced hyperelastic material models in material characterisation, using the experimental data obtained, to gain deeper insights into the mechanical properties of blood vessels. Until now, the mechanical properties of vessels in the radial direction were largely overlooked, and since vessel incompressibility is commonly assumed [261], they were approximated based on the mechanical behaviour of vessels in the other two directions. However, given the findings of this study and recent research proposing that vessel compressibility is more significant than previously thought [262], further research is required to assess and incorporate the radial properties of vessels.

B.5   Key findings

- The aorta exhibits a non-linear behaviour in the radial direction when subjected to compression and tensile.

- The progressive stiffening of the tissue happens more predominantly when compressed than in tensile.

- Compressed tissue stiffens more in the IAA than in the other studied locations of the aorta, and the dispersion of results was higher in this area.

- When subjected to tensile stress, samples from the ATA show higher stiffness than from other locations.

- Higher hysteresis can be observed in the tested samples in the DTA and the IAA than in the ATA.

- The mechanical response of the vessel in the three directions is similar in the first 1% tensile strain.

Bibliography

[1]   G. A. Mensah, G. A. Roth, and V. Fuster, "The global burden of cardiovascular diseases and risk factors," *J Am Coll Cardiol*, vol. 74, no. 20, pp. 2529–2532, 2019.

[2]   T. Vos, S. S. Lim, C. Abbafati, K. M. Abbas, M. Abbasi, M. Abbasifard, M. Abbasi-Kangevari, H. Abbastabar, F. Abd-Allah, A. Abdelalim, M. Abdollahi, I. Abdollahpour, H. Abolhassani, V. Aboyans, E. M. Abrams, L. G. Abreu, M. R. M. Abrigo, L. J. Abu-Raddad, . Abdelrahman I Abushouk, and C. J. L. Murray, "Global burden of 369 diseases and injuries in 204 countries and territories, 1990–2019: a systematic analysis for the global burden of disease study 2019," *Lancet*, vol. 396, no. 10258, pp. 1204–1222, 2020.

[3]   G. A. Roth, G. A. Mensah, C. O. Johnson, G. Addolorato, E. Ammirati, L. M. Baddour, N. C. Barengo, A. Z. Beaton, E. J. Benjamin, C. P. Benziger, A. Bonny, M. Brauer, M. Brodmann, T. J. Cahill, J. Carapetis, A. L. Catapano, S. S. Chugh, L. T. Cooper, J. Coresh, ..., and V. Fuster, "Global burden of cardiovascular diseases and risk factors, 1990–2019," *J Am Coll Cardiol*, vol. 76, no. 25, pp. 2982–3021, 2020.

[4]   J. D. Stanaway, A. Afshin, E. Gakidou, S. S. Lim, D. Abate, K. H. Abate, C. Abbafati, N. Abbasi, H. Abbastabar, F. Abd-Allah, J. Abdela, A. Abdelalim, I. Abdollahpour, R. S. Abdulkader, M. Abebe, Z. Abebe, S. F. Abera, O. Z. Abil, H. N. Abraha, ..., and C. J. L. Murray, "Global, regional, and national comparative risk assessment of 84 behavioural, environmental and occupational, and metabolic risks or clusters of risks for 195 countries and territories, 1990–2017: a systematic analysis for the global burden of disease study 2017," *Lancet*, 2018.

[5]   P. C. Evans and B. R. Kwak, "Biomechanical factors in cardiovascular disease," *Cardiovasc Res*, vol. 99, no. 2, pp. 229–231, 2013.

[6]   S. Ferrari and M. Pesce, "Stiffness and aging in cardiovascular diseases: The dangerous relationship between force and senescence," *Int J Mol Sci*, vol. 22, no. 7, p. 3404, 2021.

[7]   F. J. H. Gijsen, J. J. Wentzel, K. V. der Heiden, and P. C. Evans, "Biomechanics in vascular biology and cardiovascular disease," *Thromb Haemost*, vol. 115, no. 03, pp. 465–466, 2016.

[8]   I. E. Hoefer, B. den Adel, and M. J. A. P. Daemen, "Biomechanical factors as triggers of vascular growth," *Cardiovasc Res*, vol. 99, no. 2, pp. 276–283, 2013.

[9]   J. S. VanEpps and D. A. Vorp, "Mechanopathobiology of atherogenesis: A review," *J Surg Res*, vol. 142, no. 1, pp. 202–217, 2007.

[10]   X. Bai, X. Wang, and Q. Xu, "Endothelial damage and stem cell repair in atherosclerosis," *Vascul Pharmacol*, vol. 52, no. 5-6, pp. 224–229, 2010.

[11]   R. Virmani and A. Farb, "Pathology of in-stent restenosis," *Curr Opin Lipidol*, vol. 10, no. 6, pp. 499–506, 1999.

[12]   A. Ferrara and A. Pandolfi, "A numerical study of arterial media dissection processes," *Int J Fract*, vol. 166, no. 1-2, pp. 21–33, 2010.

[13]   J. D. Humphrey and A. D. McCulloch, "The cardiovascular system — anatomy, physiology and cell biology," in *Biomechanics of Soft Tissue in Cardiovascular Systems*, pp. 1–14, Springer Vienna, 2003.

[14]   J. I. Gupta and M. J. Shea, "Biology of the blood vessels." `https://www.msdmanuals.com/en-gb/home/heart-and-blood-vessel-disorders/biology-of-the-heart-and-blood-vessels/biology-of-the-blood-vessels`, 2022. Accessed: 2023-03-31.

[15]   G. A. Holzapfel, T. C. Gasser, and R. W. Ogden, "A new constitutive framework for arterial wall mechanics and a comparative study of material models," *J Elast*, vol. 61, no. 1/3, pp. 1–48, 2000.

[16]   H. P. Wagner and J. D. Humphrey, "Differential passive and active biaxial mechanical behaviors of muscular and elastic arteries: Basilar versus common carotid," *J Biomech Eng*, vol. 133, no. 5, 2011.

[17]   J. A. G. Rhodin, "Architecture of the vessel wall," 1980.

[18]   "Encyclopædia britannica." `https://www.britannica.com/science/artery#/media/1/36874/121565`. Accessed: 2023-04-15.

[19]   L. H. Peterson, R. E. Jensen, and J. Parnell, "Mechanical properties of arteries in vivo," *Circ Res*, vol. 8, no. 3, pp. 622–639, 1960.

[20]   F. H. Silver, P. B. Snowhill, and D. J. Foran, "Mechanical behavior of vessel wall: A comparative study of aorta, vena cava, and carotid artery," *Ann Biomed Eng*, vol. 31, no. 7, pp. 793–803, 2003.

[21] M. R. Roach and A. C. Burton, "The Reason for the Shape of the Distensibility Curves of Arteries," *Can J Biochem Physiol*, vol. 35, no. 8, pp. 681–690, 1957.

[22] J. P. V. Geest, M. S. Sacks, and D. A. Vorp, "Age dependency of the biaxial biomechanical behavior of human abdominal aorta," *J Biomech Eng*, vol. 126, no. 6, pp. 815–822, 2004.

[23] M. Jadidi, A. Desyatova, J. MacTaggart, and A. Kamenskiy, "Mechanical stresses associated with flattening of human femoropopliteal artery specimens during planar biaxial testing and their effects on the calculated physiologic stress–stretch state," *Biomech Model Mechanobiol*, vol. 18, no. 6, pp. 1591–1605, 2019.

[24] M. H. Kural, M. Cai, D. Tang, T. Gwyther, J. Zheng, and K. L. Billiar, "Planar biaxial characterization of diseased human coronary and carotid arteries for computational modeling," *J Biomech*, vol. 45, no. 5, pp. 790–798, 2012.

[25] C. Lally, A. J. Reid, and P. J. Prendergast, "Elastic behavior of porcine coronary artery tissue under uniaxial and equibiaxial tension," *Ann Biomed Eng*, vol. 32, no. 10, pp. 1355–1364, 2004.

[26] H. Bader, "Dependence of wall stress in the human thoracic aorta on age and pressure," *Circ Res*, vol. 20, no. 3, pp. 354–361, 1967.

[27] T. Kang, "Mechanical behavior of arteries under inflation and extension," *J Mech Sci Technol*, vol. 22, no. 4, pp. 621–627, 2008.

[28] W. Krasny, H. Magoariec, C. Morin, and S. Avril, "Kinematics of collagen fibers in carotid arteries under tension-inflation loading," *J Mech Behav Biomed Mater*, vol. 77, pp. 718–726, 2018.

[29] O. Trabelsi, V. Dumas, E. Breysse, N. Laroche, and S. Avril, "In vitro histomechanical effects of enzymatic degradation in carotid arteries during inflation tests with pulsatile loading," *J Mech Behav Biomed Mater*, vol. 103, p. 103550, 2020.

[30] J. Burkert, P. Kochová, Z. Tonar, R. Cimrman, T. Blassová, R. Jashari, R. Fiala, and J. Špatenka, "The time has come to extend the expiration limit of cryopreserved allograft heart valves," *Cell Tissue Bank*, vol. 22, no. 2, pp. 161–184, 2020.

[31] A. García, E. Peña, A. Laborda, F. Lostalé, M. D. Gregorio, M. Doblaré, and M. Martínez, "Experimental study and constitutive modelling of the passive mechanical properties of the porcine carotid artery and its relation to histological analysis: Implications in animal cardiovascular device trials," *Med Eng Phys*, vol. 33, no. 6, pp. 665–676, 2011.

[32]   J. A. Peña, M. Cilla, M. A. Martínez, and E. Peña, "Biomechanical characteri-
       zation and constitutive modeling of the layer-dissected residual strains and me-
       chanical properties of abdominal porcine aorta," *J Biomech*, vol. 132, p. 110909,
       2022.

[33]   A. Giudici, A. W. Khir, J. M. Szafron, and B. Spronck, "From uniaxial testing
       of isolated layers to a tri-layered arterial wall: A novel constitutive modelling
       framework," *Ann Biomed Eng*, vol. 49, no. 9, pp. 2454–2467, 2021.

[34]   J. A. Peña, M. A. Martínez, and E. Peña, "Layer-specific residual deformations
       and uniaxial and biaxial mechanical properties of thoracic porcine aorta," *J
       Mech Behav Biomed Mater*, vol. 50, pp. 55–69, 2015.

[35]   G. A. Holzapfel, G. Sommer, C. T. Gasser, and P. Regitnig, "Determina-
       tion of layer-specific mechanical properties of human coronary arteries with
       nonatherosclerotic intimal thickening and related constitutive modeling," *Am
       J Physiol Heart Circ Physiol*, vol. 289, no. 5, pp. H2048–H2058, 2005.

[36]   M. Cilla, M. M. Pérez, E. Peña, and M. A. Martínez, "Effect of diet and age
       on arterial stiffening due to atherosclerosis in ApoE-/- mice," *Ann Biomed Eng*,
       vol. 44, no. 7, pp. 2202–2217, 2015.

[37]   P. B. Dobrin, "Mechanical properties of arteries," *Physiol Rev*, vol. 58, no. 2,
       pp. 397–460, 1978.

[38]   J. Tong, Y. Cheng, and G. A. Holzapfel, "Mechanical assessment of arterial
       dissection in health and disease: Advancements and challenges," *J Biomech*,
       vol. 49, no. 12, pp. 2366–2373, 2016.

[39]   C. A. Nienaber, R. E. Clough, N. Sakalihasan, T. Suzuki, R. Gibbs, F. Mussa,
       M. P. Jenkins, M. M. Thompson, A. Evangelista, J. S. M. Yeh, N. Cheshire,
       U. Rosendahl, and J. Pepper, "Aortic dissection," *Nat Rev Dis Primers*, vol. 2,
       no. 1, 2016.

[40]   F. J. Criado, "Aortic dissection: a 250-year perspective.," *Tex Heart Inst J*,
       vol. 38, pp. 694–700, 2011.

[41]   N. T. Kouchoukos and D. Dougenis, "Surgery of the thoracic aorta," *N Engl J
       Med*, vol. 336, no. 26, pp. 1876–1889, 1997.

[42]   W. I. Schievink, "Spontaneous dissection of the carotid and vertebral arteries,"
       N Engl J Med, vol. 344, no. 12, pp. 898–906, 2001.

[43]   D. Fleischmann, R. O. Afifi, A. I. Casanegra, J. A. Elefteriades, T. G. Gleason,
       K. Hanneman, E. E. Roselli, M. J. Willemink, and M. P. F. and, "Imaging
       and surveillance of chronic aortic dissection: A scientific statement from the
       american heart association," *Circ Cardiovasc Imaging*, vol. 15, no. 3, 2022.

[44] D. P. J. Howard, A. Banerjee, J. F. Fairhead, J. Perkins, L. E. Silver, and P. M. Rothwell, "Population-based study of incidence and outcome of acute aortic dissection and premorbid risk factor control," *Circ*, vol. 127, pp. 2031–2037, 2013.

[45] M. Silaschi, J. Byrne, and O. Wendler, "Aortic dissection: medical, interventional and surgical management," *Heart*, vol. 103, pp. 78–87, 2017.

[46] A. E. Hirst, V. J. Johns, and S. W. Kime, "Dissecting aneurysm of the aorta: A review of 505 cases.," *Medicine*, vol. 37, no. 3, p. 217, 1958.

[47] J. Lewey, S. C. E. Hajj, and S. N. Hayes, "Spontaneous coronary artery dissection: New insights into this not-so-rare condition," *Annu Rev Med*, vol. 73, no. 1, pp. 339–354, 2022.

[48] A. Evangelista, E. M. Isselbacher, E. Bossone, T. G. Gleason, M. D. Eusanio, U. Sechtem, M. P. Ehrlich, S. Trimarchi, A. C. Braverman, T. Myrmel, K. M. Harris, S. Hutchinson, P. O'Gara, T. Suzuki, C. A. Nienaber, and K. A. Eagle, "Insights from the international registry of acute aortic dissection," *Circ*, vol. 137, no. 17, pp. 1846–1860, 2018.

[49] D. P. J. Howard, E. Sideso, A. Handa, and P. M. Rothwell, "Incidence, risk factors, outcome and projected future burden of acute aortic dissection.," *Ann Cardiothorac Surg*, vol. 3, pp. 278–284, 2014.

[50] S. Sherifova and G. A. Holzapfel, "Biomechanics of aortic wall failure with a focus on dissection and aneurysm: A review," *Acta Biomater*, vol. 99, pp. 1–17, 2019.

[51] K. Rajagopal, C. Bridges, and K. R. Rajagopal, "Towards an understanding of the mechanics underlying aortic dissection," *Biomech Model Mechanobiol*, vol. 6, no. 5, pp. 345–359, 2007.

[52] P. O. Daily, H. W. Trueblood, E. B. Stinson, R. D. Wuerflein, and N. E. Shumway, "Management of acute aortic dissections," *Ann Thorac Surg*, vol. 10, no. 3, pp. 237–247, 1970.

[53] S. A. LeMaire and L. Russell, "Epidemiology of thoracic aortic dissection," *Nat Rev Cardiol*, vol. 8, no. 2, pp. 103–113, 2010.

[54] I. Baimatova, H. Singh, and A. Khanafer, "Debakey vs stanford: Are they the same?," *Heart Lung Circ*, vol. 25, no. 8, p. e102, 2016.

[55] P. G. Hagan, C. A. Nienaber, E. M. Isselbacher, D. Bruckman, D. J. Karavite, P. L. Russman, A. Evangelista, R. Fattori, T. Suzuki, J. K. Oh, A. G. Moore, J. F. Malouf, L. A. Pape, C. Gaca, U. Sechtem, S. Lenferink, H. J. Deutsch, H. Diedrichs, J. M. y Robles, ..., and K. A. Eagle, "The international registry of acute aortic dissection (IRAD)," *JAMA*, vol. 283, no. 7, p. 897, 2000.

[56] M. Landenhed, G. Engström, A. Gottsäter, M. P. Caulfield, B. Hedblad, C. Newton-Cheh, O. Melander, and J. G. Smith, "Risk profiles for aortic dissection and ruptured or surgically treated aneurysms: A prospective cohort study," *J Am Heart Assoc*, vol. 4, no. 1, p. e001513, 2015.

[57] G. Sommer, T. C. Gasser, P. Regitnig, M. Auer, and G. A. Holzapfel, "Dissection properties of the human aortic media: An experimental study," *J Biomech Eng*, vol. 130, no. 2, 2008.

[58] X. Leng, B. Zhou, X. Deng, L. Davis, S. M. Lessner, M. A. Sutton, and T. Shazly, "Experimental and numerical studies of two arterial wall delamination modes," *J Mech Behav Biomed Mater*, vol. 77, pp. 321–330, 2018.

[59] J. L. Björkegren and A. J. Lusis, "Atherosclerosis: Recent developments," *Cell*, vol. 185, no. 10, pp. 1630–1645, 2022.

[60] "Canadian ultrasound institute - linkedin." `https://ca.linkedin.com/in/canadian-ultrasound-institute-93b798163`. Accessed: 2019-05-30.

[61] "Atherosclerosis stroke." `https://www.freepik.com`. Accessed: 2023-04-28.

[62] K. Islam, S. B. H. Timraz, R. Nasser, D. L. .Gater, Y. E. Pearson, N. Christoforou, and J. C. M. Teo, "Co-culture methods used to model atherosclerosis in vitro using endothelial, smooth muscle and monocyte cells," *SM J Biomed Eng*, vol. 2, no. 1, pp. 1008–100815, 2016.

[63] E. Akbari, G. B. Spychalski, K. K. Rangharajan, S. Prakash, and J. W. Song, "Flow dynamics control endothelial permeability in a microfluidic vessel bifurcation model," *Lab Chip*, vol. 18, no. 7, pp. 1084–1093, 2018.

[64] B. S. Conklin, R. P. Vito, and C. Chen, "Effect of low shear stress on permeability and occludin expression in porcine artery endothelial cells," *World J Surg*, vol. 31, no. 4, pp. 733–743, 2007.

[65] C. Kao, J. Chen, and V. Yang, "Ultrastructure and permeability of endothelial cells in branched regions of rat arteries," *Atherosclerosis*, vol. 105, no. 1, pp. 97–114, 1994.

[66] M. Okano and Y. Yoshida, "Junction complexes of endothelial cells in atherosclerosis-prone and atherosclerosis-resistant regions on flow dividers of brachiocephalic bifurcations in the rabbit aorta," *Biorheology*, vol. 31, no. 2, pp. 155–161, 1994.

[67] T. J. Forbes, D. W. Kim, W. Du, D. R. Turner, R. Holzer, Z. Amin, Z. Hijazi, A. Ghasemi, J. J. Rome, D. Nykanen, E. Zahn, C. Cowley, M. Hoyer, D. Waight, D. Gruenstein, A. Javois, S. Foerster, J. Kreutzer, N. Sullivan, ..., and T. Zellers, "Comparison of surgical, stent, and balloon angioplasty treatment of native coarctation of the aorta," *J Am Coll Cardiol*, vol. 58, no. 25, pp. 2664–2674, 2011.

[68] J. Gunn, "Coronary artery stretch versus deep injury in the development of in-stent neointima," *Heart*, vol. 88, no. 4, pp. 401–405, 2002.

[69] M. S. Kim and L. S. Dean, "In-stent restenosis," *Cardiovasc Ther*, vol. 29, no. 3, pp. 190–198, 2010.

[70] C. Nicolais, V. Lakhter, H. U. H. Virk, P. Sardar, C. Bavishi, B. O'Murchu, and S. Chatterjee, "Therapeutic options for in-stent restenosis," *Curr Cardiol Rep*, vol. 20, no. 2, 2018.

[71] J. A. Suwaidi, "Coronary artery stents," *JAMA*, vol. 284, no. 14, p. 1828, 2000.

[72] "Mayo clinic - coarctation of the aorta." `https://www.mayoclinic.org/diseases-conditions/coarctation-of-the-aorta/symptoms-causes/syc-20352529`. Accessed: 2023-04-28.

[73] P. J. Prendergast, C. Lally, S. Daly, A. J. Reid, T. C. Lee, D. Quinn, and F. Dolan, "Analysis of prolapse in cardiovascular stents: A constitutive equation for vascular tissue and finite-element modelling," *J Biomech Eng*, vol. 125, no. 5, pp. 692–699, 2003.

[74] U. Sigwart, U. Kaufmann, J.-J. Goy, M. Grbic, S. Golf, A. Essinger, A. Fischer, H. Sadeghi, V. Mirkovitch, and L. Kappenberger, "Prevention of coronary restenosis by stenting," *Eur Heart J*, vol. 9, no. suppl C, pp. 31–37, 1988.

[75] U. Sigwart, J. Puel, V. Mirkovitch, F. Joffre, and L. Kappenberger, "Intravascular stents to prevent occlusion and re-stenosis after transluminal angioplasty," *N Engl J Med*, vol. 316, no. 12, pp. 701–706, 1987.

[76] W. K. Laskey, S. Kimmel, and R. J. Krone, "Contemporary trends in coronary intervention: A report from the registry of the society for cardiac angiography and interventions," *Catheter Cardiovasc Interv*, vol. 49, no. 1, pp. 19–22, 2000.

[77] N. A. Scott, "Restenosis following implantation of bare metal coronary stents: Pathophysiology and pathways involved in the vascular response to injury," *Adv Drug Deliv Rev*, vol. 58, no. 3, pp. 358–376, 2006.

[78] G. D. Dangas, B. E. Claessen, A. Caixeta, E. A. Sanidas, G. S. Mintz, and R. Mehran, "In-stent restenosis in the drug-eluting stent era," *J Am Coll Cardiol*, vol. 56, no. 23, pp. 1897–1907, 2010.

[79] P. H. Grewe, T. Deneke, A. Machraoui, J. Barmeyer, and K.-M. Müller, "Acute and chronic tissue response to coronary stent implantation: pathologic findings in human specimen," *J Am Coll Cardiol*, vol. 35, no. 1, pp. 157–163, 2000.

[80] R. Hoffmann, G. S. Mintz, G. R. Dussaillant, J. J. Popma, A. D. Pichard, L. F. Satler, K. M. Kent, J. Griffin, and M. B. Leon, "Patterns and mechanisms of in-stent restenosis," *Circ*, vol. 94, no. 6, pp. 1247–1254, 1996.

[81] R. S. Schwartz, "Pathophysiology of restenosis: Interaction of thrombosis, hyperplasia, and/or remodeling," *Am J Card*, vol. 81, no. 7, pp. 14E–17E, 1998.

[82] V. Farooq, B. D. Gogas, and P. W. Serruys, "Restenosis," *Circ Cardiovasc Interv*, vol. 4, no. 2, pp. 195–205, 2011.

[83] H. Hara, M. Nakamura, J. C. Palmaz, and R. S. Schwartz, "Role of stent design and coatings on restenosis and thrombosis," *Adv Drug Deliv Rev*, vol. 58, no. 3, pp. 377–386, 2006.

[84] H. B. P. Putra, Q. M. Savitri, W. W. Mukhammad, A. Billah, A. Dharmasaputra, and R. N. Rosyadi, "TCTAP a-030 drug coated balloon versus drug-eluting stent for in-stent restenosis after drug-eluting stent implantation: A meta-analysis," *J Am Coll Cardiol*, vol. 77, no. 14, p. S19, 2021.

[85] G. Giustino, A. Colombo, A. Camaj, K. Yasumura, R. Mehran, G. W. Stone, A. Kini, and S. K. Sharma, "Coronary in-stent restenosis," *J Am Coll Cardiol*, vol. 80, no. 4, pp. 348–372, 2022.

[86] G. Nakazawa, M. Vorpahl, A. V. Finn, J. Narula, and R. Virmani, "One step forward and two steps back with drug-eluting-stents," *JACC: Cardiovasc Imaging*, vol. 2, no. 5, pp. 625–628, 2009.

[87] D. G. Kokkinidis, S. W. Waldo, and E. J. Armstrong, "Treatment of coronary artery in-stent restenosis," *Expert Rev Cardiovasc Ther*, vol. 15, no. 3, pp. 191–202, 2017.

[88] A. D. Singh, A. K. Singal, A. Mian, S. R. Kapadia, D. P. Hedrick, A. Kanaa'N, J. J. Khatri, R. Puri, and A. Kalra, "Recurrent drug-eluting stent in-stent restenosis: A state-of-the-art review of pathophysiology, diagnosis, and management," *Cardiovasc Revasc Med*, vol. 21, no. 9, pp. 1157–1163, 2020.

[89] R.-X. Yin, D.-Z. Yang, and J.-Z. Wu, "Nanoparticle drug- and gene-eluting stents for the prevention and treatment of coronary restenosis," *Theranostics*, vol. 4, no. 2, pp. 175–200, 2014.

[90] R. Kornowski, M. K. Hong, F. O. Tio, O. Bramwell, H. Wu, and M. B. Leon, "In-stent restenosis: Contributions of inflammatory responses and arterial injury to neointimal hyperplasia," *J Am Coll Cardiol*, vol. 31, no. 1, pp. 224–230, 1998.

[91] R. S. Schwartz, K. C. Huber, J. G. Murphy, W. D. Edwards, A. R. Camrud, R. E. Vlietstra, and D. R. Holmes, "Restenosis and the proportional neointimal response to coronary artery injury: Results in a porcine model," *J Am Coll Cardiol*, vol. 19, no. 2, pp. 267–274, 1992.

[92] C. Lally, F. Dolan, and P. Prendergast, "Cardiovascular stent design and vessel stresses: a finite element analysis," *J Biomech*, vol. 38, no. 8, pp. 1574–1581, 2005.

[93]   C. Rogers and E. R. Edelman, "Endovascular stent design dictates experimental restenosis and thrombosis," *Circ*, vol. 91, no. 12, pp. 2995–3001, 1995.

[94]   H. Zahedmanesh and C. Lally, "Determination of the influence of stent strut thickness using the finite element method: implications for vascular injury and in-stent restenosis," *Med Biol Eng Comput*, vol. 47, no. 4, pp. 385–393, 2009.

[95]   K. Manjunatha, M. Behr, F. Vogt, and S. Reese, "A multiphysics modeling approach for in-stent restenosis," *Comput Biol Med*, vol. 150, p. 106166, 2022.

[96]   M. I. Converse, R. G. Walther, J. T. Ingram, Y. Li, S. M. Yu, and K. L. Monson, "Detection and characterization of molecular-level collagen damage in overstretched cerebral arteries," *Acta Biomater*, vol. 67, pp. 307–318, 2018.

[97]   R. He, L. Zhao, V. Silberschmidt, Y. Liu, and F. Vogt, "Patient-specific modelling of stent overlap: Lumen gain, tissue damage and in-stent restenosis," *J Mech Behav Biomed Mater*, vol. 109, p. 103836, 2020.

[98]   R. He, E. Langi, R. Garrard, M. M. Attallah, V. V. Silberschmidt, F. Vogt, and L. Zhao, "In silico evaluation of additively manufactured 316l stainless steel stent in a patient-specific coronary artery," *Med Eng Phys*, vol. 109, p. 103909, 2022.

[99]   O. M. McGee, S. Geraghty, C. Hughes, P. Jamshidi, D. P. Kenny, M. M. Attallah, and C. Lally, "An investigation into patient-specific 3d printed titanium stents and the use of etching to overcome selective laser melting design constraints," *J Mech Behav Biomed Mater*, vol. 134, p. 105388, 2022.

[100] P. McHugh, A. Barakat, and S. McGinty, "Medical stents: State of the art and future directions," *Ann Biomed Eng*, vol. 44, no. 2, pp. 274–275, 2015.

[101] S. K. Misra, F. Ostadhossein, R. Babu, J. Kus, D. Tankasala, A. Sutrisno, K. A. Walsh, C. R. Bromfield, and D. Pan, "3d-printed multidrug-eluting stent from graphene-nanoplatelet-doped biodegradable polymer composite," *Adv Healthc Mater*, vol. 6, no. 11, p. 1700008, 2017.

[102] I. Ríos-Ruiz, M. Á. Martínez, and E. Peña, "Is location a significant parameter in the layer dependent dissection properties of the aorta?," *Biomech Model Mechanobiol*, vol. 21, no. 6, pp. 1887–1901, 2022.

[103] I. Ríos-Ruiz, M. Cilla, M. A. Martínez, and E. Peña, "Methodology to calibrate the dissection properties of aorta layers from two sets of experimental measurements," *Mathematics*, vol. 9, no. 14, p. 1593, 2021.

[104] D. C. Angouras, E. P. Kritharis, and D. P. Sokolis, "Regional distribution of delamination strength in ascending thoracic aortic aneurysms," *J Mech Behav Biomed Mater*, vol. 98, pp. 58–70, 2019.

[105] C. Manopoulos, I. Karathanasis, I. Kouerinis, D. C. Angouras, A. Lazaris, S. Tsangaris, and D. P. Sokolis, "Identification of regional/layer differences in failure properties and thickness as important biomechanical factors responsible for the initiation of aortic dissections," *J Biomech*, vol. 80, pp. 102–110, 2018.

[106] D. Mohan and J. W. Melvin, "Failure properties of passive human aortic tissue. i—uniaxial tension tests," *J Biomech*, vol. 15, no. 11, pp. 887–902, 1982.

[107] J. A. Peña, M. A. Martínez, and E. Peña, "Failure damage mechanical properties of thoracic and abdominal porcine aorta layers and related constitutive modeling: phenomenological and microstructural approach," *Biomech Model Mechanobiol*, vol. 18, pp. 1709–1730, 2019.

[108] P. P. Purslow, "Positional variations in fracture toughness, stiffness and strength of descending thoracic pig aorta," *J Biomech*, vol. 16, no. 11, pp. 947–953, 1983.

[109] Y. Xuan, A. D. Wisneski, Z. Wang, M. Lum, S. Kumar, J. Pallone, N. Flores, J. Inman, L. Lai, J. Lin, J. M. Guccione, E. E. Tseng, and L. Ge, "Regional biomechanical and failure properties of healthy human ascending aorta and root," *J Mech Behav Biomed Mater*, vol. 123, p. 104705, 2021.

[110] C. M. Witzenburg, R. Y. Dhume, S. B. Shah, C. E. Korenczuk, H. P. Wagner, P. W. Alford, and V. H. Barocas, "Failure of the porcine ascending aorta: Multidirectional experiments and a unifying microstructural model," *J Biomech Eng*, vol. 139, no. 3, 2017.

[111] C. van Baardwijk and M. R. Roach, "Factors in the propagation of aortic dissections in canine thoracic aortas," *J Biomech*, vol. 20, no. 1, pp. 67–73, 1987.

[112] B. FitzGibbon and P. McGarry, "Development of a test method to investigate mode II fracture and dissection of arteries," *Acta Biomater*, vol. 121, pp. 444–460, 2021.

[113] L. Horný, L. Roubalová, J. Kronek, H. Chlup, T. Adámek, A. Blanková, Z. Petřivý, T. Suchý, and P. Tichý, "Correlation between age, location, orientation, loading velocity and delamination strength in the human aorta," *J Mech Behav Biomed Mater*, vol. 133, p. 105340, 2022.

[114] M. Kozuń, "Delamination properties of the human thoracic arterial wall with early stage of atherosclerosis lesions," *J Theor Appl Mech*, vol. 54, no. 1, p. 229, 2016.

[115] M. Kozuń, M. Kobielarz, A. Chwiłkowska, and C. Pezowicz, "The impact of development of atherosclerosis on delamination resistance of the thoracic aortic wall," *J Mech Behav Biomed Mater*, vol. 79, pp. 292–300, 2018.

[116] M. Myneni, A. Rao, M. Jiang, M. R. Moreno, K. R. Rajagopal, and C. C. Benjamin, "Segmental variations in the peel characteristics of the porcine thoracic aorta," *Ann Biomed Eng*, vol. 48, no. 6, pp. 1751–1767, 2020.

[117] C. Noble, N. Smulders, R. Lewis, M. J. Carré, S. E. Franklin, S. MacNeil, and Z. A. Taylor, "Controlled peel testing of a model tissue for diseased aorta," *J Biomech*, vol. 49, no. 15, pp. 3667–3675, 2016.

[118] S. Pasta, J. A. Phillippi, T. G. Gleason, and D. A. Vorp, "Effect of aneurysm on the mechanical dissection properties of the human ascending thoracic aorta," *J Thorac Cardiovasc Surg*, vol. 143, no. 2, pp. 460–467, 2012.

[119] D. P. Sokolis and S. A. Papadodima, "Regional delamination strength in the human aorta underlies the anatomical localization of the dissection channel," *J Biomech*, p. 111174, 2022.

[120] J. Tong, T. Cohnert, P. Regitnig, J. Kohlbacher, R. Birner-Gruenberger, A. Schriefl, G. Sommer, and G. Holzapfel, "Variations of dissection properties and mass fractions with thrombus age in human abdominal aortic aneurysms," *J Biomech*, vol. 47, no. 1, pp. 14–23, 2014.

[121] R. Wang, X. Yu, and Y. Zhang, "Mechanical and structural contributions of elastin and collagen fibers to interlamellar bonding in the arterial wall," *Biomech Model Mechanobiol*, vol. 20, no. 1, pp. 93–106, 2021.

[122] J. Tong, G. Sommer, P. Regitnig, and G. A. Holzapfel, "Dissection properties and mechanical strength of tissue components in human carotid bifurcations," *Ann Biomed Eng*, vol. 39, no. 6, pp. 1703–1719, 2011.

[123] Y. Wang, J. A. Johnson, F. G. Spinale, M. A. Sutton, and S. M. Lessner, "Quantitative measurement of dissection resistance in intimal and medial layers of human coronary arteries," *Exp Mech*, vol. 54, no. 4, pp. 677–683, 2013.

[124] D. Divchev, T. Najjar, F. Tillwich, T. Rehders, H. Palisch, and C. A. Nienaber, "Predicting long-term outcomes of acute aortic dissection: a focus on gender," *Expert Rev Cardiovasc Ther*, vol. 13, no. 3, pp. 325–331, 2015.

[125] L. V. Huckaby, I. Sultan, S. Trimarchi, B. Leshnower, E. P. Chen, D. R. Brinster, T. Myrmel, A. L. Estrera, D. G. Montgomery, A. Korach, H.-H. Eckstein, J. S. Coselli, T. Ota, C. A. Kaiser, K. A. Eagle, H. J. Patel, and T. G. Gleason, "Sex-based aortic dissection outcomes from the international registry of acute aortic dissection," *Ann Thorac Surg*, vol. 113, no. 2, pp. 498–505, 2022.

[126] C. A. Nienaber, R. Fattori, R. H. Mehta, B. M. Richartz, A. Evangelista, M. Petzsch, J. V. Cooper, J. L. Januzzi, H. Ince, U. Sechtem, E. Bossone, J. Fang, D. E. Smith, E. M. Isselbacher, L. A. Pape, and K. A. Eagle, "Gender-related differences in acute aortic dissection," *Circ*, vol. 109, no. 24, pp. 3014–3021, 2004.

[127] T. C. Gasser and G. A. Holzapfel, "Modeling the propagation of arterial dissection," *Eur J Mech A Solids*, vol. 25, no. 4, pp. 617–633, 2006.

[128] C. Noble, O. van der Sluis, R. M. Voncken, O. Burke, S. E. Franklin, R. Lewis, and Z. A. Taylor, "Simulation of arterial dissection by a penetrating external body using cohesive zone modelling," *J Mech Behav Biomed Mater*, vol. 71, pp. 95–105, 2017.

[129] S. Pasta, J. A. Phillippi, A. Tsamis, A. D'Amore, G. M. Raffa, M. Pilato, C. Scardulla, S. C. Watkins, W. R. Wagner, T. G. Gleason, and D. A. Vorp, "Constitutive modeling of ascending thoracic aortic aneurysms using microstructural parameters," *Med Eng Phys*, vol. 38, no. 2, pp. 121–130, 2016.

[130] S. G. Sassani, S. Tsangaris, and D. P. Sokolis, "Layer- and region-specific material characterization of ascending thoracic aortic aneurysms by microstructure-based models," *J Biomech*, vol. 48, no. 14, pp. 3757–3765, 2015.

[131] X. Yu, B. Suki, and Y. Zhang, "Avalanches and power law behavior in aortic dissection propagation," *Sci Adv*, vol. 6, no. 21, 2020.

[132] A. BenSaïda, "Shapiro-wilk and shapiro-francia normality tests.," *(https://www.mathworks.com/matlabcentral/fileexchange/13964-shapiro-wilk-and-shapiro-francia-normality-tests), MATLAB Central File Exchange.*, 2021. Retrieved August 28, 2021.

[133] L. A. Davis, S. E. Stewart, C. G. C. III, B. A. Snyder, M. A. Sutton, and S. M. Lessner, "Characterization of fracture behavior of human atherosclerotic fibrous caps using a miniature single edge notched tensile test," *Acta Biomater*, vol. 43, pp. 101–111, 2016.

[134] A. N. Gent and S. Y. Kaang, "Effect of peel angle upon peel force," *J Adhes*, vol. 24, no. 2-4, pp. 173–181, 1987.

[135] Y. Zhang, D. Hazelton, A. Knoll, J. Duval, P. Brownsey, S. Repnoy, S. Soloveichik, A. Sundaram, R. McClure, G. Majkic, and V. Selvamanickam, "Adhesion strength study of IBAD–MOCVD-based 2g HTS wire using a peel test," *Phys C Supercond Appl*, vol. 473, pp. 41–47, 2012.

[136] H. W. Haslach, A. Siddiqui, A. Weerasooriya, R. Nguyen, J. Roshgadol, N. Monforte, and E. McMahon, "Fracture mechanics of shear crack propagation and dissection in the healthy bovine descending aortic media," *Acta Biomater*, vol. 68, pp. 53–66, 2018.

[137] M. R. Roach and S. H. Song, "Variations in strength of the porcine aorta as a function of location," *Clin Investig Med*, vol. 17, no. 4, pp. 308–318, 1994.

[138] D. P. Sokolis, G. D. Savva, S. A. Papadodima, and S. K. Kourkoulis, "Regional distribution of circumferential residual strains in the human aorta according to age and gender," *J Mech Behav Biomed Mater*, vol. 67, pp. 87–100, 2017.

[139] J. Brunet, B. Pierrat, and P. Badel, "Review of current advances in the mechanical description and quantification of aortic dissection mechanisms," *IEEE Rev Biomed Eng*, vol. 14, pp. 240–255, 2021.

[140] T. C. Gasser, R. W. Ogden, and G. A. Holzapfel, "Hyperelastic modelling of arterial layers with distributed collagen fibre orientations," *J R Soc Interface*, vol. 3, no. 6, pp. 15–35, 2005.

[141] A. J. Spencer, "Part iii. theory of invariants," *Continuum Physics*, vol. 1, pp. 239–353, 1971.

[142] J. A. Nelder and R. Mead, "A simplex method for function minimization," *Comput J*, vol. 7, no. 4, pp. 308–313, 1965.

[143] T. E. Carew, R. N. Vaishnav, and D. J. Patel, "Compressibility of the arterial wall," *Circ Res*, vol. 23, no. 1, pp. 61–68, 1968.

[144] C. Forsell and T. C. Gasser, "Numerical simulation of the failure of ventricular tissue due to deep penetration: The impact of constitutive properties," *J Biomech*, vol. 44, no. 1, pp. 45–51, 2011.

[145] J. Lemaitre, "A continuous damage mechanics model for ductile fracture," *J Eng Mater Technol*, vol. 107, no. 1, pp. 83–89, 1985.

[146] A. Giudici, B. Spronck, I. Wilkinson, and A. Khir, "Tri-layered constitutive modelling unveils functional differences between the pig ascending and lower thoracic aorta," *J Mech Behav Biomed Mater*, vol. 141, p. 105752, 2023.

[147] D. P. Sokolis, "Regional distribution of layer-specific circumferential residual deformations and opening angles in the porcine aorta," *J Biomech*, vol. 96, p. 109335, 2019.

[148] G. A. Holzapfel, K. Linka, S. Sherifova, and C. J. Cyron, "Predictive constitutive modelling of arteries by deep learning," *J R Soc Interface*, vol. 18, no. 182, p. 20210411, 2021.

[149] J.-J. Chiu, D. L. Wang, S. Chien, R. Skalak, and S. Usami, "Effects of disturbed flow on endothelial cells," *J Biomech Eng*, vol. 120, no. 1, pp. 2–8, 1998.

[150] M. H. Friedman, "Some atherosclerosis may be a consequence of the normal adaptive vascular response to shear," *Atherosclerosis*, vol. 82, no. 3, pp. 193–196, 1990.

[151] A. P. Sawchuk, J. L. Unthank, T. E. Davis, and M. C. Dalsing, "A prospective, in vivo study of the relationship between blood flow hemodynamics and atherosclerosis in a hyperlipidemic swine model," *J Vasc Surg*, vol. 19, no. 1, pp. 58–64, 1994.

[152] M. L. Jackson, A. R. Bond, and S. J. George, "Mechanobiology of the endothelium in vascular health and disease: in vitro shear stress models," *Cardiovasc Drugs Ther*, 2022.

[153] F. Gijsen, Y. Katagiri, P. Barlis, C. Bourantas, C. Collet, U. Coskun, J. Daemen, J. Dijkstra, E. Edelman, P. Evans, K. van der Heiden, R. Hose, B.-K. Koo, R. Krams, A. Marsden, F. Migliavacca, Y. Onuma, A. Ooi, E. Poon, ..., and P. Serruys, "Expert recommendations on the assessment of wall shear stress in human coronary arteries: existing methodologies, technical considerations, and clinical applications," *Eur Heart J*, vol. 40, no. 41, pp. 3421–3433, 2019.

[154] B. C. Berk, "Atheroprotective signaling mechanisms activated by steady laminar flow in endothelial cells," *Circ*, vol. 117, no. 8, pp. 1082–1089, 2008.

[155] D. N. Ku, D. P. Giddens, C. K. Zarins, and S. Glagov, "Pulsatile flow and atherosclerosis in the human carotid bifurcation. positive correlation between plaque location and low oscillating shear stress.," *Arterioscler Thromb Vasc Biol*, vol. 5, no. 3, pp. 293–302, 1985.

[156] M. E. Fallon, R. Mathews, and M. T. Hinds, "In vitro flow chamber design for the study of endothelial cell (patho)physiology," *J Biomech Eng*, vol. 144, no. 2, 2021.

[157] P. F. Davies, "Hemodynamic shear stress and the endothelium in cardiovascular pathophysiology," *Nat Clin Pract Cardiovasc Med*, vol. 6, no. 1, pp. 16–26, 2008.

[158] C. Wang, B. M. Baker, C. S. Chen, and M. A. Schwartz, "Endothelial cell sensing of flow direction," *Arterioscler Thromb Vasc Biol*, vol. 33, no. 9, pp. 2130–2136, 2013.

[159] B. L. Langille and S. L. Adamson, "Relationship between blood flow direction and endothelial cell orientation at arterial branch sites in rabbits and mice.," *Circ Res*, vol. 48, no. 4, pp. 481–488, 1981.

[160] J. Silkworth, W. Stehbens, and D. Phil, "The shape of endothelial cells in en face preparations of rabbit blood vessels," *Angiology*, vol. 26, no. 6, pp. 474–487, 1975.

[161] S. Cooper, M. Dick, A. Emmott, P. Jonak, L. Rouleau, and R. L., "In vitro leukocyte adhesion in endothelial tissue culture models under flow," in *Biomedical Science, Engineering and Technology*, InTech, 2012.

[162] F. Tovar-Lopez, P. Thurgood, C. Gilliam, N. Nguyen, E. Pirogova, K. Khosh-manesh, and S. Baratchi, "A microfluidic system for studying the effects of disturbed flow on endothelial cells," *Front Bioeng Biotechnol*, vol. 7, 2019.

[163] J. A. Frangos, L. V. McIntire, and S. G. Eskin, "Shear stress induced stimulation of mammalian cell metabolism," *Biotechnol Bioeng*, vol. 32, no. 8, pp. 1053–1060, 1988.

[164] P. Alcaide, S. Auerbach, and F. W. Luscinskas, "Neutrophil recruitment under shear flow: It's all about endothelial cell rings and gaps," *Microcirculation*, vol. 16, no. 1, pp. 43–57, 2009.

[165] B. Chung, A. Robertson, and D. Peters, "The numerical design of a parallel plate flow chamber for investigation of endothelial cell response to shear stress," *Comput Struct*, vol. 81, no. 8-11, pp. 535–546, 2003.

[166] A. K. Wong, P. LLanos, N. Boroda, S. R. Rosenberg, and S. Y. Rabbany, "A parallel-plate flow chamber for mechanical characterization of endothelial cells exposed to laminar shear stress," *Cell Mol Bioeng*, vol. 9, no. 1, pp. 127–138, 2015.

[167] J. M. Berg and T. Dallas, "Peristaltic pumps," in *Encyclopedia of Microfluidics and Nanofluidics*, pp. 1626–1633, Springer US.

[168] J.-J. Chiu and S. Chien, "Effects of disturbed flow on vascular endothelium: Pathophysiological basis and clinical perspectives," *Physiol Rev*, vol. 91, no. 1, pp. 327–387, 2011.

[169] Y. S. Chatzizisis, A. U. Coskun, M. Jonas, E. R. Edelman, C. L. Feldman, and P. H. Stone, "Role of endothelial shear stress in the natural history of coronary atherosclerosis and vascular remodeling," *J Am Coll Cardiol*, vol. 49, no. 25, pp. 2379–2393, 2007.

[170] C. F. Dewey, S. R. Bussolari, M. A. Gimbrone, and P. F. Davies, "The dynamic response of vascular endothelial cells to fluid shear stress," *J Biomech Eng*, vol. 103, no. 3, pp. 177–185, 1981.

[171] P. Azerad and E. Bänsch, "Quasi-stability of the primary flow in a cone and plate viscometer," *J Math Fluid Mech*, vol. 6, no. 3, 2004.

[172] B. R. Blackman, G. García-Cardeña, and M. A. Gimbrone, "A new in vitro model to evaluate differential responses of endothelial cells to simulated arterial shear stress waveforms," *J Biomech Eng*, vol. 124, no. 4, pp. 397–407, 2002.

[173] M. Arshad, M. Ghim, Y. Mohamied, S. J. Sherwin, and P. D. Weinberg, "Endothelial cells do not align with the mean wall shear stress vector," *J R Soc Interface*, vol. 18, no. 174, p. 20200772, 2021.

[174] C. M. Warboys, M. Ghim, and P. D. Weinberg, "Understanding mechanobiology in cultured endothelium: A review of the orbital shaker method," *Atherosclerosis*, vol. 285, pp. 170–177, 2019.

[175] P. Alpresa, S. Sherwin, P. Weinberg, and M. van Reeuwijk, "Orbitally shaken shallow fluid layers. i. regime classification," *Phys Fluids*, vol. 30, no. 3, p. 032107, 2018.

[176] P. Alpresa, S. Sherwin, P. Weinberg, and M. van Reeuwijk, "Orbitally shaken shallow fluid layers. II. an improved wall shear stress model," *Phys Fluids*, vol. 30, no. 3, p. 032108, 2018.

[177] A. Dardik, L. Chen, J. Frattini, H. Asada, F. Aziz, F. A. Kudo, and B. E. Sumpio, "Differential effects of orbital and laminar shear stress on endothelial cells," *J Vasc Surg*, vol. 41, no. 5, pp. 869–880, 2005.

[178] M. Ghim, K. T. Pang, M. Arshad, X. Wang, and P. D. Weinberg, "A novel method for segmenting growth of cells in sheared endothelial culture reveals the secretion of an anti-inflammatory mediator," *J Biol Eng*, vol. 12, no. 1, 2018.

[179] Y. Mohamied, E. M. Rowland, E. L. Bailey, S. J. Sherwin, M. A. Schwartz, and P. D. Weinberg, "Change of direction in the biomechanics of atherosclerosis," *Ann Biomed Eng*, vol. 43, no. 1, pp. 16–25, 2014.

[180] Y. Tokuda, M.-H. Song, Y. Ueda, A. Usui, T. Akita, S. Yoneyama, and S. Maruyama, "Three-dimensional numerical simulation of blood flow in the aortic arch during cardiopulmonary bypass," *Eur J Cardiothorac Surg*, vol. 33, no. 2, pp. 164–167, 2008.

[181] R. Estrada, G. A. Giridharan, M.-D. Nguyen, T. J. Roussel, M. Shakeri, V. Parichehreh, S. D. Prabhu, and P. Sethu, "Endothelial cell culture model for replication of physiological profiles of pressure, flow, stretch, and shear stress iin vitro/i," *Anal Chem*, vol. 83, no. 8, pp. 3170–3177, 2011.

[182] N. V. Menon, H. M. Tay, K. T. Pang, R. Dalan, S. C. Wong, X. Wang, K. H. H. Li, and H. W. Hou, "A tunable microfluidic 3d stenosis model to study leukocyte-endothelial interactions in atherosclerosis," *APL Bioeng*, vol. 2, no. 1, p. 016103, 2018.

[183] T. B. Owatverot, S. J. Oswald, Y. Chen, J. J. Wille, and F. C.-P. Yin, "Effect of combined cyclic stretch and fluid shear stress on endothelial cell morphological responses," *J Biomech Eng*, vol. 127, no. 3, pp. 374–382, 2005.

[184] A. Shimizu, W. H. Goh, S. Itai, M. Hashimoto, S. Miura, and H. Onoe, "ECM-based microchannel for culturing iin vitro/i vascular tissues with simultaneous perfusion and stretch," *Lab Chip*, vol. 20, no. 11, pp. 1917–1927, 2020.

[185] W. Zheng, B. Jiang, D. Wang, W. Zhang, Z. Wang, and X. Jiang, "A microfluidic flow-stretch chip for investigating blood vessel biomechanics," *Lab Chip*, vol. 12, no. 18, p. 3441, 2012.

[186] D. Meza, L. Abejar, D. A. Rubenstein, and W. Yin, "A shearing-stretching device that can apply physiological fluid shear stress and cyclic stretch concurrently to endothelial cells," *J Biomech Eng*, vol. 138, no. 3, 2016.

[187] A. Benbrahim, G. J. L'Italien, B. B. Milinazzo, D. F. Warnock, S. Dhara, J. P. Gertler, R. W. Orkin, and W. M. Abbott, "A compliant tubular device to study the influences of wall strain and fluid shear stress on cells of the vascular wall," *J Vasc Surg*, vol. 20, no. 2, pp. 184–194, 1994.

[188] J. E. Moore, E. Bürki, A. Suciu, S. Zhao, M. Burnier, H. R. Brunner, and J.-J. Meister, "A device for subjecting vascular endothelial cells to both fluid shear stress and circumferential cyclic stretch," *Ann Biomed Eng*, vol. 22, no. 4, pp. 416–422, 1994.

[189] Y. Qiu and J. M. Tarbell, "Interaction between wall shear stress and circumferential strain affects endothelial cell biochemical production," *J Vasc Res*, vol. 37, no. 3, pp. 147–157, 2000.

[190] M. Toda, K. Yamamoto, N. Shimizu, S. Obi, S. Kumagaya, T. Igarashi, A. Kamiya, and J. Ando, "Differential gene responses in endothelial cells exposed to a combination of shear stress and cyclic stretch," *J Biotechnol*, vol. 133, no. 2, pp. 239–244, 2008.

[191] P. F. Davies, A. Remuzzi, E. J. Gordon, C. F. Dewey, and M. A. Gimbrone, "Turbulent fluid shear stress induces vascular endothelial cell turnover in vitro.," *Proc Natl Acad Sci U S A*, vol. 83, no. 7, pp. 2114–2117, 1986.

[192] C. Galbraith, R. Skalak, and S. Chien, "Shear stress induces spatial reorganization of the endothelial cell cytoskeleton," *Cell Motil Cytoskelet*, vol. 40, no. 4, pp. 317–330, 1998.

[193] G. Helmlinger, R. V. Geiger, S. Schreck, and R. M. Nerem, "Effects of pulsatile flow on cultured vascular endothelial cell morphology," *J Biomech Eng*, vol. 113, no. 2, pp. 123–131, 1991.

[194] M. J. Levesque and R. M. Nerem, "The elongation and orientation of cultured endothelial cells in response to shear stress," *J Biomech Eng*, vol. 107, no. 4, pp. 341–347, 1985.

[195] E. A. Osborn, A. Rabodzey, C. F. Dewey, and J. H. Hartwig, "Endothelial actin cytoskeleton remodeling during mechanostimulation with fluid shear stress," *Am J Physiol Cell Physiol*, vol. 290, no. 2, pp. C444–C452, 2006.

[196] X. Zhang, D. J. Huk, Q. Wang, J. Lincoln, and Y. Zhao, "A microfluidic shear device that accommodates parallel high and low stress zones within the same culturing chamber," *Biomicrofluidics*, vol. 8, no. 5, p. 054106, 2014.

[197] N. Bergh, P. Larsson, E. Ulfhammer, and S. Jern, "Effect of shear stress, statins and TNF- on hemostatic genes in human endothelial cells," *Biochem Biophys Res Commun*, vol. 420, no. 1, pp. 166–171, 2012.

[198] L. Chau, M. Doran, and J. Cooper-White, "A novel multishear microdevice for studying cell mechanics," *Lab Chip*, vol. 9, no. 13, p. 1897, 2009.

[199] T. A. Russo, A. M. M. Banuth, H. B. Nader, and J. L. Dreyfuss, "Altered shear stress on endothelial cells leads to remodeling of extracellular matrix and induction of angiogenesis," *PLoS One*, vol. 15, no. 11, p. e0241040, 2020.

[200] N. Azuma, N. Akasaka, H. Kito, M. Ikeda, V. Gahtan, T. Sasajima, and B. E. Sumpio, "Role of p38 MAP kinase in endothelial cell alignment induced by fluid shear stress," *Am J Physiol Heart Circ Physiol*, vol. 280, no. 1, pp. H189–H197, 2001.

[201] S. McCue, D. Dajnowiec, F. Xu, M. Zhang, M. R. Jackson, and B. L. Langille, "Shear stress regulates forward and reverse planar cell polarity of vascular endothelium in vivo and in vitro," *Circ Res*, vol. 98, no. 7, pp. 939–946, 2006.

[202] A. Chakraborty, S. Chakraborty, V. R. Jala, B. Haribabu, M. K. Sharp, and R. E. Berson, "Effects of biaxial oscillatory shear stress on endothelial cell proliferation and morphology," *Biotechnol Bioeng*, vol. 109, no. 3, pp. 695–707, 2011.

[203] B. Wojciak-Stothard and A. J. Ridley, "Shear stress–induced endothelial cell polarization is mediated by rho and rac but not cdc42 or PI 3-kinases," *J Cell Biol*, vol. 161, no. 2, pp. 429–439, 2003.

[204] G. Dai, M. R. Kaazempur-Mofrad, S. Natarajan, Y. Zhang, S. Vaughn, B. R. Blackman, R. D. Kamm, G. García-Cardeña, and M. A. Gimbrone, "Distinct endothelial phenotypes evoked by arterial waveforms derived from atherosclerosis-susceptible and -resistant regions of human vasculature," *Proc Natl Acad Sci U S A*, vol. 101, no. 41, pp. 14871–14876, 2004.

[205] M. Ghim, K. T. Pang, S. A. Burnap, F. Baig, X. Yin, M. Arshad, M. Mayr, and P. D. Weinberg, "Endothelial cells exposed to atheroprotective flow secrete follistatin-like 1 protein which reduces transcytosis and inflammation," *Atherosclerosis*, vol. 333, pp. 56–66, 2021.

[206] G. A. Truskey, K. M. Barber, T. C. Robey, L. A. Olivier, and M. P. Combs, "Characterization of a sudden expansion flow chamber to study the response of endothelium to flow recirculation," *J Biomech Eng*, vol. 117, no. 2, pp. 203–210, 1995.

[207] D. L. Fry, "Certain chemorheologic considerations regarding the blood vascular interface with particular reference to coronary artery disease," *Circ*, vol. 40, no. 5s4, 1969.

[208] P.-A. Doriot, P.-A. Dorsaz, L. Dorsaz, E. D. Benedetti, P. Chatelain, and P. Delafontaine, "In-vivo measurements of wall shear stress in human coronary arteries," *Coron Artery Dis*, vol. 11, no. 6, pp. 495–502, 2000.

[209] E. Berthier, E. W. K. Young, and D. Beebe, "Engineers are from PDMS-land, biologists are from polystyrenia," *Lab Chip*, vol. 12, no. 7, p. 1224, 2012.

[210] S. Beverung, J. Wu, and R. Steward, "Lab-on-a-chip for cardiovascular physiology and pathology," *Micromachines*, vol. 11, no. 10, p. 898, 2020.

[211] "Test method for tensile properties of plastics."

[212] "Plásticos. determinación de las propiedades en tracción."

[213] Y. Huo and G. S. Kassab, "Effect of compliance and hematocrit on wall shear stress in a model of the entire coronary arterial tree," *J Appl Physiol*, vol. 107, no. 2, pp. 500–505, 2009.

[214] M. B. Dancu, D. E. Berardi, J. P. V. Heuvel, and J. M. Tarbell, "Asynchronous shear stress and circumferential strain reduces endothelial NO synthase and cyclooxygenase-2 but induces endothelin-1 gene expression in endothelial cells," *Arterioscler Thromb Vasc Biol*, vol. 24, no. 11, pp. 2088–2094, 2004.

[215] Y. Tardy, N. Resnick, T. Nagel, M. Gimbrone, and C. Dewey, "Shear stress gradients remodel endothelial monolayers in vitro via a cell proliferation-migration-loss cycle," *Arterioscler Thromb Vasc Biol*, vol. 17, no. 11, pp. 3102–3106, 1997.

[216] L. Rouleau, J. Rossi, and R. L. Leask, "Concentration and time effects of dextran exposure on endothelial cell viability, attachment, and inflammatory marker expression in vitro," *Ann Biomed Eng*, vol. 38, no. 4, pp. 1451–1462, 2010.

[217] A. R. Wechezak, D. E. Coan, R. F. Viggers, and L. R. Sauvage, "Dextran increases survival of subconfluent endothelial cells exposed to shear stress," *Am J Physiol Heart Circ Physiol*, vol. 264, no. 2, pp. H520–H525, 1993.

[218] F. Carrasco, E. Chornet, R. P. Overend, and J. Costa, "A generalized correlation for the viscosity of dextrans in aqueous solutions as a function of temperature, concentration, and molecular weight at low shear rates," *J Appl Polym*, vol. 37, no. 8, pp. 2087–2098, 1989.

[219] T. Pravinraj and R. Patrikar, "Modeling and characterization of surface roughness effect on fluid flow in a polydimethylsiloxane microchannel using a fractal based lattice boltzmann method," *AIP Adv*, vol. 8, no. 6, p. 065112, 2018.

[220] D. Meza, B. Musmacker, E. Steadman, T. Stransky, D. A. Rubenstein, and W. Yin, "Endothelial cell biomechanical responses are dependent on both fluid shear stress and tensile strain," *Cell Mol Bioeng*, vol. 12, no. 4, pp. 311–325, 2019.

[221] R. M. Pedrigi, K. I. Papadimitriou, A. Kondiboyina, S. Sidhu, J. Chau, M. B. Patel, D. C. Baeriswyl, E. M. Drakakis, and R. Krams, "Disturbed cyclical stretch of endothelial cells promotes nuclear expression of the pro-atherogenic transcription factor NF-b," *Ann Biomed Eng*, vol. 45, no. 4, pp. 898–909, 2016.

[222] W. Zheng, R. Huang, B. Jiang, Y. Zhao, W. Zhang, and X. Jiang, "An early-stage atherosclerosis research model based on microfluidics," *Small*, vol. 12, no. 15, pp. 2022–2034, 2016.

[223] C. S. Hughes, L. M. Postovit, and G. A. Lajoie, "Matrigel: A complex protein mixture required for optimal growth of cell culture," *Proteomics*, vol. 10, no. 9, pp. 1886–1890, 2010.

[224] P. F. Costa, H. J. Albers, J. E. A. Linssen, H. H. T. Middelkamp, L. van der Hout, R. Passier, A. van den Berg, J. Malda, and A. D. van der Meer, "Mimicking arterial thrombosis in a 3d-printed microfluidic in vitro vascular model based on computed tomography angiography data," *Lab Chip*, vol. 17, no. 16, pp. 2785–2792, 2017.

[225] J. Schindelin, I. Arganda-Carreras, E. Frise, V. Kaynig, M. Longair, T. Pietzsch, S. Preibisch, C. Rueden, S. Saalfeld, B. Schmid, J.-Y. Tinevez, D. J. White, V. Hartenstein, K. Eliceiri, P. Tomancak, and A. Cardona, "Fiji: an open-source platform for biological-image analysis," *Nat Methods*, vol. 9, no. 7, pp. 676–682, 2012.

[226] M. Ghim, P. Alpresa, S.-W. Yang, S. T. Braakman, S. G. Gray, S. J. Sherwin, M. van Reeuwijk, and P. D. Weinberg, "Visualization of three pathways for macromolecule transport across cultured endothelium and their modification by flow," *Am J Physiol Heart Circ Physiol*, vol. 313, no. 5, pp. H959–H973, 2017.

[227] S. N. Saw, C. Dawn, A. Biswas, C. N. Z. Mattar, and C. H. Yap, "Characterization of the in vivo wall shear stress environment of human fetus umbilical arteries and veins," *Biomech Model Mechanobiol*, vol. 16, no. 1, pp. 197–211, 2016.

[228] C. Conway, J. P. McGarry, and P. E. McHugh, "Modelling of atherosclerotic plaque for use in a computational test-bed for stent angioplasty," *Ann Biomed Eng*, vol. 42, no. 12, pp. 2425–2439, 2014.

[229] J. Escuer, M. Cebollero, E. Peña, S. McGinty, and M. A. Martínez, "How does stent expansion alter drug transport properties of the arterial wall?," *J Mech Behav Biomed Mater*, vol. 104, p. 103610, 2020.

[230] A. García, E. Peña, and M. Martínez, "Influence of geometrical parameters on radial force during self-expanding stent deployment. application for a variable radial stiffness stent," *J Mech Behav Biomed Mater*, vol. 10, pp. 166–175, 2012.

[231] F. Migliavacca, L. Petrini, P. Massarotti, S. Schievano, F. Auricchio, and G. Dubini, "Stainless and shape memory alloy coronary stents: a computational study on the interaction with the vascular wall," *Biomech Model Mechanobiol*, vol. 2, no. 4, 2004.

[232] H. Zahedmanesh, D. J. Kelly, and C. Lally, "Simulation of a balloon expandable stent in a realistic coronary artery—determination of the optimum modelling strategy," *J Biomech*, vol. 43, no. 11, pp. 2126–2132, 2010.

[233] H. Zahedmanesh and C. Lally, "A multiscale mechanobiological modelling framework using agent-based models and finite element analysis: application to vascular tissue engineering," *Biomech Model Mechanobiol*, vol. 11, no. 3-4, pp. 363–377, 2011.

[234] H. Zahedmanesh, H. V. Oosterwyck, and C. Lally, "A multi-scale mechanobiological model of in-stent restenosis: deciphering the role of matrix metalloproteinase and extracellular matrix changes," *Comput Methods Biomech Biomed Engin*, vol. 17, no. 8, pp. 813–828, 2012.

[235] C. J. Boyle, A. B. Lennon, M. Early, D. J. Kelly, C. Lally, and P. J. Prendergast, "Computational simulation methodologies for mechanobiological modelling: a cell-centred approach to neointima development in stents," *Philos Trans A Math Phys Eng Sci*, vol. 368, no. 1921, pp. 2919–2935, 2010.

[236] C. J. Boyle, A. B. Lennon, and P. J. Prendergast, "In silico prediction of the mechanobiological response of arterial tissue: Application to angioplasty and stenting," *J Biomech Eng*, vol. 133, no. 8, 2011.

[237] J. Escuer, M. A. Martínez, S. McGinty, and E. Peña, "Mathematical modelling of the restenosis process after stent implantation," *J R Soc Interface*, vol. 16, no. 157, p. 20190313, 2019.

[238] B. Fereidoonnezhad, R. Naghdabadi, S. Sohrabpour, and G. Holzapfel, "A mechanobiological model for damage-induced growth in arterial tissue with application to in-stent restenosis," *J Mech Phys Solids*, vol. 101, pp. 311–327, 2017.

[239] R. He, L. Zhao, V. V. Silberschmidt, and Y. Liu, "Mechanistic evaluation of long-term in-stent restenosis based on models of tissue damage and growth," *Biomech Model Mechanobiol*, vol. 19, no. 5, pp. 1425–1446, 2020.

[240] J. Hwang, B. H. San, N. J. Turner, L. J. White, D. M. Faulk, S. F. Badylak, Y. Li, and S. M. Yu, "Molecular assessment of collagen denaturation in decellularized tissues using a collagen hybridizing peptide," *Acta Biomater*, vol. 53, pp. 268–278, 2017.

[241] J. L. Zitnay, Y. Li, Z. Qin, B. H. San, B. Depalle, S. P. Reese, M. J. Buehler, S. M. Yu, and J. A. Weiss, "Molecular level detection and localization of mechanical damage in collagen enabled by collagen hybridizing peptides," *Nat Commun*, vol. 8, no. 1, 2017.

[242] J. Hwang, Y. Huang, T. J. Burwell, N. C. Peterson, J. Connor, S. J. Weiss, S. M. Yu, and Y. Li, "In situ imaging of tissue remodeling with collagen hybridizing peptides," *ACS Nano*, vol. 11, no. 10, pp. 9825–9835, 2017.

[243] Y. Li, D. Ho, H. Meng, T. R. Chan, B. An, H. Yu, B. Brodsky, A. S. Jun, and S. M. Yu, "Direct detection of collagenous proteins by fluorescently labeled collagen mimetic peptides," *Bioconjug Chem*, vol. 24, no. 1, pp. 9–16, 2013.

[244] Y. Li, C. A. Foss, D. D. Summerfield, J. J. Doyle, C. M. Torok, H. C. Dietz, M. G. Pomper, and S. M. Yu, "Targeting collagen strands by photo-triggered triple-helix hybridization," *Proc Natl Acad Sci U S A*, vol. 109, no. 37, pp. 14767–14772, 2012.

[245] Y. Li and S. M. Yu, "Targeting and mimicking collagens via triple helical peptide assembly," *Curr Opin Chem Biol*, vol. 17, no. 6, pp. 968–975, 2013.

[246] S. Morlacchi, B. Keller, P. Arcangeli, M. Balzan, F. Migliavacca, G. Dubini, J. Gunn, N. Arnold, A. Narracott, D. Evans, and P. Lawford, "Hemodynamics and in-stent restenosis: Micro-CT images, histology, and computer simulations," *Ann Biomed Eng*, vol. 39, no. 10, pp. 2615–2626, 2011.

[247] P. Mathieu, E. Fitzpatrick, M. D. Luca, P. Cahill, and C. Lally, "Native extracellular matrix orientation determines multipotent vascular stem cell proliferation in response to cyclic uniaxial tensile strain and simulated stent indentation," *Biochem Biophys Rep*, vol. 29, p. 101183, 2022.

[248] E. Müller-Schweinitzer, "Cryopreservation of vascular tissues," *Organogenesis*, vol. 5, no. 3, pp. 97–104, 2009.

[249] Z. Püspöki, M. Storath, D. Sage, and M. Unser, "Transforms and operators for directional bioimage analysis: A survey," in *Focus on Bio-Image Informatics*, pp. 69–93, Springer International Publishing, 2016.

[250] H. Y. Chen, J. Hermiller, A. K. Sinha, M. Sturek, L. Zhu, and G. S. Kassab, "Effects of stent sizing on endothelial and vessel wall stress: potential mechanisms for in-stent restenosis," *J Appl Physiol*, vol. 106, no. 5, pp. 1686–1691, 2009.

[251] A. Kastrati, J. Mehilli, J. Dirschinger, F. Dotzer, H. Schühlen, F.-J. Neumann, M. Fleckenstein, C. Pfafferott, M. Seyfarth, and A. Schömig, "Intracoronary stenting and angiographic results," *Circ*, vol. 103, no. 23, pp. 2816–2821, 2001.

[252] S. Ghazanfari, A. Driessen-Mol, S. P. Hoerstrup, F. P. Baaijens, and C. V. Bouten, "Collagen matrix remodeling in stented pulmonary arteries after transapical heart valve replacement," *Cells Tissues Organs*, vol. 201, no. 3, pp. 159–169, 2016.

[253] M. A. Geith, L. Nothdurfter, M. Heiml, E. Agrafiotis, M. Gruber, G. Sommer, T. G. Schratzenstaller, and G. A. Holzapfel, "Quantifying stent-induced damage in coronary arteries by investigating mechanical and structural alterations," *Acta Biomater*, vol. 116, pp. 285–301, 2020.

[254] R. N. Vaishnav, J. T. Young, and D. J. Patel, "Distribution of stresses and of strain-energy density through the wall thickness in a canine aortic segment," *Circ Res*, vol. 32, no. 5, pp. 577–583, 1973.

[255] C. Chuong and Y. Fung, "Compressibility and constitutive equation of arterial wall in radial compression experiments," *J Biomech*, vol. 17, no. 1, pp. 35–40, 1984.

[256] J. Walraevens, B. Willaert, G. D. Win, A. Ranftl, J. D. Schutter, and J. V. Sloten, "Correlation between compression, tensile and tearing tests on healthy and calcified aortic tissues," *Med Eng Phys*, vol. 30, no. 9, pp. 1098–1104, 2008.

[257] P. B. Dobrin and W. C. Gley, "Elastase, collagenase and the radial elastic properties of arteries," *Experientia*, vol. 41, no. 8, pp. 1040–1042, 1985.

[258] N. F. MacLean, N. L. Dudek, and M. R. Roach, "The role of radial elastic properties in the development of aortic dissections," *J Vasc Surg*, vol. 29, no. 4, pp. 703–710, 1999.

[259] G. Finet, J. Ohayon, and G. Rioufol, "Biomechanical interaction between cap thickness, lipid core composition and blood pressure in vulnerable coronary plaque: impact on stability or instability," *Coron Artery Dis*, vol. 15, no. 1, pp. 13–20, 2004.

[260] A. Tsamis, J. A. Phillippi, R. G. Koch, S. Pasta, A. D'Amore, S. C. Watkins, W. R. Wagner, T. G. Gleason, and D. A. Vorp, "Fiber micro-architecture in the longitudinal-radial and circumferential-radial planes of ascending thoracic aortic aneurysm media," *J Biomech*, vol. 46, no. 16, pp. 2787–2794, 2013.

[261] G. A. Holzapfel and R. W. Ogden, "Constitutive modelling of arteries," *Proc R Soc A Math Phys Eng Sci*, vol. 466, no. 2118, pp. 1551–1597, 2010.

[262] Z. Yosibash, I. Manor, I. Gilad, and U. Willentz, "Experimental evidence of the compressibility of arteries," *J Mech Behav Biomed Mater*, vol. 39, pp. 339–354, 2014.